A Combined Spectroscopic and Theoretical Approach to the Development of Homogeneous Catalysts for Hydrogen Transfer Chemistry

Hall, Andrew

Award date:
2019

Awarding institution:
University of Bath

A Combined Spectroscopic and Theoretical Approach to the Development of Homogeneous Catalysts for Hydrogen Transfer Chemistry

Andrew M. R. Hall

A thesis submitted for the degree of Doctor of Philosophy
University of Bath
Department of Chemistry
May 2019

“I’m being quoted to introduce something, but I have no idea what it is and certainly don’t endorse it.”

— Randall Munroe (XKCD)

TABLE OF CONTENTS

ACKNOWLEDGEMENTS

Firstly, I would like to thank my supervisors; Uli, Antoine and John, along with their respective research groups, for all the help and advice that they have given me throughout my PhD. I would also like to thank my funders: the EPSRC, the Centre for Sustainable Chemical Technologies and Bruker UK Ltd.

I would like to thank Dan Berry and Rachael Broomfield-Tagg for their assistance in performing some of the experiments for the Noyori transfer hydrogenation and photochemical reactions. I would also like to thank Catherine Lyall, Tim Woodman and Shaun Reeksting for their help with setting up and using the analytical equipment, along with Anna Codina, Pete Gierth and Matteo Pennestri at Bruker for their support and many helpful discussions.

I would also like to thank Ted King for providing me with the opportunity to undertake an industrial placement at TgK Scientific, and for his support in the design of the fourth generation FlowNMR apparatus.

Finally, I would like to thank my family and friends who have helped to make my time at Bath very enjoyable, and who also volunteered many hours of their time to help with proof-reading of this thesis – any remaining errors are entirely my own.

ABSTRACT

Understanding the speciation of homogeneous catalysts in solution under turnover conditions and their dynamic evolution over the course of the reaction presents a long-standing challenge for traditional mechanistic investigations based on initial rate analysis and stoichiometric test experiments. This thesis shows how high resolution FlowNMR spectroscopy is a powerful non-invasive tool for studying air-sensitive transition metal catalysis under working conditions in real time, as exemplified by the investigation of the photochemical oxidation of N-allybenzylamine requiring a sustained input of light and air, and the asymmetric transfer hydrogenation of aryl ketones from isopropanol using Noyori catalysts.

Four different designs of FlowNMR apparatus are presented, with comparison between the advantages and disadvantages of each design. Incorporation of additional analytical instrumentation, including Mass Spectrometry, High-Performance Liquid Chromatography and UV-Visible Spectroscopy along with process control instrumentation is discussed.

General considerations for the operation of FlowNMR apparatus are discussed, including flow effects, acquisition parameters and data treatment, which are important to consider if accurate kinetic data are to be obtained from FlowNMR experiments. Flow effects on NMR peak areas are particularly important as they can lead to large quantification errors if overlooked, but can easily be corrected for and even used to increase temporal resolution with suitably adjusted instrument settings.

The Eosin Y mediated photo-oxidation of N-allylbenzylamine was shown to produce imines as primary reaction products from which undesired aldehydes formed after longer reaction times. Facile variation of reaction conditions during the reaction in flow allowed for probe experiments to give information about the mode of action of the photocatalyst.

High quality kinetic data was obtained for the asymmetric transfer hydrogenation of aryl ketones from isopropanol using Noyori's catalyst, allowing mechanistic pathways to be probed. Application of selective excitation pulse sequences allowed fast and quantitative monitoring of a key ruthenium hydride intermediate during catalysis that is shown to interact with both substrates by polarisation transfer experiments. Comparison of reaction profiles with catalyst speciation profiles in conjunction with reaction progress kinetic analysis using variable time normalization and kinetic modelling indicated the existence of two independent catalyst deactivation/inhibition pathways from different catalytic intermediates in this

widely used chemistry. Isotopic labelling directly showed arene loss to be the entry point into deactivation pathways for (arene)Ru(TsDPEN) - type catalysts.

Investigation into the formation of diastereomeric hydride catalyst species in the reaction showed the major hydride species to be the RRS diastereomer, with interconversion between the two diastereomers possible during turnover. The major RRS catalyst diastereomer was found to be responsible for the formation of the major (R)-1-phenylethanol product in a 'lock-and-key' mechanism, whilst the minor RRR catalyst diastereomer remained inactive. Density functional theory calculations were used to predict the catalyst reaction pathway.

A new tethered catalyst is proposed, which is expected to have improved selectivity and stability compared to Noyori's catalyst. Density functional theory calculations were used to predict transition state energy barriers, and indicate that this catalyst is likely to be active in the asymmetric transfer hydrogenation of aryl ketones. A new synthetic route to the formation of this tethered catalyst is proposed, using chiral templating around the ruthenium centre.

ABBREVIATIONS

BBO	Broad Band Observe
BINAP	2,2′-bis(diphenylphosphino)-1,1′-binaphthyl
CF	Correction Factor for flow effects calibration
COSY	Correlation Spectroscopy
CPMG	Carr-Purcell-Meiboom-Gill (pulse sequence)
DCM	Dichloromethane
DFT	Density Functional Theory
DMSO	Dimethylsulfoxide
DOSY	Diffusion Ordered Spectroscopy
DPEN	Diphenyl ethylenediamine
EPR	Electron Paramagnetic Resonance (spectroscopy)
ESI	Electronic Supplementary Information
EXSY	Exchange Spectroscopy
FID	Free Induction Decay
GC	Gas Chromatography
HHLW	Half-height line width
HMBC	Heteronuclear Multiple Bond Correlation
HOL	Hydrogenation, Outer-sphere, Ligand assisted
HPLC	High Performance Liquid Chromatography
HSQC	Heteronuclear Single Quantum Correlation
ID	Inner Diameter
IPA	Isopropanol
IR	Infrared (spectroscopy)
KIE	Kinetic Isotope Effect
KOH	Potassium Hydroxide
KOiPr	Potassium *iso*-propoxide
KOtBu	Potassium *tert*-butoxide
LC	Liquid Chromatography
LED	Light Emitting Diode
MPV	Meerwein–Ponndorf–Verley (reaction)
MS	Mass Spectrometry
NaOH	Sodium Hydroxide
NaOiPr	Sodium *iso*-propoxide

NaOtBu	Sodium *tert*-butoxide
NMR	Nuclear Magnetic Resonance (spectroscopy)
NOE	Nuclear Overhauser Effect
NOESY	Nuclear Overhauser Effect Spectroscopy
NUS	Non-Uniform Sampling
OD	Outer Diameter
PEEK	Polyetheretherketone
PG	Protecting Group
PTFE	Polytetrafluoroethylene
RDS	Rate Determining Step
RF	Radio Frequency
RIV	Reduced Integral Value
RPKA	Reaction Progress Kinetic Analysis
RTD	Residence Time Distribution
SMD	Solvation Model based on Density
SSD	Stuttgart-Dresden (core potential model)
THF	Tetrahydrofuran
TLS	Turnover Limiting Step
TMB	1,3,5-trimethoxybenzene
TOCSY	Total Correlated Spectroscopy
TOF	Turnover Frequency
TOL	Transfer hydrogenation, Outer-sphere, Ligand assisted
TS	Transition State
TsDPEN	mono-tosyl diphenyl ethylenediamine
UV-Vis	Ultra-Violet/Visible (spectroscopy)
VTNA	Variable Time Normalisation Analysis
WET	Water suppression Enhanced through T_1 effects

1 INTRODUCTION

1.1 ON-LINE REACTION MONITORING

Transition metal homogeneous catalysts are amongst the most active and selective known synthetic catalysts.[1] The high degree of tunability of both ligand and metal centre allows catalysts to be designed that are able to selectively and efficiently catalyse reactions that are challenging or impossible to carry out by other means.

Knowledge of the catalyst reaction pathway is vital for the design of new homogeneous catalysts and to optimise the performance of existing catalysts. The usual method of deriving reaction mechanisms requires kinetic data for the reaction, which are used to calculate reaction orders for each component. These reaction orders can then be used alongside structural information from isolated intermediates to propose a reaction mechanism. Computational studies including Density Functional Theory (DFT) calculations are frequently used to model transition states and pathways to test the viability of proposed mechanisms.

1.1.1 Analytical techniques used for reaction monitoring

Many different analytical techniques may be used to measure reaction kinetics, and may be broadly divided into 'differential methods' such as microcalorimetry or electrochemical amperometry, where reaction rate is measured directly, and 'integral methods' including most spectroscopic techniques, where the concentration of a reagent or product is measured over time, and must be differentiated if rate data is required.[2]

Nuclear Magnetic Resonance (NMR), Infrared (IR), Ultraviolet-visible (UV-vis) and Raman spectroscopies, along with Mass Spectrometry (MS) and liquid and gas chromatographies (HPLC and GC) are amongst some of the most frequently used techniques for reaction monitoring. Each of these techniques provides different information about the reaction mixture, and some techniques will be better suited to studying a reaction process than others. In practice it would be rare for more than two or three of these techniques to be required to monitor any single reaction.

NMR and MS are the most commonly used techniques when structural information is required, as both techniques provide information that may be used to identify unknown species within a reaction. MS offers greater sensitivity than NMR, routinely measuring micro- to nano-molar sample concentrations, compared to tens of micro-molar for NMR.

Apart from NMR spectroscopy, all techniques listed above require calibration with reference samples before quantitative concentration data may be obtained. This causes practical issues for quantifying species which cannot be isolated or where the structure is unknown. The inherently quantitative nature of NMR spectroscopy means that the concentration of any species in a reaction may be determined at any point in the reaction, either with implicit reference to starting concentrations, or by explicit comparison to an inert reference compound added to the reaction mixture.

A key advantage of NMR spectroscopy that has helped secure its place as one of the most widely used chemical analytical techniques is the ability to perform two-dimensional experiments, correlating the relative positions of atoms within a molecule.[3-4] Short- and long-range homo- and hetero-nuclear correlation experiments (including COSY, HSQC and HMBC) and through-space correlation (NOESY) experiments allow detailed structural information to be determined about unknown compounds. Time dependent experiments such as Diffusion Ordered Spectroscopy (DOSY) and Exchange Spectroscopy (EXSY) allow information to be obtained about the behaviour and interaction of molecules in solution.[5] Other advanced techniques can help to overcome the inherent sensitivity limitations of NMR, resolve peaks broadened by fast relaxation or chemical exchange and suppress inter-nuclear coupling, aiding analysis of complex mixtures.[3, 6-9]

1.1.2 Approaches for monitoring a chemical reaction

The aim of reaction monitoring is to track changes that are taking place within a reaction in a non-invasive manner, without disturbing the reaction in any way, either chemically, or physically due to a change in the reaction environment.[10]

Reaction monitoring techniques may be coupled directly to a reaction vessel (*in-situ* or *in-line* monitoring), with a probe inserted into the reaction, or where the reaction is carried out inside an observation chamber such as a cuvette. Alternatively, the reaction vessel may be connected indirectly to the monitoring technique (*on-line* monitoring), with sample transferred from the reaction to the analytical instrument via hyphenated tubing or other sample transfer system.

For monitoring techniques that require the sample to be prepared prior to analysis, *off-line* techniques (sometimes referred to as *at-line* in a manufacturing context) are typically used, with samples taken from the reaction at set time-points.

In-situ methods are generally preferred as they do not introduce sampling delays and minimise the chance of disturbance to the reaction system or sample aliquot. *In-situ* methods

are not applicable to every reaction system, and in cases where significant modification to reactor design or reaction conditions is required to accommodate an *in-situ* monitoring technique, *on-line* or *off-line* monitoring may be preferable.

Reaction monitoring by NMR spectroscopy is most commonly performed *in-situ*, with the reaction carried out on a small scale in a standard sample tube within the spectrometer, or *off-line* by sampling from a reaction mixture.

In-situ measurements allow high data densities to be obtained more easily than *off-line* measurements, however the time required to prepare and load the sample into the spectrometer means that initial data points and the information that these provide about catalyst activation, induction periods and initial rates may be lost. The small volume and narrow diameter of a standard NMR tube mean that convectional mixing is limited, which combined with the lack of mechanical stirring results in significant changes to the reaction environment compared to a reaction flask. Accurate measurement of reagent quantities is more challenging at small scale, leading to greater uncertainty in concentrations. Small sample volumes and high surface area-to-volume ratio means that thermal transfer is very efficient, which may be beneficial for ensuring good thermal homogeneity, but also means that small variations in ambient temperatures will have a greater effect on the reaction. The poor mass transport due to the lack of mechanical mixing has been shown to result in significant differences in reaction rate for reactions carried out *in-situ* vs. *on-line*, leading to inaccurate kinetic data being acquired.[11]

Off-line analysis allows reactions to be carried out with minimal disturbance to the reaction conditions. Poor reproducibility is frequently found for *off-line* sampling, due to sample decomposition or incomplete quenching leading to the reaction continuing in the delay between sampling and analysis. Achieving high data density is more challenging for *off-line* sampling due to the large number of samples required.

1.1.3 Techniques for monitoring very fast reactions

Stopped flow and rapid injection techniques have been developed for NMR spectroscopy, reducing the time between initiating the reaction and first data acquisition, overcoming some of the limitations of *in-situ* monitoring by minimising the delay resulting from sample preparation and loading into the spectrometer.[12-19]

In stopped flow analysis, the reagents are loaded into two or more syringes which are connected to a rapid mixing device (either passive or active mixing) located immediately before the observation cell.[12, 15, 18-20] Both syringes are driven simultaneously, pushing the

reagents through the mixer and into the observation cell. A 'stopping syringe' is connected to the outlet of the observation cell, which stops the reagent delivery and triggers the analytical technique once a set volume of reagent has been delivered. This method allows very rapid initiation of the reaction and analysis, with sample mixing and delivery times of less than a few tens of microseconds.[20]

Other rapid injection methods have utilised a compartmentalised NMR tube, with reagents separated by a physical barrier within the tube.[21] To initiate the reaction, this barrier is removed, allowing the reagents to passively mix. A common design uses concentric tubes containing the two reagents, with mixing triggered by lifting the inner tube to release its contents.

The lengthy relaxation time (on the order of 1 to 10 seconds for ^{1}H) required for NMR acquisition limits the temporal resolution of rapid NMR reaction monitoring compared to techniques such as UV-Vis and Raman spectroscopy. However, with a sufficiently reproducible sample preparation technique, multiple datasets with different time offsets can be combined to increase temporal resolution.[12] 'Time efficient' NMR methods have also been developed that allow the acquisition of secondary experiments with different nuclei or parameters during delay times within the pulse sequence; examples include simultaneous ^{13}C-^{1}H HSQC and ^{15}N-^{1}H HSQC acquisition,[22] and TOCSY experiments using two different mixing times.[23] Another approach to circumvent long relaxation times is the use of slice selective techniques, where one spatially resolved volume of the sample may be measured whilst the previous volume is relaxing.[24-25]

1.1.4 Apparatus for on-line NMR spectroscopy

In contrast to *in-situ* and *off-line* NMR techniques that are well established and widely used by synthetic chemists, *on-line* NMR spectroscopy is a comparatively unusual technique. On-line NMR offers many benefits, as the accessibility of the reaction vessel positioned outside of the spectrometer allows variation of temperature, pressure, gas atmosphere, stirring and addition of reagents without interrupting analysis.

Early examples of hyphenated NMR techniques have their origin in combined HPLC-NMR analysis, where NMR is used for structural elucidation of compounds exiting a HPLC column.[26-28] Delivering samples continuously to the NMR spectrometer is challenging using conventional probes, leading to the development of flow probes with a 'bubble cell' design (Figure 1.1).[28] Sample exiting the HPLC column enters the bottom of the probe via narrow diameter polymer tubing before passing to the glass bubble cell, which is surrounded by the Radio Frequency (RF) coils. After exiting the observation cell, sample passes out of the flow

probe to waste or further analysis. These dedicated HPLC-NMR probes are typically only tuned to ^{1}H and ^{13}C, however triple detection probes are also available, allowing multiple nuclei decoupling and acquisition. A pseudo-2D or pseudo-3D spectrum is acquired, plotting NMR acquisition against HPLC elution time.

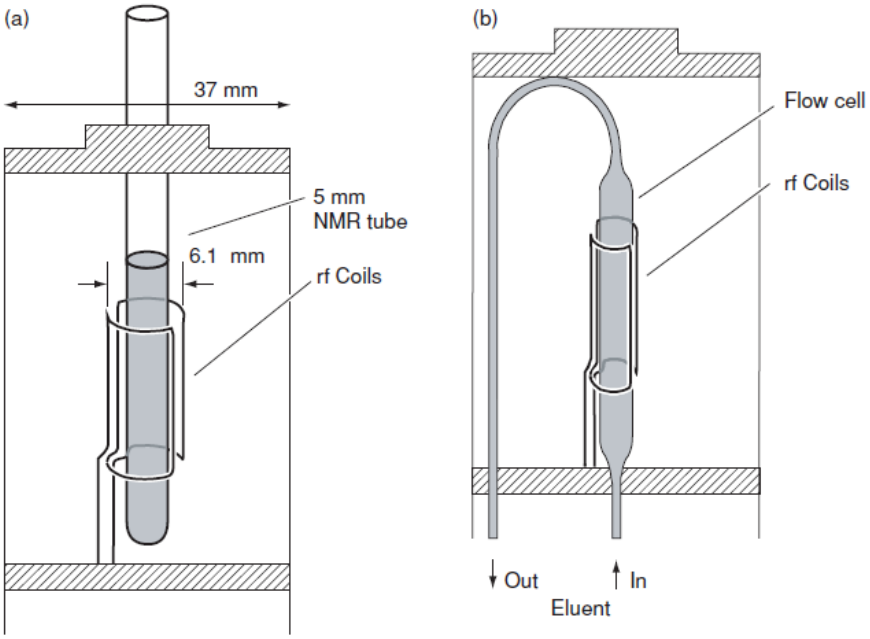

Figure 1.1: Schematics of a) conventional, and b) continuous flow probe designs compatible with cryogenic magnets. Reproduced from Albert, 2003 with permission.[28]

Both commercial and custom flow probe designs have been adapted for use in reaction monitoring.[29-34] The low volume design of HPLC-NMR probes is designed to maximise the temporal resolution of the eluted species, but leads to a poorer signal-to-noise ratio than for conventional probes.

The limitations of HPLC-NMR flow probes for reaction monitoring has led to the development of larger volume flow tubes. Whilst designs vary between different research groups, most flow tubes use a capillary to deliver reaction sample to the bottom of the NMR tube, with the sample exiting at the top of the tube (an example of such a design is shown in Figure 1.2).[35-38] This design allows the flow tube to be used interchangeably with standard NMR probes, taking advantage of the wider range of 1D and 2D experiments that are possible, along with the increased sensitivity of more modern probes, including cryoprobes. A commercial flow tube using the same design was released in 2014, making on-line NMR techniques accessible to users without experience in designing custom equipment or access to workshop facilities.[36, 39]

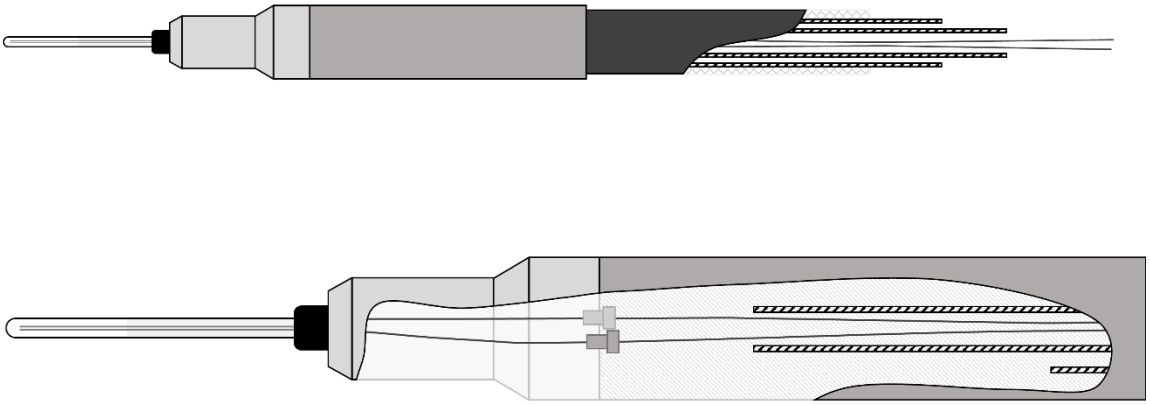

Figure 1.2: Schematic of InsightMR flow tube, showing internal connections of sample transfer and heat exchange fluid. (not to scale)

In addition to larger volume flow probes, microfluidic flow probes have been developed for use in monitoring extremely low volumes of reaction mixtures, typically of biological samples.[40-45] These flow probes feature a microfluidic reactor which is situated inside the NMR coils. In contrast to on-line monitoring techniques where reaction mixture is circulated between a batch reactor located outside the spectrometer and the NMR flow tube/probe, microfluidic flow probes operate in continuous flow, with reagents mixed as they enter the microfluidic reactor and the reaction progressing as a function of distance travelled through the reactor (proportional to residence time) rather than as a function of time.

Recent improvements in permanent magnet construction has led to a rise in the use of 'low field' (≤ 2 Tesla) spectrometers. The small size, low cost and absence of cryogens makes these spectrometers popular both for reaction monitoring in research laboratories and for process control in industry.[33, 46-53] Whilst modern low field instruments equipped with multi-nuclei receiver coils and gradients are available, the resolution and range of experiments available is still more limited than for high field instruments. Low field instruments may be useful for monitoring substrate and product concentrations to determine reaction kinetics, however high field instruments remain superior for the detection, assignment and quantification of low concentration species such as catalytic intermediates. The temperature of the static magnet used in low field spectrometers must be controlled precisely to ensure a homogeneous magnetic field, meaning that reaction samples must be cooled or heated before entering the magnet, which may lead to false reaction kinetics being observed that are not representative of the kinetics elsewhere in the apparatus.

1.1.5 Examples of reactions monitored by on-line NMR spectroscopy

On-line NMR reaction monitoring apparatus has been used to study a wide range of different reactions, including the formation of imines,[36, 54] hydrogenation reactions,[35] acetylation[55] and complex organic transformations.[56] So far, there are very few reported studies of catalytic reactions by high-field FlowNMR spectroscopy, and none that investigate the mechanism of the catalyst directly.

On-line FlowNMR is particularly useful for reactions which require conditions that are challenging for conventional NMR techniques. A good example of this is photochemical reactions, since these require a sustained input of photons for the reaction to proceed, which is very difficult to achieve inside an NMR magnet. This thesis presents the design and implementation of FlowNMR reaction monitoring apparatus, along with kinetic and mechanistic studies for two reactions which take place under conditions that are challenging for conventional NMR methods.

1.2 NMR Techniques Applicable for On-line Reaction Monitoring

One of the key advantages of NMR spectroscopy is the wide range of different experiments that can be performed, allowing complex structural information to be determined. A large number of pulse sequences and NMR experiments have been extensively documented in the literature,[3] and for the most part are applicable to reactions carried out using on-line NMR with only minor modification.

The motion of the sample through the flow probe results in 'in-flow' and 'out-flow' effects which can affect quantification of data if the sample does not have time to acquire full magnetisation before reaching the detector coils.[26, 31, 57] In-flow effects arise from incomplete magnetisation of the sample due to a fast flow rate resulting in the sample having a residence time within the magnetic field of less than the five times the T_1 relaxation time required for 'full' (>99.33%) magnetisation build-up.[58] Out-flow effects are a result of the more rapid apparent decay of the FID signal due to sample exiting the detection region and being replaced by freshly magnetised sample, leading to a reduction in the effective T_2 relaxation time, and a broadening of the NMR peaks. In-flow and out-flow effects in relation to reaction monitoring by FlowNMR are discussed in greater detail in Chapter 3.

Since NMR pulse sequences are typically dependent on a series of pulses and delays, the motion of the sample through the flow tube means that pulse sequences involving long delays may not work properly on flowing samples. This is particularly true for spatially selective pulse sequences such as diffusion ordered spectroscopy (DOSY) but is also of concern for some 2D experiments where mixing delays are used to allow evolution of spin states. For experiments that require multiple scans to construct a spectrum, lengthy acquisition times increase the likelihood of the sample changing during acquisition due to chemical reaction, resulting in time-averaging of the kinetic data.

Rapid acquisition pulse sequences have been developed that allow extremely fast acquisition of some 2D experiments.[59-61] Combined with techniques such as Non-Uniform Sampling (NUS),[62-63] these pulse sequences can reduce the acquisition time of a typical 2D spectrum from tens of minutes to just seconds, with only minimal compromise to spectral resolution. Given a sufficiently concentrated sample, this allows 2D NMR techniques to be used in reaction monitoring applications.

To prevent unwanted solvent kinetic effects from influencing the reaction, and to reduce costs when performing reactions on a larger scale, it is desirable to perform reactions in non-

deuterated solvents. The downside of this is that using non-deuterated solvents results in large solvent peaks being observed in the NMR spectra, which due to the limited range of the spectrometer analogue-to-digital signal converter can prevent the smaller peaks of interest being distinguished from the background noise. Solvent suppression and selective excitation are two different approaches may be used to overcome the problems caused by the use of non-deuterated solvents.

1.2.1 Solvent suppression

One method to improve the signal-to-noise ratio when using non-deuterated solvents is to suppress the solvent peaks, thereby allowing the analogue-to-digital converter range to be adjusted to provide the maximum possible sensitivity for the smaller peaks. The most commonly used solvent suppression methods are 'presaturation' and 'WET' (Water suppression Enhanced through T_1 effects).

Presaturation of the solvent peaks uses a selective, low power pulse with a duration of several seconds to equalise the populations of the nuclear energy levels (saturation), preventing the saturated peaks from experiencing subsequent pulses applied to the sample (Scheme 1.1). Whilst presaturation is the simplest solvent suppression technique to apply, the long pulses required give poorer results on flowing samples than other more advanced methods (Chapter 3).

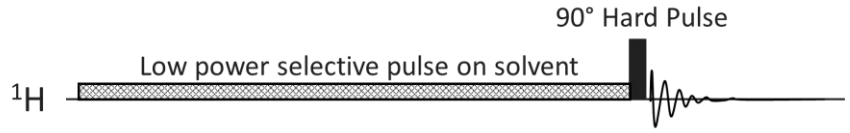

Scheme 1.1: Schematic illustration of a simple presaturation pulse sequence.

WET suppression uses a train of pulses applied selectively to the solvent peak(s), each followed by a gradient pulse which dephases (and therefore eliminates) the solvent signal. A normal hard pulse (or a composite pulse comprising of multiple hard pulses with different phasing as shown in Scheme 1.2) is then applied which acts to excite the remaining non-solvent signal.[3, 9, 64] Application of a decoupling pulse to the ^{13}C channel allows suppression of satellite peaks. WET pulse sequences are shorter and more tolerant to changes in T_1 and magnetic homogeneity than presaturation, meaning that they produce better results on flowing samples.[9]

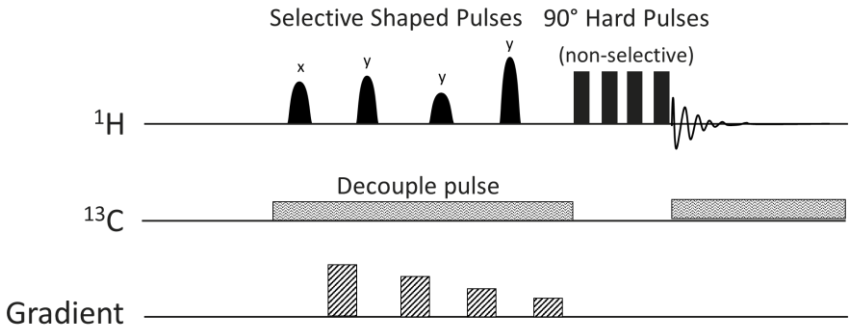

Scheme 1.2: Schematic illustration of a WET pulse sequence for solvent suppression.

1.2.2 Selective Excitation

If only a small region of the NMR spectrum is required for analysis, then selective excitation techniques often yield better results than solvent suppression. Selective excitation may be considered as the reverse of solvent suppression, with all regions of the spectrum other than that selected being suppressed.[7-8]

A 90° hard pulse is applied to bring all magnetisation into the x-y plane. Gradient fields are then used to dephase the sample, with a selective 180° pulse applied to the region of interest so that when the gradient is applied for a second time, this region is refocused (spin-echo), whilst the rest of the spectrum is dephased further (Scheme 1.3). A series of two gradient and 180° pulse elements, with different phases are typically used to obtain maximum suppression of the unwanted regions. As the larger solvent peaks are suppressed, the analogue-to-digital converter range may be adjusted to increase sensitivity towards smaller peaks, effectively increasing the signal-to-noise within the excited region.

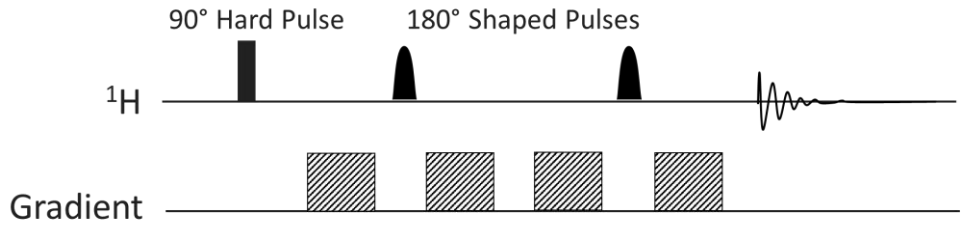

Scheme 1.3: Schematic illustration of a spin echo selective excitation pulse sequence.

1.3 Monitoring Photochemical Reactions with NMR Spectroscopy

Monitoring photochemical reactions using conventional NMR techniques is very challenging, due to the difficulty of ensuring adequate irradiation of the sample within the magnet bore. Various strategies have been used to overcome this issue using *in-situ* analysis, typically using fibre optics or light guides to direct light from an external light source into the magnet.[65-71] These methods are not without drawbacks; since the light is typically directed into the sample from the top of the NMR tube, the amount of light reaching the sample varies dramatically throughout the sample volume, which may lead to false kinetics due to different reaction rates at the top and bottom of the sample tube.[72]

For this reason, many photochemical reactions are studied using optical spectroscopies such as UV-Vis absorption or fluorescence or IR and Raman spectroscopies.[70, 73] When NMR is used as a monitoring technique for photochemical reactions, it is typically performed as off-line analysis, with samples taken from a reaction mixture which are then worked up and re-dissolved in a suitable solvent for NMR analysis.

Many photochemical reactions involve radical species containing unpaired electrons. If high concentrations of radicals are present in a reaction mixture, then this may cause faster relaxation of nuclei, resulting in an unwanted broadening of NMR peaks. Since the lifetime of free radical species in a reaction mixture is typically very short, radicals are less likely to impact on spectral quality for reactions monitored on-line or off-line than for in-situ monitoring, due to the delay between the sample leaving the illuminated reaction vessel and analysis. Radical species within a reaction mixture may studied directly using Electron Paramagnetic Resonance (EPR) spectroscopy.

Whilst there are many published examples of off-line and in-situ NMR monitoring of photochemical reactions, there are relatively few examples of the use of on-line NMR techniques. Prior to the publication of our paper investigating the photochemical oxidation of N-allylbenzylamine (Chapter 4), only two examples where on-line NMR spectroscopy was used for monitoring a photochemical reaction existed in the literature. One study utilised a HPLC-NMR flow probe to monitor the degradation of environmental pollutants under UV irradiation,[34] whilst the other used a low-field spectrometer to analyse the reaction products from a photochemical flow reactor.[74] Neither study reported reaction kinetic data or mechanistic information derived from the NMR monitoring.

Since the publication of this work, a number of other papers reporting the use of on-line NMR reaction monitoring of photochemical reactions have been published.[75-76]

1.4 CATALYTIC ASYMMETRIC TRANSFER HYDROGENATION

Transfer hydrogenation is a general category of reactions that add hydrogen across an unsaturated bond, without the use of elemental hydrogen gas. Avoiding the use of hydrogen gas enables reactions to be carried out with milder conditions, and without the risk of handling potentially explosive gas mixtures.

Whilst transfer hydrogenation may be applied to alkenes[77-78] and to imines,[79-83] it is most commonly used as a means of selective reduction of ketone functional groups to alcohols (Scheme 1.4), with a large number of different catalytic systems published in the literature.[84-87] Traditional heterogeneous hydrogenation catalysts such as Pd/C or Pt/C are mostly unselective and reduce C=O, C=N and C=C equally. Selective hydrogenation of C=O or C=N bonds in the presence of C=C functional groups has therefore tended to rely on stoichiometric reducing agents such as $NaBH_4$ and $LiAlH_4$, which have poor atom efficiency and can pose practical challenges when used on large scale.[88] Homogeneous transfer hydrogenation catalysts offer an alternative to these stoichiometric hydride donors, enabling milder reaction conditions to be used and providing greater selectivity.

Transfer hydrogenation reactions are particularly useful for the generation of chiral alcohols from prochiral ketones, or for kinetic resolution of racemic alcohol mixtures, with many chiral transfer hydrogenation catalysts known.[84, 86, 89-93] Both heterogeneous and homogeneous transfer hydrogenation catalysts are routinely used, however homogenous catalysts are generally favoured due to the higher reaction rate and greater selectivity that they offer.

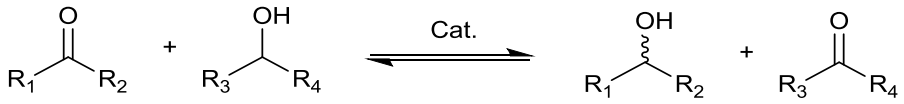

Scheme 1.4: Catalytic transfer hydrogenation reaction

The transfer hydrogenation reaction is reversible, with the equilibrium conversion determined by the relative thermodynamics of the reagents and products. When using a chiral catalyst, the selectivity is a result of competing kinetics for the R and S pathways, leading to one chiral product being favoured. As the reaction is reversible, this selectivity is eroded over time by repeated forward and reverse reaction until a racemic equilibrium mixture is obtained. To achieve a chiral product it is therefore necessary to halt the reaction once there is sufficient conversion to the desired product, but before the mixture has had time to reach the true equilibrium.

1.4.1 Catalysts and mechanism

Early systems for transfer hydrogenation such as the Meerwein–Ponndorf–Verley (MPV) reaction used metal alkoxide catalysts (typically aluminium based) to facilitate an intermolecular reaction between a ketone and an alcohol (Scheme 1.5).[94-95] In this reaction the metal alkoxide coordinates to the ketone, activating the double bond, whilst also helping to hold the two molecules in the correct geometry for the transfer of the hydrogen atom between the two carbon atoms.

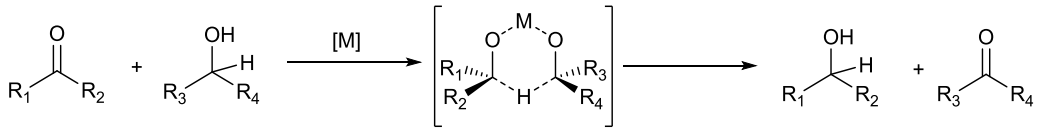

Scheme 1.5: Meerwein–Ponndorf–Verley (MPV) reaction for transfer hydrogenation of alcohols and ketones using a metal alkoxide catalyst, [M], such as an aluminium alkoxide.

Whilst the MPV reaction is a very simple and effective means of transfer hydrogenation that is used in many industrial processes including the manufacture of flavourings,[86] the reaction is unselective and a mixture of isomers will be produced if the alcohol and ketone contains two different substituents. In order for the reaction to be catalytic, the binding of the metal alkoxide to the alcohol must be reversible, otherwise the alkoxide will remain attached to the alcohol at the end of the reaction and cannot re-enter the catalytic cycle. In many cases it is necessary to add a stoichiometric quantity of alkoxide to overcome this slow exchange and achieve a good reaction rate.[95] Many metal alkoxides are water-sensitive and so may be deactivated by trace quantities of water in the reaction mixture.

To overcome the selectivity issues with the MPV reaction for alcohols and ketones containing multiple different substituents, a large number of homogeneous asymmetric transfer hydrogenation catalysts have been developed and have been reviewed extensively in the recent literature (Scheme 1.6).[86, 89] Most asymmetric transfer hydrogenation catalysts are based on group 8 and 9 transition metals such as Ru, Rh and Ir.[86] Iron based catalysts are also known and have been developed as cheaper alternatives in this reaction, however these are generally less active than catalysts based on heavier metals.[84-85, 91, 96]

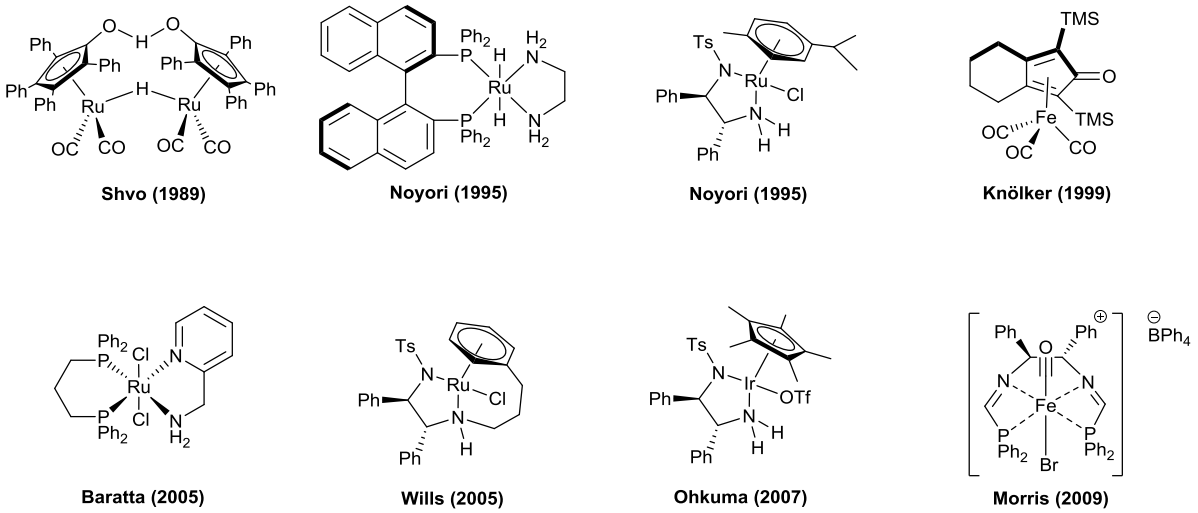

Scheme 1.6: Examples of some transfer hydrogenation catalysts.

Many catalysts feature N-heterocyclic carbene, diamine or phosphine based ligands with a protonated heteroatom bound to the metal. These ligands are proposed to act in a non-innocent manner with heteroatoms on the ligand directly involved in the hydrogen transfer mechanism.[97-99] A catalytic amount of base (typically NaOH or KOH) is often used to facilitate transfer of the alcohol OH proton, with transfer of the hydride occurring via a metal-hydride intermediate.

1.4.2 Noyori's TsDPEN catalyst

One of the best known asymmetric transfer hydrogenation catalysts is the highly active chiral Noyori catalyst **(1)** (Scheme 1.7), for which Noyori received a share in the 2001 Nobel Prize in Chemistry.[90, 100-101]

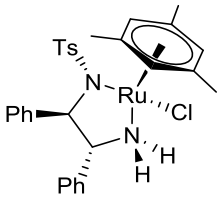

*Scheme 1.7: Noyori asymmetric transfer hydrogenation catalyst (**1**). Whilst the catalyst is shown with a mesitylene ligand, numerous other aromatic groups, including benzene, para-cymene and hexamethylbenzene are also reported to produce active catalysts.*

The Noyori catalyst is usually synthesised as a chloride pre-catalyst, **(1)**, which is a reasonably air-stable orange solid. The chloride pre-catalyst shows no catalytic activity on its own, however addition of one equivalent of base leads to the formation of a 16-electron 'unsaturated' complex, **(2)** which is thought to be the active catalyst in the reaction. This unsaturated intermediate rapidly reacts with primary and secondary (but not tertiary) alcohols to form an 18-electron hydride complex, **(3)**, producing the corresponding ketone as a by-product. This hydride intermediate has been shown to react with ketones,

asymmetrically reducing them to chiral alcohols, regenerating **(2)** in the process (Scheme 1.8).[97-98, 100, 102-103]

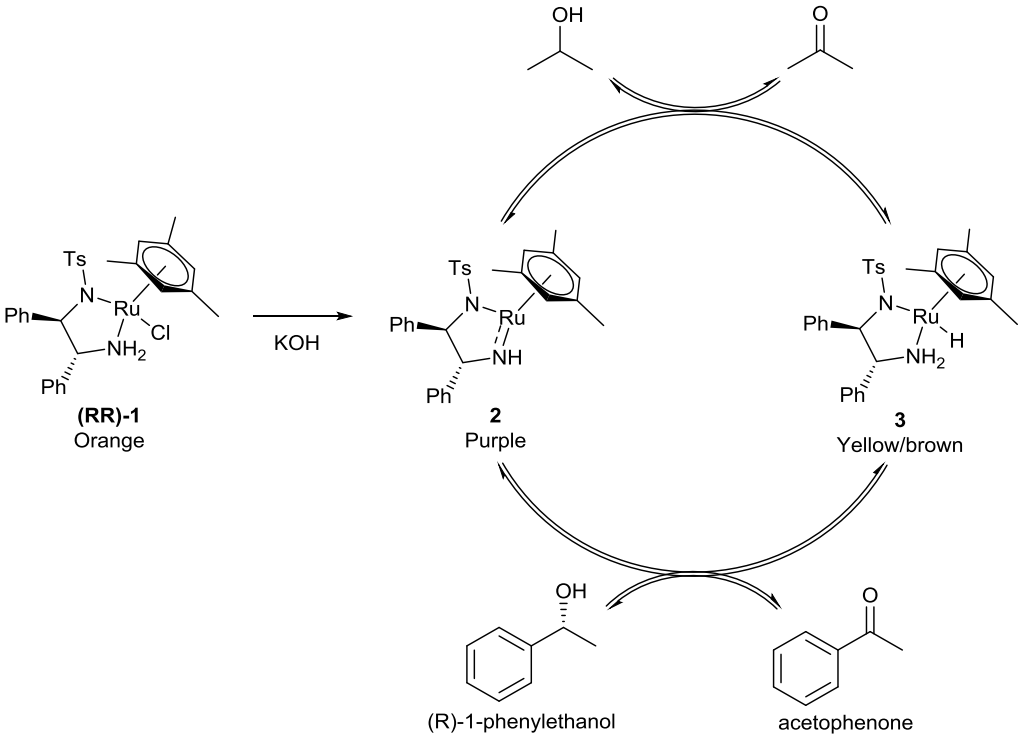

Scheme 1.8: Proposed catalytic cycle for the Noyori catalyst in the transfer hydrogenation of acetophenone to 1-phenylethanol.[100-101, 103]

1.4.3 The mechanism of hydrogen transfer

The reaction with the Noyori catalyst is thought to occur via an outer-sphere mechanism with transition states **(2')** and **(3')** (Scheme 1.9)**.** In an analogous mechanism to the MPV reaction, the H_2-donor/acceptor forms a 6-membered cyclic transition state where the protic NH interacts with the oxygen and the hydridic RuH interacts with the carbon.[103] As the NH acts as an internal base that is built in to the catalyst, no additional base is required after activation of the catalyst, unlike many other catalysts which require a catalytic quantity of base to facilitate proton transfer.[104]

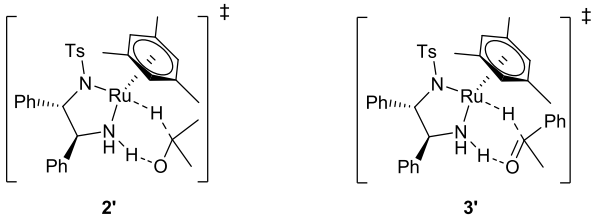

Scheme 1.9: Proposed transition states for the Noyori catalyst in the transfer hydrogenation of acetophenone.[103]

The outer-sphere mechanism is proposed to be the reason behind the 'non-innocent' behaviour of many transfer hydrogenation catalysts containing proton bearing heteroatoms

in close proximity to the metal centre, even if the heteroatom is not bound directly to the metal.

The Shvo catalyst is also thought to react via an outer-sphere mechanism (Scheme 1.10).[80] Unlike the Noyori catalyst, the ligand in the Shvo catalyst does not contain any nitrogen atoms and has no heteroatoms adjacent to the metal centre, with reaction occurring instead at an oxygen atom on the aromatic ring. As well as catalysing transfer hydrogenation of alcohols and ketones, the Shvo catalyst is also known to catalyse a number of other reactions, including the disproportionation of alcohols to esters, hydrogenation of alkynes, and reduction of imines to amines.[87, 105-106]

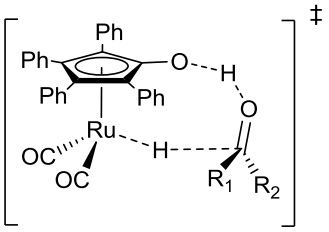

Scheme 1.10: Proposed transition state for the Shvo catalyst in the transfer hydrogenation reaction.[80]

The outer-sphere mechanism proposed by Noyori is by no means the only possible means of transferring hydrogen between complex **(3)** and a ketone. Much of the early computational work performed on the Noyori system focused on comparison with the classical inner-sphere mechanism, where the ketone binds directly to the metal centre with hydride transfer occurring via a 4-membered transition state.[99] Most studies now agree that the outer-sphere mechanism is likely to dominate in the Noyori system, due to steric hinderance at ruthenium preventing both hydride and substrate from binding simultaneously. Inner-sphere intermediates may however play a role in non-productive or off-cycle species.[102, 107-109]

Mono-alkylation of the amine NH in **(1)** does not affect the ability of the complex to catalyse transfer hydrogenation of alcohols,[110-111] however double alkylation leads to a significant drop in catalytic activity.[112-113] This has been taken as evidence that an outer-sphere mechanism must be occurring, with assistance from the NH ligand.[103, 114] The decrease in activity is less severe for imine reduction than for ketones, suggesting that an inner sphere mechanism is also possible, but at a reduced rate.[112-113]

1.4.4 The role of base in Noyori asymmetric transfer hydrogenation

One equivalent of base (typically KOH, NaOH or NaO^{i}Pr) is required to remove the chloride from **(1)**, generating the unsaturated intermediate, **(2)**. It has been shown that using pre-formed unsaturated intermediate, **(2)**, or hydride intermediate, **(3)**, catalysis may be carried

out in the absence of base, showing that base is only required for the activation of the catalyst.[115]

Despite this, numerous papers have shown that the choice of base along with concentration of base can have a significant effect on the reaction rate, both for **(1)**, and other transfer hydrogenation catalysts.[116-118] A specific example of the influence of base on the reaction is the 'potassium effect', in which the rate of reaction of $RuCl_2$(BINAP)(DPEN) catalysts is increased when potassium bases are used compared to other cations.[81, 102, 104, 119-120] The non-innocent role of the base is sometimes used as evidence of a conventional inner-sphere reaction mechanism, where the base helps to mediate the transfer of a proton from the catalyst to the substrate.

1.5 REFERENCES

1. Crabtree, R. H. In *The Organometallic Chemistry of the Transition Metals*, 4th ed.; John Wiley & Sons, Inc.: Hoboken, New Jersey, 2005; Vol. 1, pp 235-273.

2. House, J. E., In *Principles of chemical kinetics*. 2nd ed.; Elsevier Academic Press: Amsterdam, Boston, 2007.

3. Berger, S.; Braun, S., In *200 and more NMR experiments : a practical course*. 3rd ed.; Wiley-VCH: Weinheim, Germany, 2011.

4. Kupce, E.; Claridge, T. D. W., NOAH: NMR Supersequences for Small Molecule Analysis and Structure Elucidation. *Angew. Chem. Int. Ed. Engl.* **2017,** 56, 11779-11783.

5. Lokesh, N.; Seegerer, A.; Hioe, J.; Gschwind, R. M., Chemical Exchange Saturation Transfer in Chemical Reactions: A Mechanistic Tool for NMR Detection and Characterization of Transient Intermediates. *J. Am. Chem. Soc.* **2018,** 140, 1855-1862.

6. Jones, A. B.; Lloyd-Jones, G. C.; Uhrin, D., SHARPER Reaction Monitoring: Generation of a Narrow Linewidth NMR Singlet, without X-Pulses, in an Inhomogeneous Magnetic Field. *Anal. Chem.* **2017,** 89, 10013-10021.

7. Liu, H.; Zhang, S., Selective Excitation with Asymmetric Adiabatic Pulses for NMR Spectroscopy. *ChemPhysChem* **2015,** 16, 621-627.

8. Morris, G. A.; Freeman, R., Selective excitation in Fourier transform nuclear magnetic resonance. *J. Magn. Reson.* **2011,** 213, 214-243.

9. Smallcombe, S. H.; Patt, S. L.; Keifer, P. A., WET Solvent Suppression and Its Applications to LC NMR and High-Resolution NMR Spectroscopy. *J. Magn. Reson. A* **1995,** 117, 295-303.

10. Levenspiel, O., In *Chemical Reaction Engineering*. 3rd ed.; Wiley: New York ; Chichester, 1999.

11. Foley, D. A.; Dunn, A. L.; Zell, M. T., Reaction monitoring using online vs tube NMR spectroscopy: seriously different results. *Magn. Reson. Chem.* **2016,** 54, 451-456.

12. Johnston, C. P.; West, T. H.; Dooley, R. E.; Reid, M.; Jones, A. B.; King, E. J.; Leach, A. G.; Lloyd-Jones, G. C., Anion-Initiated Trifluoromethylation by $TMSCF_3$: Deconvolution of the Siliconate–Carbanion Dichotomy by Stopped-Flow NMR/IR. *J. Am. Chem. Soc.* **2018,** 140, 11112-11124.

13. Keifer, P. A., Flow injection analysis NMR (FIA–NMR): a novel flow NMR technique that complements LC–NMR and direct injection NMR (DI–NMR). *Magn. Reson. Chem.* **2003,** 41, 509-516.

14. McGarrity, J. F.; Prodolliet, J.; Smyth, T., Rapid injection NMR: A simple technique for the observation of reactive intermediates. *Org. Magn. Resonance* **1981,** 17, 59-65.

15. Harbou, E. v.; Behrens, R.; Berje, J.; Brächer, A.; Hasse, H., Studying Fast Reaction Kinetics with Online NMR Spectroscopy. *Chem. Ing. Tech.* **2016,** 89, 369-378.

16. Yushmanov, P. V.; Furo, I., A rapid-mixing design for conventional NMR probes. *J. Magn. Reson.* **2005,** 175, 264-270.

17. Kind, J.; Thiele, C. M., Still shimming or already measuring?--Quantitative reaction monitoring for small molecules on the sub minute timescale by NMR. *J. Magn. Reson.* **2015,** 260, 109-115.

18. Christianson, M. D.; Tan, E. H. P.; Landis, C. R., Stopped-flow NMR: determining the kinetics of [*rac*-(C_2H_4(1-indenyl)$_2$)ZrMe][MeB(C_6F_5)$_3$]-catalyzed polymerization of 1-hexene by direct observation. *J. Am. Chem. Soc.* **2010,** 132, 11461-11463.

19. Green, D. B.; Lane, J.; Wing, R. M., A Standard Session Stopped-Flow NMR Tube. *Appl. Spectrosc.* **1987,** 41, 847-851.

20. Cox, P. A.; Reid, M.; Leach, A. G.; Campbell, A. D.; King, E. J.; Lloyd-Jones, G. C., Base-Catalyzed Aryl-B(OH)$_2$ Protodeboronation Revisited: From Concerted Proton Transfer to Liberation of a Transient Aryl Anion. *J. Am. Chem. Soc.* **2017,** 139, 13156-13165.

21. Mix, A.; Jutzi, P.; Rummel, B.; Hagedorn, K., A Simple Double-Chamber NMR Tube for the Monitoring of Chemical Reactions by NMR Spectroscopy. *Organometallics* **2010,** 29, 442-447.

22. Sattler, M.; Maurer, M.; Schleucher, J.; Griesinger, C., A simultaneous ^{15}N,^{1}H- and ^{13}C,^{1}H-HSQC with sensitivity enhancement and a heteronuclear gradient echo. *J. Biomol. NMR* **1995,** 5, 97-102.

23. Nolis, P.; Motiram-Corral, K.; Perez-Trujillo, M.; Parella, T., Interleaved Dual NMR Acquisition of Equivalent Transfer Pathways in TOCSY and HSQC Experiments. *ChemPhysChem* **2019,** 20, 356-360.

24. Castañar, L.; Nolis, P.; Virgili, A.; Parella, T., Simultaneous Multi-Slice Excitation in Spatially Encoded NMR Experiments. *Chem. Eur. J.* **2013,** 19, 15472-15475.

25. Niklas, T.; Stalke, D.; John, M., Single-shot titrations and reaction monitoring by slice-selective NMR spectroscopy. *Chem. Commun.* **2015,** 51, 1275-1277.

26. Albert, K.; Nieder, M.; Bayer, E.; Spraul, M., Continuous-flow nuclear magnetic resonance. *J. Chromatogr. A* **1985,** 346, 17-24.

27. Albert, K.; Bayer, E., High-performance liquid chromatography—nuclear magnetic resonance on-line coupling. *TrAC, Trends Anal. Chem.* **1988,** 7, 288-293.

28. Albert, K. In *On-Line LC-NMR And Related Techniques*, John Wiley & Sons, Ltd: 2003; pp 1-22.

29. Bernstein, M. A.; Stefinovic, M.; Sleigh, C. J., Optimising reaction performance in the pharmaceutical industry by monitoring with NMR. *Magn. Reson. Chem.* **2007,** 45, 564.

30. Fyfe, C. A.; Cocivera, M.; Damji, S. W. H., Flow and stopped-flow nuclear magnetic resonance investigations of intermediates in chemical reactions. *Acc. Chem. Res.* **1978,** 11, 277-282.

31. Nordon, A.; McGill, C. A.; Littlejohn, D., Process NMR spectrometry. *Analyst* **2001,** 126, 260-272.

32. Fyfe, C. A.; Cocivera, M.; Damji, S. W. H.; Hostetter, T. A.; Sproat, D.; O'Brien, J., Apparatus for the measurement of transient species and effects in flowing systems by high-resolution nuclear magnetic resonance spectroscopy. *J. Magn. Reson.* **1976,** 23, 377-384.

33. Maiwald, M.; Fischer, H. H.; Kim, Y.-K.; Albert, K.; Hasse, H., Quantitative high-resolution on-line NMR spectroscopy in reaction and process monitoring. *J. Magn. Reson.* **2004,** 166, 135-146.

34. Bliumkin, L.; Dutta Majumdar, R.; Soong, R.; Adamo, A.; Abbatt, J. P. D.; Zhao, R.; Reiner, E.; Simpson, A. J., Development of an in Situ NMR Photoreactor To Study Environmental Photochemistry. *Environ. Sci. Technol.* **2016,** 50, 5506-5516.

35. Buser, J. Y.; McFarland, A. D., Reaction characterization by flow NMR: quantitation and monitoring of dissolved H_2 via flow NMR at high pressure. *Chem. Commun.* **2014,** 50, 4234-4237.

36. Foley, D. A.; Bez, E.; Codina, A.; Colson, K. L.; Fey, M.; Krull, R.; Piroli, D.; Zell, M. T.; Marquez, B. L., NMR flow tube for online NMR reaction monitoring. *Anal. Chem.* **2014,** 86, 12008-12013.

37. Blanazs, A.; Bristow, T. W.; Coombes, S. R.; Corry, T.; Nunn, M.; Ray, A. D., Coupling and optimisation of online nuclear magnetic resonance spectroscopy and mass spectrometry for process monitoring to cover the broad range of process concentration. *Magn. Reson. Chem.* **2017,** 55, 274-282.

38. Marquez, B. F., Michael; Colson, Kimberly L.; Krull, Robert; Bez, Eckhard; Piroli, Don; Maas, Werner E. NMR reaction monitoring flow cell. US Patent 20120092013A1, April 19, 2012.

39. InsightMR: Real-Time Data Analysis and Acquisition Control. www.bruker.com/products/mr/nmr/nmr-software/nmr-software/insightmr/overview.html (accessed 10/10/2018).

40. Fratila, R. M.; Gomez, M. V.; Sýkora, S.; Velders, A. H., Multinuclear nanoliter one-dimensional and two-dimensional NMR spectroscopy with a single non-resonant microcoil. *Nat Commun* **2014,** 5, 3025.

41. Bart, J.; Kolkman, A. J.; Oosthoek-de Vries, A. J.; Koch, K.; Nieuwland, P. J.; Janssen, H.; van Bentum, J.; Ampt, K. A. M.; Rutjes, F. P. J. T.; Wijmenga, S. S.; Gardeniers, H.; Kentgens, A. P. M., A Microfluidic High-Resolution NMR Flow Probe. *J. Am. Chem. Soc.* **2009,** 131, 5014-5015.

42. Finch, G.; Yilmaz, A.; Utz, M., An optimised detector for in-situ high-resolution NMR in microfluidic devices. *J. Magn. Reson.* **2016,** 262, 73-80.

43. Gökay, O.; Albert, K., From single to multiple microcoil flow probe NMR and related capillary techniques: a review. *Anal. Bioanal. Chem.* **2012,** 402, 647-669.

44. Jones, C. J.; Larive, C. K., Could smaller really be better? Current and future trends in high-resolution microcoil NMR spectroscopy. *Anal. Bioanal. Chem.* **2012,** 402, 61-68.

45. Zalesskiy, S. S.; Danieli, E.; Blümich, B.; Ananikov, V. P., Miniaturization of NMR Systems: Desktop Spectrometers, Microcoil Spectroscopy, and "NMR on a Chip" for Chemistry, Biochemistry, and Industry. *Chem. Rev.* **2014,** 114, 5641-5694.

46. Maiwald, M.; Fischer, H. H.; Hasse, H., Quantitative hochauflösende Online-NMR-Spektroskopie im Reaktions- und Prozessmonitoring. *Chem. Ing. Tech.* **2004,** 76, 965-969.

47. Maiwald, M.; Fischer, H. H.; Kim, Y.-K.; Hasse, H., Quantitative on-line high-resolution NMR spectroscopy in process engineering applications. *Anal. Bioanal. Chem.* **2003,** 375, 1111-1115.

48. Meyer, K.; Kern, S.; Zientek, N.; Guthausen, G.; Maiwald, M., Process control with compact NMR. *TrAC, Trends Anal. Chem.* **2016,** 83, 39-52.

49. Silva Elipe, M. V.; Milburn, R. R., Monitoring chemical reactions by low-field benchtop NMR at 45 MHz: pros and cons. *Magn. Reson. Chem.* **2016,** 54, 437-443.

50. Räntzsch, V.; Wilhelm, M.; Guthausen, G., Hyphenated low-field NMR techniques: combining NMR with NIR, GPC/SEC and rheometry. *Magn. Reson. Chem.* **2016,** 54, 494-501.

51. Zientek, N.; Laurain, C.; Meyer, K.; Paul, A.; Engel, D.; Guthausen, G.; Kraume, M.; Maiwald, M., Automated data evaluation and modelling of simultaneous ^{19}F-^{1}H medium-resolution NMR spectra for online reaction monitoring. *Magn. Reson. Chem.* **2016,** 54, 513-520.

52. Zientek, N.; Meyer, K.; Kern, S.; Maiwald, M., Quantitative Online NMR Spectroscopy in a Nutshell. *Chem. Ing. Tech.* **2016,** 88, 698-709.

53. Sans, V.; Porwol, L.; Dragone, V.; Cronin, L., A self optimizing synthetic organic reactor system using real-time in-line NMR spectroscopy. *Chem. Sci.* **2015,** 6, 1258-1264.

54. Foley, D. A.; Wang, J.; Maranzano, B.; Zell, M. T.; Marquez, B. L.; Xiang, Y.; Reid, G. L., Online NMR and HPLC as a reaction monitoring platform for pharmaceutical process development. *Anal. Chem.* **2013,** 85, 8928-8932.

55. Khajeh, M.; Bernstein, M. A.; Morris, G. A., A simple flowcell for reaction monitoring by NMR. *Magn. Reson. Chem.* **2010,** 48, 516-522.

56. Foley, D. A.; Doecke, C. W.; Buser, J. Y.; Merritt, J. M.; Murphy, L.; Kissane, M.; Collins, S. G.; Maguire, A. R.; Kaerner, A., ReactNMR and ReactIR as reaction monitoring and mechanistic elucidation tools: the NCS mediated cascade reaction of alpha-thioamides to alpha-thio-beta-chloroacrylamides. *J. Org. Chem.* **2011,** 76, 9630-9640.

57. Sudmeier, J. L.; Günther, U. L.; Albert, K.; Bachovchin, W. W., Sensitivity Optimization in Continuous-Flow FTNMR. *J. Magn. Reson. A* **1996,** 118, 145-156.

58. Claridge, T. D. W., In *High-resolution NMR techniques in organic chemistry*. 3rd ed.; Elsevier: Amsterdam, 2009.

59. Giraudeau, P.; Frydman, L., Ultrafast 2D NMR: an emerging tool in analytical spectroscopy. *Annu Rev Anal Chem (Palo Alto Calif)* **2014,** 7, 129-161.

60. Schulze-Sünninghausen, D.; Becker, J.; Luy, B., Rapid Heteronuclear Single Quantum Correlation NMR Spectra at Natural Abundance. *J. Am. Chem. Soc.* **2014,** 136, 1242-1245.

61. Ndukwe, I. E.; Shchukina, A.; Kazimierczuk, K.; Butts, C. P., Rapid and safe ASAP acquisition with EXACT NMR. *Chem. Commun.* **2016,** 52, 12769-12772.

62. Li, D.; Hansen, A. L.; Bruschweiler-Li, L.; Brüschweiler, R., Non-Uniform and Absolute Minimal Sampling for High-Throughput Multidimensional NMR Applications. *Chem. Eur. J.* **2018,** 24, 11535-11544.

63. Billeter, M. A.; Orekhov, V.; Arthanari, H., In *Novel sampling approaches in higher dimensional NMR*. Springer: Heidelberg, New York, 2012.

64. Ogg, R. J.; Kingsley, R. B.; Taylor, J. S., WET, a T1- and B1-Insensitive Water-Suppression Method for in Vivo Localized 1H NMR Spectroscopy. *Journal of Magnetic Resonance, Series B* **1994,** 104, 1-10.

65. Ball, G. E. In *Spectrosc. Prop. Inorg. Organomet. Compd.*, RSC: 2010; Vol. 41, pp 262-287.

66. Closs, G. L.; Miller, R. J., Laser flash photolysis with NMR detection. Submicrosecond time-resolved CIDNP: kinetics of triplet states and biradicals. *J. Am. Chem. Soc.* **1981,** 103, 3586-3588.

67. Feldmeier, C.; Bartling, H.; Magerl, K.; Gschwind, R. M., LED-Illuminated NMR Studies of Flavin-Catalyzed Photooxidations Reveal Solvent Control of the Electron-Transfer Mechanism. *Angew. Chem. Int. Ed.* **2015,** 54, 1347-1351.

68. Mills, A.; O'Rourke, C., Photocatalytic organic synthesis in an NMR tube: CC coupling of phenoxyacetic acid and acrylamide. *Catal. Today* **2014,** 230, 256-264.

69. Page, T. F., Jr., Method for in situ photochemical studies by high resolution nuclear magnetic resonance. *Chem. Ind.* **1969**, 1462-3.

70. Seegerer, A.; Nitschke, P.; Gschwind, R. M., Combined In Situ Illumination-NMR-UV/Vis Spectroscopy: A New Mechanistic Tool in Photochemistry. *Angew. Chem. Int. Ed. Engl.* **2018,** 57, 7493-7497.

71. Torres, O.; Procacci, B.; Halse, M. E.; Adams, R. W.; Blazina, D.; Duckett, S. B.; Eguillor, B.; Green, R. A.; Perutz, R. N.; Williamson, D. C., Photochemical Pump and NMR Probe: Chemically Created NMR Coherence on a Microsecond Time Scale. *J. Am. Chem. Soc.* **2014,** 136, 10124-10131.

72. Mills, A.; O'Rourke, C., In Situ, Simultaneous Irradiation and Monitoring of a Photocatalyzed Organic Oxidation Reaction in a TiO_2-Coated NMR Tube. *J. Org. Chem.* **2015,** 80, 10342-10345.

73. Roig, B.; Touraud, E.; Thomas, O., Photochemical reaction monitoring by ultra-violet spectrophotometry. *Spectrochim. Acta Mol. Biomol. Spectrosc.* **2002,** 58, 2925-2930.

74. Emmanuel, N.; Mendoza, C.; Winter, M.; Horn, C. R.; Vizza, A.; Dreesen, L.; Heinrichs, B.; Monbaliu, J.-C. M., Scalable Photocatalytic Oxidation of Methionine under Continuous-Flow Conditions. *Org. Process Res. Dev.* **2017,** 21, 1435-1438.

75. Rehm, T. H.; Hofmann, C.; Reinhard, D.; Kost, H.-J.; Löb, P.; Besold, M.; Welzel, K.; Barten, J.; Didenko, A.; Sevenard, D. V.; Lix, B.; Hillson, A. R.; Riegel, S. D., Continuous-flow synthesis of fluorine-containing fine chemicals with integrated benchtop NMR analysis. *Reaction Chemistry & Engineering* **2017,** 2, 315-323.

76. Zhao, F.; Cambié, D.; Hessel, V.; Debije, M. G.; Noël, T., Real-time reaction control for solar production of chemicals under fluctuating irradiance. *Green Chem.* **2018,** 20, 2459-2464.

77. Brunel, J. M., Pd/P(^{t}Bu)$_3$: A Mild Catalyst for Selective Reduction of Alkenes under Transfer-Hydrogenation Conditions. *Synlett* **2007,** 2007, 0330-0332.

78. Paryzek, Z.; Koenig, H.; Tabaczka, B., Ammonium Formate/Palladium on Carbon: A Versatile System for Catalytic Hydrogen Transfer Reductions of Carbon-Carbon Double Bonds. *Synthesis* **2003,** 2003, 2023-2026.

79. Casey, C. P.; Bikzhanova, G. A.; Guzei, I. A., Stereochemistry of Imine Reduction by a Hydroxycyclopentadienyl Ruthenium Hydride. *J. Am. Chem. Soc.* **2006,** 128, 2286-2293.

80. Casey, C. P.; Singer, S. W.; Powell, D. R.; Hayashi, R. K.; Kavana, M., Hydrogen Transfer to Carbonyls and Imines from a Hydroxycyclopentadienyl Ruthenium Hydride: Evidence for Concerted Hydride and Proton Transfer. *J. Am. Chem. Soc.* **2001,** 123, 1090-1100.

81. John, J. M.; Takebayashi, S.; Dabral, N.; Miskolzie, M.; Bergens, S. H., Base-Catalyzed Bifunctional Addition to Amides and Imides at Low Temperature. A New Pathway for Carbonyl Hydrogenation. *J. Am. Chem. Soc.* **2013,** 135, 8578-8584.

82. Wills, M., Imino Transfer Hydrogenation Reductions. *Top. Curr. Chem.* **2016,** 374, 1-14.

83. Blackmond, D. G.; Ropic, M.; Stefinovic, M., Kinetic Studies of the Asymmetric Transfer Hydrogenation of Imines with Formic Acid Catalyzed by Rh–Diamine Catalysts. *Org. Process Res. Dev.* **2006,** 10, 457-463.

84. Lagaditis, P. O.; Lough, A. J.; Morris, R. H., Iron complexes for the catalytic transfer hydrogenation of acetophenone: steric and electronic effects imposed by alkyl substituents at phosphorus. *Inorg. Chem.* **2010,** 49, 10057-66.

85. Pagnoux-Ozherelyeva, A.; Pannetier, N.; Mbaye, M. D.; Gaillard, S.; Renaud, J.-L., Knölker's Iron Complex: An Efficient In Situ Generated Catalyst for Reductive Amination of Alkyl Aldehydes and Amines. *Angew. Chem. Int. Ed.* **2012,** 51, 4976-4980.

86. Wang, D.; Astruc, D., The golden age of transfer hydrogenation. *Chem. Rev.* **2015,** 115, 6621-6686.

87. Warner, M. C.; Casey, C. P.; Backvall, J. E., Shvo's Catalyst in Hydrogen Transfer Reactions. *Top Organometal Chem* **2011,** 37, 85-125.

88. Bullock, R. M., Catalytic Ionic Hydrogenations. *Chem. Eur. J.* **2004,** 10, 2366-2374.

89. Cruchter, T.; Larionov, V. A., Asymmetric catalysis with octahedral stereogenic-at-metal complexes featuring chiral ligands. *Coord. Chem. Rev.* **2018,** 376, 95-113.

90. Hashiguchi, S.; Fujii, A.; Takehara, J.; Ikariya, T.; Noyori, R., Asymmetric Transfer Hydrogenation of Aromatic Ketones Catalyzed by Chiral Ruthenium(II) Complexes. *J. Am. Chem. Soc.* **1995,** 117, 7562-7563.

91. Misal Castro, L. C.; Li, H.; Sortais, J.-B.; Darcel, C., When iron met phosphines: a happy marriage for reduction catalysis. *Green Chem.* **2015,** 17, 2283-2303.

92. Baratta, W.; Ballico, M.; Baldino, S.; Chelucci, G.; Herdtweck, E.; Siega, K.; Magnolia, S.; Rigo, P., New Benzo[*h*]quinoline-Based Ligands and their Pincer Ru and Os Complexes for Efficient Catalytic Transfer Hydrogenation of Carbonyl Compounds. *Chem. Eur. J.* **2008,** 14, 9148-9160.

93. Lagaditis, P. O.; Mikhailine, A. A.; Lough, A. J.; Morris, R. H., Template synthesis of iron(II) complexes containing tridentate P-N-S, P-N-P, P-N-N, and tetradentate P-N-N-P ligands. *Inorg. Chem.* **2010,** 49, 1094-102.

94. Braude, E. A.; Linstead, R. P., Hydrogen transfer. Part I. Introductory survey. *J. Chem. Soc. (Resumed)* **1954,** 1954, 3544.

95. de Graauw, C. F.; Peters, J. A.; van Bekkum, H.; Huskens, J., Meerwein-Ponndorf-Verley Reductions and Oppenauer Oxidations: An Integrated Approach. *Synthesis* **1994,** 1994, 1007-1017.

96. Moyer, S. A.; Funk, T. W., Air-stable iron catalyst for the Oppenauer-type oxidation of alcohols. *Tetrahedron Lett.* **2010,** 51, 5430-5433.

97. Clapham, S. E.; Hadzovic, A.; Morris, R. H., Mechanisms of the H_2-hydrogenation and transfer hydrogenation of polar bonds catalyzed by ruthenium hydride complexes. *Coord. Chem. Rev.* **2004,** 248, 2201-2237.

98. Eisenstein, O.; Crabtree, R. H., Outer sphere hydrogenation catalysis. *New J. Chem.* **2013,** 37, 21-27.

99. Yamakawa, M.; Ito, H.; Noyori, R., The Metal–Ligand Bifunctional Catalysis: A Theoretical Study on the Ruthenium(II)-Catalyzed Hydrogen Transfer between Alcohols and Carbonyl Compounds. *J. Am. Chem. Soc.* **2000,** 122, 1466-1478.

100. Noyori, R., Asymmetric catalysis: Science and opportunities (Nobel lecture). *Angew. Chem.* **2002,** 41, 2008-2022.

101. Noyori, R.; Hashiguchi, S., Asymmetric Transfer Hydrogenation Catalyzed by Chiral Ruthenium Complexes. *Acc. Chem. Res.* **1997,** 30, 97-102.

102. Dub, P. A.; Henson, N. J.; Martin, R. L.; Gordon, J. C., Unravelling the mechanism of the asymmetric hydrogenation of acetophenone by [RuX_2(diphosphine)(1,2-diamine)] catalysts. *J. Am. Chem. Soc.* **2014,** 136, 3505-3521.

103. Ohkuma, T.; Utsumi, N.; Tsutsumi, K.; Murata, K.; Sandoval, C.; Noyori, R., The Hydrogenation/Transfer Hydrogenation Network: Asymmetric Hydrogenation of Ketones

with Chiral η 6 -Arene/ N -Tosylethylenediamine–Ruthenium(II) Catalysts. *J. Am. Chem. Soc.* **2006,** 128, 8724-8725.

104. Hartmann, R.; Chen, P., Noyori's Hydrogenation Catalyst Needs a Lewis Acid Cocatalyst for High Activity. *Angew. Chem. Int. Ed.* **2001,** 40, 3581-3585.

105. Conley, B. L.; Pennington-Boggio, M. K.; Boz, E.; Williams, T. J., Discovery, applications, and catalytic mechanisms of Shvo's catalyst. *Chem. Rev.* **2010,** 110, 2294-312.

106. Karvembu, R.; Prabhakaran, R.; Natarajan, K., Shvo's diruthenium complex: a robust catalyst. *Coord. Chem. Rev.* **2005,** 249, 911-918.

107. Futera, Z.; Klenko, J.; Sponer, J. E.; Sponer, J.; Burda, J. V., Interactions of the "piano-stool" [ruthenium(II) (η^6-arene)(en)Cl]$^+$ complexes with water and nucleobases; ab initio and DFT study. *J. Comput. Chem.* **2009,** 30, 1758-1770.

108. Dub, P. A.; Gordon, J. C., The mechanism of enantioselective ketone reduction with Noyori and Noyori-Ikariya bifunctional catalysts. *Dalton Trans* **2016,** 45, 6756-6781.

109. Dub, P. A.; Ikariya, T., Quantum chemical calculations with the inclusion of nonspecific and specific solvation: asymmetric transfer hydrogenation with bifunctional ruthenium catalysts. *J. Am. Chem. Soc.* **2013,** 135, 2604-2619.

110. Martins, J. E.; Clarkson, G. J.; Wills, M., Ru(II) complexes of N-alkylated TsDPEN ligands in asymmetric transfer hydrogenation of ketones and imines. *Org. Lett.* **2009,** 11, 847-50.

111. Dub, P. A.; Scott, B. L.; Gordon, J. C., Why Does Alkylation of the N-H Functionality within M/NH Bifunctional Noyori-Type Catalysts Lead to Turnover? *J. Am. Chem. Soc.* **2017,** 139, 1245-1260.

112. Soni, R.; Cheung, F. K.; Clarkson, G. C.; Martins, J. E.; Graham, M. A.; Wills, M., The importance of the N-H bond in Ru/TsDPEN complexes for asymmetric transfer hydrogenation of ketones and imines. *Org Biomol Chem* **2011,** 9, 3290-3294.

113. Fujii, A.; Hashiguchi, S.; Uematsu, N.; Ikariya, T.; Noyori, R., Ruthenium(II)-Catalyzed Asymmetric Transfer Hydrogenation of Ketones Using a Formic Acid–Triethylamine Mixture. *J. Am. Chem. Soc.* **1996,** 118, 2521-2522.

114. Dub, P. A.; Gordon, J. C., The role of the metal-bound N–H functionality in Noyori-type molecular catalysts. *Nature Reviews Chemistry* **2018,** 2, 396-408.

115. Haack, K.-J.; Hashiguchi, S.; Fujii, A.; Ikariya, T.; Noyori, R., The Catalyst Precursor, Catalyst and Intermediate in the Ru(II)-Promoted Asymmetric Hydrogen Transfer between Alcohols and Ketones. *Angew. Chem. Int. Ed.* **1997,** 36, 285-288.

116. Strotman, N. A.; Baxter, C. A.; Brands, K. M. J.; Cleator, E.; Krska, S. W.; Reamer, R. A.; Wallace, D. J.; Wright, T. J., Reaction Development and Mechanistic Study of a Ruthenium Catalyzed Intramolecular Asymmetric Reductive Amination en Route to the Dual Orexin Inhibitor Suvorexant (MK-4305). *J. Am. Chem. Soc.* **2011,** 133, 8362-8371.

117. Vaclavik, J.; Sot, P.; Vilhanova, B.; Pechacek, J.; Kuzma, M.; Kacer, P., Practical aspects and mechanism of asymmetric hydrogenation with chiral half-sandwich complexes. *Molecules* **2013,** 18, 6804-6828.

118. Kuzma, M.; Vaclavik, J.; Novak, P.; Prech, J.; Januscak, J.; Cerveny, J.; Pechacek, J.; Sot, P.; Vilhanova, B.; Matousek, V.; Goncharova, II; Urbanova, M.; Kacer, P., New insight into the role of a base in the mechanism of imine transfer hydrogenation on a Ru(II) half-sandwich complex. *Dalton Trans* **2013,** 42, 5174-5182.

119. Hartmann, R.; Chen, P., Numerical Modeling of Differential Kinetics in the Asymmetric Hydrogenation of Acetophenone by Noyori's Catalyst. *Adv. Synth. Catal.* **2003,** 345, 1353-1359.

120. Hamilton, R. J.; Bergens, S. H., An Unexpected Possible Role of Base in Asymmetric Catalytic Hydrogenations of Ketones. Synthesis and Characterization of Several Key Catalytic Intermediates. *J. Am. Chem. Soc.* **2006,** 128, 13700-13701.

2 APPARATUS DESIGN AND HARDWARE DEVELOPMENT

Online techniques for reaction monitoring allow reactions to be studied in real time, with minimal disruption to the reaction conditions. Whilst off-line and in-situ techniques are well developed for NMR spectroscopy, taking advantage of the large amount of structural information that can be gained about unknown compounds and the inherently quantitative nature of the technique, online techniques are still relatively uncommon.

At the time that this project began, no commercial systems for online NMR reaction monitoring existed, with the few examples in the literature all using custom equipment.[26, 28, 30-32, 54-56, 121] During this project, four different apparatus designs have been used, each building on the knowledge and experience gained from previous designs:

2.1 FIRST GENERATION DESIGN

The equipment used for FlowNMR has its origins in combined HPLC-NMR analysis, where flow probes were designed to allow samples to be flowed from the HPLC instrument to the NMR spectrometer for structural analysis.[9, 27-28, 122] As HPLC typically uses very small quantities of sample, the priority with flow probe designs was on minimising sample volume. Therefore, most commercial flow probes feature a tubular glass flow cell, which sits directly within the detector coils, with connections made at either end to narrow gauge plastic HPLC tubing (Figure 1.1b).

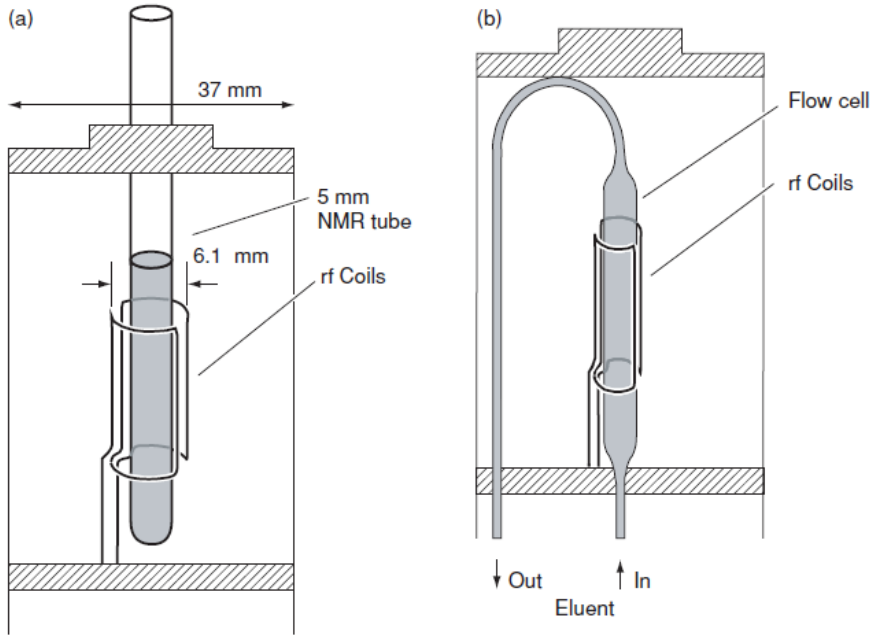

Figure 2.1: Schematics of a) conventional, and b) continuous flow probe designs compatible with cryogenic magnets. Reproduced from Albert, 2003 with permission.[28]

The first generation FlowNMR apparatus used at the University of Bath (constructed by Jon Chouler) used a flow probe of this design, in common with many other FlowNMR reaction monitoring setups.[29, 33, 47]

In order to minimise the delay time between a change occurring in the reaction vessel and the arrival of the sample in the spectrometer for detection it is desirable to ensure that the volume of the tubing connecting the reaction vessel to the spectrometer is minimised, therefore narrow diameter polyetheretherketone (PEEK) tubing (1.588 mm o.d., 0.762 mm i.d., Upchurch Scientific) was used for connections between the reaction vessel, pump and flow probe. PEEK was chosen for its chemical compatibility and good mechanical properties (pH 0 – 14, -50 – 100 °C, >300 bar) along with low gas permeability. A dual piston HPLC pump (JASCO PU-2085 Plus) with a semi-micro pump head was used to circulate the reaction mixture between the flask and the flow probe (Figure 2.2). A by-pass loop was added to allow the flow probe to be by-passed in case of leak or blockage.

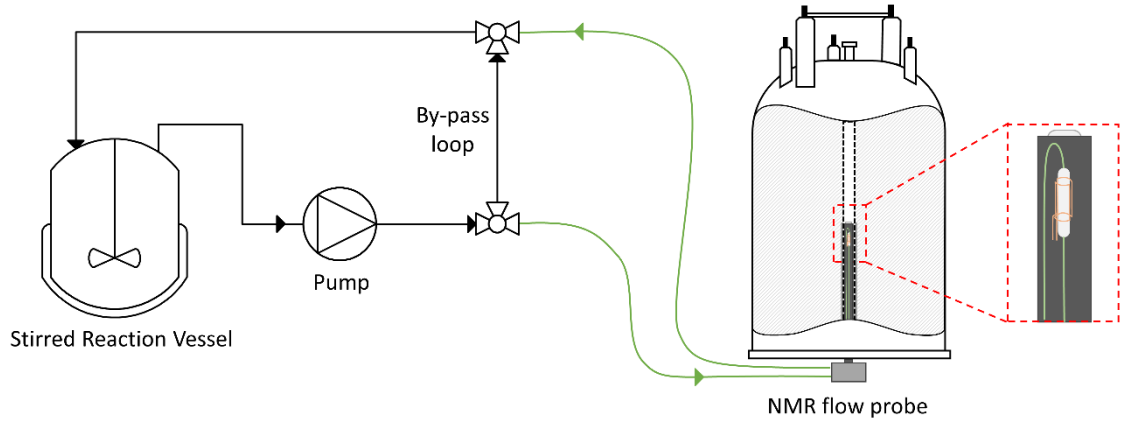

Figure 2.2: First generation FlowNMR apparatus schematic.

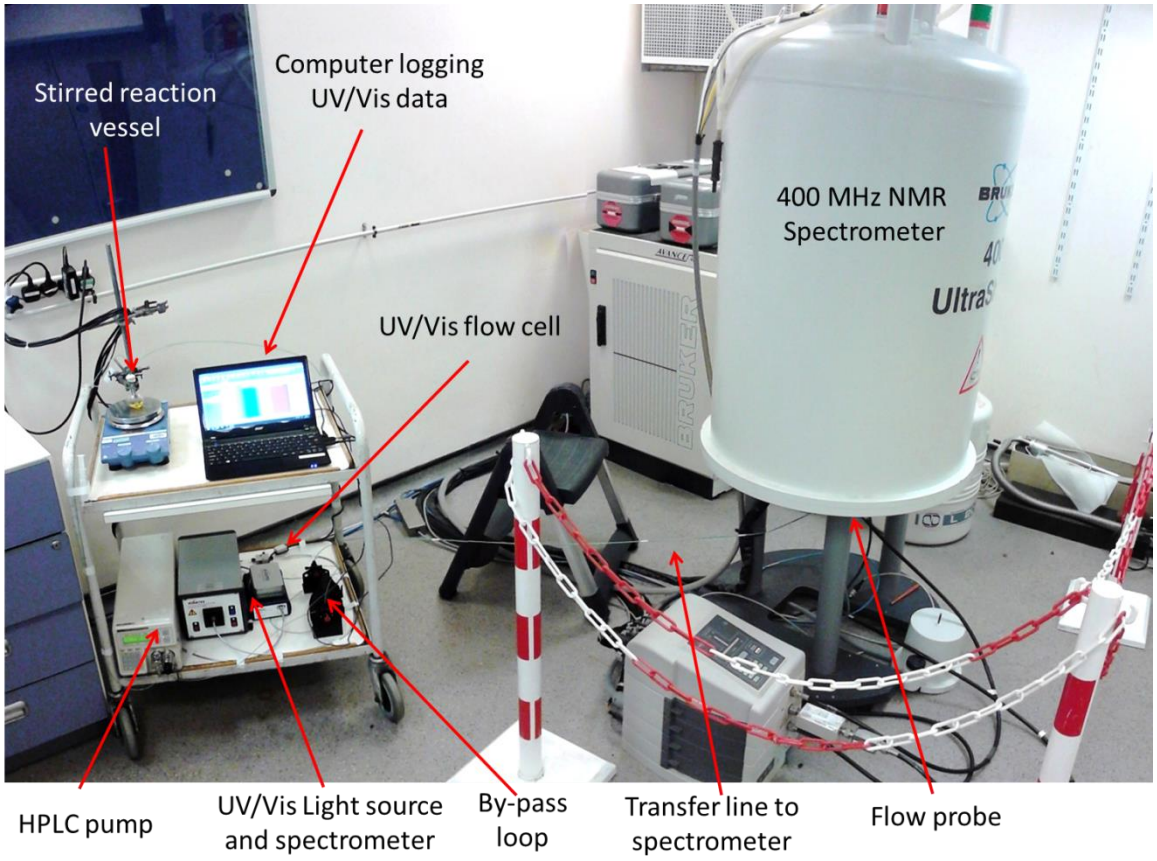

Figure 2.3: First generation FlowNMR apparatus, showing location of pump and reaction vessel on trolley next to spectrometer. UV-Vis spectrometer used for residence time distribution measurements also shown.

This simple apparatus allowed reaction species, including catalyst, substrate and product to be detected and reaction kinetics determined, however the lack of heating/cooling and ability to withstand pressure of the flow probe design limited the range of reaction conditions that the system was able to monitor. The low volume design of the flow probe – optimised for

HPLC analysis – proved to be a hindrance for reaction monitoring, due to the reduction in sensitivity and signal-to-noise ratio (Figure 2.4). The flow probe design was also restricted to monitoring ^{1}H and ^{13}C nuclei only.

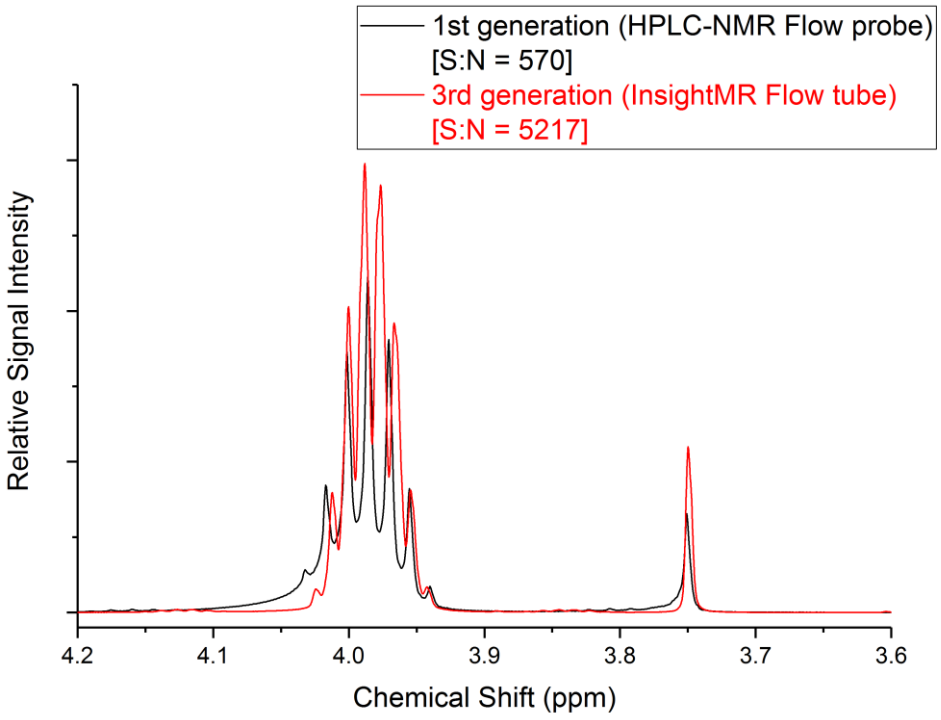

Figure 2.4: Comparison between ^{1}H spectra of isopropanol CH and 1,3,5-trimethoxy benzene CH_3 peaks in isopropanol using first-generation (HPLC-NMR flow probe, 400 MHz magnet with room-temperature BBO probe) and third-generation (InsightMR flow tube, 500 MHz magnet with N_2 BBO cryoprobe) designs. (1s acquisition time, 4 s relaxation delay, 0.3 Hz line broadening). Data courtesy of Dan Berry.

2.2 SECOND GENERATION DESIGN

Improved designs for NMR flow systems for reaction monitoring have been devised by several groups,[35-36, 55] with the first commercial design being produced by Bruker in 2015 (Figure 2.5).[39] These designs typically have a larger sample volume than the conventional HPLC-NMR flow probes, enabling measurements with greater signal-to-noise. Rather than building an entire probe, complete with RF coils as was done for HPLC-NMR flow probes, the flow tubes are designed to replicate the shape of a 5 mm NMR tube and spinner, allowing them to be used with any 5 mm probe. This means that the flow tubes can take advantage of advances in NMR probe design, allowing multi-nuclei receiver and cryo-probes to be used.

As noted above, minimising the volume of FlowNMR apparatus is important to minimise the delay in transferring sample between the reaction flask and observation cell. In the InsightMR design, the sample is carried to and from the spectrometer in two polytetrafluoroethylene (PTFE) capillary tubes (0.794 mm o.d., 0.500 mm i.d.).[36, 38] The sample transfer lines pass inside two concentric tubes which take heat exchanger fluid (50:50 ethylene glycol : water) to and from the flow tube (Figure 1.2). Foam insulation surrounds the heat exchanger fluid tubing.

The observation cell is designed to mimic a standard 5 mm NMR tube and spinner. A plastic 'spinner adaptor' contains connections for the sample flow cell and acts as the terminus for heat transfer fluid. The two PTFE sample capillaries are connected to the glass flow cell, with the inlet capillary continuing to the end of the flow cell. Sample passes down the capillary before flowing back along the glass flow cell to the return tubing.

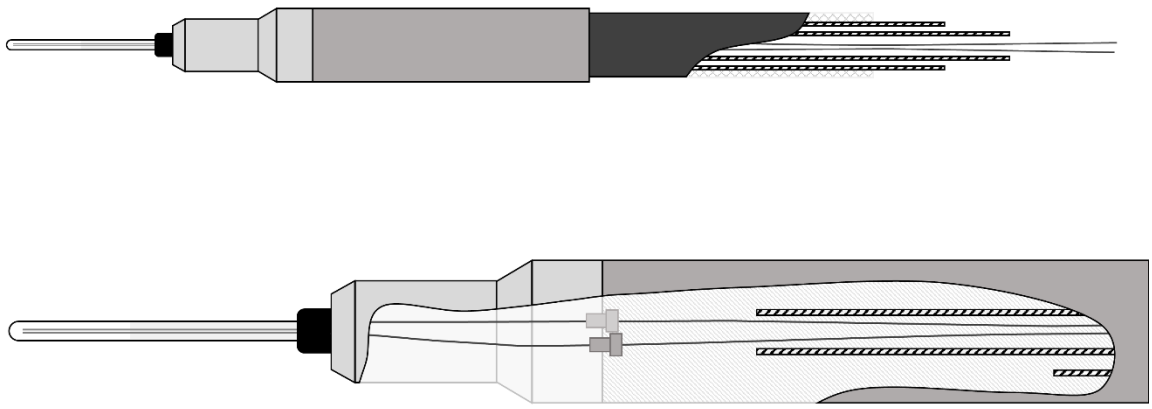

Figure 2.5: Schematic of InsightMR flow tube, showing internal connections of sample transfer and heat exchange fluid. (not to scale)

The second generation FlowNMR apparatus, constructed as part of this project, used an InsightMR flow tube. Reactions were carried out in a standard glass round-bottomed flask, with connections made using the same PEEK tubing and pump as for the first-generation design (Figure 2.6). All equipment was positioned on a mobile trolley made of plastic (Rubbermaid), allowing the equipment to be transported between the laboratory and the spectrometer as required. The trolley and apparatus were able to be placed at a minimum distance of 0.5 m from the shielded magnet without experiencing adverse magnetic effects.

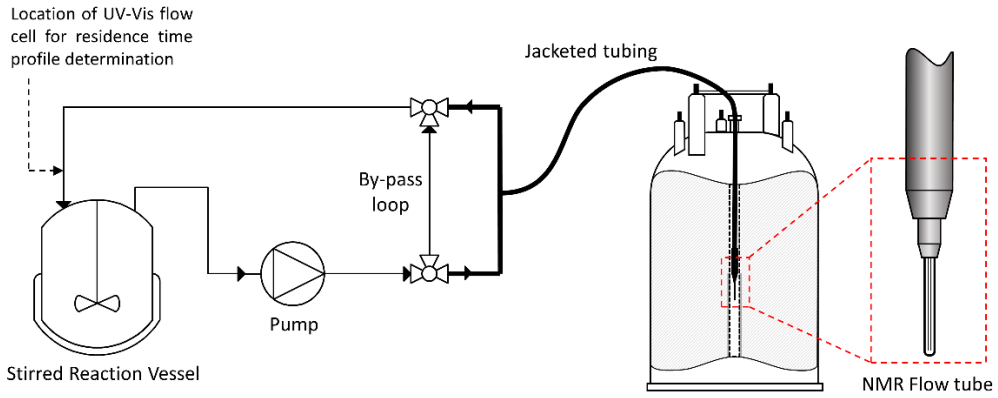

Figure 2.6: Flow scheme and instrumentation diagram for the FlowNMR reaction monitoring apparatus (not to scale).

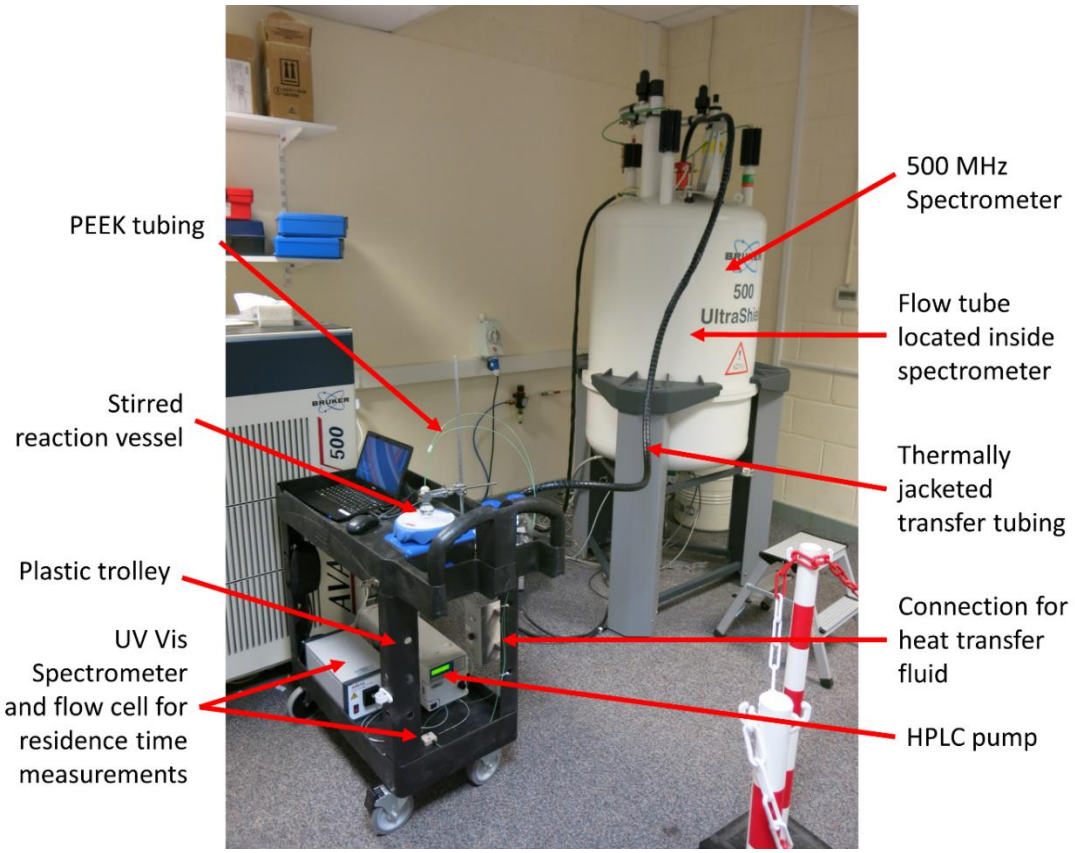

Figure 2.7: 2nd Generation FlowNMR experimental setup, showing location of apparatus on trolley next to NMR spectrometer.

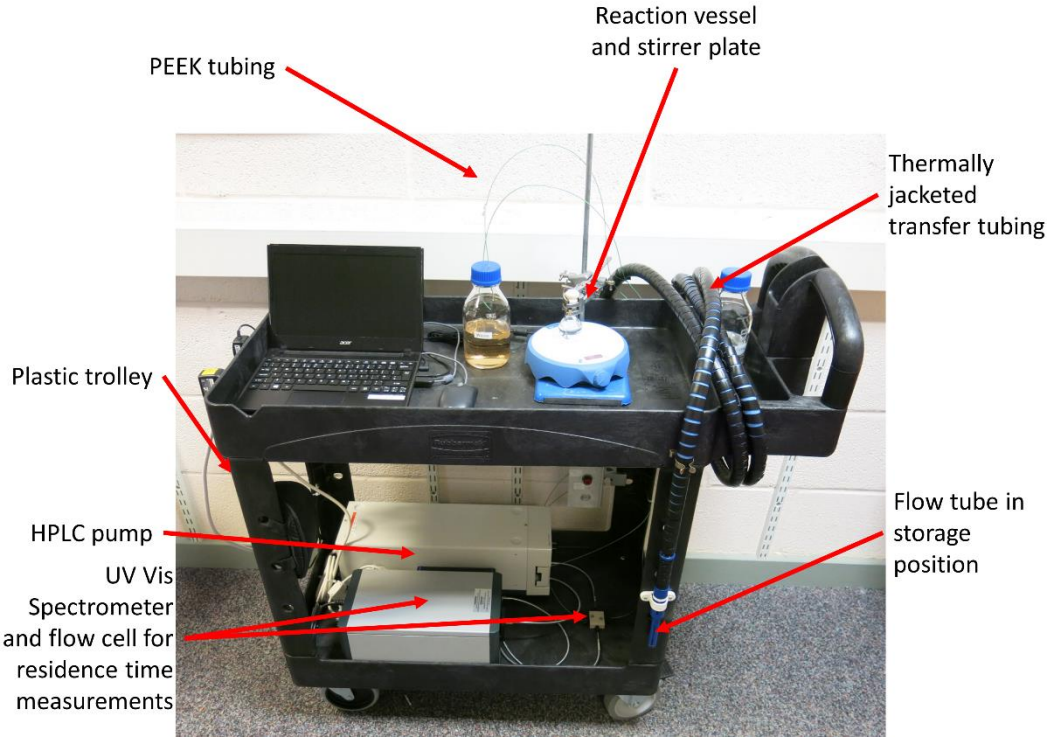

Figure 2.8: 2nd Generation FlowNMR experimental setup, showing apparatus in storage position.

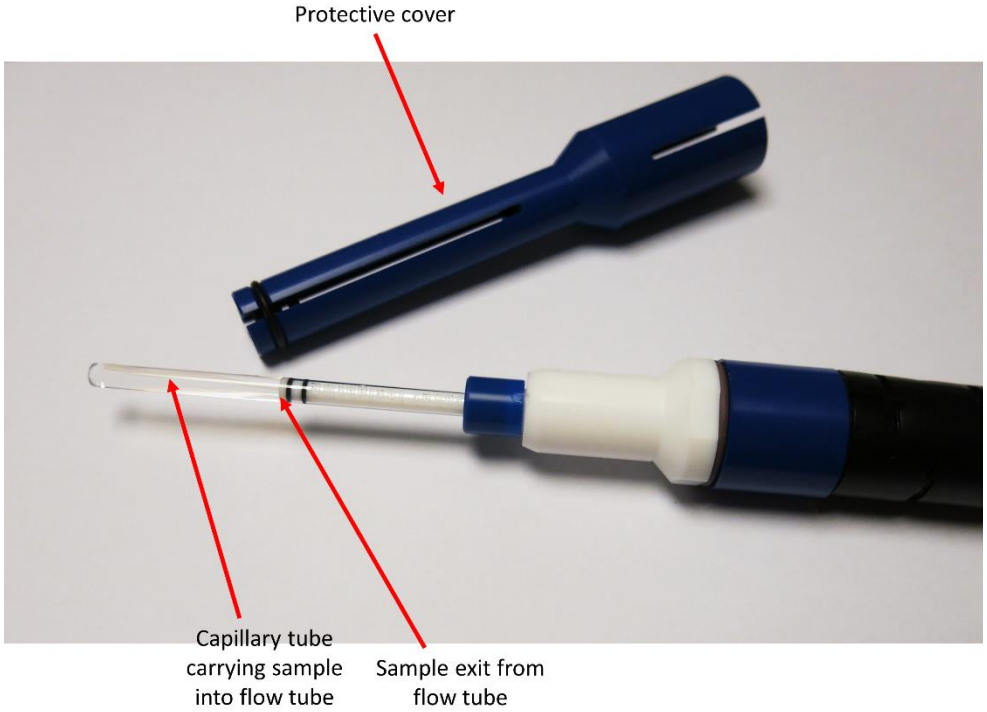

Figure 2.9: InsightMR flow tube.

The InsightMR flow tube design allows the apparatus to be used with any standard 5 mm probe, taking advantage of the higher resolution and sensitivity offered by modern probes and higher field magnets. The InsightMR flow tube is compatible with a much broader range of conditions than the flow probe, allowing reaction temperatures of -40 to +80 °C and pressures of up to 10 bar.[39] This allows a much wider range of reactions to be studied, and more sophisticated NMR techniques to be used than for the first-generation design.

2.3 THIRD GENERATION (DREAM FACILITY)

Although NMR is able to detect and quantify a wide range of compounds, the sensitivity and inherent properties of the technique mean that there will always be some compounds that NMR is unable to detect. It is therefore desirable to combine data from multiple analytical techniques, to gain as much information as possible about a reaction. Using multiple techniques also allows results to be cross-referenced and validated, increasing confidence in the data.[123]

Previous generations of FlowNMR apparatus were mounted on trolleys, allowing the equipment to be transported between the laboratory and the NMR instrument. The third-generation apparatus was constructed as part of the Dynamic Reaction Monitoring facility (DReaM), which provides a permanent space for reaction monitoring apparatus, including a dedicated fume hood for carrying out reactions.

2.3.1 UV-Vis spectroscopy

The first technique to be integrated alongside NMR was Ultra-Violet/Visible (UV-Vis) spectroscopy. Although UV-Vis provides far less structural information than NMR, and only works for complexes possessing a suitable chromophore, it remains one of the most sensitive analytical techniques available.

A variable pathlength UV-Vis flow cell (Ocean Optics) was inserted into the flow path after the NMR flow tube, with fibre optic cables used to connect the flow cell to the light source (Ocean Optics DH-2000-BAL) and UV-Vis spectrometer (Ocean Optics QE-Pro) (Figure 2.10). To correct for any variability in light intensity over the course of long reaction times, an electronically controlled shutter (Ocean Optics FOS-2X2-TTL) was included, allowing automated spectral re-referencing via a separate reference channel. The location of the UV-Vis flow cell after the flow tube allows it to be used for determining residence time distribution (Figure 3.2).

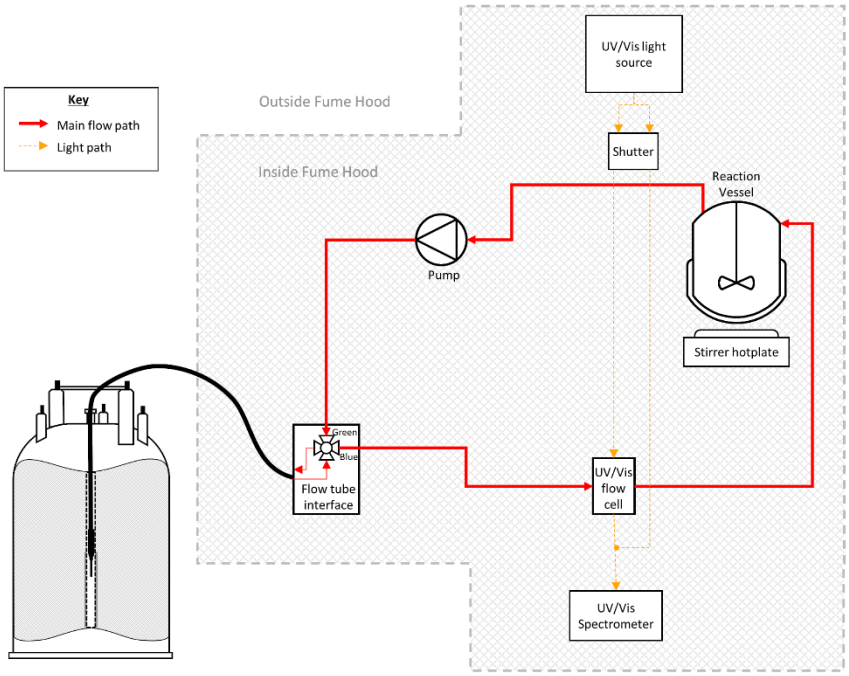

Figure 2.10: Schematic of FlowNMR apparatus showing position of UV-Vis flow cell.

2.3.2 High Performance Liquid Chromatography

NMR is unable to distinguish between different enantiomers without the use of chiral resolving agents. To enable enantioselective reactions such as those discussed in Chapter 5 and 6 to be studied, a technique that can distinguish different enantiomers is required.

The most commonly used techniques for measuring enantiomeric ratio in liquid samples are polarimetry and chiral High-Performance Liquid Chromatography (HPLC). In the case of the Noyori asymmetric transfer hydrogenation reaction discussed in Chapters 5 and 6, the presence of a chiral catalyst can distort optical rotation measurements, so chiral HPLC is the favoured technique.[124]

A protocol has previously been developed for off-line analysis of the Noyori transfer hydrogenation reaction, and involves dilution of a reaction sample in hexane before passing through a silica plug to remove the catalyst, followed by HPLC analysis using a Chiracel OD-H chiral column (4.6 mm diameter, 250 mm length, 5 µm particle size), eluted with 90 : 10 Hexane : Isopropanol.[125] To ensure that metal catalysts do not damage the HPLC column, a sacrificial guard column (Chiracel OD-H, 4.6 mm diameter, 10 mm length, 5 µm particle size) was used to remove any traces of catalyst before entering the column.

HPLC may be classed as a destructive analytical technique for reaction monitoring purposes, since the dilution of the sample in eluent solvent means that the sample cannot be returned

to the reaction after analysis. A different approach to integrating HPLC into the reaction flow loop is therefore required than for UV-Vis or NMR analysis.

The simplest way of taking a sample from the reaction loop would be to use a two-position, six-port valve, where the reaction passes through one side of the valve, and the HPLC solvent on the other (Figure 2.11a). This valve configuration is similar to that used for manual injection into the HPLC flow path. When the valve is in the position as shown in Figure 2.11a, with ports 1 and 6 connected, the reaction mixture flows through the sample loop. When the valve is switched so that ports 1 and 2 are connected, the volume of reaction sample within the loop enters the HPLC flow path and is diluted, ready for analysis. Although this simple design operates well for manual injection of samples, the small volume of HPLC solvent that is in the valve will enter the reaction loop when the valve is switched. Whilst this may only be a few microliters, it may be enough to quench sensitive reactions, particularly if the HPLC instrument is operating in reverse phase with aqueous solvents.

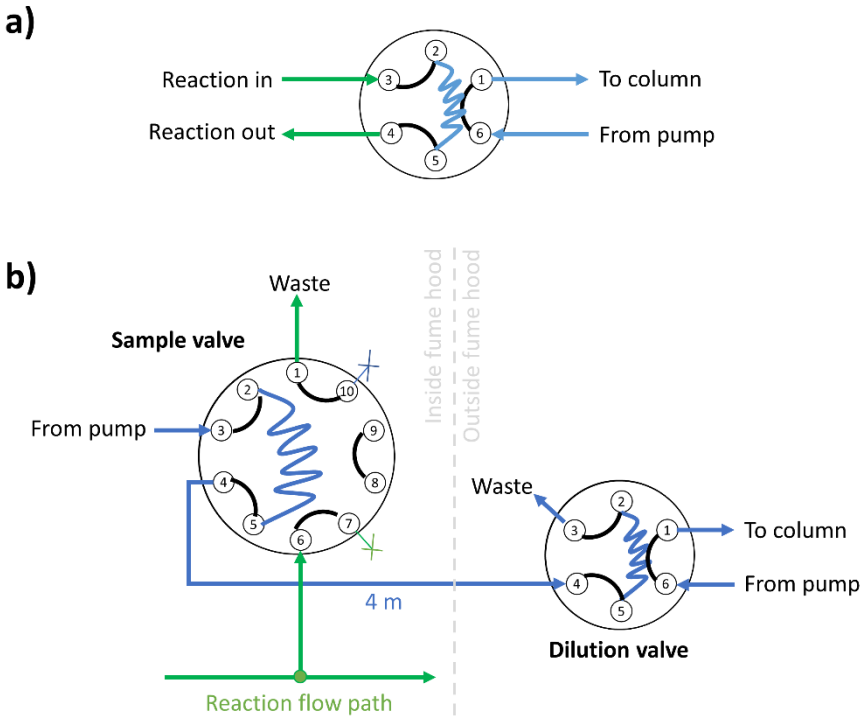

Figure 2.11: Schematic of HPLC valve configurations; a) 6-port, 2-position valve, b) 10 port, 2-position sample valve, with 6-port, 2-position dilution valve outside fume hood.

To overcome the potential problems due to HPLC solvent entering the reaction path, a 10-port, 2-position valve (Agilent 1260 Infinity II) was used to sample from the reaction mixture (Figure 2.11b). Rather than flowing the reaction mixture through the valve, the valve was connected to the flow path with a T-piece connector (Upchurch Scientific) and a short (~2 cm) length of tubing (PEEK, 1.588 mm O.D., 0.762 mm I.D., Upchurch Scientific). This ensures that the HPLC solvent can never enter the main reaction flow path, whilst minimising the

volume reaction mixture required for each sample. In the 'closed' position shown, the reaction mixture is prevented from flowing through the valve by a blanking nut at port 7. To take a sample from the reaction, the valve is switched so that ports 1 and 2 are connected. This allows the reaction mixture to flow through the sample loop to a waste bottle. After the valve has been left open for sufficient time for the T-piece, tubing and sample loop to be purged with fresh reaction sample, the valve is closed, injecting the contents of the sample loop into the HPLC flow path.

A tracer dye (Rose Bengal, approx. 1 mg/100 mL) was used to measure the minimum time that the valve must be left in the 'sample' position to ensure that the volume of the T-piece, tubing and sample loop is completely replaced with fresh reaction mixture. At a reaction mixture flow rate of 4 mL/min, the sample volume was completely refreshed 30 s after opening the valve.

To avoid increasing the length of the reaction flow path too much, the HPLC sample valve was located inside the fume hood, immediately after the UV-Vis flow cell. This meant that approximately 4 m of tubing was required to connect the sample valve to the HPLC column chamber, located outside of the fume hood. The transfer time from the sample valve to the HPLC instrument is between 10 - 15 s. Despite using narrow diameter (180 µm) tubing to promote laminar flow, significant back-mixing was observed within the transfer line, leading to peak tailing in the HPLC (Figure 2.12).

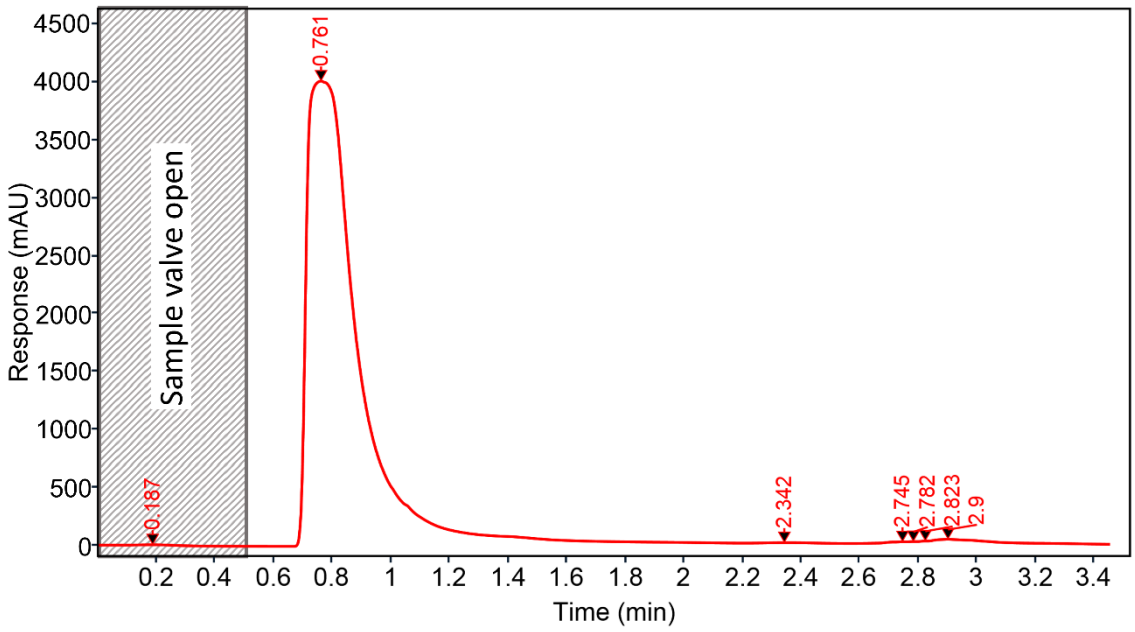

Figure 2.12: UV absorption response (254 nm) at HPLC detector for direct sampling (no HPLC column or refocusing) of a mock reaction mixture containing 0.4 M acetophenone in isopropanol using a single HPLC sample valve located 4 meters from the HPLC instrument, showing peak tailing due to back-mixing within the transfer tubing.

A second valve was used to 'refocus' the sample prior to entering the HPLC column (Figure 2.11b). This valve, located next to the HPLC instrument, resamples and dilutes the output from the first valve, ready for analysis. The resampling process eliminates peak tailing due to back-mixing in the transfer line, leading to sharp, well-resolved peaks (Figure 2.13). The valve timings must be carefully synchronised, however by using separate solvent pumps for each of the valves, flow rate and solvent composition can be changed independently for the sample/dilution and analysis loops. A schematic illustration of the timing sequence used for HPLC data acquisition is shown in Figure 2.14.

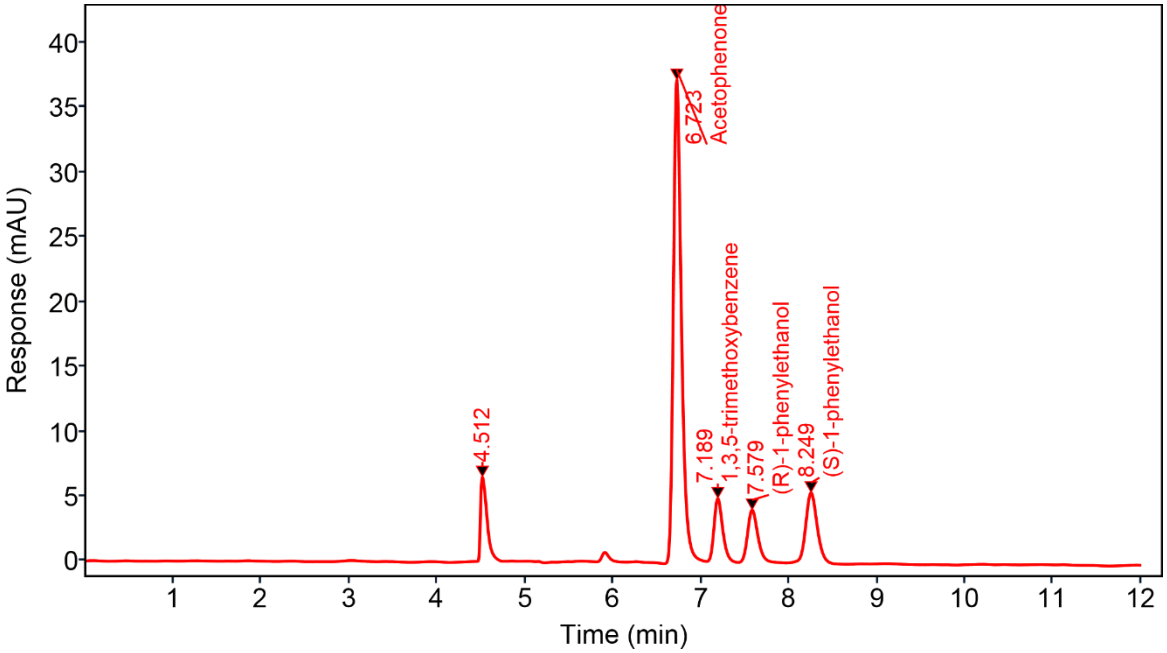

Figure 2.13: Example chromatogram acquired from a mock reaction mixture containing acetophenone (200 mM), rac-1-phenylethanol (200 mM) and 1,3,5-trimethoxybenzene (0.1 M) in isopropanol. Peaks eluting before 6 minutes are background signals from the solvent.

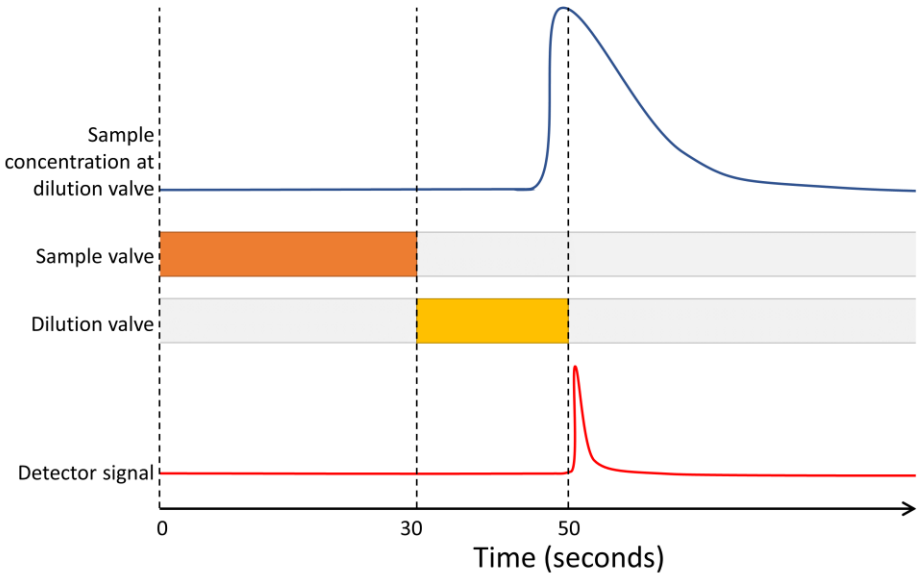

Figure 2.14: Schematic illustration of timing sequence for HPLC valves for at-line analysis from a reaction (not to scale).

Automated sampling directly from the reaction loop eliminates variation due to sample workup procedure or sample decomposition prior to analysis, leading to minimal scatter between samples taken at different time points during a reaction (Figure 2.15).

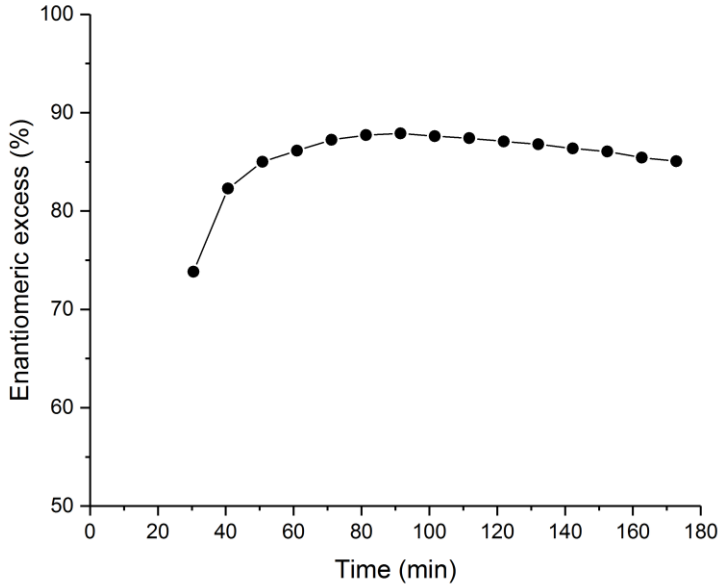

Figure 2.15: Example enantioselectivity data acquired using in-line HPLC with automated sampling from a reaction mixture (Noyori asymmetric transfer hydrogenation of acetophenone to 1-phenylethanol, 2 mM cat., 400 mM Acetophenone, 10 mM KOH, 10 mL isopropanol, 20°C. See Chapter 5 for further details.).

2.3.3 Mass Spectrometry

After NMR, Mass Spectrometry (MS) is probably the next most commonly used chemical characterisation technique. Like NMR, MS supplies high resolution data that can be used to deduce structural information about compounds. MS is a much more sensitive technique than NMR, enabling extremely dilute samples to be studied. As MS is not inherently quantitative, calibration curves must be measured before concentrations can be calculated, limiting the usefulness of the technique for monitoring unknown species during a reaction.

Since MS is also a destructive technique, and requires similar sample dilution to HPLC, it makes sense to combine these two techniques. As MS data is acquired continuously, with time averaging performed during data processing, peak tailing is not an issue and refocusing of the sample plug is unnecessary. Therefore, the MS was simply connected to the output of the second HPLC valve (Figures 2.16 to 2.19). Using separate pumps for each of the HPLC valves allows different solvents to be used for MS and HPLC analysis, which is of key importance when developing HPLC and MS analysis procedures. A custom cable was constructed to connect the HPLC to the MS, allowing the HPLC software to trigger MS data acquisition.

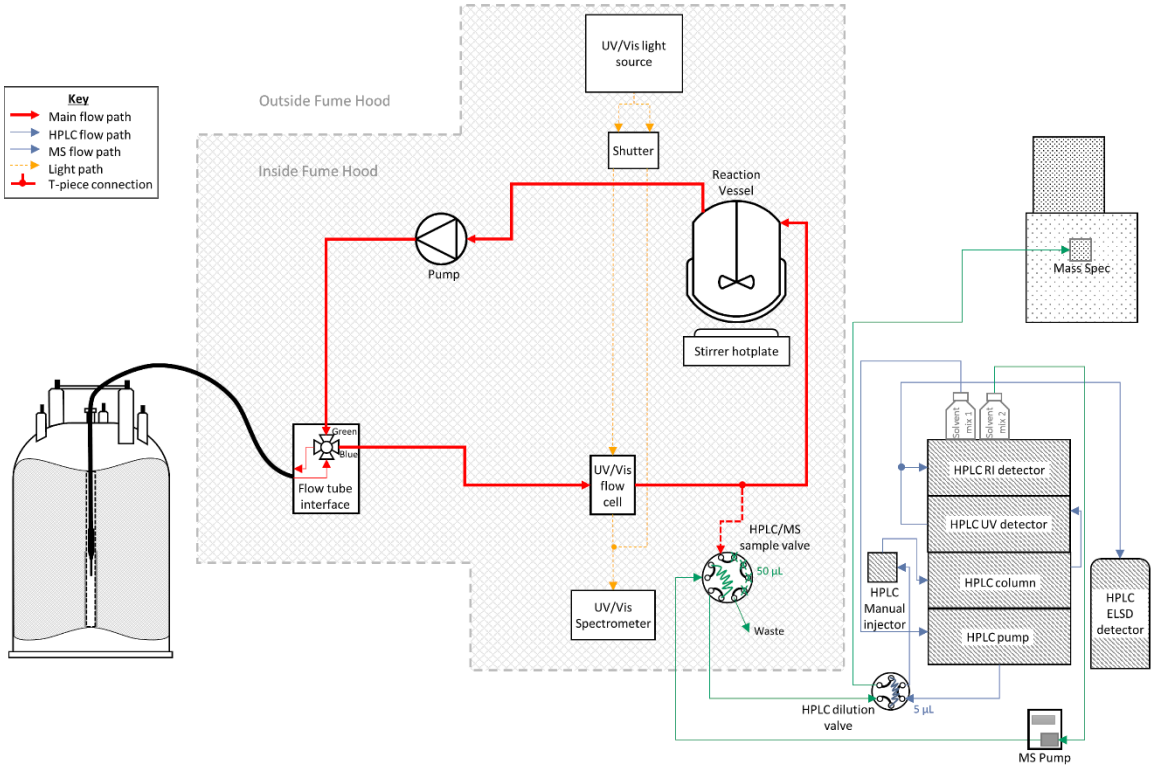

Figure 2.16: Schematic of FlowNMR apparatus, including integration of UV-Vis, HPLC and MS instruments.

Figure 2.17: Photograph of third generation apparatus, with HPLC/MS flow path highlighted.

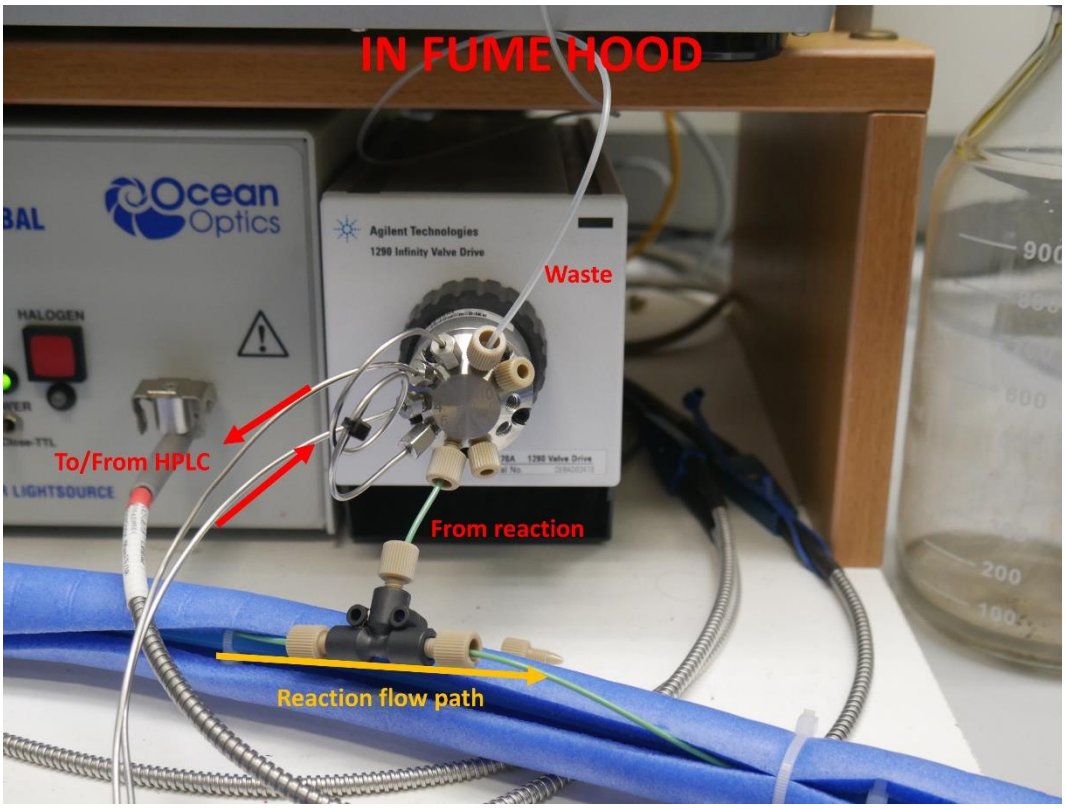

Figure 2.18: Photograph of HPLC sample valve and connections, located within fume hood.

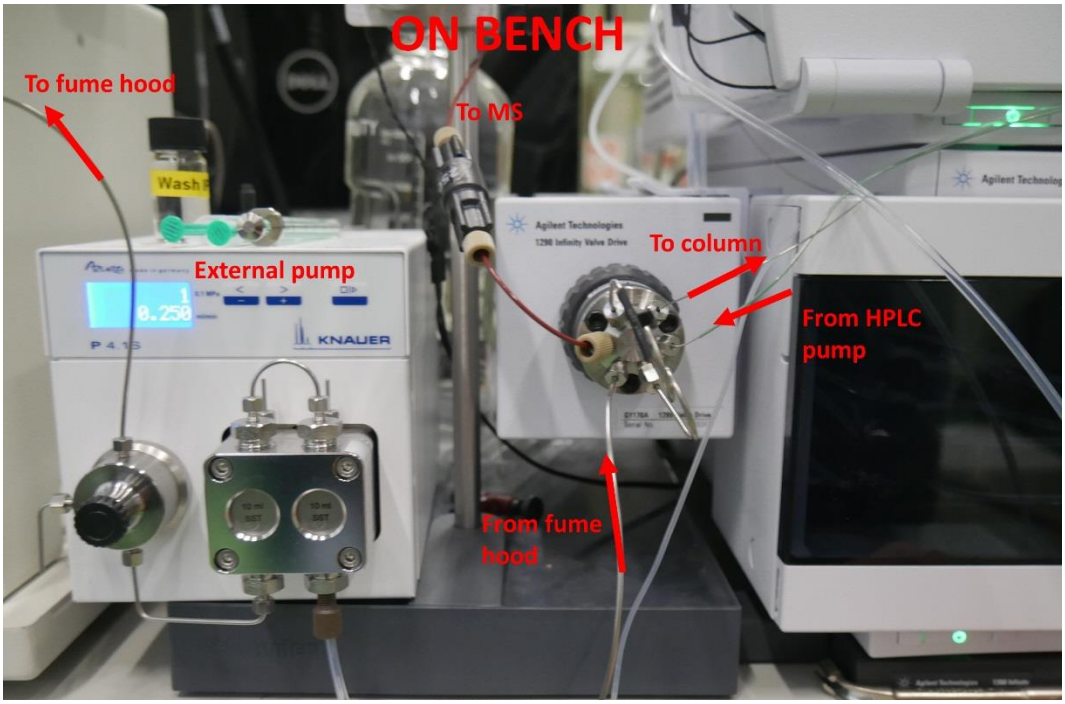

Figure 2.19: Photograph of HPLC 'refocusing' and dilution valve and external pump, located next to HPLC instrument.

2.3.4 Process control

Accurate control of reaction temperature and pressure is vital for ensuring reliable and reproducible kinetics.

The InsightMR flow tube has a triple walled design (Figure 2.20a), allowing heat transfer fluid to be flowed around the outside of the sample transfer lines, keeping them at a constant temperature all the way to the magnet. The connections between the flow tube, reactor, pump, UV-Vis and HPLC valve, however, are not temperature regulated, leading to large heat losses.*

Jacketing the transfer lines in a similar way to the flow tube proved challenging, due to the number of connections to other instruments where the transfer line would be required to exit the heating jacket. Instead, a simpler parallel tubing design was used, where the tubing containing the heat transfer fluid ran alongside the sample transfer lines, with both tubes wrapped in foam insulation (Figure 2.20b). A downside of this method is that heat transfer is less efficient than in the multi-walled design, however by heating the jacketed tubing above the desired reaction temperature, a constant temperature (±10%) can be maintained around the entire flow circuit.

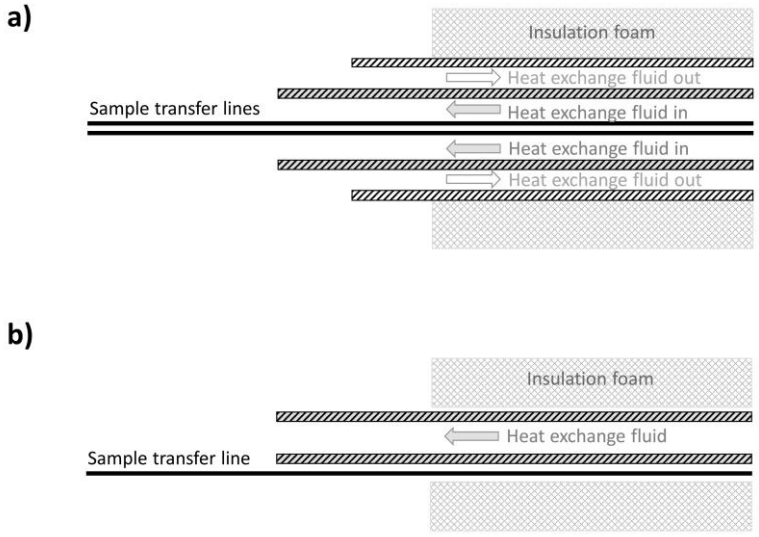

Figure 2.20: Cross-section schematic of heat transfer tubing; a) triple walled design used in flow tube, b) parallel tubing design used in rest of system.

Two heater/chiller units (Julabo CorioCD 300F) were used to regulate the reaction temperature, with one supplying the flow tube and jacketed tubing with a 50:50 mixture of water and ethylene glycol, and the other the reaction flask (Drysyn Snowstorm heat

* Experimentally, it was found that without additional jacketing, the temperature of the tubing had equilibrated to room temperature within 0.5 m of leaving a reaction flask heated to 50°C.

exchanger) (Figure 2.21). Since heat transfer is more efficient within the flow tube than the rest of the jacketed tubing, the flow tube was placed at the end of the heat exchanger fluid circuit. Setting the heater/chiller so that the correct temperature is measured in the flow tube means that a higher heat exchange fluid temperature is recorded in the rest of the flow system, compensating for the poorer heat transfer.

To monitor the reaction temperature, five thermocouples were placed at strategic points in the system; in the reaction flask, after the pump, in the flow tube, after the flow tube and in the heater/chiller water bath (Figure 2.21). Pressure sensors (DJ Instruments DF2-TI-01) were placed before and after the flow tube, allowing any blockages or leaks in the system to be detected. Readings from the temperature and pressure sensors were logged using a LabView programme created by Catherine Lyall.

A 250 psi pressure relief valve (Upchurch Scientific) was fitted after the pump to prevent damage to the flow tube in case of blockage. An injection port before the pump allows reagents to be added directly into the reaction loop if required.

Knowledge of the reaction flow rate is important for calculating the residence time (and therefore the volume) of a reaction sample within the flow apparatus and NMR flow cell, which has important implications for NMR pulse sequences and selection of reaction conditions (see Chapter 3 for further details). As discussed above, the flow rate also affects integration of other techniques, including timing of HPLC valves. Whilst flow rate is not expected to vary significantly between experiments with similar reaction conditions, changing solvent or temperature will impact viscosity, which may lead to variation in flow rate. A flow meter (Bronkhorst mini CORI-FLOW M13) was therefore fitted on a bypass loop, allowing flow rate to be checked as required.

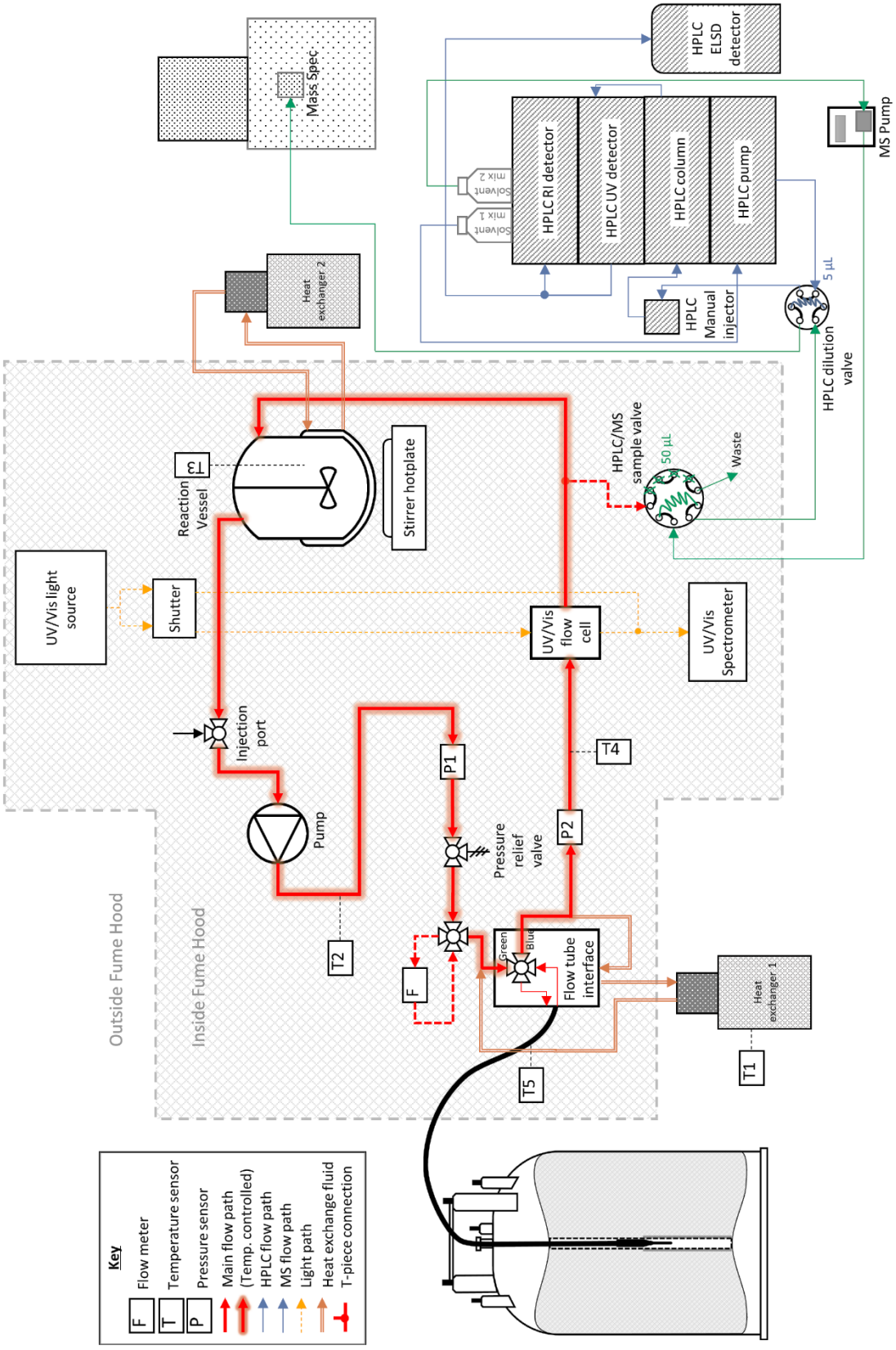

Figure 2.21: Schematic of FlowNMR apparatus, including integration of UV-Vis, HPLC and MS instruments, and temperature and pressure control systems.

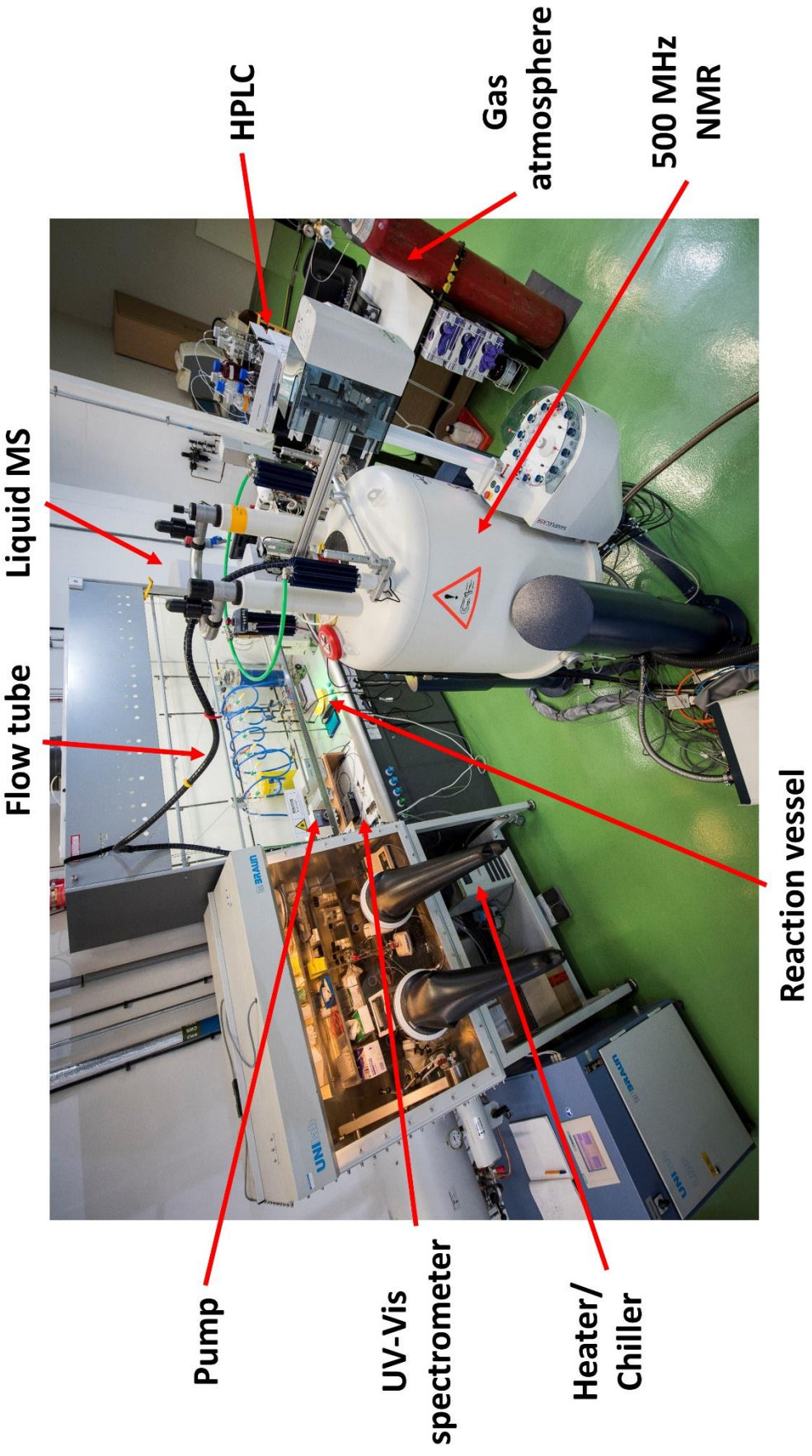

Figure 2.22: Photograph of third generation FlowNMR apparatus.

2.3.5 Material choice

The standard InsightMR flow tube design uses PTFE tubing for all sample transfer lines. Whilst PTFE has one of the greatest range of chemical compatibilities of any polymer, its mechanical strength is relatively poor. The thin walls and small diameter (0.794 mm o.d., 0.500 mm i.d.) of the PTFE tubing in the InsightMR flow tube means that the tubing is prone to damage if bent or kinked, which leads to weaknesses in the tubing wall, blockages and leaks.

Polyetheretherketone (PEEK) is a tough polymer which is commonly used for machined parts due to its hardness and durability. Whilst the chemical compatibility of PEEK is slightly poorer than PTFE, it is still compatible with the vast majority of commonly used chemicals. PEEK has a lower gas permeability than PTFE, and so is more suitable for reactions performed at elevated pressure.

The second-generation FlowNMR apparatus used the standard PTFE tubing within the flow tube, however bending of exposed sections of the PTFE tubing led to leaks on several occasions. To reduce the chance of leaks due to damaged tubing, and to take advantage of the improved gas permeability properties of PEEK, the transfer lines within the flow tube were replaced with PEEK tubing (0.794 mm i.d., 0.500 mm i.d., Upchurch Scientific).

2.3.6 Pump

The first and second-generation FlowNMR apparatus both used a dual piston HPLC pump to circulate the reaction mixture around the apparatus. This pump is designed for use at high pressures with pure solvent only, and so is prone to blockage due to restrictions within the pump check valves, and may be corroded by some strongly acid or basic reaction mixtures.

For the third-generation design, the piston pump was replaced with a peristaltic pump (Vaportec SF-10). This pump is designed for reagent and gas dosing, and so offers high chemical compatibility and accurate flow rate. Since the reaction mixture never encounters the mechanical drive components, the risk of contamination or corrosion is greatly reduced. The peristaltic pump is unable to operate at high pressures, with a maximum pressure of 10 bar, however the flow tube is also restricted to the same maximum pressure.

2.4 Fourth Generation (TgK Scientific)

Both the second and third generation FlowNMR apparatus designs used the commercial InsightMR flow tube. The commercial flow tube design uses a continuous length of 1/32" PTFE or PEEK tubing from the by-pass valve all the way to the glass flow cell tip. Minimising the number of connections within the flow tube reduces possible sources of leaks, however the flexible nature of both PTFE and PEEK allows the tubing to twist within the glass flow cell (Figure 2.23a), resulting in turbulent sample flow and poorer shimming.

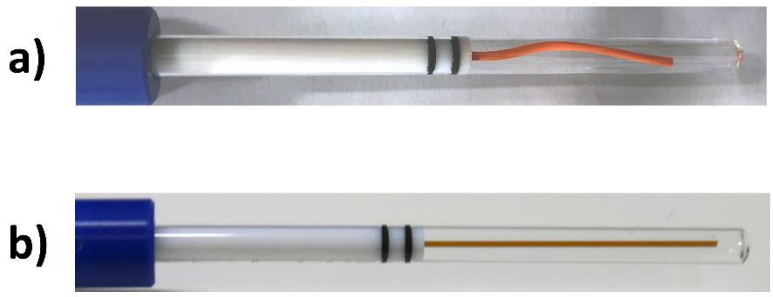

Figure 2.23: Photograph of flow tube tip and glass flow cell, a) third generation apparatus, showing twisting of PEEK tubing (orange); b) fourth generation design using fused silica capillary.

A stopped flow (InsightXpress) version of the InsightMR flow tube has been developed by the University of Edinburgh in collaboration with TgK Scientific.[12] Due to the high flow rates required for stopped flow, a rigid fused-silica capillary (Figure 2.23b) is used for the final section of tubing within the glass flow cell, preventing the capillary from moving during acquisition.

For the fourth generation FlowNMR apparatus, a hybrid flow tube design was used (Figure 2.24), combining the fused-silica capillary of the InsightXpress design with the continuous flow InsightMR design. To connect the inlet PEEK tubing to the fused silica capillary, a piece of 0.030" ID PEEK tubing (approx. 4 cm length) was used as an adaptor to connect the two 1/32" OD tubing. Connections were made by push fitting the smaller tubing into the larger tubing to a depth of 2-3 mm. 6-40 1/16" fittings were then placed over the connection so that when tightened the fitting would compress the outer tubing onto the inner, preventing leaks.

A 6-40 union (TgK Scientific) was placed over the connection between the 1/32" and the 1/16" OD PEEK tubing to provide a socket for the fitting to be tightened into, securing the connection. A 0.040" sleeve was used to cover the PEEK tubing on the other side of the union to help keep the tubing central in the union.

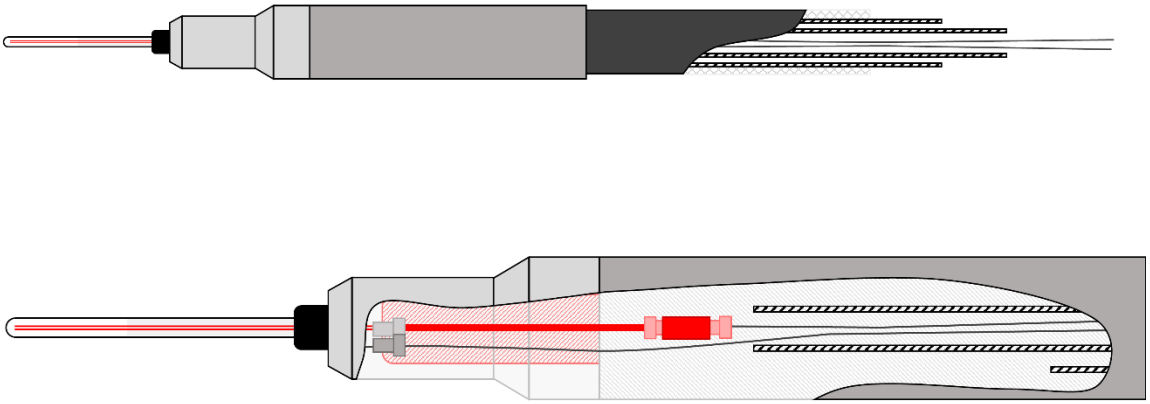

Figure 2.24: Schematic of modified flow tube design, showing replacement of tubing within flow cell with fused silica, recessed fittings within spinner-adaptor and connection to the 1/32" PEEK transfer lines via 1/16" PEEK tubing and union. Modified parts shown in red.

The improvement in magnetic field homogeneity with the modified flow tube is relatively modest for many samples (reduction in half-height line width of around 0.5 Hz), since peaks are approaching the natural linewidth. The greatest improvements are seen for samples where convection or poor sample homogeneity results in broadened peaks (Figure 2.25). The reduction in turbulence in the glass flow cell using the fused silica tubing appears to reduce the magnetic inhomogeneities caused by biphasic mixtures, reducing peak broadening and producing spectra with better resolution. A similar effect is observed for samples acquired at elevated temperature.

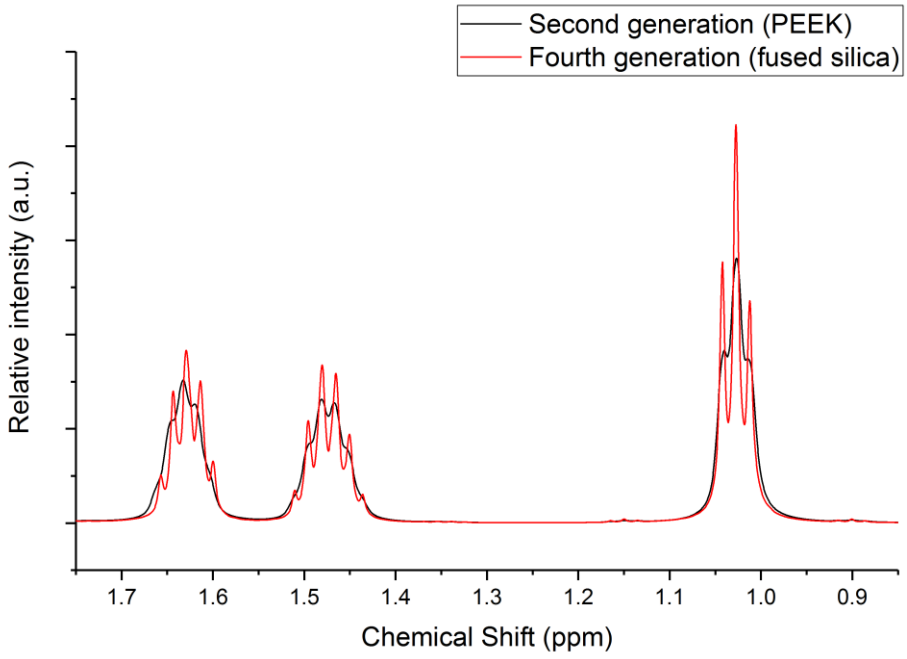

Figure 2.25: Comparison between ^1H spectra of n-butanol CH_3 and CH_2 peaks in a bi-phasic mixture of water and n-butanol using second-generation (PEEK) and fourth-generation (fused silica) flow tube designs. (3.28 s acquisition time, 1 s relaxation delay, 0.3 Hz line broadening). Data courtesy of Rachael Broomfield-Tagg.

2.5 CONCLUSIONS

To monitor reactions by on-line NMR spectroscopy requires the construction of FlowNMR apparatus. Four different generations of FlowNMR apparatus have been developed in this project, with each building on previous designs.

The recent commercialisation of NMR flow tubes has allowed FlowNMR spectroscopy to become much more widely available. The flow tube design allows reaction monitoring to be carried out on any NMR spectrometer with a standard 5 mm probe. This makes the technique more accessible and allows multiple nuclei 1D and 2D NMR methods to be used than were not possible with early FlowNMR designs using HPLC-NMR flow probes.

Combining FlowNMR spectroscopy with other analytical techniques including mass spectrometry, UV-Vis spectroscopy and HPLC provides a much more detailed understanding of reaction mechanism than may be gained by any individual technique. Connecting techniques with different analytical timescales and sampling methods has required different approaches, with UV-Vis spectroscopy used as an on-line technique, whilst MS and HPLC analysis are performed in-line.

Regulating reaction temperature and pressure throughout the entire analytical setup is vital to ensure accurate kinetic data. Jacketing the sample transfer tubing with a separate tube carrying heat transfer fluid has allowed the sample temperature to be maintained throughout the entire sample pathway. Flow, temperature and pressure sensors have been incorporated into the FlowNMR apparatus design, allowing parameters to be monitored throughout the course of a reaction.

The choice of materials used in the FlowNMR apparatus is important due to differences in chemical and material properties. The PTFE tubing used in the standard InsightMR flow tube design was found to be prone to damage by mechanical stress, leading to leaks in the flow system. PEEK tubing was therefore used throughout the FlowNMR apparatus due to the higher mechanical strength and lower gas permeability that this material offers. Twisting of the PTFE/PEEK tubing within the flow cell was found to cause poorer magnetic homogeneity within the sample, leading to peak broadening. Replacement of the tubing within the flow cell with a fused silica capillary design used in stopped flow NMR apparatus was found to lead to an improvement in shim quality and narrower peak linewidths, resulting in higher quality spectra.

The FlowNMR apparatus designs described within this chapter are used for monitoring of the reactions discussed in subsequent chapters, with additional testing and calibration of the FlowNMR apparatus discussed in Chapter 2.

2.6 REFERENCES

1. Albert, K. In *On-Line LC-NMR And Related Techniques*, John Wiley & Sons, Ltd: 2003; pp 1-22.

2. Albert, K.; Nieder, M.; Bayer, E.; Spraul, M., Continuous-flow nuclear magnetic resonance. *J. Chromatogr. A* **1985,** 346, 17-24.

3. Foley, D. A.; Doecke, C. W.; Buser, J. Y.; Merritt, J. M.; Murphy, L.; Kissane, M.; Collins, S. G.; Maguire, A. R.; Kaerner, A., ReactNMR and ReactIR as reaction monitoring and mechanistic elucidation tools: the NCS mediated cascade reaction of alpha-thioamides to alpha-thio-beta-chloroacrylamides. *J. Org. Chem.* **2011,** 76, 9630-9640.

4. Foley, D. A.; Wang, J.; Maranzano, B.; Zell, M. T.; Marquez, B. L.; Xiang, Y.; Reid, G. L., Online NMR and HPLC as a reaction monitoring platform for pharmaceutical process development. *Anal. Chem.* **2013,** 85, 8928-8932.

5. Foley, D. A.; Zell, M. T.; Marquez, B. L.; Kaerner, A., NMR Reaction-Monitoring as a Process Analytical Technique. *Pharm. Technol.* **2011,** 11, S19.

6. Fyfe, C. A.; Cocivera, M.; Damji, S. W. H., Flow and stopped-flow nuclear magnetic resonance investigations of intermediates in chemical reactions. *Acc. Chem. Res.* **1978,** 11, 277-282.

7. Fyfe, C. A.; Cocivera, M.; Damji, S. W. H.; Hostetter, T. A.; Sproat, D.; O'Brien, J., Apparatus for the measurement of transient species and effects in flowing systems by high-resolution nuclear magnetic resonance spectroscopy. *J. Magn. Reson.* **1976,** 23, 377-384.

8. Khajeh, M.; Bernstein, M. A.; Morris, G. A., A simple flowcell for reaction monitoring by NMR. *Magn. Reson. Chem.* **2010,** 48, 516-522.

9. Nordon, A.; McGill, C. A.; Littlejohn, D., Process NMR spectrometry. *Analyst* **2001,** 126, 260-272.

10. Albert, K.; Bayer, E., High-performance liquid chromatography—nuclear magnetic resonance on-line coupling. *TrAC, Trends Anal. Chem.* **1988,** 7, 288-293.

11. Albert, K.; Kunst, M.; Bayer, E.; Spraul, M.; Bermel, W., Reversed-phase high-performance liquid chromatography-nuclear magnetic resonance on-line coupling with solvent non-excitation. *J. Chromatogr. A* **1989,** 463, 355-363.

12. Smallcombe, S. H.; Patt, S. L.; Keifer, P. A., WET Solvent Suppression and Its Applications to LC NMR and High-Resolution NMR Spectroscopy. *J. Magn. Reson. A* **1995,** 117, 295-303.

13. Maiwald, M.; Fischer, H. H.; Kim, Y.-K.; Hasse, H., Quantitative on-line high-resolution NMR spectroscopy in process engineering applications. *Anal. Bioanal. Chem.* **2003,** 375, 1111-1115.

14. Maiwald, M.; Fischer, H. H.; Kim, Y.-K.; Albert, K.; Hasse, H., Quantitative high-resolution on-line NMR spectroscopy in reaction and process monitoring. *J. Magn. Reson.* **2004,** 166, 135-146.

15. Bernstein, M. A.; Stefinovic, M.; Sleigh, C. J., Optimising reaction performance in the pharmaceutical industry by monitoring with NMR. *Magn. Reson. Chem.* **2007,** 45, 564.

16. Foley, D. A.; Bez, E.; Codina, A.; Colson, K. L.; Fey, M.; Krull, R.; Piroli, D.; Zell, M. T.; Marquez, B. L., NMR flow tube for online NMR reaction monitoring. *Anal. Chem.* **2014,** 86, 12008-12013.

17. Buser, J. Y.; McFarland, A. D., Reaction characterization by flow NMR: quantitation and monitoring of dissolved H_2 via flow NMR at high pressure. *Chem. Commun.* **2014,** 50, 4234-4237.

18. InsightMR: Real-Time Data Analysis and Acquisition Control. www.bruker.com/products/mr/nmr/nmr-software/nmr-software/insightmr/overview.html (accessed 10/10/2018).

19. Marquez, B. F., Michael; Colson, Kimberly L.; Krull, Robert; Bez, Eckhard; Piroli, Don; Maas, Werner E. NMR reaction monitoring flow cell. US Patent 20120092013A1, April 19, 2012.

20. Chung, R.; Hein, J. E., The More, The Better: Simultaneous In Situ Reaction Monitoring Provides Rapid Mechanistic and Kinetic Insight. *Top. Catal.* **2017,** 60, 594-608.

21. Hashiguchi, S.; Fujii, A.; Haack, K.-J.; Matsumura, K.; Ikariya, T.; Noyori, R., Kinetic Resolution of Racemic Secondary Alcohols by Ru(II)-Catalyzed Hydrogen Transfer. *Angew. Chem. Int. Ed.* **1997,** 36, 288-290.

22. Chouler, J. Flow NMR for in-operando Investigation of Homogeneous Catalysts. MRes Thesis, University of Bath, 2014.

23. Johnston, C. P.; West, T. H.; Dooley, R. E.; Reid, M.; Jones, A. B.; King, E. J.; Leach, A. G.; Lloyd-Jones, G. C., Anion-Initiated Trifluoromethylation by $TMSCF_3$: Deconvolution of the Siliconate–Carbanion Dichotomy by Stopped-Flow NMR/IR. *J. Am. Chem. Soc.* **2018,** 140, 11112-11124.

3 Practical Aspects of Reaction Monitoring with FlowNMR Spectroscopy

The work presented in this chapter has been published in the journal '*Catalysis Science and Technology*, volume 54, issue 1, pages 30-33 and is reproduced with the permission of the Royal Society of Chemistry. Page, reference and figure numbers have been altered for consistency. Some figures originally published in the Electronic Supplementary Information have been included in the main text where they are referred to.

3.1 Introduction to Published Work

In Chapter 2, design considerations for the construction of FlowNMR apparatus and hardware were discussed, including selection of materials and integration with other analytical techniques. The next chapter addresses some practical aspects of using FlowNMR spectroscopy for reaction monitoring.

Unlike conventional NMR spectroscopy, where a static sample remains unchanged over time, FlowNMR spectroscopy is a dynamic technique, with both sample motion through the flow cell and chemical reaction to consider. The dynamic nature of the technique leads to challenges not usually faced in conventional NMR spectroscopy, as time pressures rule out experiments requiring long acquisition times or large number of transients. If the sample flow rate through the flow tube is similar or greater than the rate of magnetisation build up and T_1/T_2 relaxation then in-flow and out-flow effects are also observed, which can alter peak intensities and shapes.[26, 28]

Whilst some flow effects have been discussed previously in the context of HPLC-NMR spectroscopy,[27-28] these effects are dependent on the apparatus and spectrometer used, and so will be different for a flow tube than for a flow probe. For this reason, the effects of sample flow were investigated for the apparatus discussed in Chapter 2,[†] along with other general considerations and NMR techniques that are relevant to FlowNMR.

[†] The experiments in this chapter were carried out using the second-generation apparatus discussed in Chapter 2, however the findings are generally applicable to all FlowNMR setups discussed.

3.2 STATEMENT OF AUTHORSHIP

This declaration concerns the article entitled:									
Practical Aspects of Real-time Reaction Monitoring using Multi-nuclear High Resolution FlowNMR Spectroscopy									
Publication status (tick one)									
draft manuscript		**Submitted**		**In review**		**Accepted**		**Published**	✓
Publication details (reference)	A. M. R. Hall, J. C. Chouler, A. Codina, P. T. Gierth, J. P. Lowe and U. Hintermair, Catal. Sci. Tech., 2016, 6, 8406-8417.								
Candidate's contribution to the paper (detailed, and also given as a percentage).	**The candidate contributed to/ considerably contributed to/predominantly executed the…** **Formulation of ideas:** 20% Initial ideas from UH and JL. Theoretical work; JL, AH, UH with reference to literature. **Design of methodology:** 20% Initial apparatus design by JC. Experimental design by UH and JL. Second generation apparatus used for majority of measurements was constructed by AH. **Experimental work:** 100% All experimental work was carried out by AH. **Presentation of data in journal format:** 70% The figures and initial draft was prepared by AH, with editing and further material contributed by UH and JL. The manuscript was proof-read by PG and AC.								
Statement from Candidate	This paper reports on original research I conducted during the period of my Higher Degree by Research candidature.								
Signed					**Date**				

3.3 PRACTICAL ASPECTS OF REAL-TIME REACTION MONITORING USING MULTI-NUCLEAR HIGH RESOLUTION FLOWNMR SPECTROSCOPY

Andrew M. R. Hall,[a] Jonathan C. Chouler,[a] Anna Codina,[b] Peter T. Gierth,[b] John P. Lowe[c]* and Ulrich Hintermair[a]*

a) Centre for Sustainable Chemical Technologies, University of Bath, Bath BA2 7AY, United Kingdom.
b) Bruker UK Ltd., Banner Lane, Coventry CV4 9GH, United Kingdom.
c) Department of Chemistry, University of Bath, Bath BA2 7AY, United Kingdom.

** Corresponding authors: J.Lowe@bath.ac.uk, U.Hintermair@bath.ac.uk*

FlowNMR spectroscopy is an excellent technique for non-invasive real-time reaction monitoring under relevant conditions that avoids many of the limitations that bedevil other reaction monitoring techniques. With the recent commercial availability of FlowNMR hard- and software solutions for high resolution spectrometers it is enjoying increased popularity in both academia and industry. We present an account on practical aspects of high field multi-nuclear FlowNMR for reaction monitoring including apparatus design, flow effects, acquisition parameters and data treatment, which are important to consider if accurate kinetic data are to be obtained from FlowNMR experiments. Flow effects on NMR peak areas are particularly important as they can lead to large quantification errors if overlooked, but can easily be corrected for and even used to increase temporal resolution with suitably adjusted instrument settings.

3.3.1 Introduction

The ability to monitor chemical reactions by simultaneously following the concentration of different species in real time under reaction conditions is a vital tool for determination of reaction kinetics and elucidation of reaction mechanisms, as well as for process development and monitoring on an industrial scale. In principle a variety of methods are suitable for application in real-time reaction monitoring, including spectroscopic techniques such as Infrared (IR), Raman, Ultraviolet-Visible (UV-Vis) and Nuclear Magnetic Resonance (NMR) spectroscopies along with other methods such as calorimetry, mass spectrometry, electrochemistry, chromatography and chemical analysis. In practice, the ideal reaction monitoring technique would provide information about all species within a reaction mixture under normal reaction conditions, with high sensitivity and temporal resolution, whilst remaining accessible to a non-specialist and at minimum cost. Whilst none of the above

methods are able to fulfil these rather exacting conditions, one of the most commonly used techniques is NMR spectroscopy, which is particularly useful due to the large amount of information it can provide about the structure of the species under investigation and its inherently quantitative nature.

Reaction monitoring techniques may be coupled directly to a reaction vessel, with a probe inserted into the vessel (*in-situ* or *in-line* monitoring) or with the reaction vessel connected to the instrument via hyphenated tubing (*on-line* monitoring). Alternatively, reaction monitoring may be performed remotely from the reaction vessel by sampling (*at-line* or *off-line* monitoring). In-situ methods are generally preferred as they do not introduce sampling delays and minimise the risk of disturbing the reaction system or changing the aliquot taken, which is vital for accurate mapping of the reaction kinetics. Reaction monitoring by NMR is typically performed either by off-line sampling or by in-situ monitoring of a reaction carried out a on small scale in a standard sample tube within the spectrometer.[21] Despite the many intrinsic benefits of NMR spectroscopy both approaches have significant practical limitations: off-line sampling introduces delays in the order of several minutes and exposes the sample to different conditions potentially leading to compositional changes, whilst the lack of mixing in commonly used 5 mm NMR tubes may cause unrepresentative kinetic data to be acquired. A recent study by Foley et al. clearly demonstrates the significance of mass transfer limitations when using static NMR tubes for reaction monitoring, leading to strikingly different kinetic results for the same reaction when monitored by different NMR techniques.[11]

An alternative to these established techniques is the growing field of on-line NMR monitoring, which is amenable to a wide range of reaction conditions including reactions requiring heating, cooling and inert or reactive gas atmospheres,[35, 126-127] and in principle can circumvent the above limitations. Performing the reaction outside of the spectrometer allows reagents to be added without stopping data acquisition and the reaction to be properly mixed to ensure that the reaction kinetics measured are not obscured by diffusional effects. This means that reactions can be performed under realistic conditions and without the delay that is introduced by sampling techniques.

Flow techniques in NMR spectroscopy are well known in the context of High Performance Liquid Chromatography (HPLC) NMR coupled setups for multi-technique analysis and high-throughput characterisation.[27, 50, 122, 128] Recently, however, interest in flow techniques for on-line reaction monitoring has grown, both on a laboratory scale[33, 54, 56, 126] and for process monitoring and control in industry.[29, 31, 121, 129] This has in part been driven by the recent development and commercialisation of a number of systems for on-line NMR reaction

monitoring for both high field[36, 130] and low field[49] approaches. Whilst modern low field instruments with good field stability have proven increasingly useful for process monitoring in industrial settings due to their lower cost and portable design,[48, 52, 131] low field spectrometers lack the resolution and variety of experiments required for studying most catalytic mechanisms and kinetics in a research setting, where the reaction by-products and intermediates may not be well known.[49] In addition, due to the high degree of temperature control required for magnetic field stability in low field instruments, the reaction sample must be brought to the magnet temperature before passing through the spectrometer to avoid disrupting the magnetic field homogeneity.[49] Multi-nuclear spectra have become possible with modern low field instruments, and deconvolution techniques can be used to alleviate some of the constraints on spectral resolution,[52-53] but high field instruments are clearly much more useful for reaction and catalyst development due to higher spectral resolution, increased sensitivity, and the ability to study a wide range of nuclei and perform advanced measurements. A significant advance in high field reaction monitoring has been the recent development of integrated flow tubes that can be inserted into a standard spectrometer probe without having to use specialised flow probes such as those developed for HPLC-NMR[27, 122] or microfluidic devices,[40-45] reducing costs and greatly facilitating use of the technique.[36, 55]

With all these benefits of performing on-line reaction monitoring by continuous-flow high resolution NMR spectroscopy, the presence of flow can have significant effects on the quality and quantification of the NMR signal, and it is important that these effects are considered if accurate data are to be generated. Although some basic principles of how NMR data acquisition is affected by moving samples have been known for some time,[27, 122] and the use of low field NMR spectroscopy in process monitoring has been well covered in the recent literature,[33, 52, 131-132] we felt it necessary to re-investigate the considerations required for real-time reaction monitoring using high field FlowNMR with contemporary instruments and software. Here we report a summary of the most important effects and parameters that need to be considered when using multi-nuclear high resolution FlowNMR for accurate reaction monitoring with the aim of analysing kinetics and elucidating reaction mechanisms in the research laboratory.

3.3.2 Results and Discussion

3.3.2.1 Hardware configuration and design

On-line NMR reaction monitoring may be performed either with continuous flow, where data is acquired whilst the sample is moving through the receiver coil, or with a pulsed flow, where the flow is halted during measurement. Most on-line-NMR reaction monitoring systems use continuous flow[33, 35, 54-55, 131] as this means that the sample within the spectrometer is continually refreshed to ensure that the volume measured is always representative of the mixture within the reaction vessel; however, pulsed systems have been developed for use with some low field spectrometers where continuous flow is not possible.[133] For all on-line NMR reaction monitoring setups there is an inherent time required for the sample to be pumped from the reaction vessel to the spectrometer, leading to a slight delay between a change occurring in the reaction vessel and detection. This delay means that standard on-line NMR is not suitable for monitoring reactions with half-lives of less than a few minutes that are triggered by an external stimulus (such as the addition of a reagent). Fast-injection methods, including stopped-flow NMR techniques, have been developed to overcome this, although these typically use a static sample that is discarded after measurement.[13-14, 16, 19, 30, 134-136] Capturing fast events that are naturally occurring in a flowing sample during the reaction, however, is not limited by the pump delay but the NMR acquisition parameters.

We have used a closed-loop continuously recirculating flow system[‡] based on a simple setup using off-the-shelf commercial components (Figure 2.6). The reaction vessel may be anything from an open beaker to a Schlenk flask or a pressure reactor. As long as adequate mixing in the reaction vessel is provided, ensuring that the sample circulated through the spectrometer is representative of the bulk, there is no upper limit on the reaction volume. A standard HPLC pump with 1/16" HPLC tubing was used to circulate the sample through the system, with a bypass loop fitted for safety reasons. A NMR flow tube with a flexible, thermally jacketed transfer line and 5 mm glass sample tip inserted into a standard 500 MHz spectrometer was used as the flow module. Details on all components used can be found in the experimental section.

[‡] Note that whilst NMR data is acquired on a flowing aliquot, the reaction itself is performed as a batch process in a continuously stirred reaction vessel, yielding reaction profiles as a function of time rather than of reactor length or flow velocity as would be the case for continuous flow mode.[137]

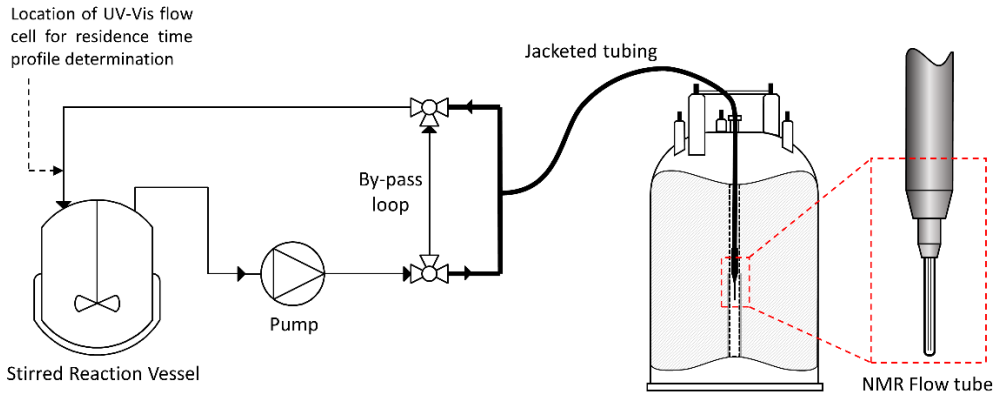

Figure 3.1: Flow scheme and instrumentation diagram for the FlowNMR reaction monitoring apparatus (not to scale; for details see the experimental section).

As expected for such small dimensions, under typical conditions (4 $mLmin^{-1}$ flow rate, water-like densities and viscosities) the hydrodynamics of the system are characterised by a low Reynolds number of R_e = 113 operating in the laminar flow regime. Laminar flow leads to back-mixing within the flowing sample due to shearing, causing a symmetrical broadening of the residence time distribution.[10] In order to quantify the degree of back-mixing and check for additional dead volumes within the system, residence time distribution profiles were recorded by step tracer experiments quantified by an in-line UV-vis flow cell positioned at the exit (cf.Figure 3.1). Figure 3.2a shows the difference between the residence time distribution (RTD) of the apparatus with the flow tube bypassed, and with the flow tube included. At 4 $mLmin^{-1}$ (acetone, 25°C) the pump and tubing alone have a reasonably sharp RTD with a mean residence time of τ = 18.7 sec with only minor tailing, signifying negligible hold-up by non-uniform flow paths.§ Adding the flow tube to the system shifts the total mean residence time to τ = 53.7 sec, showing the total internal volume to be 3.6 mL. As expected, the RTD profile broadening is increased after the longer travel, but also a slightly more pronounced tailing is seen with the flow tube included. Visual analysis of the flow tube during injection and displacement of a tracer dye illustrates the non-ideal plug flow in the tip end of the flow tube, where the narrow transport tubing expands into the 5 mm analysis tube and back out again (see sample hold-up in Figure 3.2b and c, and the video in the electronic supporting information).

§All experiments were performed with the internal pressure sensor of the pump disconnected due to additional sample holdup within the sensor (Figure). Sample holdup and tailing analysis are strictly qualitative.

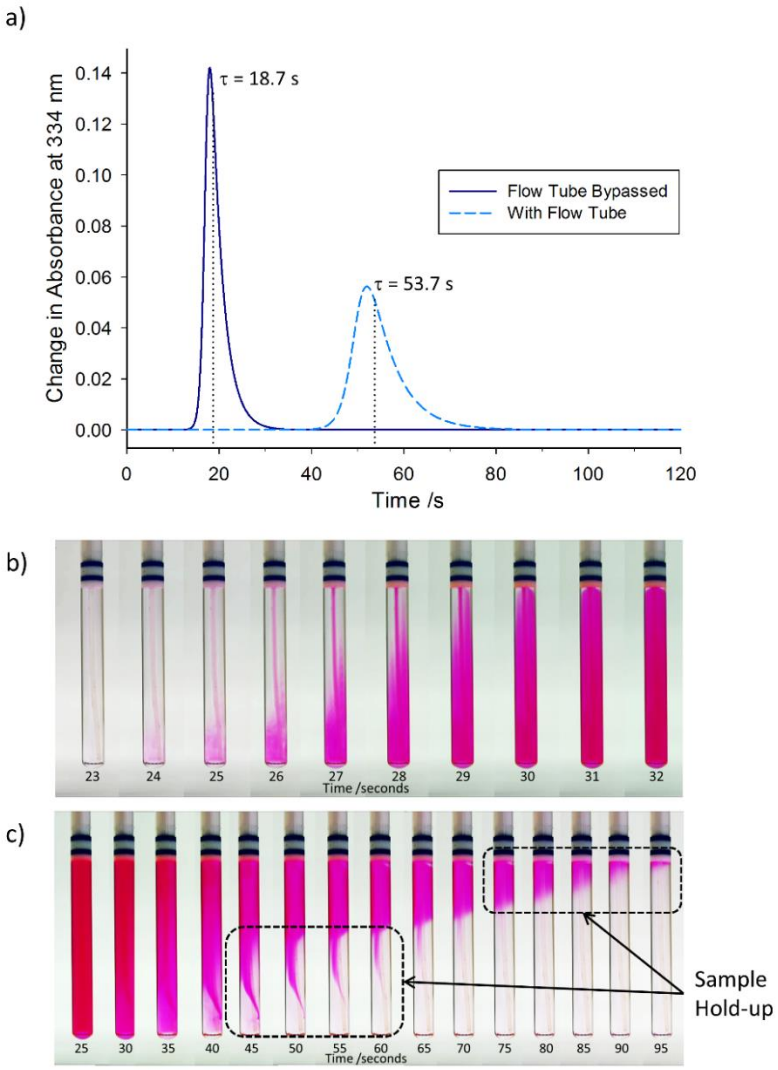

Figure 3.2: a) Residence time distribution profiles for the apparatus described in Figure 2.6 at a flow rate of 4 mLmin^{-1} (acetone, 25˚C), comparing the effects on residence time distribution with and without the flow tube. Still images captured at different time points during the b) addition and c) removal of a tracer dye solution into the flow tube at a flow rate of 4 mLmin^{-1} (video available at dx.doi.org/10.1039/C6CY01754A). Note: Time values in a) correspond to a complete circuit of the apparatus returning to the reaction vessel, whilst time values in b) and c) are the time taken to travel between the reaction vessel and flow tube only.

3.3.2.2 Intrinsic flow effects on NMR quantification

The hydrodynamics of a NMR flow system are not only important for quantifying internal volumes, residence times and sample back-mixing, but they also directly impact on NMR signal acquisition as they determine the time a given volume element experiences the magnetic field (pre-magnetisation) and spends in the detector coil. In our setup, the volume of the tubing between the sample entering the magnet and arriving at the flow tube is approximately 0.2 mL, leading to a residence time within the magnet, before entering the detector coil region, of approximately 3 seconds (at a flow rate of 4 mLmin^{-1}). The volume of the flow tube itself is approximately 0.5 mL, corresponding to a residence time of around 8 seconds in the detector. As the residence time within the magnet prior to detection is significantly less than the 5 times the T_1 relaxation time delay required for complete

magnetisation for many nuclei, this may impact on signal intensity and quantification in a way that is not an issue for conventional NMR spectroscopy on static samples. This effect and its impact on NMR data has been studied in some detail in the context of HPLC-NMR,[27, 122] however, there has been some recent discussion of flow effects in the context of on-line reaction monitoring.[31, 33, 35, 47]

To illustrate how flow may affect the signal intensity of peaks in the NMR spectrum, the apparatus may be divided into three sections (Figure 3.3): Section A is outside the influence of the magnetic field (B = 0); section B is defined as within the magnet but before the detector ($0 < B < B_0$), whilst section C encompasses the sample volume within the detector (at B_0). For simplicity and to aid explanation, the schematic in Figure 3.3 assumes three distinct regions, whereas in reality there would be a gradual increase in magnetic field strength as the sample approaches sections B and C. Before entering the magnet (A), all nuclei have random spin orientations, leading to an overall magnetisation vector of zero. Upon entering the magnetic field (B), the nuclear spins start to align along the Z axis, leading to an increase in the magnitude of the overall magnetisation vector, M. For a given flow rate, the extent of this process is dependent on the individual T_1 relaxation times of each of the respective nuclei, with nuclei with short T_1 values (Figure 3, solid red line) building up magnetisation faster than those with longer T_1 relaxation times (Figure 3, dashed and dotted red lines).

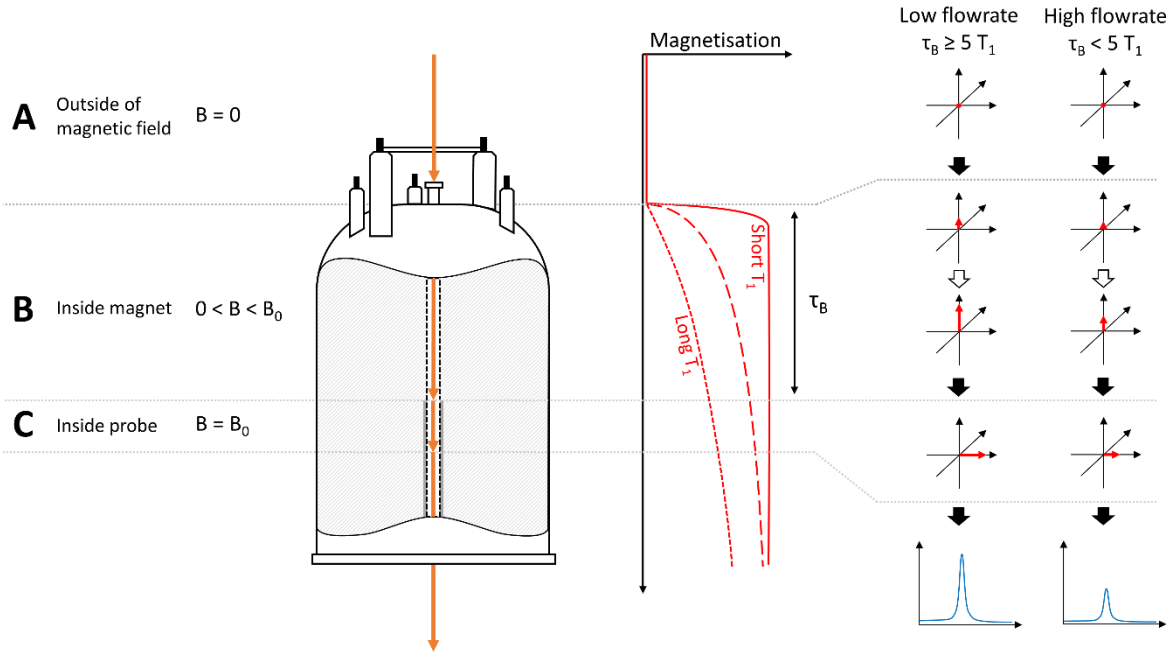

Figure 3.3: Schematic illustration of magnetisation build-up effects in flow, resulting in non-quantitative results for nuclei with long T_1 relaxation times or for high flow rates, where $\tau_B < 5 \times T_1$. B = magnetic field strength, τ_B = residence time of sample in magnet prior to entering detector. Note: for the purpose of clarity, the sample is shown as exiting through the base of the instrument in this diagram, whereas in reality the sample returns by a path parallel to that it entered the instrument by (see Figure 2.6). Stray field effects are ignored in this example.

Thus if the flow rate is "fast" or the nuclei have "long" T_1 values (or both), the residence time (τ_B) within the magnet (section B) will be insufficient to allow full build-up of magnetisation before the sample reaches the detector region (C). In this case the free induction decay (FID) detected in the receiver coils will be less than it would be if the nuclei were fully magnetised, leading to an underestimation of signal intensity. Most importantly however, since the T_1 relaxation time will be different for each nucleus within a molecule or reaction mixture, the amount of magnetisation of the nuclei as they enter the detector will be different (see example in Figure 3.4). This causes the signal intensity to vary for each nucleus, affecting the ability to quantify reaction progress based on different peak areas in flow, an issue which doesn't arise with static samples in which all nuclei will have had sufficient time for full magnetisation build-up before acquisition.

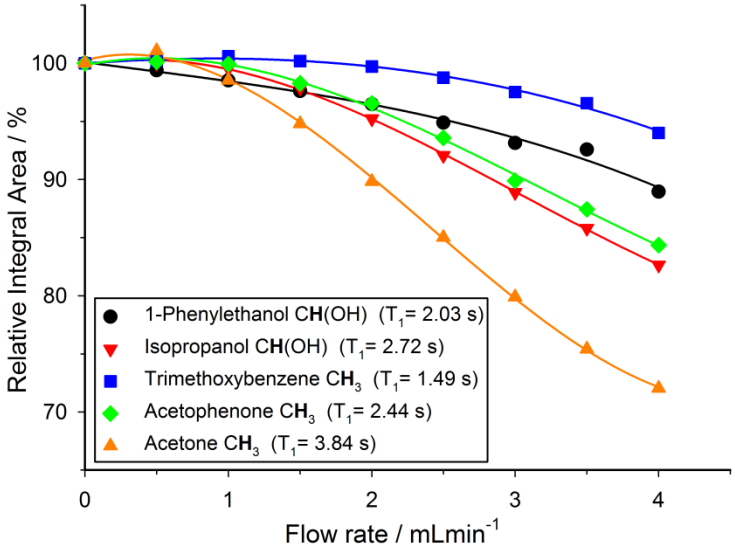

Figure 3.4: Variation of relative ^{1}H NMR integral areas for a mixture of organic molecules over flow rate (isopropanol, 25°C, 30° pulse, 4 sec acquisition time, 1 sec relaxation delay).

As can be seen inFigure 3.4, relative ^{1}H peak area discrepancies induced by flow can be as high as 25% at flow rates of 4 mLmin^{-1}. If unaccounted for, such differences would directly translate to erroneous kinetic data being acquired with a technique that is otherwise valued for being inherently quantitative. Of course, this effect is not restricted to ^{1}H but equally applies to other common hetero-nuclei often used for reaction monitoring such as ^{19}F, ^{11}B, ^{31}P and ^{13}C. At a given flip angle, the decrease in peak integral area at a given flow rate only depends on the intrinsic T_1 relaxation time of the nucleus. ^{1}H and ^{19}F have relatively short relaxation times and thus are affected to a lesser degree by flow effects, which are much more pronounced for ^{31}P and ^{13}C which have longer T_1 times causing up to 70% signal loss at 4 mLmin^{-1}. Such severe signal reductions may not only falsify quantification by relative integration but even lead to missing transient reaction intermediates. Figure 3.5shows an

overview plot of relative integral area reduction induced by flow for various nuclei (for details see the experimental section and Appendix 8.1.2).

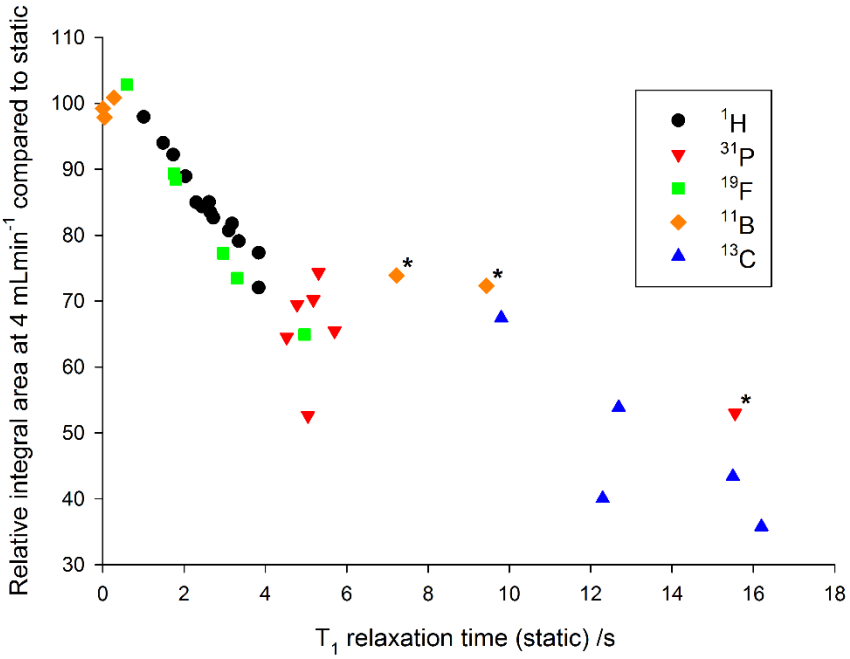

*Figure 3.5: Correlation between the decrease in integral area at a flow rate of 4 mLmin^{-1} and the T_1 relaxation time at a flow rate of 0 mLmin^{-1} for a variety of commonly used NMR nuclei (25°C, 30° pulse, inverse gated decoupling for ^{31}P and ^{13}C, various delay and acquisition times – see experimental section for details). *Highly symmetrical compounds such as BH_4^-, BF_4^- and PPh_3 result in unusually long relaxation times.*[138-139]

Fortunately, this so-called in-flow effect on peak area is relatively easy to correct for. Previously reported methods for preventing quantification errors have included the addition of a pre-magnetisation loop within the magnetic field to increase τ_B for complete magnetisation of the sample,[33] or simply restriction to lower flow rates to ensure operation within the regime where in-flow effects are negligible.[131] Both of these methods suffer from an increased delay between a change occurring in the reaction vessel and the change being detected in the spectrometer, which may be undesirable for fast reacting systems. An alternative which does not require any modification of equipment or additional delays in data acquisition is simply to record two spectra of the same sample mixture; one with the sample flowing at the desired flow rate and one with a stationary (fully pre-magnetised, quantitative conditions) sample. These additional spectra may easily be acquired at the start and end of the reaction, or by temporarily halting the flow when there are intermediate species of interest. A correction factor may then be calculated for each peak using the simple mathematical formula expressed below (I = peak integral, CF = correction factor).

Equation 3.1: $$I_{Corrected} = CF \times I$$

Equation 3.2: $$CF = \frac{I_{Static}}{I_{Flow}}$$

For reactions where the starting material and products have significantly different T_1 values, the difference between the corrected and uncorrected reaction profiles can be significant as demonstrated below for the oxidation of triphenylphosphine as followed by ^{31}P FlowNMR spectroscopy at 4 mLmin^{-1} (Figure 3.6).

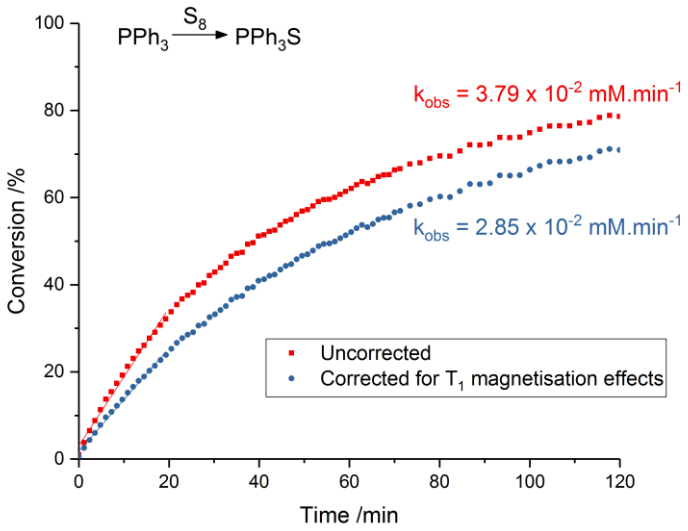

Figure 3.6: Comparison between uncorrected and corrected reaction progress data of the oxidation of triphenylphosphine [T_1 = 15.6 sec] to triphenylphosphine sulphide [T_1 = 4.8 sec] from ^{31}P FlowNMR accounting for incomplete pre-magnetisation (toluene, 25°C, 30° pulse, inverse gated decoupling, 0.8 sec acquisition time, 2 sec relaxation delay). Both datasets corrected for relaxation delay quantification effects (see experimental section for details).

In addition to in-flow effects due to incomplete pre-magnetisation, flowing the sample through the detector also has the effect of continuously replenishing the polarised nuclei within the detection region C with fresh material for each scan. This so-called out-flow effect (cf. Figure 3.3) leads to a faster decay of the FID under flow conditions, and faster restoration of Z-magnetisation, because nuclei with detectable magnetisation in the XY plane at the start of the acquisition period are leaving the detector before they have fully relaxed, being replaced by either fresh Z-magnetisation from nuclei in region B (if flow is relatively slow and/or T_1 relatively fast) or at least partial Z-magnetisation (if flow is relatively fast and/or T_1 is relatively slow).

This out-flow effect on the effective T_1 relaxation time for different ^1H environments can be directly observed by standard T_1 measurements, with effective T_1 reductions of up to 66% at 4 mLmin^{-1} as compared to static samples (Figure 3.7). Whilst the absolute (intrinsic) T_1 relaxation times remain unaffected by the motion of the sample, the *effective* T_1 value that is observed under flow conditions (T_1*) decreases as flow rate is increased in a manner that is

proportional to the static T_1 value. This decrease in measured T_1 relaxation time has been documented previously as a feature of HPLC-NMR,[27] and is governed by the following equation, where τ_B is the residence time within the magnetic field, prior to entering the detector (cf. Figure 3.3):

Equation 3.3: $$\frac{1}{T_{1,Flow}} = \frac{1}{T_{1,Static}} + \frac{1}{\tau_B}$$

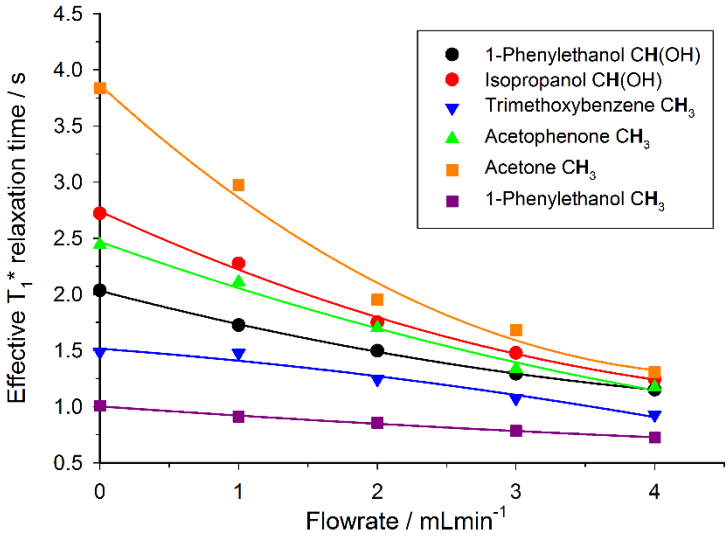

Figure 3.7: Measured ^1H T_1 relaxation times for a mixture of organic molecules over flow rate (isopropanol, 25°C, 2 sec acquisition time, 20 sec relaxation delay).*

Under favourable conditions (e.g. slow flow rates where essentially all the sample arriving in the detector region is freshly Z-magnetised) this may allow for shorter repetition times to be used between scans without compromising on quantitation, since under static conditions leaving 4.6 x T_1 between scans is required for recovery of 99% of the equilibrium magnetisation. A similar principle has previously been applied to increase signal acquisition rate on static samples,[140] and in 'moving tube' experiments.[141] However, at higher flow rates, in-flow effects dominate and are the major factor to be considered if quantitative data are required (see below and Figure 3.10).

The faster decay in the FID brought about by the out-flow effect necessarily leads to a concomitant decrease in the measured T_2 relaxation time (Figure 3.8) which is governed by an analogous equation to that for T_1 relaxation: [27]

Equation 3.4: $$\frac{1}{T_{2,Flow}} = \frac{1}{T_{2,Static}} + \frac{1}{\tau_B}$$

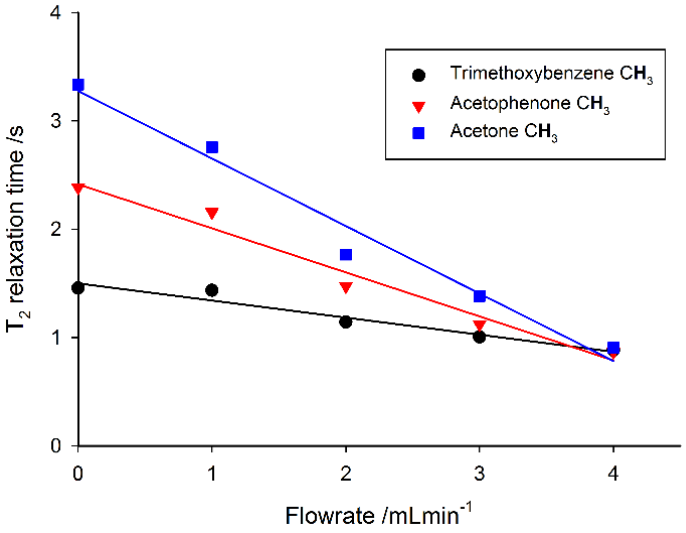

Figure 3.8: Decrease in ^1H T_2 relaxation times with increasing flow rate (Isopropanol, 25°C, CPMG pulse sequence, 4 s acquisition time, 15 s relaxation delay)

This decrease in effective T_2 with increasing flow rate causes an increase in peak linewidth as flow rate is increased, however, in practice when using the flow tube for reaction monitoring, linewidths are dominated by magnetic inhomogeneity effects caused by the presence, and asymmetry in the positioning, of the capillary within the flow tube. Therefore, the impact of increasing flow rate on the effective T_2 value, T_2*, is actually minimal (Figure 3.9).

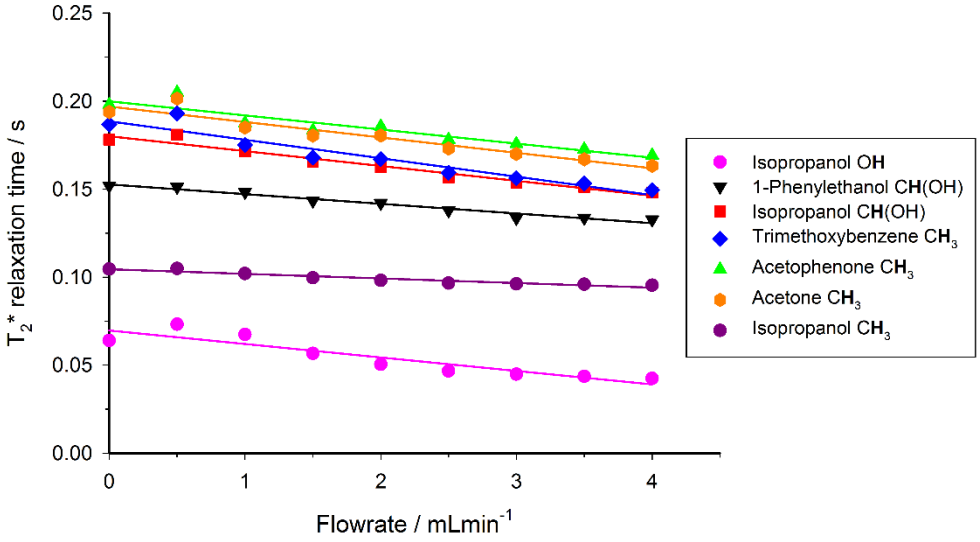

Figure 3.9: Decrease in ^1H T_2 relaxation times with increasing flow rate (isopropanol, 25°C, 30° pulse, 4 sec acquisition time, 15 sec relaxation delay).*

Under certain conditions it is also possible to observe an initial enhancement in signal intensity when flowing a sample through the detector, compared to a static sample. This effect may occur when the relaxation delay time between pulses is set too short, and a return to the Boltzmann distribution between scans is not achieved in the absence of flow. Under slow flow conditions, the rate of return to Boltzmann distribution is then artificially increased by the

influx of freshly polarised nuclei (from region B of Figure 3.3). This effect is more pronounced for large flip angle pulses, since the return to equilibrium takes longer (Figure 3.10). At progressively higher flow rates, in-flow effects of incompletely magnetised fresh sample mean that the signal intensity drops off (Figure 3.4); but under conditions where insufficient relaxation times have been left between scans, the relative integral area remains higher when using a 90 degree pulse rather than a 30 degree pulse since the in-flow of even partially Z-magnetised nuclei contributes to a faster return to the Boltzmann distribution and an increase in relative integral area (Figure 3.10).

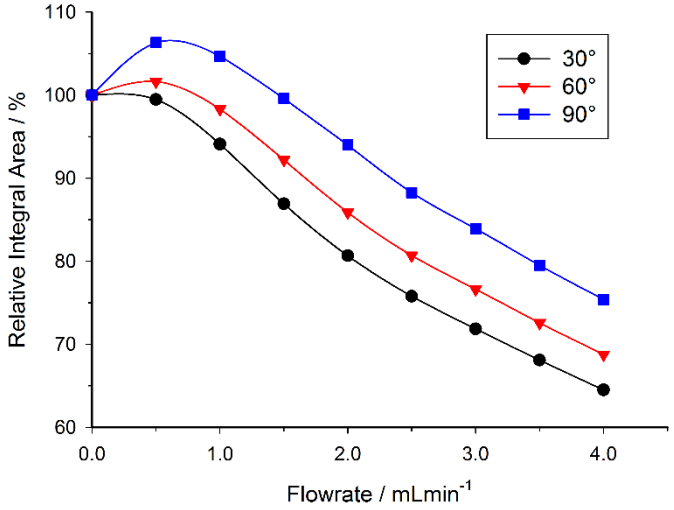

Figure 3.10: Variation in ^1H integral area of acetone CH_3 peak with increase in flow rate for different flip angles, showing increase in integral areas due to relaxation delay time effects for flip angles greater than 30°. (25°C, 3.2 sec acquisition time, 4 sec relaxation delay).

Since this effect is only significant if the relaxation times between pulses is set too short (which would also result in non-quantitative results under static conditions), it is unlikely to be an issue for quantitative FlowNMR studies using appropriate relaxation time delays. However, use of the methods already described (Equations 1 and 2) would be able to compensate for any such errors should they arise.

If the interpulse delay is set long enough to allow full T_1 relaxation in the absence of flow, no signal enhancements caused by out-flow effects are observed at any flip angle when starting to flow (Figure 3.11).

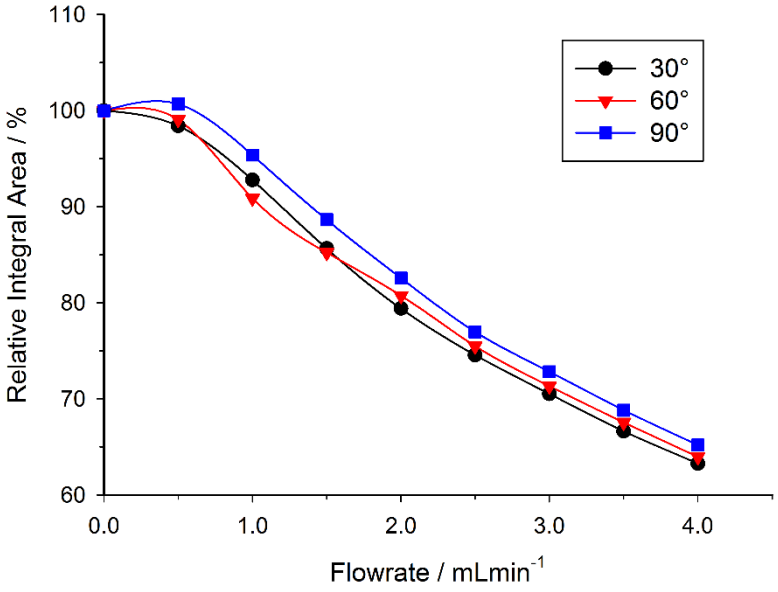

Figure 3.11: Variation in integral area of acetone ^{1}H peak with increase in flowrate for different flip angles, showing increase in integral areas due to relaxation delay time effects for flip angles greater than 30°. (25°C, 3.17 sec acquisition time, 15 sec relaxation delay).

The extent of all flow effects on NMR signal quantification discussed here are dependent on the exact specifications of the probe and spectrometer used. For instance, the design of the magnet and its shielding can greatly modify the amount of stray field experienced by the sample as it approaches the detector, leading to large differences in the results obtained between different instruments even at the same nominal field strength (Figure 3.12). We therefore recommend our results to be taken as a qualitative guideline, and any compensation calculations and parameter fine-tuning should be based on data acquired with the instrument used for reaction monitoring in flow.

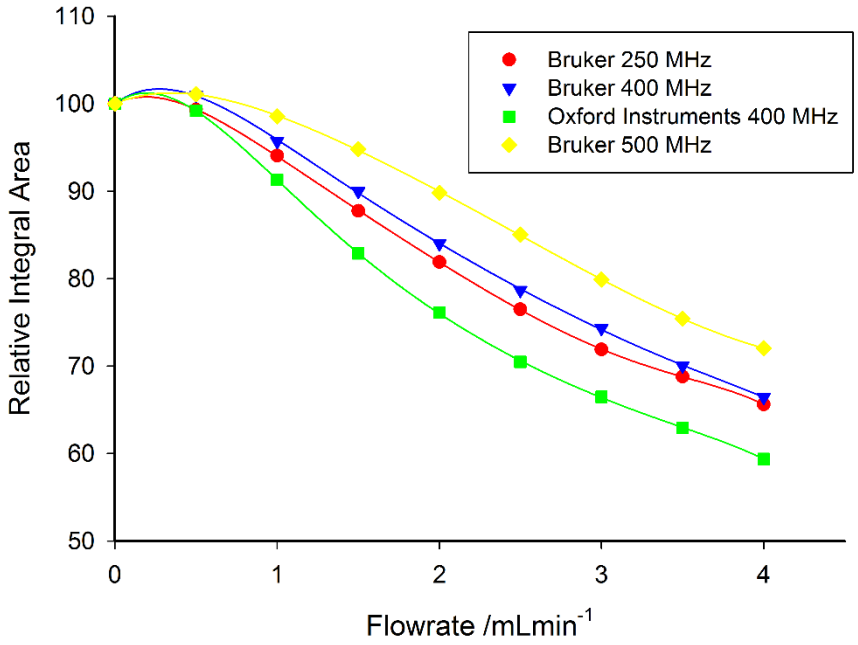

Figure 3.12: Comparison of in-flow effects on relative integral area of the acetone ^{1}H resonance using the same flow tube setup with different spectrometers (25°C, 30° flip angle, 4 sec acquisition time, 15 sec relaxation delay).

3.3.2.3 Practical aspects of data acquisition and processing

Due to the high cost of deuterated solvents and the amount of solvent required for a typical flow experiment (about one order of magnitude higher than tube experiments), it is generally not practical to carry out FlowNMR reactions in deuterated solvents.[142-143] In addition, from a mechanistic perspective deuterated solvents may also cause problems when interacting with reaction intermediates or actively participating in the reaction (H/D exchange), falsifying measured kinetics through isotope effects.[47] It is therefore desirable to carry out FlowNMR reactions in non-deuterated solvents; however, this leads to decreased spectral intensity due to the need to adjust the receiver gain of the spectrometer to ensure that the dominant solvent peaks do not overwhelm the detector, otherwise causing severe distortions to the spectrum.

In order to improve the relative signal intensity of peaks of interest when using non-deuterated solvents it is common to use solvent suppression pulse sequences that reduce solvent peak intensity, allowing the receiver gain to be increased to reach satisfactory signal-to-noise values of the smaller peaks of interest.[9, 142] Standard presaturation sequences typically used for solvent suppression are unfortunately of limited use in FlowNMR, since some of the solvent molecules that have been presaturated during the relaxation delay will have been replaced by fresh unsaturated solvent molecules with full signal intensity when the actual FID is recorded.[9] WET pulse sequences are much more effective in suppressing solvent signals in flow than pre-saturation due to the significantly shorter pulse sequences employed

in WET which are less affected by sample motion.[28, 57] With advanced WET techniques it is also possible to simultaneously suppress multiple resonances (Figure 3.13) including their carbon satellites very effectively (Figure 3.14; for details see the supplementary information).

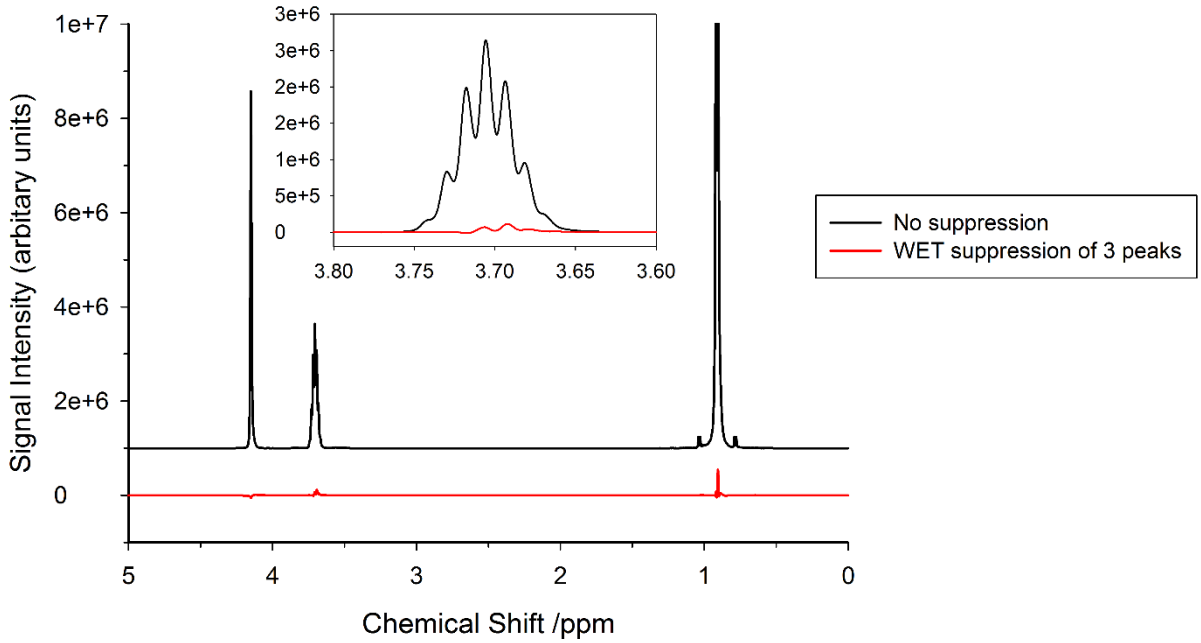

Figure 3.13: Triple solvent suppression of all isopropanol ^{1}H resonances using WET pulse sequence with automated peak detection and suppression including ^{13}C decoupling, leading to an approximately 100-fold reduction in peak intensity (500 MHz, 25°C, 2 sec acquisition time, 4 sec relaxation delay, 0 mLmin^{-1} flow rate).

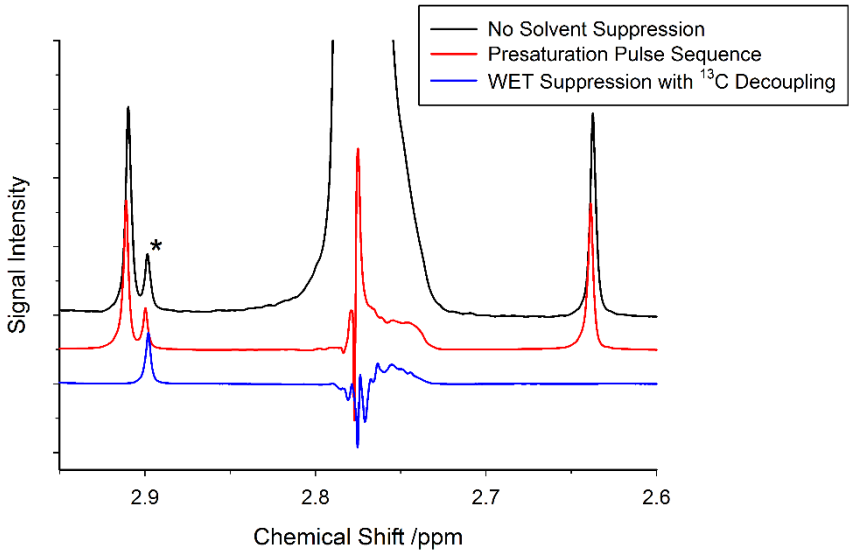

*Figure 3.14: Suppression of the acetonitrile CH_3 peak in flow comparing a simple presaturation pulse sequence with a WET pulse sequence including ^{13}C decoupling, leading to an approximately 500-fold reduction in peak intensity (500 MHz, 25°C, 3.17 sec acquisition time, 4 sec relaxation delay, 4 mLmin^{-1} flow rate). * Solvent impurity peak not suppressed, demonstrating selectivity of WET suppression.*

In addition to eliminating solvent peaks, deuterated solvents are traditionally also used to perform field locking and shimming of the spectrometer. While with most high field spectrometers it is still not possible to perform field locking without an internal ^{2}H standard, modern instruments are capable of maintaining a high level of field stability over extended periods of time. For instance, signal drifts for the 500 MHz Bruker Ultrashield spectrometer used in this study are in the order of 0.1 Hz/h (0.0002 ppm/h), which is quite acceptable for most reaction monitoring time scales. Where field drift is significant, the spectrometer can usually be set to compensate continuously for the measured drift. Shimming of the magnetic field can easily be performed on solvent proton signals using automated shimming programs, however, if a high degree of field homogeneity is required then manual fine tuning of the shims may be required. Using the setup described in Figure 3.1, due to the capillary within the flow tube there is a substantial increase in magnetic inhomogeneity in the XY plane, meaning that particular attention must be paid to ensuring good shimming in these planes. Slight differences in tube positioning will require a shim check before each run, though this can easily be performed starting from previously saved parameters. As internal and external differences in magnetic susceptibility can affect the local magnetic field, the shim quality may drift over the course of a reaction monitoring experiment. Although we haven't found this to be an issue over periods as long as 24 hours using a shielded 500 MHz instrument (variation in HHLW <0.05 Hz/h), it is possible to include periodic shimming routines in the reaction monitoring sequence should significant drifting occur during a long term experiment.

Once good data has been recorded it is vital to ensure that all spectra are well phased and have a flat base line to avoid errors when integrating various peaks across multiple spectra for deriving quantitative reaction profiles. The amount of data generated (easily hundreds to thousands of spectra) generally means that one has to rely on automated processing, which can be performed with a variety of contemporary NMR software packages. Whilst most of these offer multi-spectra commands for automatic phasing and baseline correction, manual adjustment of the parameters used is recommended to achieve high accuracy and precision. For instance, we often find substantial improvements in data quality when phasing and baseline corrections are performed within manually defined ranges of interest rather than the full spectral window as the standard setting, as spectra often include bent edges of varying size and phasing that can cause severe data scattering through baseline jumps or tilts when using automated correction commands (Figure 3.15).

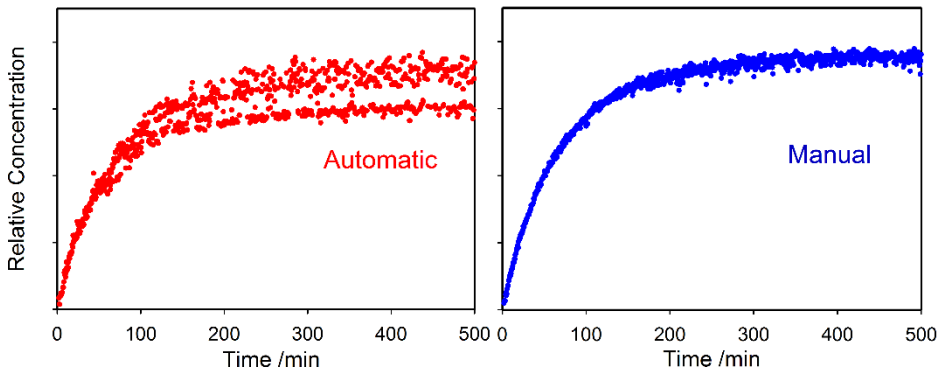

Figure 3.15: Comparison between the same ^{1}H reaction progress data processed using automatic phase and baseline corrections (left) and with manual refinement of parameters to reduce baseline distortions and data scatter (right). Note that a particularly noisy data set was chosen for illustration purposes, and higher quality reaction profiles are typically obtained from FlowNMR experiments (see e.g. Figures 6 and 13).

Even with the above precautions, drifting peaks and overlapping signals may pose additional challenges to extracting the desired information from the data generated. Recent software solutions offer the ability to track moving peaks across multiple spectra for accurate integration, and perform automatic deconvolution of overlapping signals. Spectral deconvolution is used extensively in quantitative process monitoring by UV-vis and IR spectroscopies, and has recently been discussed at great length as an important tool for low field NMR reaction monitoring where spectral resolution is similarly low.[52] Although not always required, these advances can also be applied to high field measurements with equal success, where not having to rely on well-separated diagnostic peaks for each molecule of interest within a dynamic mixture adds to the utility of reaction monitoring by NMR. Below in Figure 3.16 we show an example where overlapping resonances have been deconvoluted to yield the same reaction profile as derived from fully separated signals in other parts of the spectra.

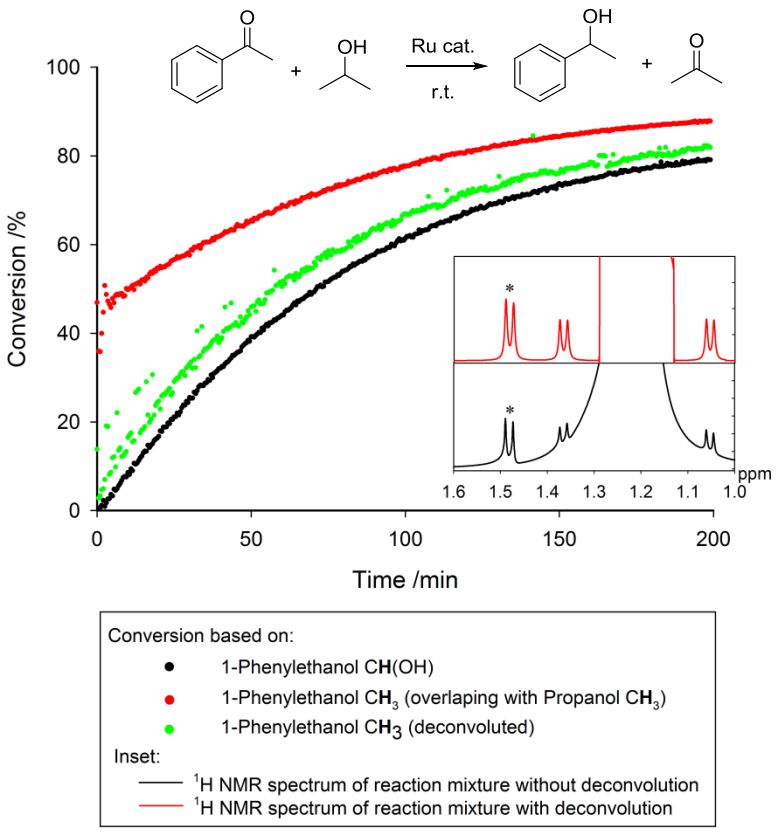

Figure 3.16: Comparison of reaction conversion profiles calculated for the transfer hydrogenation reaction of acetophenone and isopropanol to 1-phenylethanol and acetone, based on the peak areas of the CH(OH) and CH_3 peaks in 1-phenylethanol (the latter overlapping with the CH_3 peak in isopropanol), with and without spectral alignment and deconvolution (isopropanol, 25°C, 30° pulse, 1 sec acquisition time, 4 sec relaxation delay, 4 $mLmin^{-1}$). Increased scattering in the deconvoluted data (green) is due to slight shifts in peak positions in some spectra, leading to deconvolution inaccuracies. Inset: ^1H NMR spectrum of reaction mixture with and without peak deconvolution, indicating location of 1-phenylethanol CH(OH) peak (*) on shoulder of isopropanol CH_3 peak, in close proximity to isopropanol ^{13}C satellites.

3.3.3 Conclusions

High field on-line NMR is a particularly versatile and useful tool for real time reaction monitoring as it offers direct insight into complex mixtures without the need of external calibration and is applicable to a wide range of reaction conditions. FlowNMR systems are easy to set up, using commercially available apparatus and software, and are a time and cost efficient means of analysing reaction kinetics and studying mechanisms. Reactions may be studied under realistic conditions with efficient mixing, whilst allowing reagents to be added during the course of the reaction. Suitable solvent suppression techniques can remove the need for deuterated solvents, reducing cost and avoiding unwanted isotope effects.

The inherently quantitative nature of NMR is of great benefit for reaction monitoring, however, precautions must be taken when accurate results are required from reactions where T_1 relaxation times are similar or greater than the residence time of the sample within the magnet at the chosen flow rate. Residence time effects may lead to a decrease in the amount of signal detected, which has the potential to cause inaccuracies when comparing concentrations of species with different relaxation times. However, these in-flow effects can easily be corrected by simple mathematical calculation.

Out-flow effects, reducing the delay time required between scans, may be used to increase the amount of data that can be acquired within a given time period. This allows increasing either the temporal resolution of the experiment (more spectra per time) or the quality of the data (more scans per spectrum) as required.

A number of software packages are available to assist with the acquisition and processing of FlowNMR data, and include methods for suppressing solvent peaks and tracking peak drift over time. Care must be taken when applying automatic multiple spectra commands for phasing and base line correction, and manual adjustment of the parameters is recommended. We hope that our account will be of use to others in quickly generating high quality data from FlowNMR experiments.

3.3.4 Experimental

Reactions were carried out in a standard glass round-bottomed flask, with a double-piston HPLC pump (JASCO PU-2085 Plus) with a semi-micro pump head used to circulate the mixture around the system to an InsightMR flow tube (Bruker) located within the spectrometer (Bruker 500 MHz Avance II+ Ultrashield equipped with a broadband BBO probe). In order to minimise the delay time between a change occurring in the reaction vessel and the arrival of the sample to the spectrometer for detection it is desirable to ensure that the volume of the tubing connecting the reaction vessel to the spectrometer is minimised, therefore narrow diameter polyetheretherketone (PEEK) tubing (0.762 mm I.D., Upchurch Scientific) was used. The PEEK tubing offers high chemical and mechanical stability (pH 0 – 14, -50 – 100 °C, >300 bar) along with good flexibility and low gas permeability. For reactions at atmospheric pressure standard rubber seals were used to connect the tubing with the reaction solution, and found effective for air-sensitive systems over prolonged times (>10 hours) when sealed off with silicone grease. All other connections were made using standard HPLC-type PEEK connectors (Upchurch Scientific), allowing the apparatus to be purged with inert or reactive gases as required. All equipment was positioned on a mobile trolley made of plastic (Rubbermaid), allowing the equipment to be transported between the laboratory and the spectrometer as required. The trolley and apparatus were able to be placed at a minimum distance of 0.5 m from the shielded magnet without experiencing adverse magnetic effects. Data acquisition was performed without lock and with shimming performed using automated ^{1}H shimming routines, followed by manual fine tuning. Data processing was performed using commercially available software. All samples were prepared using reagents purchased from Sigma Aldrich or Alfa Aesar at reagent grade or higher and were used without further purification.

Residence time distribution profiles were obtained by concentration step using a tracer dye. Acetone was flowed through the apparatus at a continuous flow rate of 4 $mLmin^{-1}$ before the sample inlet was switched to a solution of Fluorescein in acetone (1 gdm^{-3}). The change in absorbance at 334 nm at the outlet tubing was monitored over time using a fibre optic light source (Avantes AvaLight-DH-S-BAL), flow cell and spectrometer (Avantes AvaSoft 2048L) until no further change was observed. The input was then switched back to clean acetone and the process repeated. Data was fitted using a 5 parameter sigmodal function and the fitted data differentiated to provide the residence time distribution. Photographs and video of the sample hold-up within the flow tube were recorded by concentration step using a Rose Bengal dye (1 gdm^{-3}, acetone) in an analogous way to the residence time distribution profiles.

^{1}H T_1 relaxation time measurements were performed on a mixture of acetophenone, 1-phenylethanol, acetone and 1,3,5-trimethoxybenzene in isopropanol using an inversion-recovery pulse sequence with variable delay times of 0.01, 0.25, 0.5, 1, 2, 3, 5, 7.5, 10 and 15 seconds and a relaxation delay time between data acquisition of 15 seconds (4 sec acquisition time), averaged over 8 scans with 4 dummy scans to ensure an equilibrium state was attained prior to data acquisition. Data was processed and fitted using the Topspin 't1guide' utility. ^{1}H integral area measurements were performed on the same sample using a standard 30° pulse sequence (1 sec delay, 4 sec acquisition time, 8 scans) at flow rates between 0-4 $mLmin^{-1}$.

^{19}F T_1 relaxation time measurements were performed on a mixture of α,α,α-trifluorotoluene, 2-fluorotoluene, trifluoroethanol, trifluoroacetic acid, tetrabutylammonium hexafluorophosphate, and tetrabutylammonium fluoride in acetone using an inversion-recovery pulse sequence with variable delay times of 0.05, 0.25, 0.5, 1, 1.5, 2, 3, 5, 7.5 and 10 seconds and a relaxation delay time of 10 seconds (4.65 sec acquisition time), averaged over 8 scans with 2 dummy scans. Due to limited pulse excitation width, data was acquired separately for regions -50 – -90 ppm, -105 – -135 ppm and -170 – -200 ppm. Data was zero filled to quadruple the size of the FID before data processing using the 't1guide' utility. ^{19}F integral area measurements were performed on the same sample using a standard 30° pulse sequence (10 sec delay, 4.65 sec acquisition time, 16 scans) at flow rates between 0-4 $mLmin^{-1}$. Integral area data was zero filled and linear back prediction (128 points) used to remove broad spectral distortions due to fluorine in the probe prior to integration.

^{31}P T_1 relaxation time measurements were performed on a mixture of dichlorophenylphosphine, chlorodiphenylphosphine, triphenylphosphine oxide, triphenylphosphine sulphide, triphenylphosphine, triphenylphosphate and tetrabutylammonium hexafluorophosphate in acetone using an inversion-recovery pulse sequence modified to include an adiabatic 180° pulse and inverse gated proton decoupling. Variable delay times of 0.05, 0.25, 0.5, 1, 2, 3, 5, 10, 20 and 30 seconds were used with a relaxation delay time of 30 seconds (2 sec acquisition time), averaged over 8 scans with 4 dummy scans. Data was zero filled to quadruple the size of the FID before data processing using the 't1guide' utility. ^{31}P integral area measurements were performed on the same sample using a standard 30° pulse sequence with inverse gated ^{1}H decoupling (45 sec delay, 2 sec acquisition time, 8 scans) at flow rates between 0-4 $mLmin^{-1}$.

^{11}B T_1 relaxation time measurements were performed on a mixture of phenylboronic acid, bis(pinacolato)diboron, tri(isopropyl)boron, sodium tetrafluoroborate and sodium borohydride in 1 M aqueous sodium hydroxide solution using an inversion-recovery pulse

sequence. Due to the range of ^{11}B T_1 values observed for this mixture, the experiment was performed in two sections, the first using variable delay times of 0.0005, 0.001, 0.0015, 0.002, 0.003, 0.004, 0.005, 0.0075, 0.01, 0.02, 0.03, 0.05, 0.075, 0.1, 0.15, 0.2, 0.3, 0.5, 0.75 and 1 seconds with a relaxation delay time of 1.5 seconds (0.8 sec acquisition time), averaged over 8 scans with 4 dummy scans, and the second using variable delay times of 0.1, 0.5, 1, 2, 3, 4, 5, 7.5, 10 and 25 seconds with a relaxation delay time of 30 seconds (0.8 sec acquisition time), averaged over 8 scans with 4 dummy scans. Data was zero filled to quadruple the size of the FID before data processing using the 't1guide' utility. ^{11}B integral area measurements were performed on the same sample using a standard 30° pulse sequence (30 sec delay, 1 sec acquisition time, 4 scans) at flow rates between 0-4 $mLmin^{-1}$. Integral area data was zero filled and linear back prediction (128 points) used to remove broad spectral distortions due to the borosilicate glassware prior to integration.

^{13}C T_1 relaxation time measurements were performed on a mixture of equal volumes of toluene, ethanol, cyclohexane and acetone using an inversion-recovery pulse sequence modified to include an adiabatic 180° pulse and inverse gated proton decoupling. Variable delay times of 0.05, 0.1, 0.5, 1, 3, 5, 7.5, 10, 15, 20, 30, 40, 60 and 90 seconds were used with a relaxation delay time of 90 seconds (0.82 sec acquisition time), averaged over 16 scans with 4 dummy scans for the spectral region 40 – -40 ppm. Data was zero filled to quadruple the size of the FID before data processing using the 't1guide' utility. ^{13}C integral area measurements were performed on the same sample using a standard 30° pulse sequence with inverse gated ^{1}H decoupling (80 sec delay, 3.72 sec acquisition time, 8 scans) at flow rates between 0-4 $mLmin^{-1}$.

^{1}H T_2 relaxation time measurements were performed on a mixture of acetophenone, 1-phenylethanol, acetone and 1,3,5-trimethoxybenzene in isopropanol using a CPMG pulse program with a 20 ms delay between successive 180 degree pulses, and variable loop counts of 2, 10, 20, 40, 60, 100, 150, 200, 300 and 500, giving echo times of between 40 and 10000 ms. A 15 sec delay time between data acquisition was used, and the signal averaged over 8 scans with 16 dummy scans. Data was processed and fitted using the Topspin 't1guide' utility.

T_2^* values were calculated from ^{1}H peak linewidths from the same sample as the ^{1}H integral area measurements (15 sec delay, 4 sec acquisition time, 30° pulse, 8 scans). Peaks were deconvoluted from the spectra and peak widths at half height (HHLW) taken from the fitted Lorentzian peaks. T_2^* were calculated using the following equation:

$$T_2^* = \frac{1}{\pi(HHLW)}$$

^{1}H flip angle variation experiments were performed on a mixture of acetophenone, 1-phenylethanol, acetone and 1,3,5-trimethoxybenzene in isopropanol using a standard 90° pulse program (4 or 15 sec delay, 3.17 sec acquisition time, 4 scans). The pulse length was varied manually between 15° and 90° and data acquired at flow rates between 0-4 mLmin^{-1}.

Solvent suppression was performed on a sample of 1% benzaldehyde in acetonitrile at a flow rate of 4 mLmin^{-1}. Spectra were acquired using a standard 30° pulse program (4 sec delay, 3.17 sec acquisition, 8 scans, receiver gain = 6.35, transmitter frequency offset = 2.78 ppm), a presaturation pulse sequence (4 sec delay, 3.17 sec acquisition, 8 scans, receiver gain = 114, transmitter frequency offset = 2.78ppm) and a WET pulse sequence with a shaped pulse and low power ^{13}C decoupling during acquisition (4 sec delay, 3.17 sec acquisition, 8 scans, receiver gain = 203, transmitter frequency offset = 2.78ppm).

3.3.4.1 Reaction of triphenylphosphine with sulfur

Following the general procedure for FlowNMR experiments given in the ESI, the FlowNMR apparatus was purged with toluene and then filled with a solution of triphenylphosphine (0.624 g, 2.4 mmol) in toluene (13.6 mL). ^{31}P data was acquired for the static sample (inverse gated ^{1}H decoupled, 2 sec delay, 0.803 sec acquisition time, 30° pulse, 16 scans). Flow of sample around the apparatus was started (4 mLmin^{-1}) and a second spectrum acquired. Both spectra were integrated and the absolute integral values compared to calculate a flow correction factor for triphenylphosphine. An additional spectrum acquired under quantitative conditions (inverse gated ^{1}H decoupled, 60 sec delay, 0.803 sec acquisition time, 30° pulse) was used to calculate a second correction factor which was applied to both datasets to compensate for the non-quantitative conditions required during reaction monitoring.** A solution of S_8 (87 mg, 0.34 mmol) in toluene (10 mL) was added to the stirred reaction flask and data acquisition started (1 spectrum per minute for the first hour of data acquisition, 1 spectrum every 2 minutes for the second and third hour or acquisition). After three hours, data acquisition was halted. Spectra were recorded at flow rates of 0 and 4 mLmin^{-1} and a second correction factor calculated for the triphenylphosphine sulphide product. All spectra were integrated and the integrals scaled by the correction factor for each peak respectively to give the corrected integral for conversion calculation.

3.3.4.2 Transfer hydrogenation of acetophenone

The FlowNMR apparatus was purged with dry nitrogen for 30 min to remove any traces or air or moisture. The apparatus was filled with 10 mL of a stock solution of potassium

** In practice, both effects may be corrected for simultaneously by ensuring that the static spectrum acquired for the calculation of a correction factor for flow effects is acquired under quantitative conditions.

hydroxide (anhydrous, 0.112 g, 2 mmol) and 1,3,5-trimethoxybenzene (3.364 g, 0.02 mol) in dry, degassed isopropanol (200 mL) and acetophenone (0.47 mL, 4 mmol) was added. Data acquisition was started (4 sec delay, 1 sec acquisition time, 30° pulse, 4 scans) and a solution of the catalyst (S,S)-(TsDPEN)mesitylruthenium chloride (12 mg, 0.02 mmol) in isopropanol (1 mL) was added to start the reaction.

Concentrations of species were determined by peak integrals and referenced to 1,3,5-trimethoxybenzene as internal standard. For deconvolution of the 1-phenylethanol peaks (overlapping with isopropanol) spectra were first aligned before automatic deconvolution of spectra was performed. Deconvoluted spectra were integrated in the usual manner to obtain peak areas for concentration determination.

3.3.5 Associated Content

Electronic Supporting Information containing additional photographs, diagrams, calculations, experimental details and a video of the RTD experiment (Figure 3.2) is available free of charge via the Internet at dx.doi.org/10.1039/C6CY01754A.

3.3.6 Author information

Corresponding authors: j.lowe@bath.ac.uk, u.hintermair@bath.ac.uk

Notes: A.C. and P.G. are employees of Bruker UK Ltd., manufacturer and supplier of NMR hard- and software solutions that have been used in this research. The other authors declare no competing financial interest.

3.3.7 Acknowledgements

This work was supported by a Research Grant from the Royal Society (Y0603), the EPSRC Centre for Doctoral Training in Sustainable Chemical Technologies (EP/L016354/1), and Bruker UK Ltd. UH thanks the Centre for Sustainable Chemical Technologies for a Whorrod Research Fellowship. The authors would like to thank Dr Tim Woodman and Dr Antoine Buchard from the University of Bath for their support and assistance with this project and for many useful discussions.

3.4 COMMENTARY AND CONCLUSIONS

To ensure quantitative results when using online FlowNMR spectroscopy to measure reaction kinetics requires a number of precautions to be taken. In-flow and out-flow effects can lead to changes in the measured signal intensity of different peaks for flowing samples, when T_1 relaxation times are similar or greater than the residence time within the magnet. If left uncorrected, this may result in inaccurate concentrations of reaction species being calculated. It is therefore vital that these effects are understood, and a mathematical correction applied for every apparatus and reaction.

Whilst the results presented in this chapter apply to the second-generation apparatus design discussed in Chapter 2, the conclusions are general and apply to all FlowNMR apparatus. In the case of the third-generation apparatus used to acquire data in subsequent chapters, mean residence times are given in Table 3.1 below.

Table 3.1: Mean residence time for different third-generation FlowNMR apparatus configurations (Figure 2.21).

Apparatus configuration	Mean residence time (s)
With flow tube	57
Flow tube bypassed	41
With flow meter, flow tube bypassed	57
With flow tube and flow meter	95

The residence time of the third-generation apparatus is slightly longer than for the second-generation (Figure 3.2), reflecting the increased flow path distance due to inclusion of UV-Vis, HPLC/MS and process control instruments. Inclusion of the flow meter significantly increases the residence time of the system; hence the flow meter is usually bypassed unless required (Figure 2.21).

Having established methods to acquire, correct and process FlowNMR data, these techniques were applied to monitoring the reactions discussed in Chapters 4 – 6.

3.5 REFERENCES

1. Albert, K. In *On-Line LC-NMR And Related Techniques*, John Wiley & Sons, Ltd: 2003; pp 1-22.

2. Albert, K.; Nieder, M.; Bayer, E.; Spraul, M., Continuous-flow nuclear magnetic resonance. *J. Chromatogr. A* **1985,** 346, 17-24.

3. Albert, K.; Bayer, E., High-performance liquid chromatography—nuclear magnetic resonance on-line coupling. *TrAC, Trends Anal. Chem.* **1988,** 7, 288-293.

4. Mix, A.; Jutzi, P.; Rummel, B.; Hagedorn, K., A Simple Double-Chamber NMR Tube for the Monitoring of Chemical Reactions by NMR Spectroscopy. *Organometallics* **2010,** 29, 442-447.

5. Foley, D. A.; Dunn, A. L.; Zell, M. T., Reaction monitoring using online vs tube NMR spectroscopy: seriously different results. *Magn. Reson. Chem.* **2016,** 54, 451-456.

6. Buser, J. Y.; McFarland, A. D., Reaction characterization by flow NMR: quantitation and monitoring of dissolved H_2 via flow NMR at high pressure. *Chem. Commun.* **2014,** 50, 4234-4237.

7. Goldbach, M.; Danieli, E.; Perlo, J.; Kaptein, B.; Litvinov, V. M.; Blümich, B.; Casanova, F.; Duchateau, A. L. L., Preparation of Grignard reagents from magnesium metal under continuous flow conditions and on-line monitoring by NMR spectroscopy. *Tetrahedron Lett.* **2016,** 57, 122-125.

8. Vargas, M. A.; Cudaj, M.; Hailu, K.; Sachsenheimer, K.; Guthausen, G., Online Low-Field 1H NMR Spectroscopy: Monitoring of Emulsion Polymerization of Butyl Acrylate. *Macromolecules* **2010,** 43, 5561-5568.

9. Albert, K.; Kunst, M.; Bayer, E.; Spraul, M.; Bermel, W., Reversed-phase high-performance liquid chromatography-nuclear magnetic resonance on-line coupling with solvent non-excitation. *J. Chromatogr. A* **1989,** 463, 355-363.

10. Räntzsch, V.; Wilhelm, M.; Guthausen, G., Hyphenated low-field NMR techniques: combining NMR with NIR, GPC/SEC and rheometry. *Magn. Reson. Chem.* **2016,** 54, 494-501.

11. Silva Elipe, M. V., In *LC-NMR and Other Hyphenated NMR Techniques*. John Wiley & Sons, Inc.: 2011; p 220.

12. Maiwald, M.; Fischer, H. H.; Kim, Y.-K.; Albert, K.; Hasse, H., Quantitative high-resolution on-line NMR spectroscopy in reaction and process monitoring. *J. Magn. Reson.* **2004,** 166, 135-146.

13. Foley, D. A.; Wang, J.; Maranzano, B.; Zell, M. T.; Marquez, B. L.; Xiang, Y.; Reid, G. L., Online NMR and HPLC as a reaction monitoring platform for pharmaceutical process development. *Anal. Chem.* **2013,** 85, 8928-8932.

14. Foley, D. A.; Doecke, C. W.; Buser, J. Y.; Merritt, J. M.; Murphy, L.; Kissane, M.; Collins, S. G.; Maguire, A. R.; Kaerner, A., ReactNMR and ReactIR as reaction monitoring and mechanistic elucidation tools: the NCS mediated cascade reaction of alpha-thioamides to alpha-thio-beta-chloroacrylamides. *J. Org. Chem.* **2011,** 76, 9630-9640.

15. Merritt, J. M.; Buser, J. Y.; Campbell, A. N.; Fennell, J. W.; Kallman, N. J.; Koenig, T. M.; Moursy, H.; Pietz, M. A.; Scully, N.; Singh, U. K., Use of Modeling and Process Analytical Technologies in the Design of a Catalytic Amination Reaction: Understanding Oxygen

Sensitivity at the Lab and Manufacturing Scales. *Org. Process Res. Dev.* **2014,** 18, 246-256.

16. Foley, D. A.; Zell, M. T.; Marquez, B. L.; Kaerner, A., NMR Reaction-Monitoring as a Process Analytical Technique. *Pharm. Technol.* **2011,** 11, S19.

17. Bernstein, M. A.; Stefinovic, M.; Sleigh, C. J., Optimising reaction performance in the pharmaceutical industry by monitoring with NMR. *Magn. Reson. Chem.* **2007,** 45, 564.

18. Nordon, A.; McGill, C. A.; Littlejohn, D., Process NMR spectrometry. *Analyst* **2001,** 126, 260-272.

19. Foley, D. A.; Bez, E.; Codina, A.; Colson, K. L.; Fey, M.; Krull, R.; Piroli, D.; Zell, M. T.; Marquez, B. L., NMR flow tube for online NMR reaction monitoring. *Anal. Chem.* **2014,** 86, 12008-12013.

20. Bruker InsightMR: Real-Time Data Analysis and Acquisition Control - the Solution for Process Monitoring. www.bruker.com/products/mr/nmr/nmr-software/software/insightmr/overview.html (accessed 02/01/2016).

21. Silva Elipe, M. V.; Milburn, R. R., Monitoring chemical reactions by low-field benchtop NMR at 45 MHz: pros and cons. *Magn. Reson. Chem.* **2016,** 54, 437-443.

22. Zientek, N.; Meyer, K.; Kern, S.; Maiwald, M., Quantitative Online NMR Spectroscopy in a Nutshell. *Chem. Ing. Tech.* **2016,** 88, 698-709.

23. Dalitz, F.; Cudaj, M.; Maiwald, M.; Guthausen, G., Process and reaction monitoring by low-field NMR spectroscopy. *Prog. Nucl. Magn. Reson. Spectrosc.* **2012,** 60, 52-70.

24. Meyer, K.; Kern, S.; Zientek, N.; Guthausen, G.; Maiwald, M., Process control with compact NMR. *TrAC, Trends Anal. Chem.* **2016,** 83, 39-52.

25. Sans, V.; Porwol, L.; Dragone, V.; Cronin, L., A self optimizing synthetic organic reactor system using real-time in-line NMR spectroscopy. *Chem. Sci.* **2015,** 6, 1258-1264.

26. Jones, C. J.; Larive, C. K., Could smaller really be better? Current and future trends in high-resolution microcoil NMR spectroscopy. *Anal. Bioanal. Chem.* **2012,** 402, 61-68.

27. Gökay, O.; Albert, K., From single to multiple microcoil flow probe NMR and related capillary techniques: a review. *Anal. Bioanal. Chem.* **2012,** 402, 647-669.

28. Bart, J.; Kolkman, A. J.; Oosthoek-de Vries, A. J.; Koch, K.; Nieuwland, P. J.; Janssen, H.; van Bentum, J.; Ampt, K. A. M.; Rutjes, F. P. J. T.; Wijmenga, S. S.; Gardeniers, H.; Kentgens, A. P. M., A Microfluidic High-Resolution NMR Flow Probe. *J. Am. Chem. Soc.* **2009,** 131, 5014-5015.

29. Finch, G.; Yilmaz, A.; Utz, M., An optimised detector for in-situ high-resolution NMR in microfluidic devices. *J. Magn. Reson.* **2016,** 262, 73-80.

30. Fratila, R. M.; Gomez, M. V.; Sýkora, S.; Velders, A. H., Multinuclear nanoliter one-dimensional and two-dimensional NMR spectroscopy with a single non-resonant microcoil. *Nat Commun* **2014,** 5, 3025.

31. Zalesskiy, S. S.; Danieli, E.; Blümich, B.; Ananikov, V. P., Miniaturization of NMR Systems: Desktop Spectrometers, Microcoil Spectroscopy, and "NMR on a Chip" for Chemistry, Biochemistry, and Industry. *Chem. Rev.* **2014,** 114, 5641-5694.

32. Khajeh, M.; Bernstein, M. A.; Morris, G. A., A simple flowcell for reaction monitoring by NMR. *Magn. Reson. Chem.* **2010,** 48, 516-522.

33. Nordon, A.; Diez-Lazaro, A.; Wong, C. W. L.; McGill, C. A.; Littlejohn, D.; Weerasinghe, M.; Mamman, D. A.; Hitchman, M. L.; Wilkie, J., Consideration of some sampling problems in the on-line analysis of batch processes by low-field NMR spectrometry. *Analyst* **2008,** 133, 339-347.

34. Thermo Scientific NMR Reaction Monitoring Accessory. https://tools.thermofisher.com/content/sfs/brochures/PS52672-E-0315M-NMR-Accessory.pdf (accessed 28/05/2016).

35. Fyfe, C. A.; Cocivera, M.; Damji, S. W. H., Flow and stopped-flow nuclear magnetic resonance investigations of intermediates in chemical reactions. *Acc. Chem. Res.* **1978,** 11, 277-282.

36. Yushmanov, P. V.; Furo, I., A rapid-mixing design for conventional NMR probes. *J. Magn. Reson.* **2005,** 175, 264-270.

37. Green, D. B.; Lane, J.; Wing, R. M., A Standard Session Stopped-Flow NMR Tube. *Appl. Spectrosc.* **1987,** 41, 847-851.

38. Keifer, P. A., Flow injection analysis NMR (FIA–NMR): a novel flow NMR technique that complements LC–NMR and direct injection NMR (DI–NMR). *Magn. Reson. Chem.* **2003,** 41, 509-516.

39. McGarrity, J. F.; Prodolliet, J.; Smyth, T., Rapid injection NMR: A simple technique for the observation of reactive intermediates. *Org. Magn. Resonance* **1981,** 17, 59-65.

40. Christianson, M. D.; Tan, E. H. P.; Landis, C. R., Stopped-Flow NMR: Determining the Kinetics of [rac-(C2H4(1-indenyl)2)ZrMe][MeB(C6F5)3]-Catalyzed Polymerization of 1-Hexene by Direct Observation. *J. Am. Chem. Soc.* **2010,** 132, 11461-11463.

41. McGarrity, J. F.; Prodolliet, J., High-field rapid injection NMR: observation of unstable primary ozonide intermediates. *J. Org. Chem.* **1984,** 49, 4465-4470.

42. Denmark, S. E.; Williams, B. J.; Eklov, B. M.; Pham, S. M.; Beutner, G. L., Design, Validation, and Implementation of a Rapid-Injection NMR System. *J. Org. Chem.* **2010,** 75, 5558-5572.

43. Valera, F. E.; Quaranta, M.; Moran, A.; Blacker, J.; Armstrong, A.; Cabral, J. T.; Blackmond, D. G., The Flow's the Thing…Or Is It? Assessing the Merits of Homogeneous Reactions in Flask and Flow. *Angew. Chem. Int. Ed.* **2010,** 49, 2478-2485.

44. Levenspiel, O., In *Chemical Reaction Engineering*. 3rd ed.; Wiley: New York ; Chichester, 1999; p 668.

45. Maiwald, M.; Fischer, H. H.; Kim, Y.-K.; Hasse, H., Quantitative on-line high-resolution NMR spectroscopy in process engineering applications. *Anal. Bioanal. Chem.* **2003,** 375, 1111-1115.

46. Wilkie, C. A., Carbon and phosphorus relaxation in some phenylphosphorus compounds. *J. Magn. Reson.* **1979,** 33, 127-134.

47. Seymour, S. J.; Jonas, J., ^{31}P and ^{1}H Spin–Lattice Relaxation in Several Substituted Phenylphosphines in the Liquid State. *J. Chem. Phys.* **1971,** 54, 487-491.

48. Wagner, G. E.; Sakhaii, P.; Bermel, W.; Zangger, K., Monitoring fast reactions by spatially-selective and frequency-shifted continuous NMR spectroscopy: application to rapid-injection protein unfolding. *Chem. Commun.* **2013,** 49, 3155-3157.

49. Donovan, K. J.; Allen, M.; Martin, R. W.; Shaka, A. J., Improving the double quantum filtered COSY experiment by "Moving Tube" NMR. *J. Magn. Reson.* **2012,** 219, 41-45.

50. Hoye, T. R.; Eklov, B. M.; Ryba, T. D.; Voloshin, M.; Yao, L. J., No-D NMR (no-deuterium proton NMR) spectroscopy: a simple yet powerful method for analyzing reaction and reagent solutions. *Org. Lett.* **2004,** 6, 953-6.

51. Maiwald, M.; Fischer, H. H.; Kim, Y. K.; Albert, K.; Hasse, H., Quantitative high-resolution on-line NMR spectroscopy in reaction and process monitoring. *J. Magn. Reson.* **2004,** 166, 135.

52. Smallcombe, S. H.; Patt, S. L.; Keifer, P. A., WET Solvent Suppression and Its Applications to LC NMR and High-Resolution NMR Spectroscopy. *J. Magn. Reson. A* **1995,** 117, 295-303.

53. Sudmeier, J. L.; Günther, U. L.; Albert, K.; Bachovchin, W. W., Sensitivity Optimization in Continuous-Flow FTNMR. *J. Magn. Reson. A* **1996,** 118, 145-156.

4 Online Monitoring of a Photochemical Reaction

The work presented in this chapter has been published in the journal '*Chemical Communications*', volume 54, issue 1, pages 30-33 and is reproduced with the permission of the Royal Society of Chemistry. Page, reference and figure numbers have been altered for consistency. Some figures originally published in the Electronic Supplementary Information have been included in the main text where they are referred to.

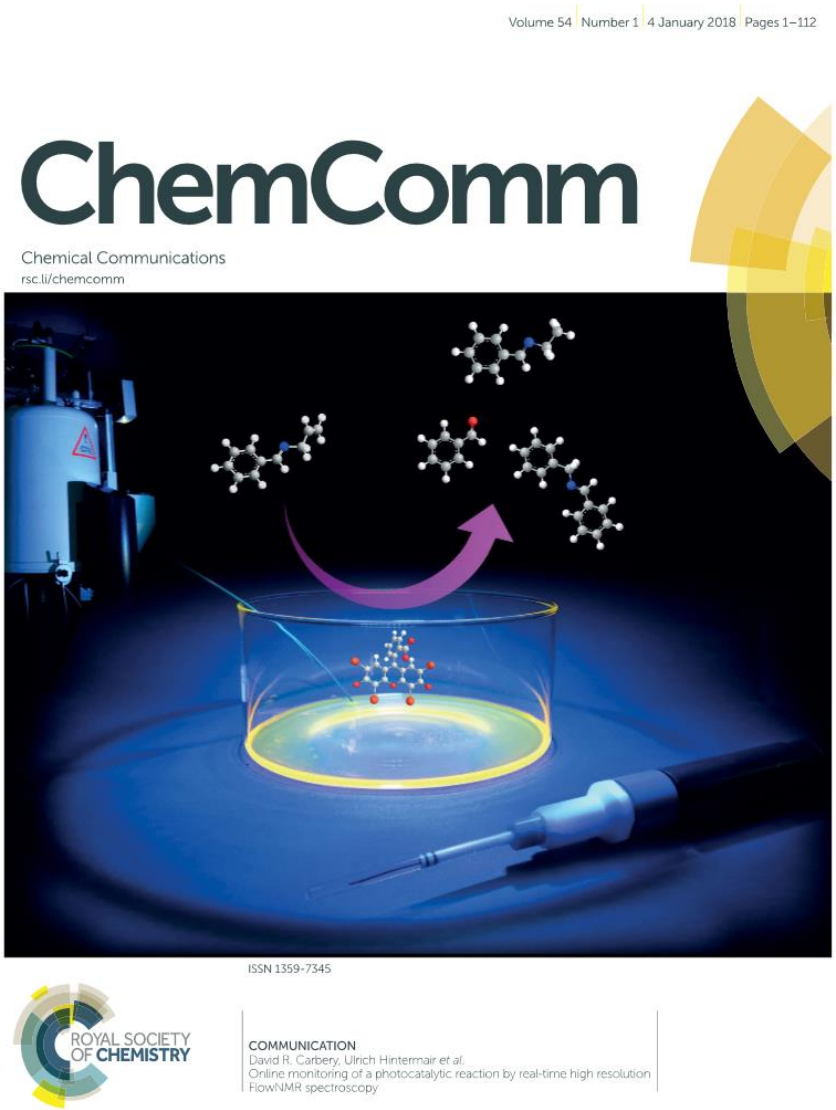

4.1 INTRODUCTION TO PUBLISHED WORK

As discussed in Chapter 2, FlowNMR has the potential to allow monitoring of reactions that would be challenging to study using conventional NMR techniques. To test the scope of the FlowNMR apparatus for monitoring reactions that are challenging for traditional methods, a photochemical reaction was chosen for investigation.

Photochemical reactions have previously proved to be very challenging to study by NMR spectroscopy, as ensuring constant and homogenous irradiation of the sample within the spectrometer is very difficult.[34, 65] For this reason, most photochemical reactions using NMR for reaction monitoring are performed off-line, with samples taken from the reaction for analysis at a later stage.

The reaction selected for analysis (Scheme 4.1) is currently under investigation by the Carbery group at the University of Bath as a new synthetic route for the formation of N-Benzylidenebenzylamine derivatives.[144-145]

Prior to investigation using FlowNMR spectroscopy, analysis of reaction kinetics had been performed off-line. A sample was removed from the reaction after a given time and the solvent evaporated, before re-dissolving in deuterated solvent for NMR analysis. Data acquired using this method produced very scattered conversion profiles, due to variability in the work-up and analysis delay between different samples (Figure 4.2). All samples were found to contain benzaldehyde as an impurity, however the concentration did not correlate well to reaction time.

For the photochemical reaction, a modified version of the apparatus described in Chapter 2 was required. As photochemical reactions are very sensitive to changes in light intensity due to positioning of the light source and reaction vessel, it was important to use the same equipment for reaction monitoring in flow as had been used previously for the off-line measurements. In this case, the inlet and outlet tubing from the FlowNMR apparatus were simply placed into the glass dish filled with the reaction solution (Figure 4.1).

This simple setup allowed the reaction to be monitored in real time, whilst maintaining constant illumination and air flow over the sample, both of which have proved crucial to the reaction. Having demonstrated the ability of the FlowNMR apparatus to produce reliable results for the photochemical reaction, conditions were varied, providing insights into the reaction mechanism.

4.2 STATEMENT OF AUTHORSHIP

<table>
<tr><th colspan="10">This declaration concerns the article entitled:</th></tr>
<tr><td colspan="10">Online Monitoring of a Photocatalytic Reaction by Real-time High Resolution FlowNMR Spectroscopy</td></tr>
<tr><td colspan="10">Publication status (tick one)</td></tr>
<tr><td>draft manuscript</td><td></td><td>Submitted</td><td></td><td>In review</td><td></td><td>Accepted</td><td></td><td>Published</td><td>✓</td></tr>
<tr><td>Publication details (reference)</td><td colspan="9">A. M. R. Hall, R. Broomfield-Tagg, M. Camilleri, D. R. Carbery, A. Codina, D. T. E. Whittaker, S. Coombes, J. P. Lowe and U. Hintermair, Chem Commun (Camb), 2018, 54, 30-33.</td></tr>
<tr><td>Candidate's contribution to the paper (detailed, and also given as a percentage).</td><td colspan="9">The candidate contributed to/ considerably contributed to/predominantly executed the…

Formulation of ideas: 50%
The original idea for this collaboration came from a discussion between AH and MC, with further input from UH, RBT and JL during the experimental stages.

Design of methodology: 40%
Photochemical reaction was designed by MC and DC. FlowNMR methods were designed by AH, UH, RBT and JL with input from AC.

Experimental work: 50%
FlowNMR studies were carried out jointly by AH and RBT, with synthesis of compounds performed by MC.

Presentation of data in journal format: 70%
The figures and initial draft were prepared by AH, with RBT, UH and JL contributing further material during editing.</td></tr>
<tr><td>Statement from Candidate</td><td colspan="9">This paper reports on original research I conducted during the period of my Higher Degree by Research candidature.</td></tr>
<tr><td>Signed</td><td colspan="5"></td><td>Date</td><td colspan="3"></td></tr>
</table>

4.3 ONLINE MONITORING OF A PHOTOCATALYTIC REACTION BY REAL-TIME HIGH RESOLUTION FLOWNMR SPECTROSCOPY

Andrew M. R. Hall,[a] Rachael Broomfield-Tagg,[b] Matthew Camilleri,[a] David R. Carbery,[b]* Anna Codina,[c] David T. E. Whittaker,[d] Steven Coombes,[d] John P. Lowe,[b] and Ulrich Hintermair[a]*

a) Centre for Sustainable Chemical Technologies, University of Bath, Claverton Down, Bath BA2 7AY, United Kingdom.
b) Department of Chemistry, University of Bath, Claverton Down, Bath BA2 7AY, United Kingdom.
c) Bruker UK Ltd., Banner Lane, Coventry CV4 9GH, United Kingdom.
d) AstraZeneca, Charter Way, Macclesfield SK10 2NA, United Kingdom.

** Corresponding authors: D.Carbery@bath.ac.uk, U.Hintermair@bath.ac.uk*

We demonstrate how FlowNMR spectroscopy can readily be applied to investigate photochemical reactions that require sustained input of light and air to yield mechanistic insight under realistic conditions. The Eosin Y mediated photo-oxidation of N-allylbenzylamine is shown to produce imines as primary reaction products from which undesired aldehydes form after longer reaction times. Facile variation of reaction conditions during the reaction in flow allows for probe experiments that give information about the mode of action of the photocatalyst.

4.3.1 Introduction

Photochemical reactions are an important part of the modern synthetic chemists' repertoire due to the unique chemistry occurring in the excited state.[146-150] Visible light photo(redox)catalysis is of particular current interest due to the potential for utilization of sunlight as sustainable energy source in chemical synthesis.[151-156]

In order to gain an understanding of the mechanisms involved in these reactions it is necessary to have a means of producing high quality kinetic data under realistic conditions. Spectroscopic techniques such as Ultra-violet visible (UV-vis), Infrared (IR) and fluorescence spectroscopies have been widely used for monitoring photochemical reactions, however, these techniques are only able to provide limited structural information about reaction species and require calibration before use.[34, 65-66, 73, 146] Mass Spectrometry offers a complimentary technique with higher sensitivity and resolution, but structural information may still be limited for novel complexes where fragmentation patterns are not known, and

calibration with each compound is required before quantitative results may be attained.[157-158]

Although less sensitive, Nuclear Magnetic Resonance (NMR) spectroscopy provides a wealth of structural information over a wide detection range and does not require external calibration. However, conventional NMR techniques are incompatible with photochemical reactions due to the difficulties in irradiating the sample once it is inside the magnet.[34, 65]

For this reason, most NMR monitoring of photochemical reactions is performed off-line, but the delays and sample work-up procedures between reaction and analysis often entail compositional changes. *In-situ* approaches including setups where light is guided from an external source to the sample inside the spectrometer using mirrors or fibre-optic cables,[69, 72] special sample tubes with miniature LED light sources inside the spectrometer[67, 159] and modified NMR probes have been developed[34, 65] but these require custom-made equipment and are the domain of specialists. In addition, these setups do not allow for mixing of the sample or changes in reaction conditions,[11] and often deliver light at one point only.[65, 67, 72, 159] The lack of control of light intensity across the sample means that recreating realistic conditions is difficult, which may result in different rates or/and mechanisms for reactions that are limited by photon density.

The use of NMR as online monitoring technique has been known for some years, primarily as a detection method in HPLC-NMR coupled analysis,[27-28] but only recently gained interest as a method for real-time reaction monitoring. This has been spurred on by the recent commercialisation of a number of dedicated FlowNMR monitoring systems[36, 49, 55, 121] accompanied by several reports detailing general considerations for their use.[52, 121, 160]

Online FlowNMR techniques utilize an external reaction vessel, situated outside of the influence of the magnetic field, with sample continuously pumped into the spectrometer through a dedicated NMR flow tube located within a standard NMR probe before returning to the reaction vessel (Figure 4.1).[36, 160] This setup permits full control over the reaction conditions during the analysis, including mixing, addition of reagents, temperature regulation as well as irradiation of the sample.[11] Advanced solvent suppression techniques allow the use of non-deuterated reaction solvents without compromising data quality, reducing cost and avoiding unwanted isotope effects.[9]

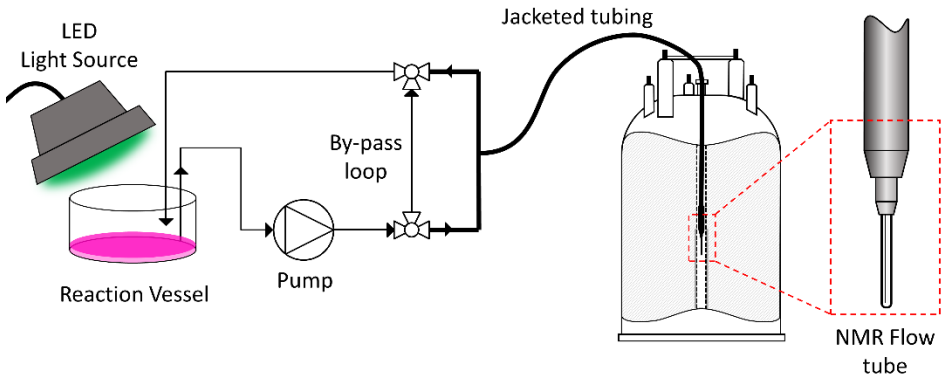

Figure 4.1: FlowNMR setup for monitoring photochemical reactions (not to scale).

Two recent papers have explored the possibility of utilizing online NMR reaction monitoring to study photochemical reactions, with one study investigating the photochemical degradation of environmental pollutants,[34] and another using a low-field NMR spectrometer for analysis of products exiting from a photochemical flow reactor.[74] Neither study reports reaction kinetics or mechanism, and to the best of our knowledge, no examples of high-resolution FlowNMR reaction monitoring for kinetic and mechanistic investigations of photochemical reactions have thus far been reported.

4.3.2 Results and Discussion

Examples of visible light photocatalysis are abundant in nature, forming the basis of many key biological processes.[146-147, 150] Flavins, based on a tricyclic isoalloxazine ring system, are an important class of natural photocatalysts.[147, 161-163] Synthetic fluorescent dyes mimicking the core structure of flavins have been developed as staining agents for biological systems, including compounds such as Fluorescein, Eosin and Rose Bengal.

In the presence of visible light and air, Flavin and Eosin Y have been found to catalyse reactions of secondary amines to give a mixture of inter- and intramolecular oxidation products (Scheme 4.1).[145] The reaction proceeds at room temperature in acetonitrile solution under white or green light irradiation in air (Scheme 4.1).

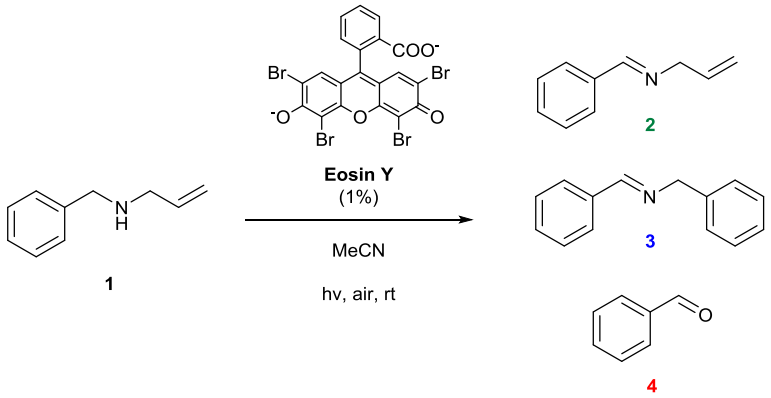

Scheme 4.1: Structure of Eosin Y and photocatalytic oxidation of allylic amines.

Sampling off-line ^{1}H NMR analysis of the reaction showed the major products to be oxidation product **2** and intermolecular coupling product **3** (Figure 4.2). Small amounts of benzaldehyde were also observed throughout the reaction as an undesired by-product. Even with utmost care, data from off-line sampling was always scattered and difficult to reproduce due to slight variations between different samples and the need for work-up before the analysis (Figure 4.2).

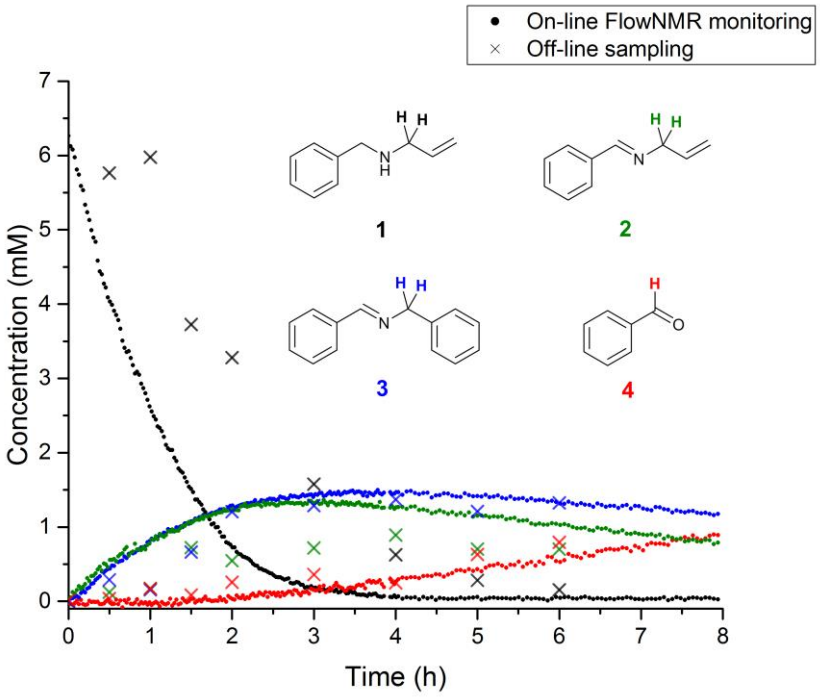

Figure 4.2: Off-line and on-line FlowNMR reaction profiles of N-allylbenzylamine (1) in MeCN (6.4 mM) at 20°C in the presence of Eosin Y catalyst (1 mol%) under green LED illumination (633 µW) to form 2, 3 and 4. (On-line: 100 mL, 4 mLmin^{-1} flowrate, WET solvent suppression, 1.64 s acquisition time, 3 s relaxation delay, 12 scans. Off-line: 300 mL, 3 s acquisition time, 1 s relaxation decay, 16 scans. 20 mL samples were periodically withdrawn from the reaction mixture and concentrated under reduced pressure before dissolving in $CDCl_3$ for analysis). See the experimental (Section 4.3.6.3) for details.

Monitoring the reaction under the same conditions by online ^{1}H FlowNMR spectroscopy however (Figure 4.1) yielded smooth and highly reproducible concentration profiles of all

components from a single experiment (Figure 4.2). The ~30 second time lapse between leaving the continuously illuminated vessel and reaching the NMR probe was sufficient to avoid adverse effects on NMR data acquisition by photo-generated radicals, and the returning aliquot resumed turnover once returned to the illuminated vessel.

††

The data obtained revealed a steady consumption of the N-allylbenzylamine starting material with corresponding increase in concentration of products **2** and **3** in a 1:1 ratio at virtually identical rates. The rate of the reaction was constant until about 65% conversion, indicating pseudo-zero order kinetics in **1** under the conditions applied.

Interestingly, no benzaldehyde formation was observed by FlowNMR during the initial stages of the reaction; the associated peaks did not appear until about 2 hours into the reaction, corresponding to >80% substrate consumption. This clearly showed benzaldehyde to be a secondary reaction product formed from imines **2** and **3** rather than from amine **1**, which appeared much more pronounced in the off-line reaction monitoring data due to degradation between sampling and data acquisition.

Under the conditions applied, substrate conversion reached completion after ~4 hours, after which the concentration of benzaldehyde continued to increase at the expense of both **2** and **3**, although degradation of allylphenylimine **2** was slightly faster than the more stable benzylphenylimine **3**.

Increasing the concentration of **1** seven-fold resulted in a lengthening of the reaction time, again with constant rates during the first 6 hours up to ~65% conversion indicative of saturation kinetics (Figure 4.3).

†† Total volume of FlowNMR apparatus = 3.7 mL. For a 100 mL reaction volume the sample spends 4% of the reaction time outside the reaction vessel (on average).

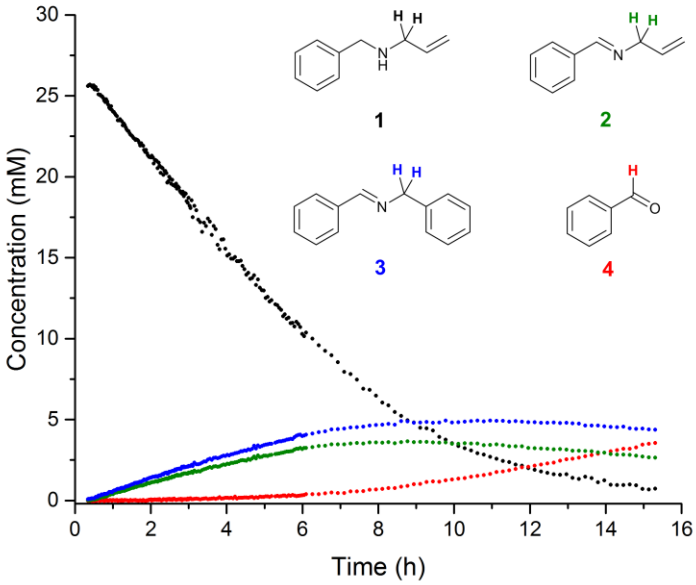

*Figure 4.3: Kinetic data for the reaction of N-allylbenzylamine **(1)** (25.6 mM) in the presence of green light and Eosin Y catalyst (1 mol% soln. in acetonitrile (100 mL)) to form **2**, **3** and **4**. (20°C, Green LED light source (100 W), WET solvent suppression, 1.64 s acquisition time, 3 s relaxation delay, 12 scans, 4 mLmin^{-1} flowrate).*

Over these longer reaction times a number of other (currently unidentified) by-products were observed to form at low concentration, as evidenced by the appearance of a variety of small peaks in the ^{1}H spectra (Figure 4.4).

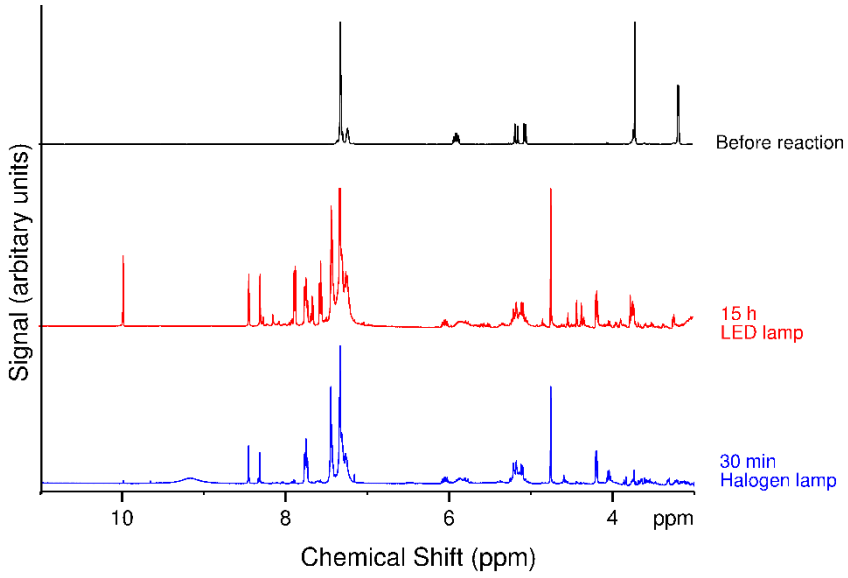

Figure 4.4: ^{1}H NMR spectra (solvent suppressed) of the reaction mixture a) before irradiation, b) after irradiation for 15 h with a green LED light source (633 µW at 510 nm) and c) after irradiation for 30 min with a white halogen light source (250 mW at 510 nm). (WET solvent suppression, 1.64 s acquisition time, 3 s relaxation delay, 12 scans).

Sum integration of the aromatic region remained constant over the course of the reaction, however, demonstrating that the reaction mass-balance was maintained (Figure 4.5).

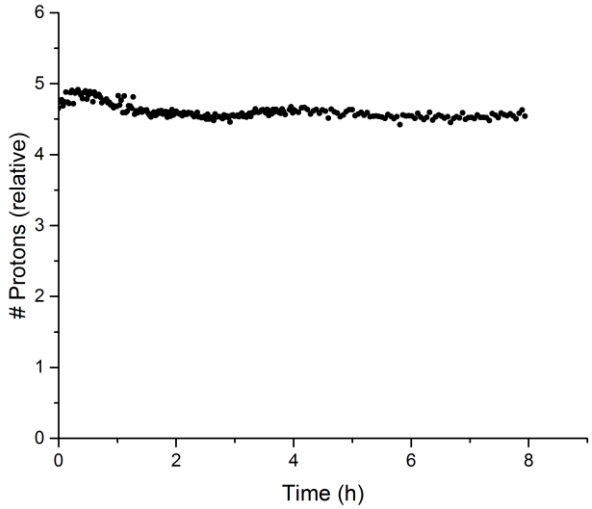

*Figure 4.5: Sum integration of aromatic region (8.25 – 7 ppm) throughout course of the reaction of N-allylbenzylamine **(1)** (6.4 mM) in the presence of green light and Eosin Y catalyst (1 mol% soln. in acetonitrile (100 mL)) to form **2**, **3** and **4**. (20°C, Green LED light source (633 μW at 510 nm), WET solvent suppression, 1.64 s acquisition time, 3 s relaxation delay, 12 scans, 4 mLmin^{-1} flowrate).*

Having access to the reaction vessel during FlowNMR experiments means that the mode and power of illumination may easily be changed while ensuring even light input across the sample, as a way of investigating whether the reaction is limited by the availability of photons.

When using a more powerful light source (250 mW halogen lamp) the reaction became much faster, reaching completion in just 30 minutes at 0˚C (Figure 4.6), with fewer by-products formed than with lower power LED light sources that required longer reaction times.

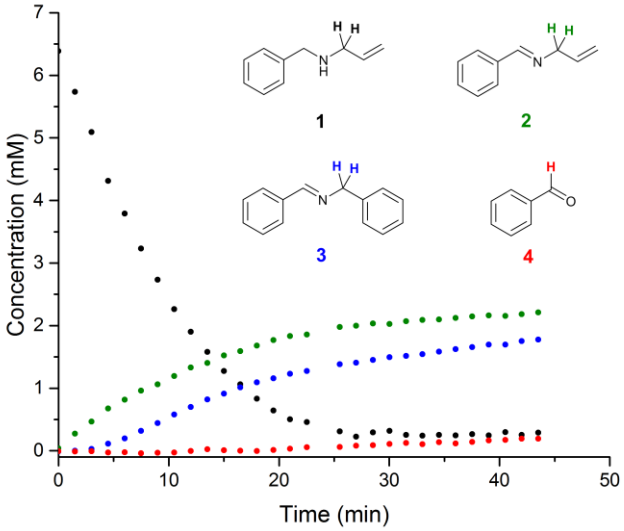

*Figure 4.6: ^{1}H FlowNMR reaction profiles of N-allylbenzylamine **(1)** in MeCN (6.4 mM) at 0°C in the presence of Eosin Y catalyst (1 mol%) under halogen light illumination (250 mW) to form **2**, **3** and **4** (200 mL, 4 mLmin^{-1} flowrate, WET solvent suppression, 4 s acquisition time, 1 s relaxation delay, 16 scans).*

Since the Eosin Y exhibits a sharp absorption peak at 535 nm, with minimal absorption at other wavelengths emitted by the lamp (Figure 4.7), this difference in reaction rate is attributed to the greater light intensity, rather than absorption of photons of different wavelengths. This is confirmed by performing the reaction using a filter to remove higher energy photons, which shows a comparable reaction rate to the reaction using the full spectral range, allowing for a small amount of light scattered or absorbed by the filter (Figure 4.8).

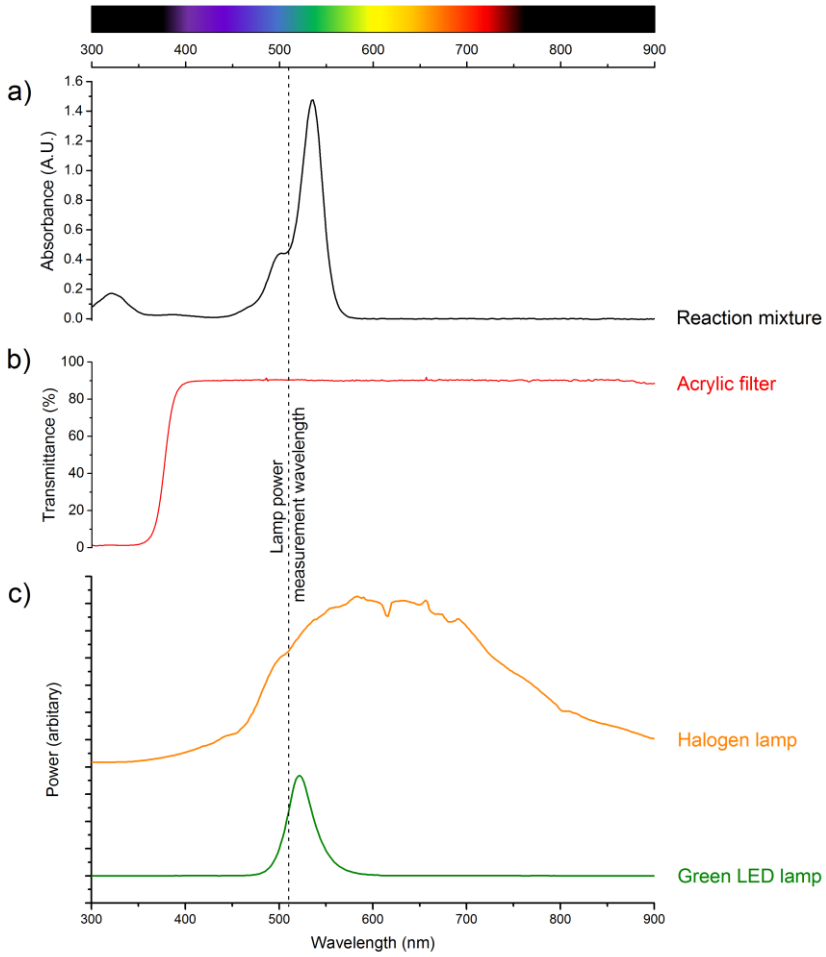

Figure 4.7: a) UV-vis absorption spectrum for the reaction mixture (6.4 mM N-allylbenzylamine, 7.0 mM DMSO and 1 mol% Eosin Y soln. in acetonitrile); b) UV-vis transmission spectrum for acrylic UV filter used in Figure 4.8; c) Power spectra for the two lamps used in the study (NB. The power scale is arbitrary and is not comparable for the two lamps due to different slit sizes required when acquiring the data).

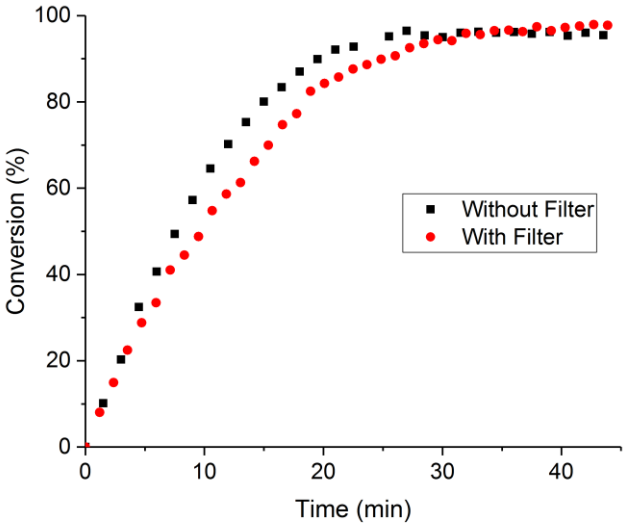

*Figure 4.8: Conversion profiles for the reaction of N-allylbenzylamine **(1)** (6.4 mM) in the presence of white light and Eosin Y catalyst (1 mol% soln. in acetonitrile (100 mL)) to form **2**, **3** and **4**; a) without filtering of light source, and b) with a colourless acrylic filter to block UV wavelengths (400 nm cut-off). (20°C, White halogen light source (250 mW at 510 nm), WET solvent suppression, 1.64 s acquisition time, 3 s relaxation delay, 16 scans, 4 mLmin^{-1} flowrate).*

The formation of benzaldehyde was not significantly affected by light intensity, proceeding at roughly the same rate regardless of light source once appreciable amounts of **2** and **3** had formed in the reaction mixture.

Varying light intensity further revealed the reaction to be photon-limited under typical conditions, with higher lamp powers yielding increased initial reaction rates (Table 4.1 & Figure 4.9).

Table 4.1: Measured power outputs of light sources used at 510 nm. Green LED lamp (high setting) measured at 9 cm from reaction surface.

Light source	Nominal power /W	Measured power output at 9 cm /mW
Green LED lamp (high setting)	50	633×10^{-3}
Green LED lamp (low setting)	50	95×10^{-3}
White Halogen lamp	400	250

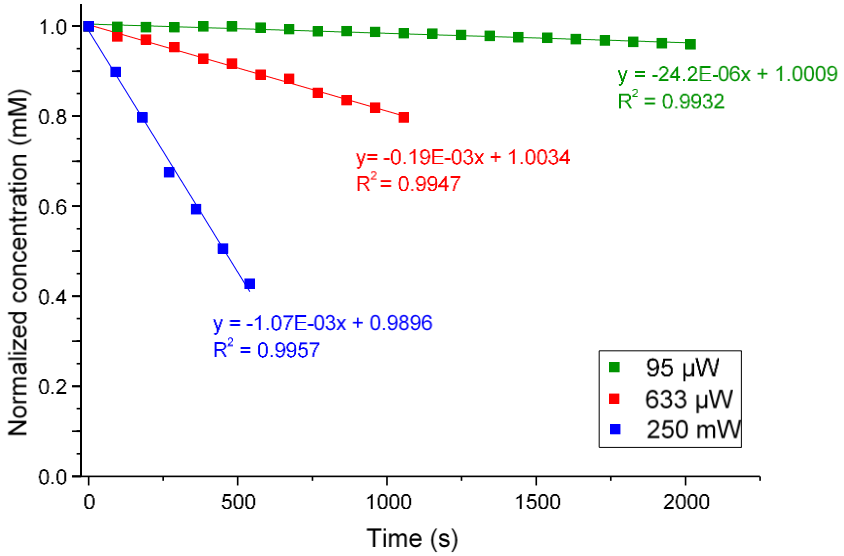

*Figure 4.9: Initial first order reaction rates on the consumption of N-allylbenzylamine **(1)** (6.4 mM) in the presence of green light and Eosin Y catalyst (1 mol% soln. in acetonitrile (50 mL)) with varying lamp power. All reactions were carried out with same mode of illumination (top) and exposed surface area (19 cm diameter dish).*

While under photon-limited conditions, **2** and **3** appeared to form in parallel (Figure 4.2), under high illumination conditions **2** formed as soon as the light was switched on, but formation of **3** occurred only after an induction period of 2-3 minutes (Figure 4.6). This observation suggests the formation of **3** to proceed via reaction of **2** with **1** activated by the excited photocatalyst system (most likely an α-aminoradical),[145] leading to coupling and loss of two allylic groups. No allylic signals other than those from **1** were ever observed by NMR, but spiking a reaction mixture with allylamine showed it to rapidly disappear from the spectra as soon as the reaction was restarted by illumination (Figure 4.10), showing likely by-products of the formation of **3** and **4** to be undetectable under the conditions applied.

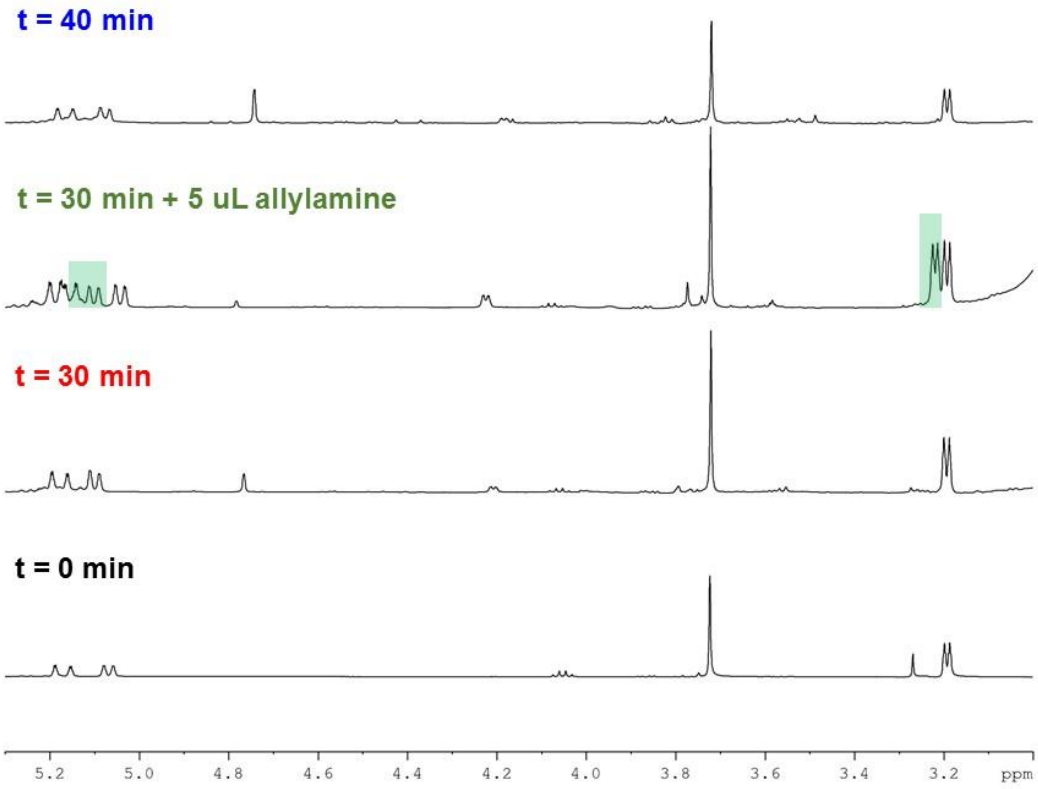

Figure 4.10: ^{1}H NMR spectra (solvent suppressed) of the reaction mixture a) before irradiation b) after irradiation for 30 min (633 µW at 510 nm) c) addition of 5 µL allylamine and d) continuation of the reaction for 10 min. (WET solvent suppression, 1.64 s acquisition time, 3 s relaxation decay, 16 scans).

To investigate the nature of the photo-initiated radical reaction system, variations of atmosphere and illumination were undertaken during the reaction. A chopped illumination experiment performed in air (Figure 4.11) revealed that no further reaction took place in the absence of light after initial irradiation, showing the photo-generated reactive species to have short lifetimes and only operate under sustained input of photons.

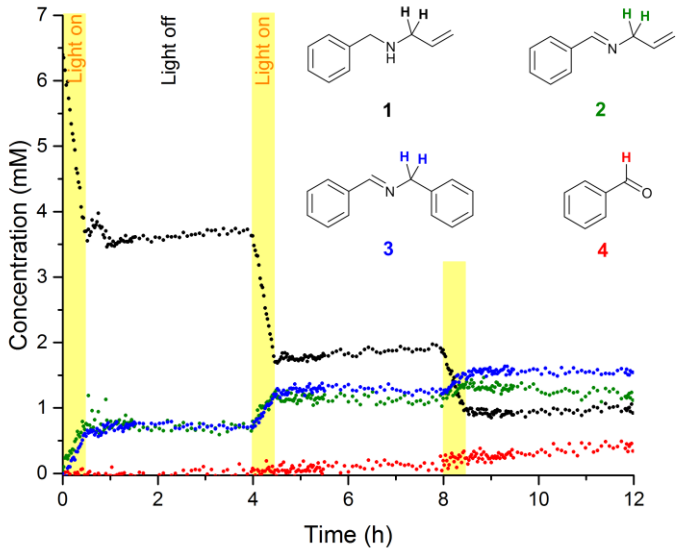

*Figure 4.11: ^{1}H FlowNMR reaction profiles of N-allylbenzylamine **(1)** in MeCN (6.4 mM) at 20°C in the presence of Eosin Y catalyst (1 mol%) under chopped green LED illumination (633 µW) to form **2**, **3** and **4** (100 mL, 4 mLmin^{-1} flowrate, WET solvent suppression, 1.46 s acquisition time, 3 s relaxation delay, 12 scans).*

Product distribution profiles were identical to experiments performed under continuous illumination. Altering reaction atmospheres during light variation showed that some product formed very slowly in an illuminated reaction mixture under dry argon, and no reaction took place when air was introduced but the light switched off (Figure 4.12). Only when illuminated under aerobic conditions product formation occurred, and the reaction stalled immediately when the light was switched off again.

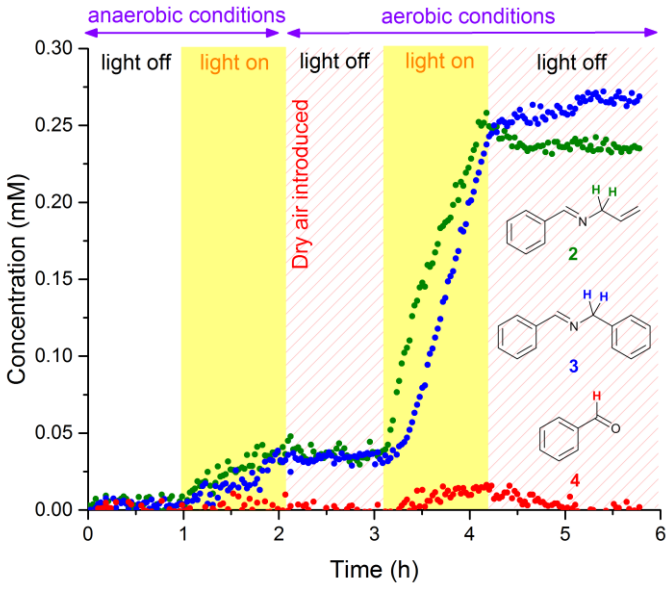

*Figure 4.12: ^{1}H FlowNMR reaction profiles of N-allylbenzylamine **(1)** in MeCN (6.4 mM) at 20°C in the presence of Eosin Y catalyst (1 mol%) under chopped green LED illumination (633 µW) and different atmospheres (argon to dry air) to form **2**, **3** and **4** (50 mL, 4 mLmin^{-1} flowrate, WET solvent suppression, 1.46 s acquisition time, 3 s relaxation delay, 16 scans).*

The formation of benzaldehyde **4** seemed to occur only under illumination in air (Figure 4.12). Test reactions showed the imine products **2** and **3** to be resistant to hydrolysis in the absence of Eosin Y,[144] and addition of water to an anhydrous photocatalytic FlowNMR experiment did not affect the amount of benzaldehyde formation (Figure 4.13).

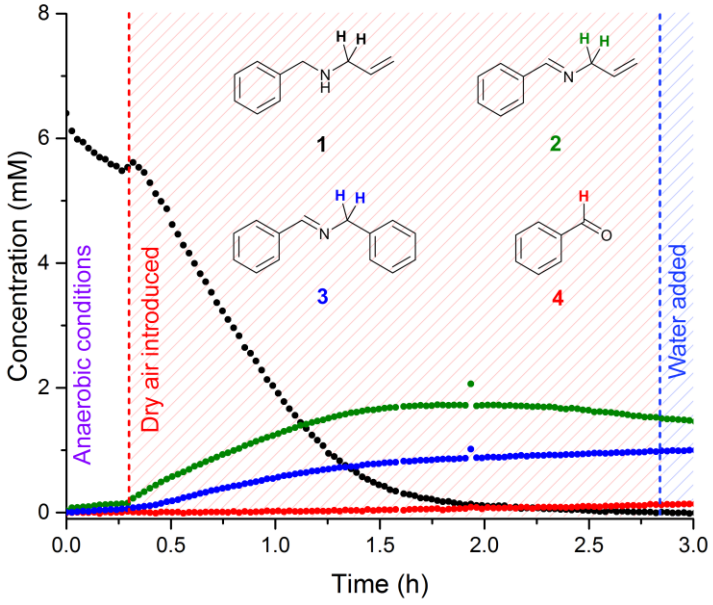

*Figure 4.13: Kinetic data for the reaction of N-allylbenzylamine **(1)** (6.4 mM) in the presence of green light and Eosin Y catalyst (1 mol% soln. in acetonitrile (50 mL)) to form **2**, **3** and **4**. Reaction performed under anhydrous conditions, with a continuous flow of dry air over the reaction. Reaction spiked with 100 µL distilled water after 170 min. (20°C, Green LED light source (633 µW at 510 nm), WET solvent suppression, 1.64 s acquisition time, 3 s relaxation delay, 16 scans, 4 mLmin^{-1} flowrate)*

Thus, product degradation to the undesired aldehydes must be a parallel photo-initiated process rather than a simple hydrolysis reaction. This may proceed via the formation of the corresponding iminoradicals,[145] or due to the presence of singlet oxygen formed upon excitation of Eosin Y.[164] Combining all these observations leads to the proposed reaction network shown in Scheme 4.2.

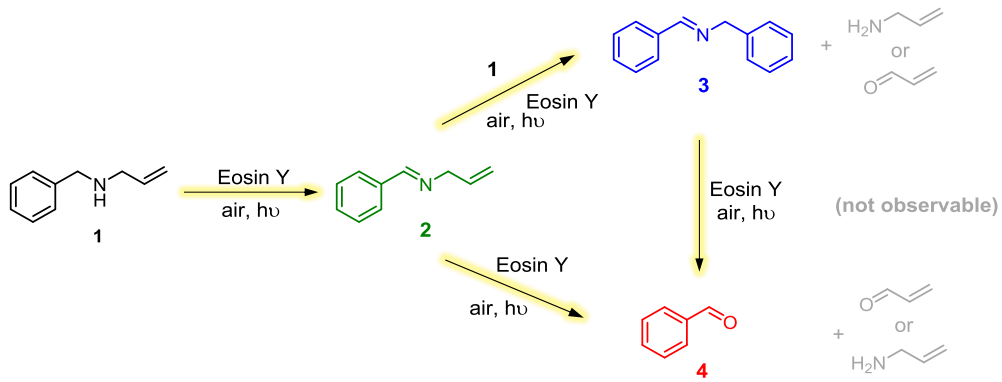

Scheme 4.2: Reaction network based on experimentally observed product and by-product formation profiles, and conditions.

4.3.3 Conclusions

We have shown how FlowNMR spectroscopy can be readily applied to investigate photochemical reactions under realistic conditions to provide valuable mechanistic insight. Substrate consumption profiles showed the reaction to operate under saturation kinetics (photon starvation), and product formation profiles revealed their relative order of formation. Variation of light intensities and reaction atmospheres in conjunction with chopped illumination experiments gave insight into the mode of action of the Eosin Y photocatalyst system, and showed aldehyde formation to occur from the imines via a parasitic photocatalytic pathway. This information, not easily accessible by alternative reaction monitoring techniques, will allow swift optimisation of reaction conditions and assist the design of improved photocatalytic systems in the future.

4.3.4 Conflicts of interest

A.C. is an employee of Bruker UK Ltd., manufacturer and supplier of NMR hard- and software solutions that have been used in this research. The other authors declare no competing financial interest.

4.3.5 Acknowledgements

This work was supported by a Research Grant from the Royal Society (Y0603), the EPSRC Centre for Doctoral Training in Sustainable Chemical Technologies (EP/L016354/1), the Dynamic Reaction Monitoring Facility at the University of Bath (EP/P001475/1), Bruker UK Ltd., and AstraZeneca. U.H. acknowledges the Centre for Sustainable Chemical Technologies for a Whorrod Research Fellowship. The authors would like to thank Joshua Tibbets, Dr Catherine Lyall and Dr Emma Emanuelsson from the University of Bath for support and assistance with this project.

4.3.6 Experimental

(Originally published as part of the Electronic Supplementary Information)

4.3.6.1 Equipment and reagents

Reactions were carried out in air in an open glass dish (19 cm diameter), with either a double-piston HPLC pump (JASCO PU-2085 Plus) with a semi-micro pump head or peristaltic pump (Vaportech SF-10) used to circulate the mixture around the system to an InsightMR flow tube (Bruker) located within the spectrometer (Bruker Avance II + 500 MHz Ultrashield equipped with a broadband observe probe). In order to minimise the delay time between a change occurring in the reaction vessel and the arrival of the sample to the spectrometer for detection it is desirable to ensure that the volume of the tubing connecting the reaction vessel to the spectrometer is minimised, therefore narrow diameter polyetheretherketone (PEEK) tubing (0.762 mm i.d., Upchurch Scientific) was used. The PEEK tubing offers high chemical and mechanical stability (pH 0 – 14, -50 – 100 °C, >300 bar) along with good flexibility and low gas permeability. All other connections were made using standard HPLC-type PEEK connectors (Upchurch Scientific). All equipment was positioned inside a fume hood, located approximately 1 m from the shielded NMR spectrometer, without experiencing any adverse magnetic effects.

Photochemical reactions were performed using either a 50 W green LED light source (TechBox T50W flood lamp) or a 400 W white halogen light source (Maplin Electronics 400 W halogen flood lamp) positioned 9 cm above the open reaction mixture.

Controlled atmosphere reactions were carried out in a Schlenk flask (100 mL) positioned horizontally 9 cm above the lamp, using standard Schlenk technique and dry, degassed solvents. Flasks were kept under a positive pressure of argon or dry air for anaerobic and aerobic reactions respectively. A rubber seal was used to connect the tubing with the reaction solution, and found effective for air-sensitive systems over prolonged times (>10 hours) when sealed off with silicone grease. The sample depth in the Schlenk flask was comparable to that in the open dish reactor.

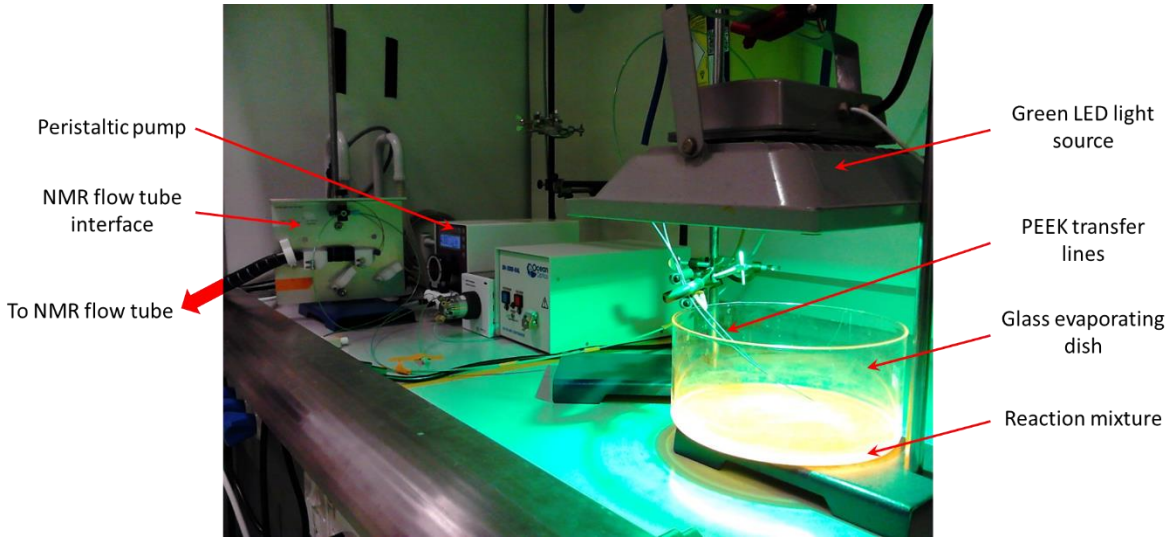

Figure 4.14: FlowNMR reaction setup inside fume hood.

Data acquisition was performed without lock and with shimming performed using automated ^{1}H shimming routines, followed by manual fine tuning. Data processing was performed using commercially available software. Solvent suppression of the acetonitrile resonance using a WET pulse sequence with a shaped pulse and low power ^{13}C decoupling during acquisition was carried out with the Bruker pulse program "wetdc", using a standard LC-NMR automated acquisition program, "au_lc1d" that first acquires a scout scan to identify and subsequently suppress the desired number of solvent peaks.

All samples were prepared using reagents and catalyst purchased from Sigma Aldrich at reagent grade or higher. All reactions were performed using non-deuterated solvents.

4.3.6.2 N-allylbenzylamine synthesis

Benzaldehyde (5 mL, 5.2 g, 49 mmol) and allylamine (4 mL, 3.1 g, 53 mmol) were dissolved in dichloromethane (20 mL) and stirred at room temperature for 2 h. Solvent was evaporated under reduced pressure before redissolving in ethanol (20 mL) and cooling in an ice bath. Sodium borohydride (3.250 g, 85.9 mmol) was added slowly and the reaction left to stir for 5 h, before addition of saturated ammonium carbonate solution (10 mL) to quench the reaction. The solvent was evaporated under reduced pressure and the product extracted with ethyl acetate (3 x 25 mL). The crude was purified by column chromatography (eluent: petroleum ether/ethyl acetate 8:2), to produce the final product as a pale-yellow oil (yield = 87%, 36 mmol)

4.3.6.3 Photochemical reactions

The FlowNMR apparatus was purged with acetone for 5 min at 4 mL/min. The apparatus was filled with a stock solution of 1 mol% Eosin Y in acetonitrile (4 mg/100 mL) (3.7 mL) and connected to the reaction vessel containing 1 mol% Eosin Y in acetonitrile (100 mL), N-

allylbenzylamine (100 μL, 0.638 mmol) and Dimethylsulfoxide (50 μL, 0.704 mmol) as an internal concentration reference.

The flow tube was then inserted into the spectrometer and automated shimming and tuning routines were performed. Best results were obtained if automated shimming and tuning was performed on static samples, however acceptable results were still obtained in flow. Frequency lock was switched off when using non-deuterated solvents, and shimming performed on proton peaks. Manual fine tuning of X and Y shims was often required to get a good peak line width. Spectra of the reagents were recorded without flow and again at the flowrate desired for the reaction. Comparison of the integral area of the peaks in each spectrum was used to calculate a correction factor for each reagent peak. (I = peak integral, CF = correction factor).[160]

$$I_{Corrected} = CF \times I$$

$$CF = \frac{I_{Static}}{I_{Flow}}$$

With the sample flowing, data acquisition was started using an automated kinetic routine or dedicated InsightMR reaction monitoring software, with solvent suppressed ^{1}H spectra recorded at specified time intervals. To start the reaction the light source was switched on.

At the end of the reaction, or if intermediates of interest were observed, additional spectra were recorded with and without flow, and correction factors were calculated for the intermediate or product peaks, which were applied to each spectrum to give the final peak areas for calculation of species concentration and plotting of kinetic data. Concentrations of species were determined by peak integrals referenced to DMSO internal standard.

4.4 COMMENTARY

4.4.1 By-products

As noted in Figure 4.4, many small peaks were seen to grow during the course of the reaction which are attributed to minor by-products from radical side reactions. These minor by-products are the reason why the final product concentration never reaches that of the starting material (Figure 4.3), however as shown in Figure 4.5, the mass balance remained constant across the entire reaction.

In addition to allylamine, hydrogen is another possible by-product of the oxidation of **1**. Whilst several small NMR peaks were observed in the region of 4.5 ppm, bubbling hydrogen into the reaction mixture confirmed that none of these matches the exact chemical shift of hydrogen in acetonitrile (Figure 4.15). As with allylamine (Figure 4.10), hydrogen is extremely volatile, and therefore would not be expected to remain in solution long enough for detectable concentrations to build up.

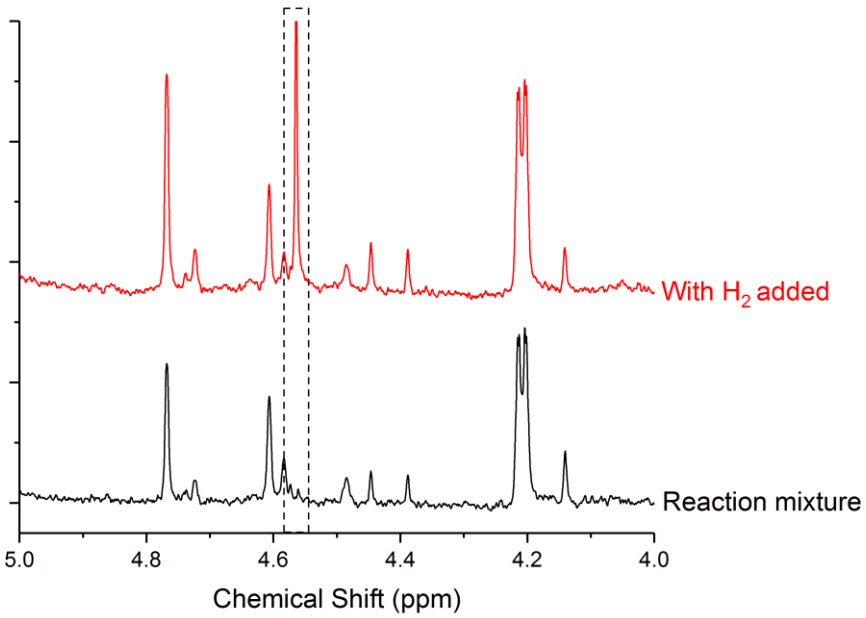

Figure 4.15: ^{1}H NMR spectra (solvent suppressed) of the reaction mixture a) before bubbling H_2 b) after bubbling H_2 gas (WET solvent suppression, 1.64 s acquisition time, 3 s relaxation decay, 16 scans).

4.5 CONCLUSIONS

Using the FlowNMR apparatus discussed in Chapter 2, the photochemical oxidation of N-allyl benzylamine was successfully monitored, enabling important information about the reaction pathway to be determined.

Data from the online measurements have less scatter and are more reproducible than reactions run with off-line sampling, as the need to work-up samples before analysis, and the variability that this introduces are eliminated. Varying reaction conditions (light intensity, reaction atmosphere) allowed a reaction network to be constructed, showing the origins of products and by-products. Spiking the reaction mixture with suspected by-products not observed in the NMR spectrum of the reaction revealed these to be unstable under reaction conditions.

The experiments discussed in this chapter demonstrate how FlowNMR spectroscopy can be applied to the study of reactions that are challenging to study by conventional NMR methods. Although photochemical reactions have been studied before using online NMR, this is the first example of the use of FlowNMR spectroscopy to build a mechanistic understanding of a photocatalytic reaction.

Having demonstrated that the FlowNMR apparatus constructed in Chapter 2 is able to successfully monitor a challenging photochemical reaction, the technique was next applied to the study of an industrially relevant catalytic process (Chapters 5 and 6).

4.6 REFERENCES

1. Ball, G. E. In *Spectrosc. Prop. Inorg. Organomet. Compd.*, RSC: 2010; Vol. 41, pp 262-287.

2. Bliumkin, L.; Dutta Majumdar, R.; Soong, R.; Adamo, A.; Abbatt, J. P. D.; Zhao, R.; Reiner, E.; Simpson, A. J., Development of an in Situ NMR Photoreactor To Study Environmental Photochemistry. *Environ. Sci. Technol.* **2016,** 50, 5506-5516.

3. Murray, A. Development of Novel Flavin - Catalysed Transformations. Doctor of Philosophy, University of Bath, 2015.

4. Murray, A. T.; Dowley, M. J.; Pradaux-Caggiano, F.; Baldansuren, A.; Fielding, A. J.; Tuna, F.; Hendon, C. H.; Walsh, A.; Lloyd-Jones, G. C.; John, M. P.; Carbery, D. R., Catalytic Amine Oxidation under Ambient Aerobic Conditions: Mimicry of Monoamine Oxidase B. *Angew. Chem. Int. Ed. Engl.* **2015,** 54, 8997-9000.

5. König, B., In *Chemical Photocatalysis*. De Gruyter: Berlin, 2013; p 386.

6. Heelis, P. F., The photophysical and photochemical properties of flavins (isoalloxazines). *Chem. Soc. Rev.* **1982,** 11, 15-39.

7. Hoffmann, N., Photochemical Reactions as Key Steps in Organic Synthesis. *Chem. Rev.* **2008,** 108, 1052-1103.

8. Inoue, Y., Asymmetric photochemical reactions in solution. *Chem. Rev.* **1992,** 92, 741-70.

9. Szacilowski, K.; Macyk, W.; Drzewiecka-Matuszek, A.; Brindell, M.; Stochel, G., Bioinorganic Photochemistry: Frontiers and Mechanisms. *Chem. Rev.* **2005,** 105, 2647-2694.

10. Balzani, V.; Credi, A.; Venturi, M., Photochemical Conversion of Solar Energy. *ChemSusChem* **2008,** 1, 26-58.

11. Li, J.-T.; Yang, J.-H.; Han, J.-F.; Li, T.-S., Reductive coupling of aromatic aldehydes and ketones in sunlight. *Green Chem.* **2003,** 5, 433.

12. Oelgemöller, M.; Jung, C.; Mattay, J., Green photochemistry: Production of fine chemicals with sunlight. *Pure Appl. Chem.* **2007,** 79, 1939-1947.

13. Prier, C. K.; Rankic, D. A.; MacMillan, D. W. C., Visible Light Photoredox Catalysis with Transition Metal Complexes: Applications in Organic Synthesis. *Chem. Rev.* **2013,** 113, 5322-5363.

14. Narayanam, J. M. R.; Stephenson, C. R. J., Visible light photoredox catalysis: applications in organic synthesis. *Chem. Soc. Rev.* **2011,** 40, 102-113.

15. Yoon, T. P.; Ischay, M. A.; Du, J., Visible light photocatalysis as a greener approach to photochemical synthesis. *Nat. Chem.* **2010,** 2, 527-532.

16. Closs, G. L.; Miller, R. J., Laser flash photolysis with NMR detection. Submicrosecond time-resolved CIDNP: kinetics of triplet states and biradicals. *J. Am. Chem. Soc.* **1981,** 103, 3586-3588.

17. Roig, B.; Touraud, E.; Thomas, O., Photochemical reaction monitoring by ultra-violet spectrophotometry. *Spectrochim. Acta Mol. Biomol. Spectrosc.* **2002,** 58, 2925-2930.

18. Luo, J.; Oliver, A. G.; Scott McIndoe, J., A detailed kinetic analysis of rhodium-catalyzed alkyne hydrogenation. *Dalton Trans.* **2013,** 42, 11312-11318.

19. Theron, R.; Wu, Y.; Yunker, L. P. E.; Hesketh, A. V.; Pernik, I.; Weller, A. S.; McIndoe, J. S., Simultaneous Orthogonal Methods for the Real-Time Analysis of Catalytic Reactions. *ACS Catalysis* **2016,** 6, 6911-6917.

20. Page, T. F., Jr., Method for in situ photochemical studies by high resolution nuclear magnetic resonance. *Chem. Ind.* **1969**, 1462-3.

21. Mills, A.; O'Rourke, C., In Situ, Simultaneous Irradiation and Monitoring of a Photocatalyzed Organic Oxidation Reaction in a TiO_2-Coated NMR Tube. *J. Org. Chem.* **2015,** 80, 10342-10345.

22. Feldmeier, C.; Bartling, H.; Magerl, K.; Gschwind, R. M., LED-Illuminated NMR Studies of Flavin-Catalyzed Photooxidations Reveal Solvent Control of the Electron-Transfer Mechanism. *Angew. Chem. Int. Ed.* **2015,** 54, 1347-1351.

23. Feldmeier, C.; Bartling, H.; Riedle, E.; Gschwind, R. M., LED based NMR illumination device for mechanistic studies on photochemical reactions – Versatile and simple, yet surprisingly powerful. *J. Magn. Reson.* **2013,** 232, 39-44.

24. Foley, D. A.; Dunn, A. L.; Zell, M. T., Reaction monitoring using online vs tube NMR spectroscopy: seriously different results. *Magn. Reson. Chem.* **2016,** 54, 451-456.

25. Albert, K. In *On-Line LC-NMR And Related Techniques*, John Wiley & Sons, Ltd: 2003; pp 1-22.

26. Albert, K.; Bayer, E., High-performance liquid chromatography—nuclear magnetic resonance on-line coupling. *TrAC, Trends Anal. Chem.* **1988,** 7, 288-293.

27. Foley, D. A.; Bez, E.; Codina, A.; Colson, K. L.; Fey, M.; Krull, R.; Piroli, D.; Zell, M. T.; Marquez, B. L., NMR flow tube for online NMR reaction monitoring. *Anal. Chem.* **2014,** 86, 12008-12013.

28. Foley, D. A.; Zell, M. T.; Marquez, B. L.; Kaerner, A., NMR Reaction-Monitoring as a Process Analytical Technique. *Pharm. Technol.* **2011,** 11, S19.

29. Khajeh, M.; Bernstein, M. A.; Morris, G. A., A simple flowcell for reaction monitoring by NMR. *Magn. Reson. Chem.* **2010,** 48, 516-522.

30. Silva Elipe, M. V.; Milburn, R. R., Monitoring chemical reactions by low-field benchtop NMR at 45 MHz: pros and cons. *Magn. Reson. Chem.* **2016,** 54, 437-443.

31. Hall, A. M. R.; Chouler, J. C.; Codina, A.; Gierth, P. T.; Lowe, J. P.; Hintermair, U., Practical Aspects of Real-time Reaction Monitoring using Multi-nuclear High Resolution FlowNMR Spectroscopy. *Catal. Sci. Tech.* **2016,** 6, 8406-8417.

32. Zientek, N.; Meyer, K.; Kern, S.; Maiwald, M., Quantitative Online NMR Spectroscopy in a Nutshell. *Chem. Ing. Tech.* **2016,** 88, 698-709.

33. Smallcombe, S. H.; Patt, S. L.; Keifer, P. A., WET Solvent Suppression and Its Applications to LC NMR and High-Resolution NMR Spectroscopy. *J. Magn. Reson. A* **1995,** 117, 295-303.

34. Emmanuel, N.; Mendoza, C.; Winter, M.; Horn, C. R.; Vizza, A.; Dreesen, L.; Heinrichs, B.; Monbaliu, J.-C. M., Scalable Photocatalytic Oxidation of Methionine under Continuous-Flow Conditions. *Org. Process Res. Dev.* **2017,** 21, 1435-1438.

35. Hari, D. P.; König, B., Eosin Y Catalyzed Visible Light Oxidative C–C and C–P bond Formation. *Org. Lett.* **2011,** 13, 3852-3855.

36. Pan, Y.; Wang, S.; Kee, C. W.; Dubuisson, E.; Yang, Y.; Loh, K. P.; Tan, C.-H., Graphene oxide and Rose Bengal: oxidative C-H functionalisation of tertiary amines using visible light. *Green Chem.* **2011,** 13, 3341-3344.

37. Romero, N. A.; Nicewicz, D. A., Organic Photoredox Catalysis. *Chem. Rev.* **2016,** 116, 10075-10166.

38. Amat-Guerri, F.; López-González, M. M. C.; Martínez-Utrilla, R.; Sastre, R., Singlet oxygen photogeneration by ionized and un-ionized derivatives of Rose Bengal and Eosin Y in diluted solutions. *J. Photochem. Photobiol. A: Chem.* **1990,** 53, 199-210.

5 Noyori Asymmetric Transfer Hydrogenation: Kinetics and Mechanism

The work presented in this chapter has been published in the journal '*ACS Catalysis*' and is reproduced with permission from *ACS Catalysis,* **2019**, 9 (3), 2079-2090. Copyright 2019 American Chemical Society. Page, reference and figure numbers have been altered for consistency. Experimental conditions and some figures originally submitted for publication as part of the Electronic Supplementary Information have been included in the main text where they are referred to.

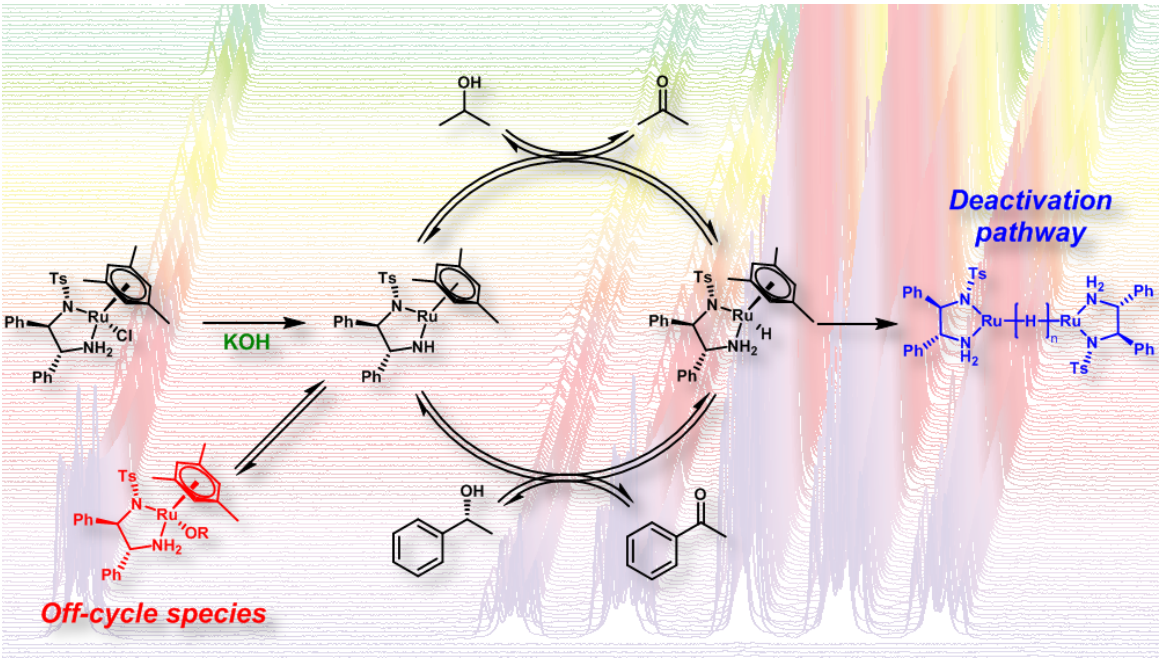

5.1 Introduction to Submitted Work

An example of how FlowNMR spectroscopy can be applied to the study of a photochemical reaction was shown in Chapter 4, where the photocatalytic oxidation of N-benzylamine was investigated to help derive a reaction network. In this chapter, a reaction involving air-sensitive metal catalysts is investigated, demonstrating the ability of FlowNMR spectroscopy to provide detailed kinetic data, including information about catalyst speciation.

Catalytic asymmetric transfer hydrogenation is an industrially important reaction, used widely as a means of introducing chirality into a molecule.[86] A large number of transition metal catalysts are known to catalyse the reaction, with many of the most successful catalysts being Ru, Rh, Ir or Fe based. One of the earliest and most active catalysts is Noyori's RuCl(TsDPEN)(arene).[90] Noyori's catalyst converts prochiral ketones to chiral alcohols with high yield and selectivity, using a sacrificial alcohol (usually ethanol or propanol) or formic acid as the hydrogen donor (Scheme 5.1).

The mechanism of the Noyori catalyst has been studied in detail by many different groups, with the majority focusing on the origins of enantioselectivity and the possible inner-sphere and outer-sphere hydrogen transfer mechanisms.[97-99, 102, 116, 165-166] A 18-electron ruthenium-hydride and a 16-electron "unsaturated" complex have been isolated and characterised, and are proposed as intermediates in the reaction.[115] Despite the interest in this reaction, little is known about the deactivation pathway of the catalyst, and the role that the auxiliary base plays in the reaction.

The catalytic asymmetric transfer hydrogenation of acetophenone with the Noyori catalyst was selected for investigation by FlowNMR as the well characterised intermediates provide an opportunity for direct observation of the catalyst under turnover conditions. Although it would be possible to monitor this reaction using *insitu* or offline NMR techniques, FlowNMR allows continuous data acquisition whilst reagents are added, allowing fast changes to be monitored, as well as stirring to ensure good mass transport within the reaction.

The Noyori catalyst is known to undergo slow decomposition in solution, which is accelerated in the presence of air.[167] To minimise catalyst decomposition during the reaction, inert conditions are required (dry, degassed solvents and inert atmosphere). Since the FlowNMR apparatus discussed in Chapter 2 is completely sealed, air can be excluded from the reaction and the apparatus flushed with inert gas prior to use. Online UV-Vis, HPLC and MS instruments were also used to follow the reaction, alongside NMR.

5.2 STATEMENT OF AUTHORSHIP

<table>
<tr><th colspan="10">This declaration concerns the article entitled:</th></tr>
<tr><td colspan="10">Kinetics of Asymmetric Transfer Hydrogenation, Catalyst Deactivation, and Inhibition with Noyori Complexes as Revealed by Real-time High Resolution FlowNMR Spectroscopy</td></tr>
<tr><td colspan="10">Publication status (tick one)</td></tr>
<tr><td>draft manuscript</td><td></td><td>Submitted</td><td></td><td>In review</td><td></td><td>Accepted</td><td></td><td>Published</td><td>✓</td></tr>
<tr><td>Publication details (reference)</td><td colspan="9">A. M. R. Hall, P. Dong, A. Codina, J. P. Lowe and U. Hintermair, ACS Catalysis, 2019, 9 (3), 2079-2090</td></tr>
<tr><td>Candidate's contribution to the paper (detailed, and also given as a percentage).</td><td colspan="9">The candidate contributed to/ considerably contributed to/predominantly executed the…

Formulation of ideas: 50%
Ideas from discussion between AH and UH.

Design of methodology: 30%
Original methodology by UH and JL. Additional experiment design by AH, UH and JL.

Experimental work: 95%
Except for Figure 5.17 which was acquired by PD, all data was acquired by AH.

Presentation of data in journal format: 75%
The figures and initial draft was prepared by AH, with editing and additional material by UH. The manuscript was proof-read by JL and AC.</td></tr>
<tr><td>Statement from Candidate</td><td colspan="9">This paper reports on original research I conducted during the period of my Higher Degree by Research candidature.</td></tr>
<tr><td>Signed</td><td colspan="5"></td><td>Date</td><td colspan="3"></td></tr>
</table>

5.3 KINETICS OF ASYMMETRIC TRANSFER HYDROGENATION, CATALYST DEACTIVATION, AND INHIBITION WITH NOYORI COMPLEXES AS REVEALED BY REAL-TIME HIGH RESOLUTION FLOWNMR SPECTROSCOPY

Andrew M. R. Hall,[a] Peilong Dong,[b] Anna Codina,[c] John P. Lowe,[b] Ulrich Hintermair[a]*

a) Centre for Sustainable Chemical Technologies, University of Bath, Claverton Down, Bath BA2 7AY, United Kingdom.
b) Department of Chemistry, University of Bath, Claverton Down, Bath BA2 7AY, United Kingdom.
c) Bruker UK Ltd., Banner Lane, Coventry CV4 9GH, United Kingdom.

** Corresponding author: U.Hintermair@bath.ac.uk*

Catalytic hydrogen transfer from basic iso-propanol to aryl-ketones mediated by [(arene)(TsDPEN)RuCl] complexes has been investigated by operando 1H NMR spectroscopy using a recirculating flow setup. Selective excitation pulse sequences allowed fast and quantitative monitoring of the key [(mesitylene)(TsDPEN)Ru-H] intermediate during catalysis, which is shown to interact with both substrates by polarisation transfer experiments. Comparison of reaction profiles with catalyst speciation traces in conjunction with reaction progress kinetic analysis using variable time normalization and kinetic modelling showed the existence of two independent catalyst deactivation/inhibition pathways: whereas excess base exerted a non-competitive inhibition effect on the unsaturated catalyst intermediate, the active hydride suffered from an inherent first order decay that is not evident in early stages of the reaction where turnover is fast. Isotopic labelling directly showed arene loss to be the entry point into deactivation pathways to Ru nanoparticles via hydride-bridged intermediates.

5.3.1 Introduction

Homogeneous catalysis is an extremely powerful tool for chemical synthesis, offering molecular engineering of complex transformations with unrivalled precision under mild conditions.[1, 168-169] Understanding the reactivity displayed by the catalyst, including possible inhibition and deactivation pathways,[170] is key to improving existing systems and developing new catalytic technologies.[171-173] Due to the complex and dynamic nature of catalytic systems operating under kinetic control this is still a significant challenge. Reaction progress monitoring and kinetic analysis can guide catalyst development, but require high quality data and don't provide information on how the catalyst accomplishes the transformation.[123, 174-177] *Operando* methods that allow measuring the kinetics of the reaction and observing the speciation of the catalyst under realistic conditions are thus key to advancing catalysis research.[178] Online or *in-situ* techniques such as UV-vis, Infrared (IR) and Raman spectroscopies, along with sampling Gas Chromatography (GC), Mass Spectrometry (MS), or High Performance Liquid chromatography (HPLC) are often used for reaction monitoring and analysis,[54, 179-183] and can be very powerful for selected analytes. However, most of these techniques require calibration before use and are not always amenable to non-invasive observation of *a-priori* unknown catalytic intermediates. Multi-nuclear high resolution FlowNMR spectroscopy has recently emerged as a powerful tool for real-time reaction monitoring,[11, 33, 36-37, 47, 160, 184] providing a wealth of information about complex mixtures and overcoming many of the limitations of alternative *in-situ* and off-line techniques due to the ability of maintaining realistic reaction conditions, including good mass transport and temperature control (Figure 5.1). As long as residence time and flow effects on signal quantification are considered, highly accurate data may be obtained without any modification of the NMR spectrometer.[36, 47, 52, 160]

Transition-metal catalysed asymmetric transfer hydrogenation reactions are an important synthetic procedure commonly used to introduce chirality into a molecule through reduction of pro-chiral ketones or imines to alcohols and amines with high enantioselectivities.[86, 88, 91-92, 98, 101, 185-187] One of the earliest examples and still most powerful catalyst systems are Noyori's original TsDPEN complexes which contain a chiral diamine ligand bound to a ruthenium centre.[90, 115] These combine exquisite chemoselectivities, high reaction rates and excellent stereoselectivities for a range of aryl ketones, work with both isopropanol and formic acid as the reductant, and tolerate a range of auxiliary bases.[100, 117] Despite their effectiveness and ease of use, however, turnover numbers are still limited due to catalyst deactivation.[170] A lot of effort has been devoted to understanding the mechanism of hydrogen transfer,[97-98, 102, 115-117, 165] but little is known about the origin and nature of catalyst deactivation in these systems.

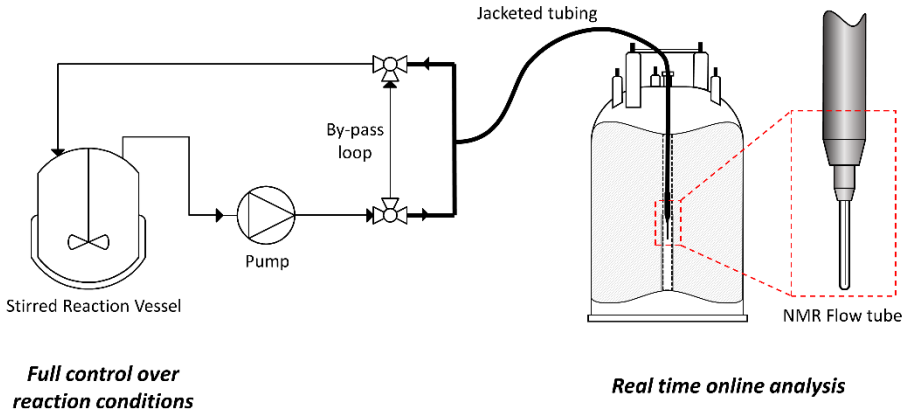

Figure 5.1: FlowNMR apparatus schematic (not to scale).

Here we investigate the asymmetric transfer hydrogenation of acetophenone with Noyori's RuCl[(R,R)-TsDPEN](mesitylene) catalyst, **1**, using real-time FlowNMR spectroscopy to readily obtain high quality kinetic data on this air-sensitive, transition metal catalysed transformation that includes and explains inhibition and deactivation pathways.

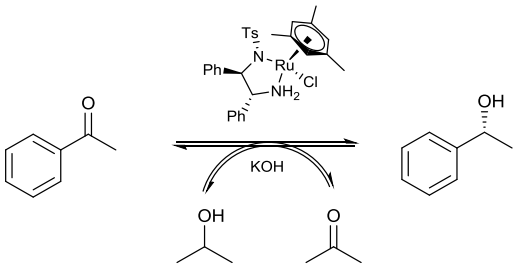

*Scheme 5.1: Catalytic asymmetric transfer hydrogenation of acetophenone to (R)-1-phenylethanol with RuCl[(R,R)-TsDPEN](mesitylene) **(1)**.*

5.3.2 Results and Discussion

We found that no modification of the reaction conditions (scale, concentrations, solvent, reaction vessel, etc.) was required for the analysis by FlowNMR spectroscopy; all experiments discussed in the following were performed under literature conditions (V=10 mL, 0.4 M substrate, 0.25-1 mol% [Ru], 1-20 equivalents KOH, inert atmosphere, room temperature, *iso*-propanol-H_8). For a 10 mL sample volume, the sample spends approximately 37% of the reaction time within the flow apparatus (V=3.7 mL).[160] The volume of the NMR flow cell is approximately 0.5 mL, corresponding to a mean residence time within the detection region of 8 seconds at a flow rate of 4 $mLmin^{-1}$.[160] As described earlier,[160] the high field and shim stability of modern spectrometers together with application of advanced multiple solvent suppression techniques allows the use of non-deuterated solvents, which is particularly important in cases like transfer hydrogenation, where deuterated solvents would otherwise lead to unwanted isotope effects (as demonstrated further below). Like its many variations, the original Noyori catalyst is known to be air sensitive in solution, gradually decomposing to Ru nanoparticles[83, 167] that progressively erode reaction rates and stereoselectivity (Table 5.1). Thus, all reagents and solvents were dried and degassed, and the FlowNMR apparatus (consisting mainly of HPLC grade PEEK and Teflon tubing) purged with argon and flushed with dry solvent prior to use. The reactions were carried out in a standard Schlenk-type glass flask with magnetic stirring under dry argon atmosphere, with the sample tubing to and from the FlowNMR tube fed through a rubber seal. At typical flow rates of 4 mL/min residence times in the FlowNMR apparatus were about one minute, resulting in a 30 second time lapse between the reaction vessel and NMR detection. Continuous NMR spectra acquisition was set up and started on a flow of solvent, and the reaction initiated by sequential addition of reagents via air-tight syringes.

With this setup (Figure 5.1) and using optimised ^1H NMR acquisition parameters accounting for flow effects[160] (for details see experimental Section 5.4.3) we were able to follow catalytic product formation in real time, providing high quality kinetic reaction profiles (Figure 5.2). The solution of the FlowNMR experiment went through the same colour changes over time as a separate control experiment in a sealed Schlenk flask, and comparing conversions and enantioselectivities over time as derived from the *operando* FlowNMR experiment with data from off-line sampling showed identical values (Figure 5.2). This proves that the chemistry in solution is not affected by the flow and proceeds the same even after several hundred residence times, but more and better data is generated by the FlowNMR experiment at reduced experimental effort.

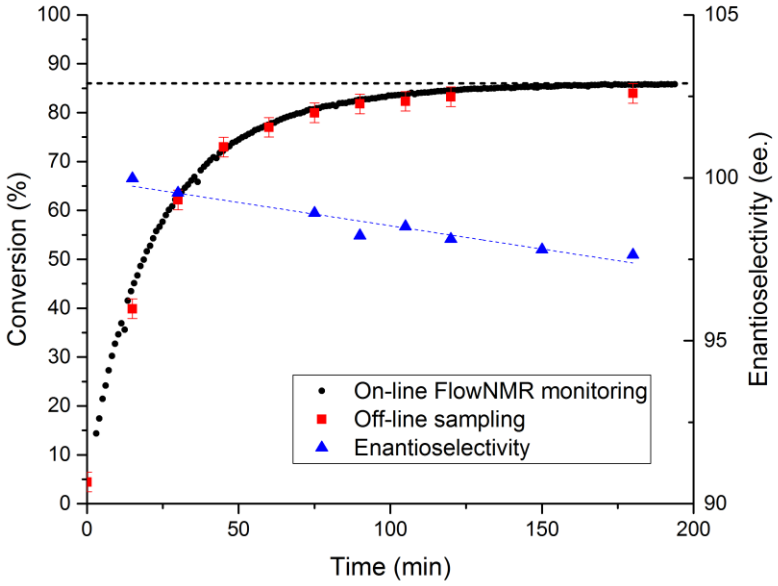

*Figure 5.2: Reaction progress and enantioselectivity data for the catalytic transfer hydrogenation of acetophenone to (R)-1-phenylethanol (400 mM acetophenone, 10 mM KOH, 2 mM **(1)**, 9.5 mL dry isopropanol, 20°C) monitored using on-line ^{1}H FlowNMR spectroscopy and off-line ^{1}H NMR spectroscopy on samples taken from the reaction mixture at different timepoints throughout the reaction. Off-line reaction performed in sealed Schlenk flask under inert atmosphere. On-line FlowNMR reaction performed in sealed round bottom flask under inert conditions (see SI for details). Enantioselectivity determined by chiral HPLC analysis (see SI for details).*

The reaction profile smoothly converged to equilibrium (86 ± 2% conversion under the conditions applied) over the course of a few hours, with no noticeable induction period once the catalyst precursor **1** was added to a solution of acetophenone and KOH in deaerated isopropanol. Enantioselectivity towards *(R)*-1-phenylethanol was >99% *e.e.* up to about 50% conversion, then started to decrease to 98% *e.e.* near equilibrium conversion, and continued to fall when the reaction was left for longer. This behaviour is known and typically ascribed to the reversibility of the reaction,[101] but catalyst deactivation to less selective species also contributes to the erosion of enantioselectivity over time (Figure 5.2).

The quantitative nature and high quality of the reaction profiles obtained from FlowNMR means that the data are exquisitely well suited for reaction progress kinetic analysis (RPKA).[174] Variable Time Normalisation Analysis (VTNA) has recently been shown to be particularly useful for performing RPKA directly on integral rate data such as derived from spectroscopy.[175, 188] Applying variable time normalization to reaction profiles obtained with different amounts of **1** showed good overlay when plotted against (time × $[cat]^n$) with n = 1.0, revealing a first order rate dependence on ruthenium concentration (Figure 5.3) and first order in substrate (Figure 5.4). This reaction order is in agreement with that derived from initial rate data (Figure 8.6), and with the proposed mechanism involving monomeric

ruthenium species in the turnover limiting step (TLS).[99, 109] However, while the overlay is very good in the initial regime of the reaction up to ~50% conversion, and identical equilibrium conversions were reached at longer reaction times, lower normalized rates were evident for lower catalyst loadings at intermediate reaction stages (Figure 5.3, inset), indicating some catalyst deactivation over the course of the reaction.

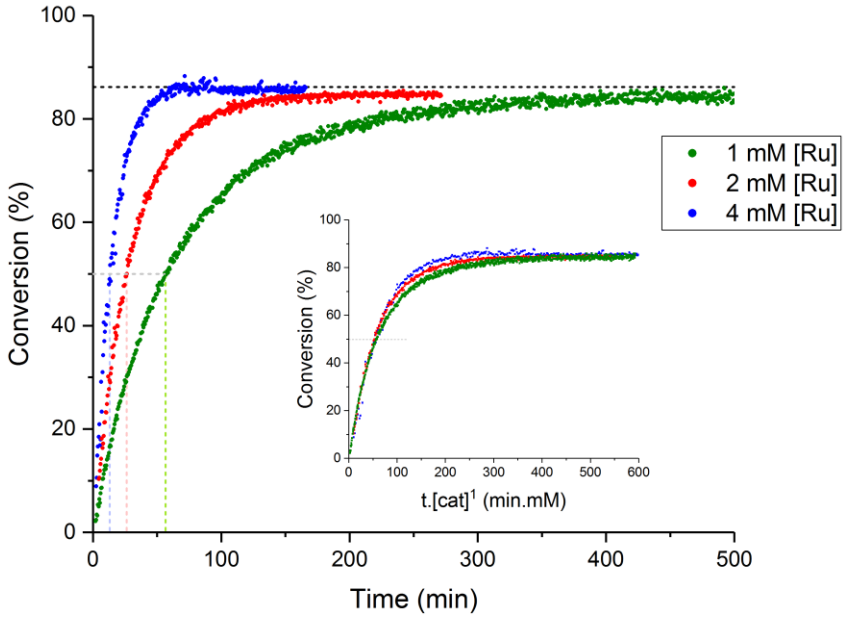

*Figure 5.3: Conversion plots for the catalytic transfer hydrogenation of acetophenone to (R)-1-phenylethanol with various amounts of **(1)** (400 mM acetophenone, 10 mM KOH, 9.5 mL dry isopropanol, 20°C), showing dependence of catalyst concentration on reaction rate. Inset: Variable Time Normalisation Analysis (VTNA) of conversion data.*

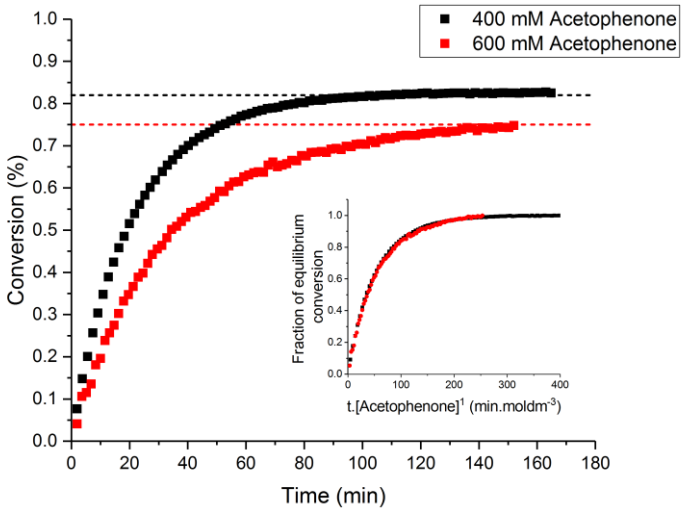

*Figure 5.4: Conversion plots for the catalytic transfer hydrogenation of acetophenone to (R)-1-phenylethanol with various amounts of acetophenone (2 mM **1**, 10 mM KOH, 9.5 mL dry isopropanol, 20°C), showing dependence of acetophenone concentration on reaction rate. Inset: Variable Time Normalisation Analysis (VTNA) of conversion data, normalised for different equilibrium position due to change in reaction conditions, showing first order dependence of reaction rate on acetophenone concentration.*

The reverse reaction starting with acetone and racemic 1-phenylethanol resulted in a conversion of 16% of the *(R)*-1-phenylethanol to acetophenone with negligible conversion of *(S)*-1-phenylethanol (Figure 5.5a), confirming the reversibility of the reaction and the final conversion values seen in the forward reaction to be equilibrium under the conditions applied. Injection of a second portion of substrate showed the catalyst to remain active after the initial end-point had been reached (Figure 5.5b), albeit with only about half the initial reaction rate and reduced enantioselectivity.

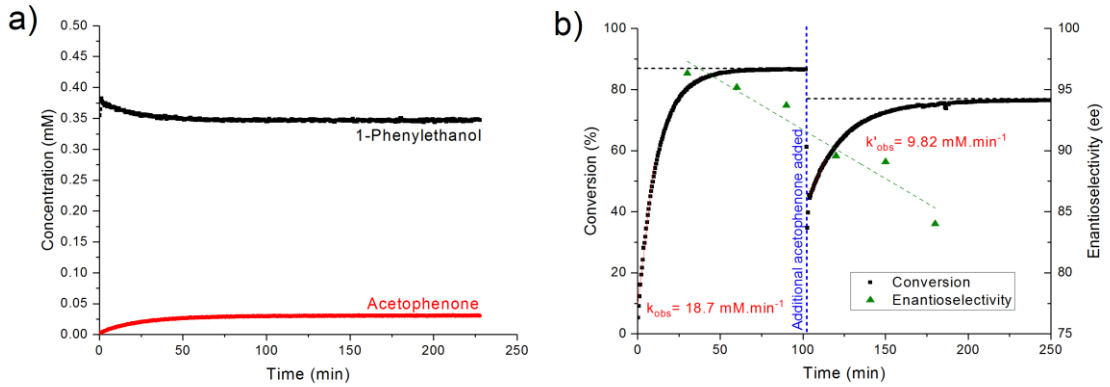

*Figure 5.5: a) Reaction profiles for the transfer hydrogenation of racemic 1-phenylethanol and acetone to acetophenone and isopropanol (400 mM rac-1-phenylethanol, 10 mM KOH, 9.5 mL dry acetone, 2 mM **1**, 20°C). b) Reaction profiles and enantioselectivity for the catalytic transfer hydrogenation of acetophenone to (R)-1-phenylethanol (400 mM acetophenone, 10 mM KOH, 4 mM **1**, 9.5 mL dry isopropanol, 20°C) where an additional 4 mmol acetophenone was added after 100 minutes (800 mM total acetophenone concentration).*

The ability to readily acquire high quality reaction profiles suitable for kinetic analyses without prior calibration makes FlowNMR an attractive tool for reaction development and optimisation. For mechanistic investigations in catalysis however it would be even more desirable to also follow catalyst speciation at the same time, because if intermediates can be observed under the same conditions as product formation takes place we can understand their kinetic relevance, a crucial link that is missing from traditional *ex-situ* analyses and model reactions.[178] We thus strived to detect catalyst intermediates during acetophenone reduction from isopropanol catalysed by **1** directly under the standard literature conditions used.

Akin to related olefin reduction, the traditional Meerwein-Ponndorf-Verley (MPV) mechanism for ketone reduction involves direct (i.e. inner sphere) coordination of the substrates to the metal, from which the alkoxide product is liberated after hydride addition to the activated carbonyl.[97-98] An alternative mechanism explaining the very high chemoselectivities of C=O versus C=C reduction observed with ruthenium diamine complexes involves an outer sphere pathway, where hydrogen atoms are transferred from a metal hydride and amine proton in a metal-ligand bifunctional manner (HOL / TOL (Hydrogenation/Transfer hydrogenation, Outer sphere, Ligand assisted) mechanisms in Morris' classification[97]) that does not require the substrates to coordinate to the metal.[98, 100-101, 115] As shown by Noyori, treatment of the precursor complex **1** with a base such as potassium hydroxide leads to deprotonation of the bound amine and loss of the chloride ligand resulting in the 'unsaturated' 16 electron complex **2** (Scheme 5.2). Addition of a reducing alcohol to **2** then results in the formation of the 18 electron mono-hydride complex **3** along with the corresponding ketone. **3** may transfer the reducing equivalents to another ketone, leading to re-formation of **2** and the corresponding alcohol (with stereo-control in this case).

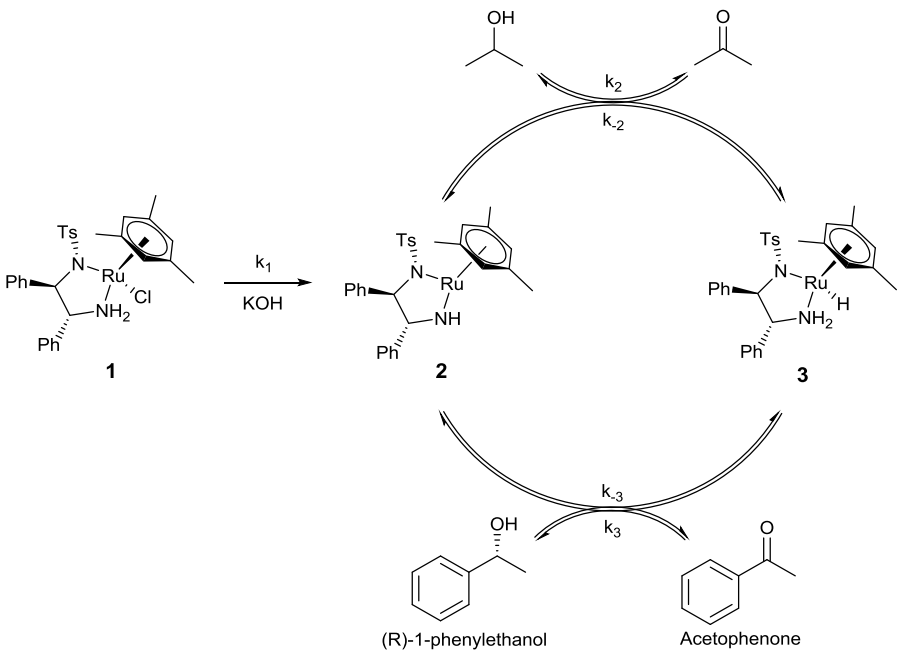

$$rate = (k_3[Acp] - k_{-3}[PE]K_{cat})(K_{cat} + 1)^{-1}[Ru]$$

$$K_{cat} = \frac{[2]}{[3]} = \frac{k_{-2}[Ac] + k_3[Acp]}{k_2[IPA] + k_{-3}[PE]} = \frac{k_{-2}\,\chi[Acp]_0 + k_3[Acp]_0(1-\chi)}{k_2[IPA]_0 + k_{-3}\,\chi[Acp]_0}$$

*Scheme 5.2: Commonly accepted mechanism of the catalytic asymmetric transfer hydrogenation of acetophenone using RuCl[(R,R)-TsDPEN](mesitylene) **1** in basic isopropanol and its corresponding rate law.*

It is important to note that although various versions of this mechanism based on different transition states have been discussed,[109] the involvement of **2** and **3** as the key catalytic intermediates is common to all these scenarios.[99] Thus, our following mechanistic discussion is based on **2** and **3** as the main in-cycle species, and in this study we refrain from speculating on how these interconvert during turnover.

Because all in-cycle events are fully reversible when using isopropanol as the reductant, the rate law for this simple mechanism contains four rate constants, and the distribution of catalyst during turnover expressed as $K_{cat} = \frac{[2]}{[3]}$ is a function of all of these as well as the reaction progress χ (Scheme 5.2). Kinetic modelling of the catalyst speciation over the course of the reaction shows an initial 1:1 distribution between **2** and **3** which asymptotically falls to $K_{cat} = \frac{[2]}{[3]} = 0.88$ over the course of the reaction under the conditions applied (Figure 5.6). The fact that K_{cat} is predicted not to change further once final conversion values have been reached reflects the reversibility of the reaction, and shows the catalyst to remain busy cycling in the equilibrium mixture.

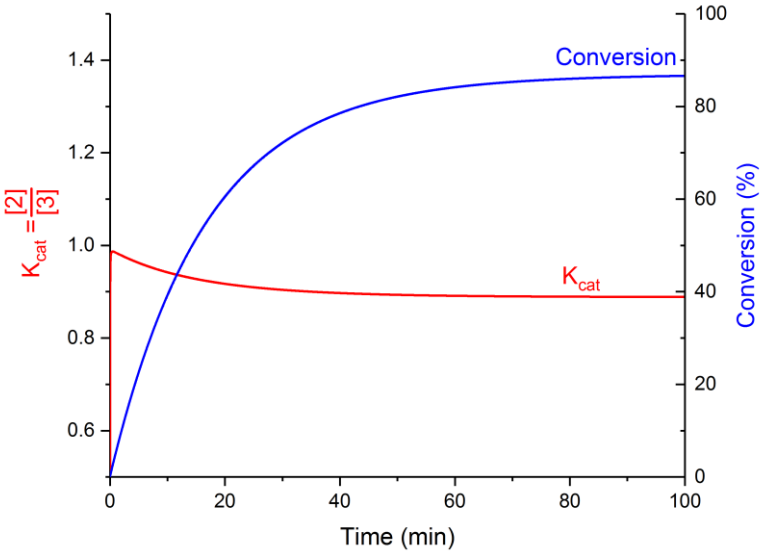

Figure 5.6: Simulation of the change in K_{cat} and conversion during course of reaction (see SI for details of simulation, kinetic parameters and derivation of rate laws).

The reduced catalyst intermediate **3** contains a ruthenium mono-hydride that is characterized by a singlet peak reported at -5.47 ppm (d_8-toluene) in the ^{1}H NMR spectrum,[115] which presents itself as a convenient spectroscopic handle as no other component of the reaction mixture has any resonances in this chemical shift range. However, the low concentration of catalyst (0.25 – 1 mol% relative to substrate) means that under catalytic conditions, where only a part of the ruthenium exists as **3**, the hydride peak is within the noise level of the ^{1}H NMR spectrum at 500 MHz (Figure 5.7) because the receiver gain of the instrument is limited by the much larger solvent and substrate signals. Use of a shaped excitation pulse sequence however enabled the hydride region of the spectrum to be amplified selectively, with minimal excitation of off-resonance peaks. This allowed the receiver gain to be adjusted to increase the S/N for the hydride peak of **3**, effectively amplifying its signal by >1000 times (Figure 5.7).

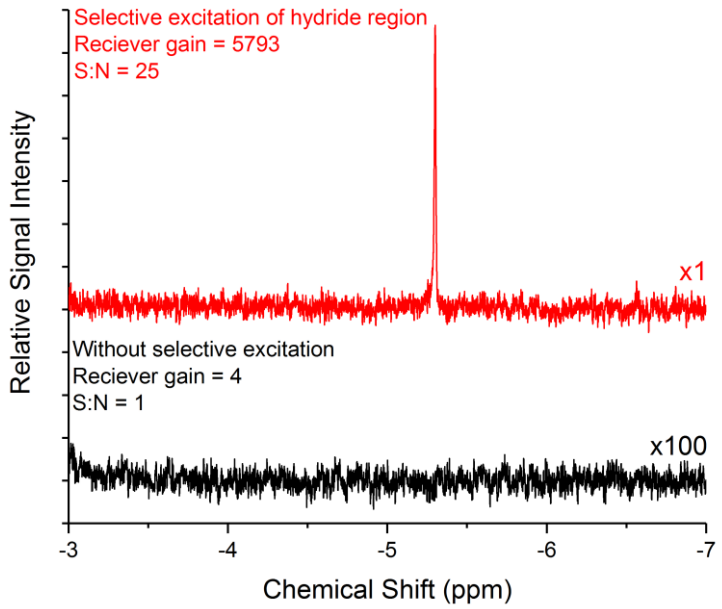

*Figure 5.7: Selective ^{1}H excitation of the hydride peak of **3** under turnover conditions in flow (4 mL/min) using a gradient spin echo pulse sequence with a shaped 180° pulse centred at -5.4 ppm, resulting in >1000 times increase in signal amplification. (Without selective excitation: 4 scans, 1 s acquisition time, 4 s delay time; Selective excitation: 24 scans, 1 s acquisition time, 1 s delay time, 880 µs Gaussian shaped pulse; both spectra processed with 0.5 Hz exponential line broadening). Data for experiment without selective excitation multiplied by a factor of 100 for visual clarity.*

Although no significant change in linewidth was detectable throughout the reaction at room temperature, polarisation transfer experiments (EXSY NMR) of **3** thus observed under reaction conditions showed a (on the NMR timescale) fast exchange between the ruthenium hydride and both the isopropanol and 1-phenylethanol CH protons (Figure 5.8). This data is direct proof for **3** to be an in-cycle catalytic species undergoing continuous reversible exchange with both substrate and product (Scheme 5.2),[189] and represents key information for mechanistic interpretation of the intermediate observed that would be very difficult to obtain using other reaction monitoring techniques.

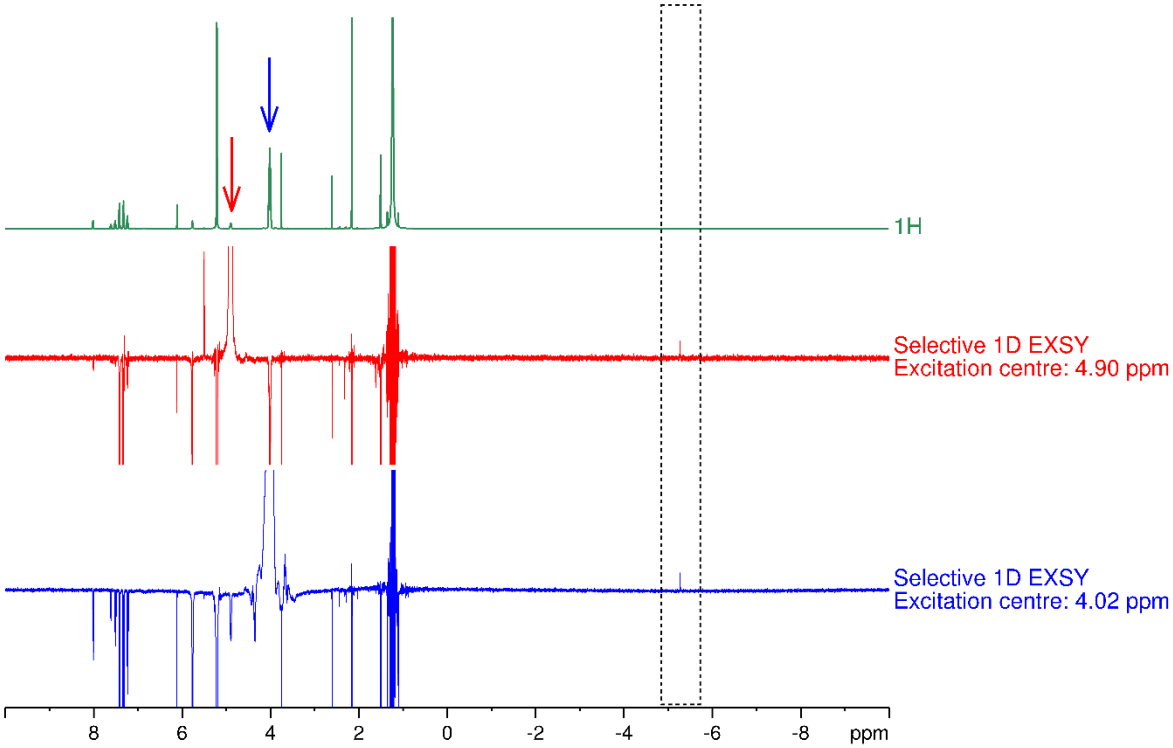

*Figure 5.8: Selective 1D EXSY NMR data showing excitation of isopropanol and 1-phenylethanol alcohol CH peaks, and the resulting exchange signal (-5.3 ppm) attributed to **3**. Negative-phase peaks are NOESY interactions of isopropanol and 1-phenylethanol respectively. (0.8 M acetophenone, 0.01 M KOH, 0.5 mL dry isopropanol, 20 mM **1**, 0.1 M 1,3,5-trimethoxybenzene (internal concentration reference), 25°C). Selective NOESY with gradient refocusing (128 scans, 2.18 s acquisition time, 2 s delay time, 80000 µs Gaussian excitation peak, 0.5 s mixing time).*

A selectively excited ^{1}H spectrum with good S/N could be acquired in less than one minute, and was found to be fully compatible with continuous flow conditions. The spectrometer used (see Experimental Section 5.4.1 for details) exhibited a linear signal response with increasing receiver gain, allowing for quantitative integration of the selectively excited peak (Figure 5.22). Thus, interleaving normal +10 – 0 ppm ^{1}H scans with selectively excited 0 – -10 ppm ^{1}H scans allowed us to track both the reaction progress as well the catalyst speciation under the same conditions in a single ^{1}H FlowNMR experiment, all the while giving the operator full control over the reaction conditions.

The versatility and power of this setup is demonstrated in the experiment shown in Figure 5.9, from which a wealth of information can be derived. Addition of **1** to the reaction vessel containing a stirred solution of KOH in isopropanol-H_8 lead to the rapid formation of a peak at -5.3 ppm indicative of **3**. This showed the activation of the precursor **1** to be fast and quantitative under the conditions applied, in line with the absence of any noticeable induction periods in the conversion profiles (Figure 5.2). As no substrate was present at this point, the catalyst resided exclusively in the reduced hydride form, however, with some noticeable

decrease in concentration over time (discussed below). Addition of acetophenone substrate (0.47 mL, 4 mmol) caused the concentration of the hydride complex **3** to drop to 54% of the concentration prior to substrate addition, indicating catalytic turnover taking place that involves cycling of the catalyst through the unsaturated intermediate **2** to give an experimentally determined K_{cat} = 0.85 close to the predicted value of 0.88 (Figure 5.6).

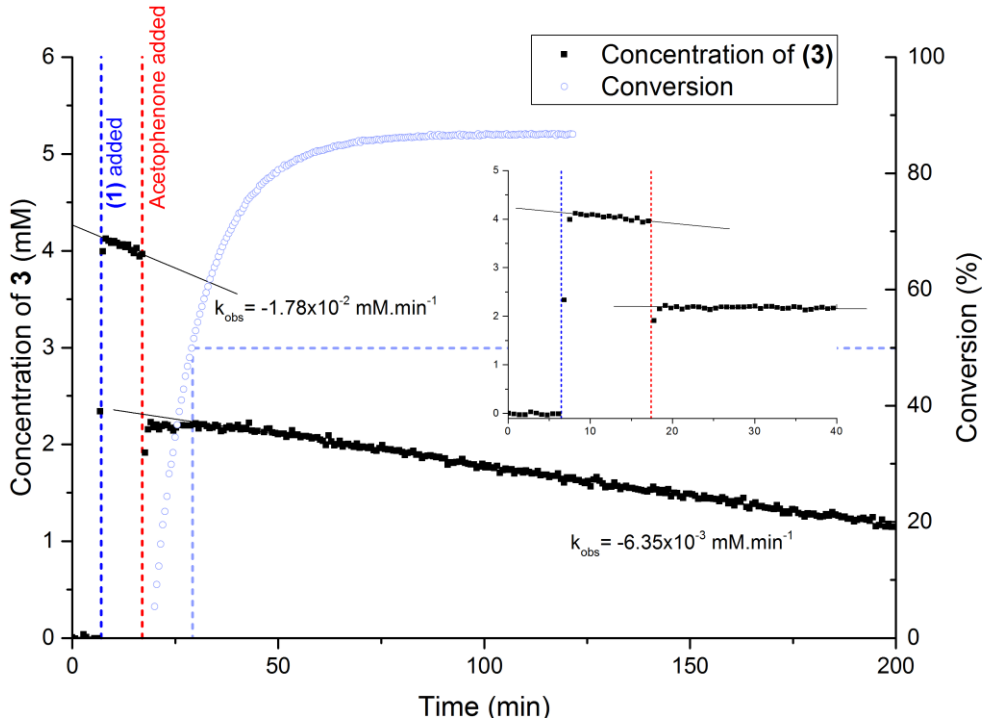

*Figure 5.9: Concentration profile of the hydride peak of **3** at -5.3 ppm, and conversion profile of acetophenone to (R)-1-phenylethanol, during the course of catalytic transfer hydrogenation of acetophenone to (R)-1-phenylethanol in flow at 4 mL/min (400 mM acetophenone, 10 mM KOH, 4 mM **1**, 9.5 mL dry isopropanol, 20°C). Selective excitation of **3** using a gradient spin echo pulse sequence with a shaped 180° pulse centred at -5.3 ppm (8 scans, 2 s acquisition time, 1 s delay time, 1600 µs Gaussian shaped pulse; spectra processed with 0.1 Hz exponential line broadening).*

The concentration of **3** remained steady during the initial stages of the reaction up to 50% conversion, after which another, slower decrease in concentration set in over the later stage of the reaction which was not predicted by the kinetic modelling of the simple mechanism (Figure 5.6). This correlated exactly with the deviation seen in the VTNA of the reaction progress profiles (Figure 5.3) and further indicated catalyst deactivation, consistent with the reduced reaction rates observed upon catalyst reuse (Figure 5.5b). Visual observation of gradual darkening of the reaction mixture over time suggested the eventual formation of Ru black (Figure 5.10), a transformation that was faster and more pronounced when the reaction was performed in air (Table 5.1), consistent with the known oxygen sensitivity of the activated catalyst.[83, 167]

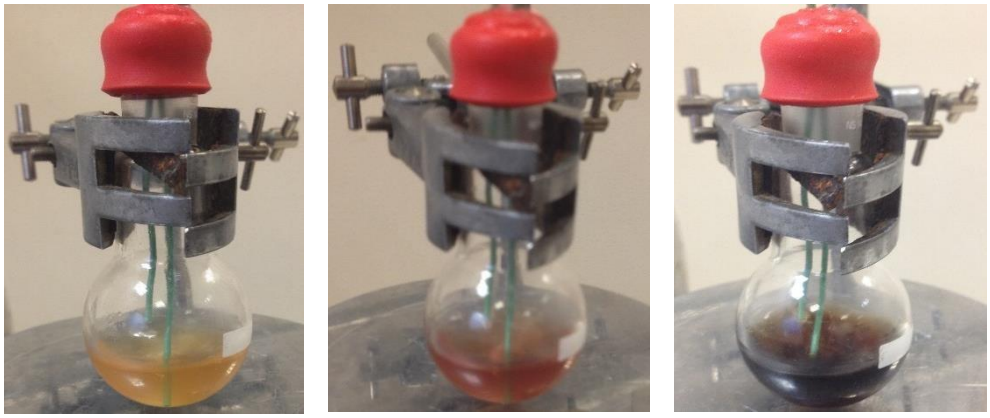

*Figure 5.10: Photographs of a) **1** dissolved in 0.01 M KOH solution in isopropanol, b) **1** dissolved in 0.01 M KOH solution in isopropanol with 0.4 M acetophenone added, c) **1** dissolved in 0.01 M KOH solution in isopropanol with 0.4 M acetophenone added after exposure to air.*

*Table 5.1: Conversion data for transfer hydrogenation of acetophenone to (S)-1-phenylethanol performed under inert atmosphere (Schlenk tube, Ar atmosphere) and with the reaction vessel exposed to air. (0.4 M acetophenone, 0.01 M KOH, 9.5 mL dry isopropanol, 2 mM **1**, 0.1 M 1,3,5-trimethoxybenzene (internal concentration reference), 20°C).*

Catalyst concentration (mM)	Reaction time (h)	Conversion under air	Conversion under inert atmosphere
4	2	84%	90%
2	4	80%	88%
1	6	67%	87%

The rate of catalyst deactivation being greatest before the addition of acetophenone substrate (Figure 5.9, inset) suggests the process to occur directly from the hydride intermediate **3**, which is the dominant ruthenium species prior to the system entering turnover. Upon taking up substrate turnover the rate of deactivation is decreased, as a smaller percentage of catalyst is present in the hydride form quickly interconverting to **2** and back.

The conventional TOL mechanism[97] shown in Scheme 5.2 does not account for catalyst deactivation, and kinetic modelling of the concentration of **3** over the course of the reaction showed that none of the decreases in the concentration of **3** observed experimentally are described by its rate law (Figure 5.11a). Introduction of a slow, irreversible catalyst deactivation pathway producing an inactive species **5** from **3** introduces a deactivation term to the rate law that decreases the amount of ruthenium available to productively cycle between **2** and **3**. Kinetic modelling of this expanded rate law reproduced the experimentally observed catalyst profile both before and after substrate addition (Figure 5.11b).

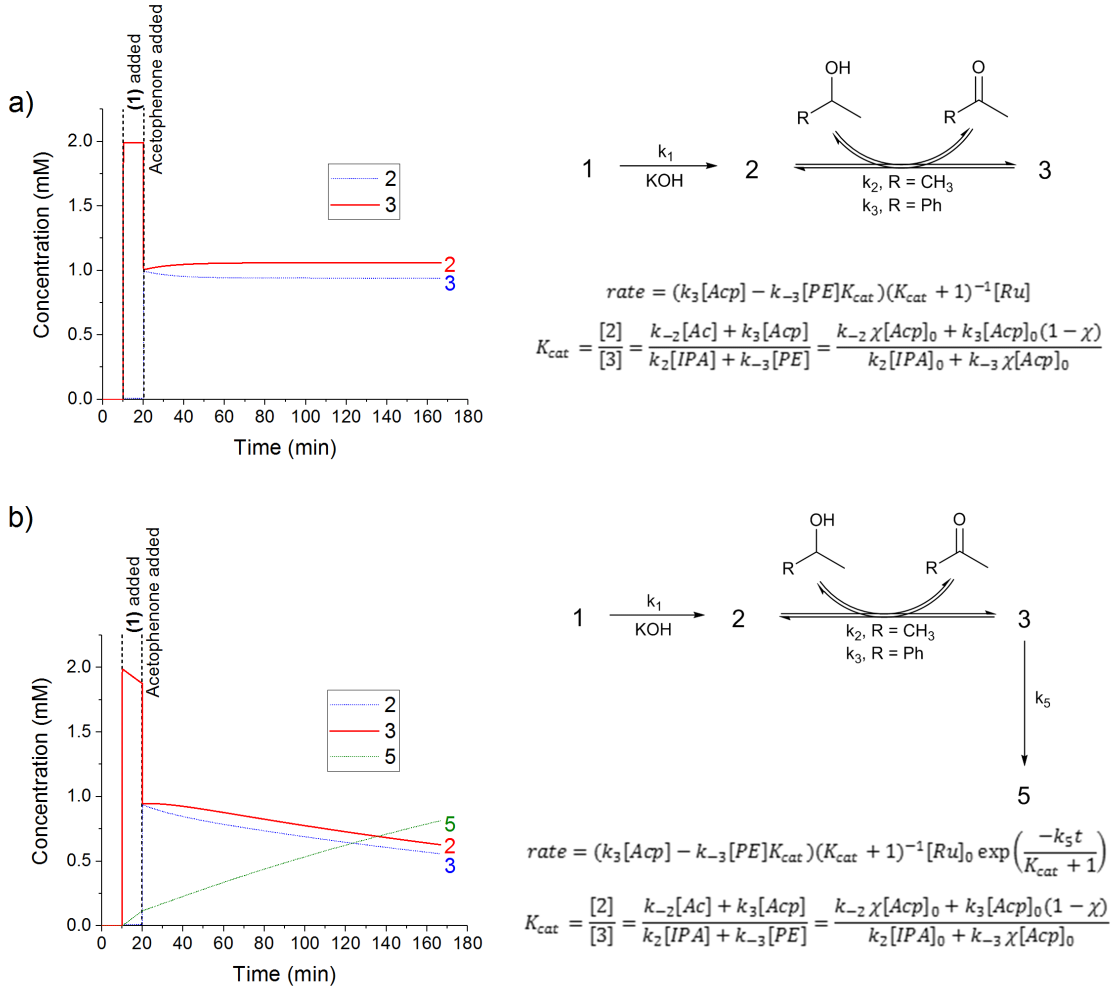

*Figure 5.11: Simulated catalyst distribution profiles for a): Conventional mechanism of catalytic transfer hydrogenation of acetophenone considering only active intermediates **2** and **3**; b): with inclusion of irreversible catalyst deactivation from **3**. See SI for details of simulation, kinetic parameters and derivation of rate laws.*

The auxiliary base, KOH in this case, is another important part of the catalyst system that is known to affect its performance.[97] In metal-ligand bifunctional transfer hydrogenation catalysis the external base is not thought to be involved in any in-cycle transformations,[99, 115] so in theory one equivalent per ruthenium suffices to initiate the catalysis. In practice however, various amounts of excess base are used to ensure fast and complete precursor activation.[90, 101, 115] As noted by others before,[166] we found that increasing base concentration also led to a decrease in the rate of product formation (Figure 5.12), with VTNA revealing an order of -¼ for the influence of excess KOH. [As hydroxide (pK_a 15.7) and isopropoxide (pK_a 16.5) are in equilibrium in solution this value may not easily be interpreted directly].

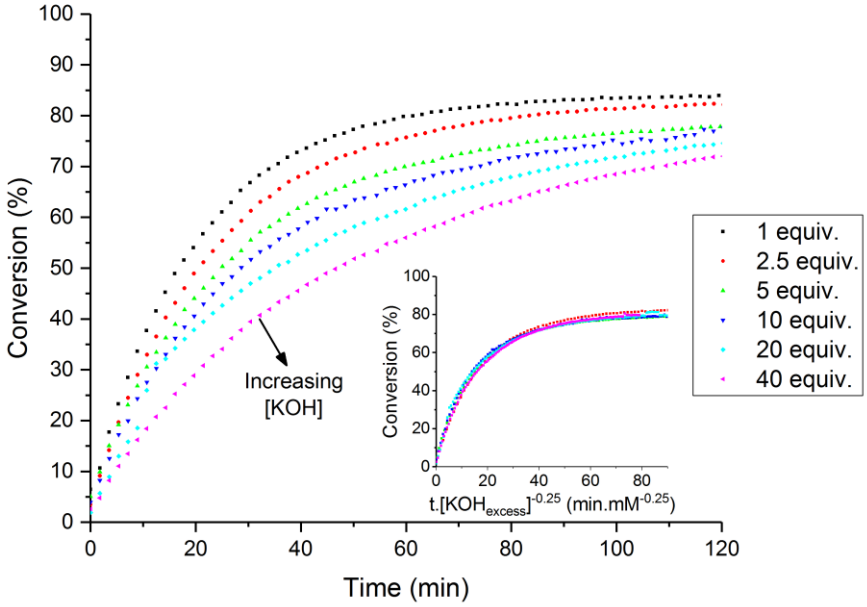

*Figure 5.12: Conversion plots for the catalytic transfer hydrogenation of acetophenone to (R)-1-phenylethanol (400 mM acetophenone, 2 mM **1**, 9.5 mL dry isopropanol, 20°C) with varying equivalents of KOH per [Ru] (1 scan, 1.64 s acquisition time, 1 s relaxation delay time). Inset: VTNA plot of conversion data, indicating a -0.25 order in excess KOH on reaction rate.*

This observation alone might suggest the involvement of KOH in the catalyst deactivation discussed above, however, monitoring the concentration of **3** during reactions with various amounts of excess base showed the rate of catalyst deactivation, as indicated by the slope of the decay of **3** over time, to be independent of base concentration (Figure 5.13). Instead, increasing base concentration led to a decrease in the amount of hydride present during turnover.‡‡ The fact that prior to entering catalysis the same amount of **3** is generated in all cases, with similar decreases due to progressive formation of **5**, strongly suggests a second, independent inhibition mechanism caused by the action of excess base on **2**.

‡‡ As shown by the rate law, a base-induced shift in K_{cat} would not lead to decreased product formation rates.

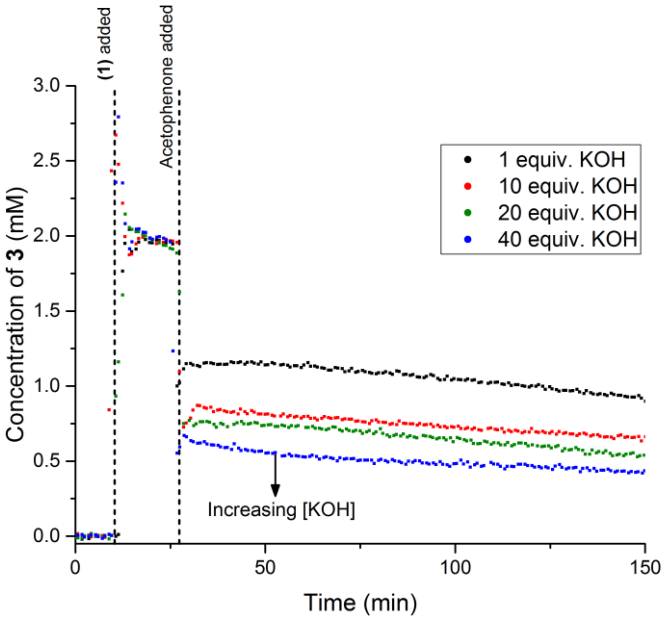

*Figure 5.13: Concentration profiles of the hydride peak of **3** at -5.3 ppm during the course of catalytic transfer hydrogenation of acetophenone to (R)-1-phenylethanol in flow at 4 mL/min (400 mM acetophenone, 2 mM **1**, 9.5 mL dry isopropanol, 20°C) with varying equivalents of KOH per [Ru]. Selective excitation of **3** using a gradient spin echo pulse sequence with a shaped 180° pulse centred on the hydride peak (20°C, 8 scans, 2 s acquisition time, 1 s delay time, 1600 µs Gaussian shaped pulse).*

This data therefore revealed the existence of another off-cycle ruthenium species **4** that further reduces the concentration of active ruthenium available to the catalytic cycle, causing the apparent decrease in concentration of **3** via consumption of **2**, thereby leading to the observed reduction in turnover rate (Scheme 5.3). Indeed, a classical Lineweaver-Burk analysis of reaction rates at different base loadings showed excess base to exert competitive inhibition behaviour on product formation (Figure 5.14).

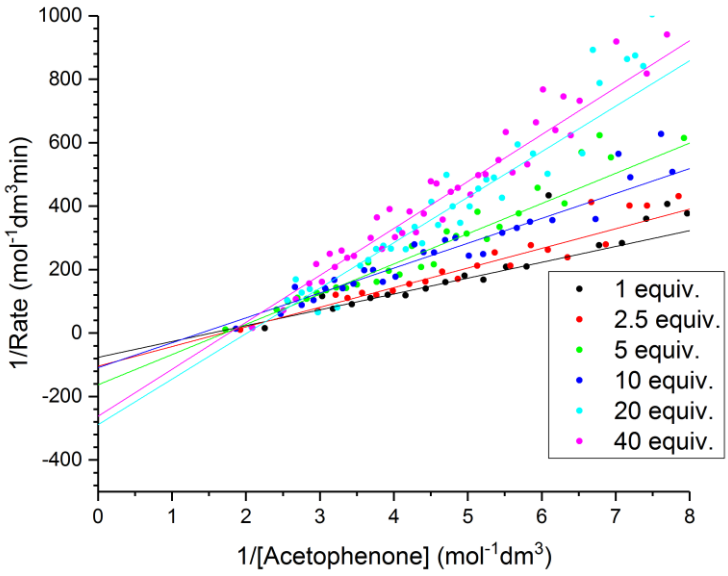

*Figure 5.14: Lineweaver-Burk analysis of catalytic transfer hydrogenation of acetophenone to (R)-1-phenylethanol (400 mM acetophenone, 2 mM **1**, 9.5 mL dry isopropanol, 0.1 M 1,3,5-trimethoxybenzene (internal concentration reference), 20°C) with varying equivalents of KOH per [Ru] (1 scan, 1.64 s acquisition time, 1 s relaxation delay time).*

A further expansion of the mechanism and associated rate law including off-cycle species **4** formed by reaction of **2** with base (either hydroxide or isopropoxide) enabled our kinetic model to accurately reproduce the effects of increasing base on both the product formation kinetics as well as the hydride concentration profiles (Figure 5.15). Without inclusion of **4** there is no difference between the simulated kinetic profiles at different base concentrations.

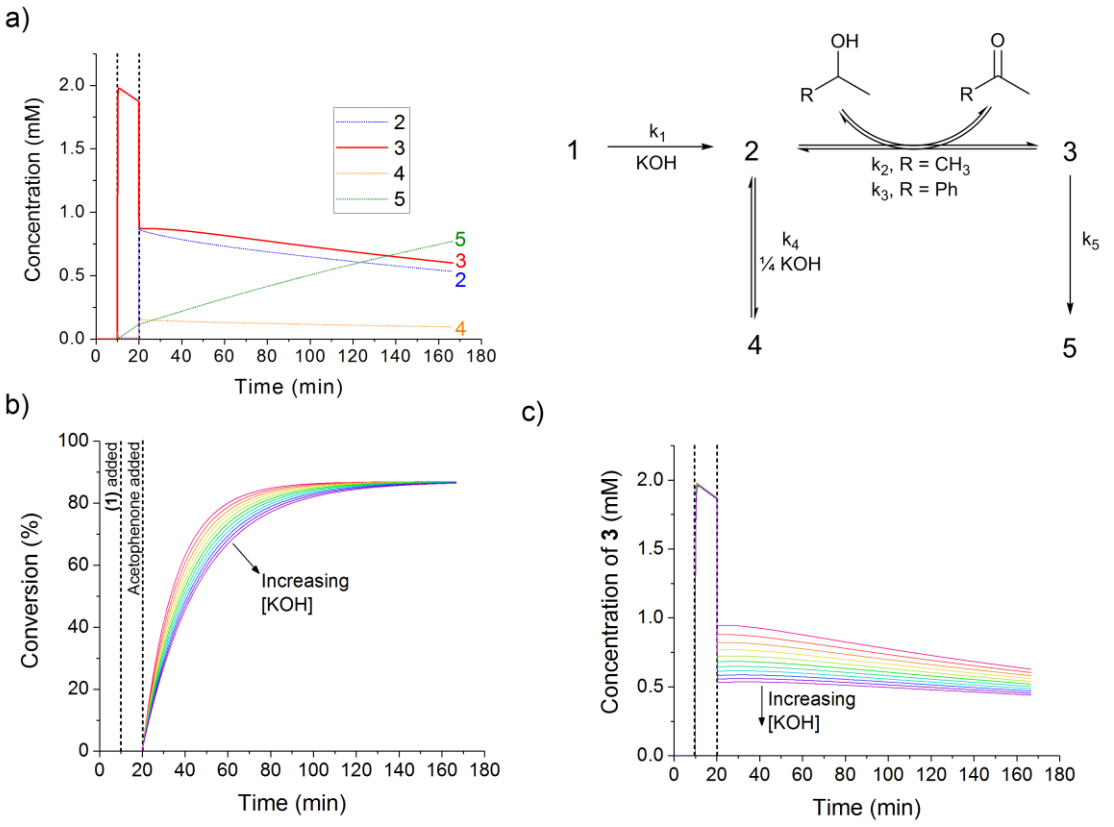

$$rate = (k_3[Acp] - k_{-3}[PE]K_{cat})\left(K_{cat} + 1 + \frac{k_4 K_{cat}[KOH]^{0.25}}{k_{-4}}\right)^{-1}[Ru]_0 \exp\left(-\left(K_{cat} + 1 + \frac{k_4 K_{cat}[KOH]^{0.25}}{k_{-4}}\right)^{-1} k_5 t\right)$$

$$K_{cat} = \frac{[2]}{[3]} = \frac{k_{-2}[Ac] + k_3[Acp]}{k_2[IPA] + k_{-3}[PE]} = \frac{k_{-2}\,\chi[Acp]_0 + k_3[Acp]_0(1-\chi)}{k_2[IPA]_0 + k_{-3}\,\chi[Acp]_0}$$

*Figure 5.15: Simulated reaction kinetics for proposed modification of the catalytic transfer hydrogenation mechanism of **1** (Scheme 5.3), including the effect of varying KOH concentration on a) catalyst speciation, b) reaction progress, and c) hydride profiles. See SI for details of simulation, kinetic parameters and derivation of rate laws.*

Combining catalyst inhibition by formation of **4** from **2** and catalyst deactivation by formation of **5** from **3** yields the modified reaction mechanism shown in Scheme 5.3, which accounts for all experimental observations describing both the reaction progress as well as catalyst speciation by its associated rate law.

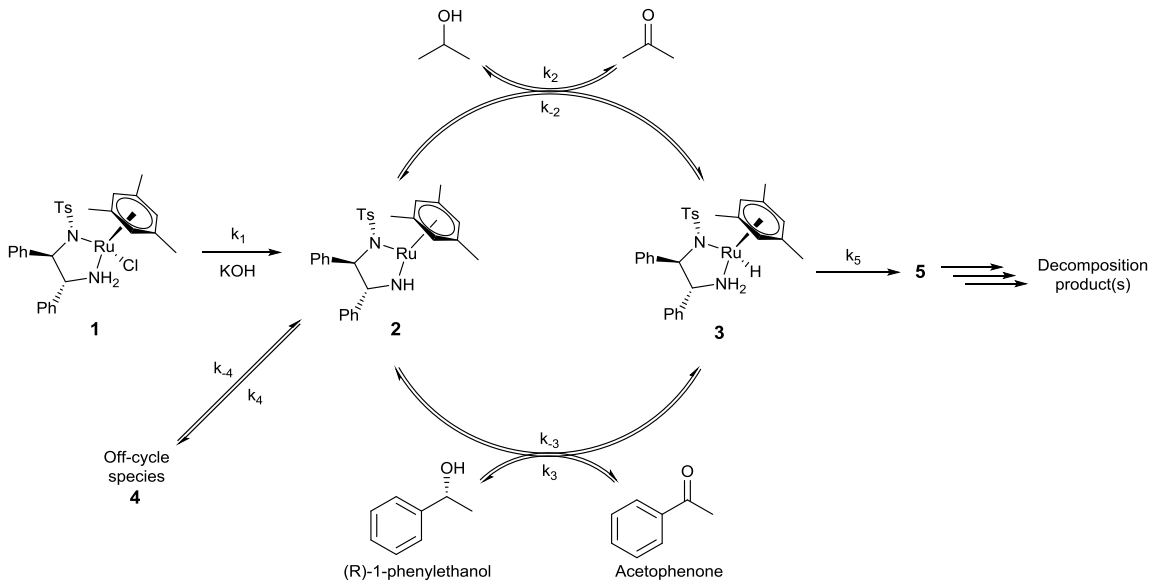

$$rate = (k_3[Acp] - k_{-3}[PE]K_{cat})\left(K_{cat} + 1 + \frac{k_4 K_{cat}[KOH]^{0.25}}{k_{-4}}\right)^{-1}[Ru]_0 \exp\left(-\left(K_{cat} + 1 + \frac{k_4 K_{cat}[KOH]^{0.25}}{k_{-4}}\right)^{-1} k_5 t\right)$$

$$K_{cat} = \frac{[2]}{[3]} = \frac{k_{-2}[Ac] + k_3[Acp]}{k_2[IPA] + k_{-3}[PE]} = \frac{k_{-2}\,\chi[Acp]_0 + k_3[Acp]_0(1-\chi)}{k_2[IPA]_0 + k_{-3}\,\chi[Acp]_0}$$

*Scheme 5.3: Expanded mechanism for catalytic transfer hydrogenation using **1** including base-induced formation of off-cycle species **4** from **2** and deactivation of **3** to **5** with the associated rate law.*

Once the various catalyst deactivation phenomena have been quantitatively identified, they can be factored into the RPKA analysis to check whether they now accurately describe the global kinetic behaviour of the system.[175, 188] Including the deactivation rates from our expanded rate law (Scheme 5.3) in the VTNA of the reaction profiles at different Ruthenium loadings (Figure 5.3) indeed produced excellent overlay across the entire profile (Figure 5.16).

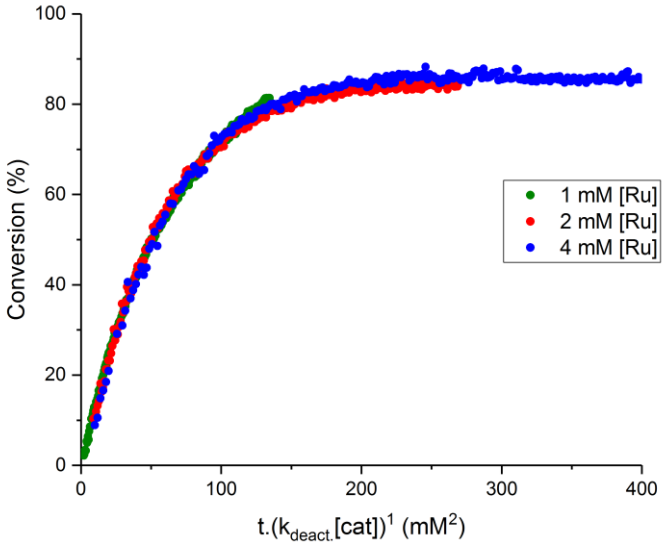

*Figure 5.16: Variable Time Normalisation Analysis (VTNA) plot for the catalytic transfer hydrogenation of acetophenone to (R)-1-phenylethanol with various amounts of **1**, adjusted for experimentally observed catalyst deactivation (Figure 5.9) (400 mM acetophenone, 10 mM KOH, 9.5 mL dry isopropanol, 20°C).*

The final piece of information required to improve the catalysis is understanding the molecular origin of the deactivation/inhibition events identified. In this case, based on the kinetic evidence of competitive base inhibition, off-cycle species **4** are most likely simple base adducts of **2** (Scheme 5.4). Indeed, an earlier computational study by Noyori *et al.* proposed the reversible formation of stable alkoxide complexes by reaction of **2** with alcohols or other protic compounds potentially acting as off-cycle reservoirs of **2** in the catalytic cycle.[99] Similarly, the related formate adducts are known and have been shown to inhibit transfer hydrogenation catalysis from formic acid / triethylamine mixtures.[116, 165] Thus, although the structures of **4** are currently not known with certainty, (all of our attempts at detecting or isolating various base adducts of **1** or **2** have so far failed, and no structurally characterized examples have been reported in the literature either) the fact their formation may be limited simply by using a minimum amount of base (i.e. stoichiometric in **1**) together with the observation that any excess base (if present) does not contribute to other deactivation phenomena during the course of the reaction is sufficient information for optimal use of **1** with regards to the amount of base added.

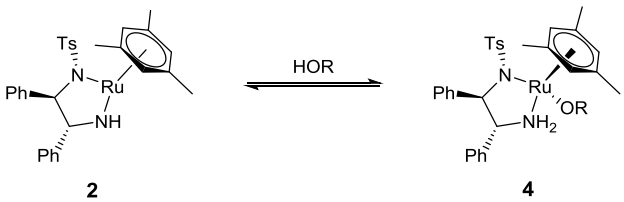

2 **4**

*Scheme 5.4: Formation of base adduct complexes **4** from the unsaturated intermediate **2**. For isopropanol or 1-phenylethanol these would be in-cycle, and for KOH/H_2O off-cycle.*

The instability of **3** that leads to gradual catalyst decomposition is more intriguing, as it appears to be an inherent feature of the catalyst that limits its effective turnover number and progressively erodes its enantioselectivity over time (Figure 5.5b). Complete ligand loss and formation of ruthenium black has been observed before in this chemistry,[167] however, as we have found the rate of this multi-step degradation pathway to be first order in **3** (Figure 5.17, see also Figure 6.5 for deactivation profile over longer time) its rate-determining step (as described by k_5) must involve a key transformation of the molecular hydride intermediate.

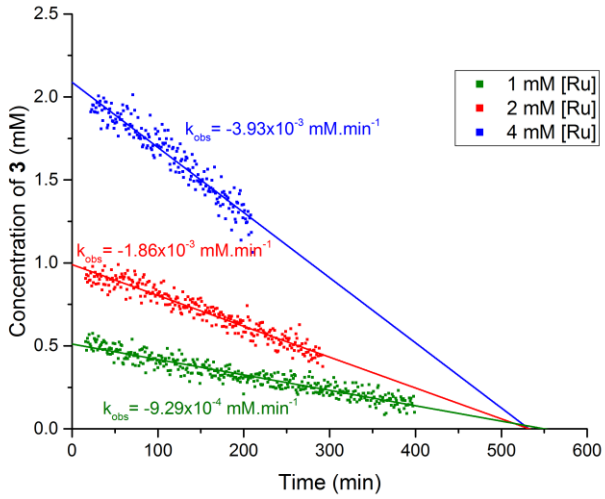

*Figure 5.17: Concentration profiles of the hydride peak at -5.3 ppm attributed to **3** during the course of catalytic transfer hydrogenation reaction of acetophenone to 1-phenylethanol in flow at 4 mL/min (400 mM acetophenone, 10 mM KOH, 9.5 mL dry isopropanol, 0.1 M 1,3,5-trimethoxybenzene (internal concentration reference), 20°C, 16 scans, 1.64 s acquisition time, 1 s delay time), showing first order deactivation of **3** at varying catalyst loadings. Selective excitation of **3** using a gradient spin echo pulse sequence with a shaped 180° pulse centred on the hydride peak (20°C, 24 scans, 1 s acquisition time, 1 s delay time, 880 µs Gaussian shaped pulse).*

In a typical ^{1}H FlowNMR experiment carried out under literature conditions, most ligand signals were obscured by dominant solvent, substrate and product peaks. Various NMR strategies for resolving minor signals underneath dominant peaks exist (including advanced spectral deconvolution,[49, 51-52] multiple solvent suppression,[9, 190] and 2D experiments with T_1, T_2 or diffusion filtering[191-193]), these may be challenging in cases where multiple, *a priori* unknown minor signals are to be detected and quantified in the vicinity of much more intense peaks. Chemical modification of the system by way of isotopic labelling is an alternative strategy for discriminating different species or functionalities using different NMR frequencies. In this case perdeuterated solvent is commercially available, so using this with the standard (i.e. non-deuterated) Noyori catalyst moves these dominant resonances into the ^{2}H domain, allowing multiple catalyst signatures to be resolved in the ^{1}H spectra (Scheme 5.5).

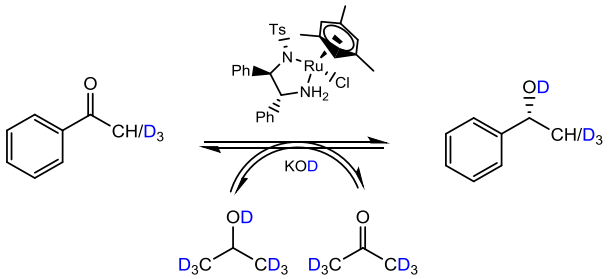

*Scheme 5.5: Catalytic asymmetric transfer hydrogenation of acetophenone to (R)-1-phenylethanol with RuCl[(R,R)-TsDPEN](mesitylene) **1** in isopropanol-d_8 solution.*

As mentioned above, deuteration of the solvent entailed a significant composite kinetic isotope effect of $k_H/k_D = 5.85$ on the reaction (Figure 5.18) proceeding through a series of X-H/D cleavage steps (X = C, O, Ru) each expected to result in a primary KIE.

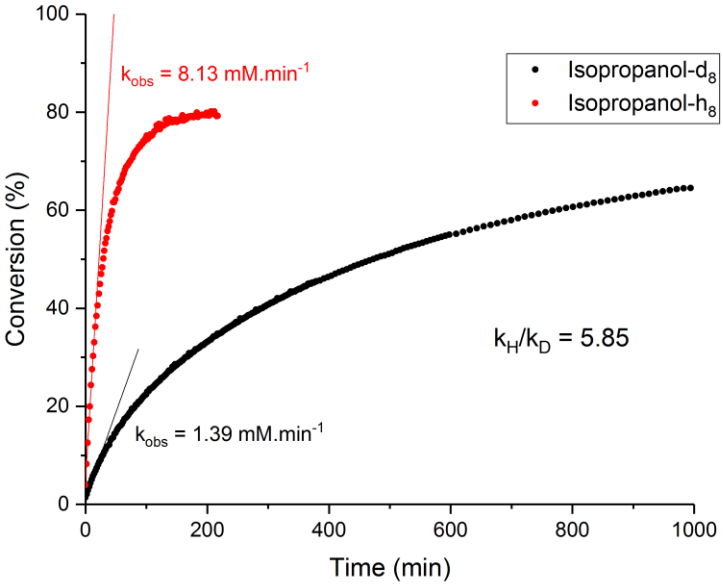

*Figure 5.18: Kinetic data for transfer hydrogenation reaction of acetophenone to 1-phenylethanol perfromed in Isopropanol-h_8 or Isopropanol-d_8 demonstrating a strong kinetic isotope effect of 5.85, (0.4 M acetophenone, 0.02 M KOH, 9.5 mL isopropanol, 2 mM **1**, 0.1 M 1,3,5-trimethoxybenzene (internal concentration reference), 20°C). Selective excitation using spin echo shaped pulse sequence (8 scans, 2 s acquisition time, 1 s delay time, 1600 µs Gaussian excitation peak).*

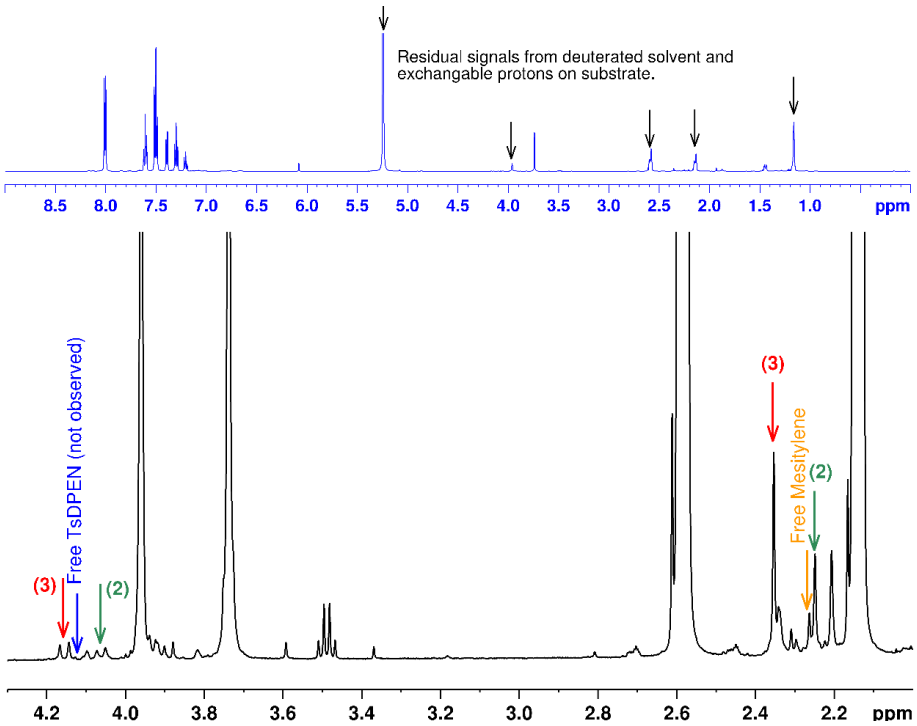

*Figure 5.19: Sample spectrum for the catalytic transfer hydrogenation reaction of acetophenone to (R)-1-phenylethanol in flow at 2 mL/min, showing the position of TsDPEN and mesitylene peaks of **2** + **3**, along with free TsDPEN and free mesitylene as determined by spiking reaction mixture. (2 mM **1**, 400 mM acetophenone, 20 mM KOD, 9.5 mL isopropanol-d_8, 20°C, 16 scans, 1.64 s acquisition time, 1 s delay time).*

Furthermore, rapid exchange of the acetophenone CH_3 protons with deuterium was observed under the conditions applied (Figure 5.19), as expected for an enolisable ketone. More importantly, however, interleaving ^1H and ^2H FlowNMR acquisitions on this partially deuterated system allowed us to follow the fate of the mesitylene and TsDPEN ligands bound to the ruthenium over the course of the reaction. As previously seen from the profiles of **3** using selective excitation of the hydride signal, the concentrations of both **2** and **3** were observed to decrease over time as the catalysis converged to equilibrium (Figure 5.20). Whereas virtually all detectable TsDPEN signals originated from metal-bound species, the continuous liberation of mesitylene from the ruthenium centre was clearly observed (as confirmed by spiking with authentic samples at the end of the reaction).

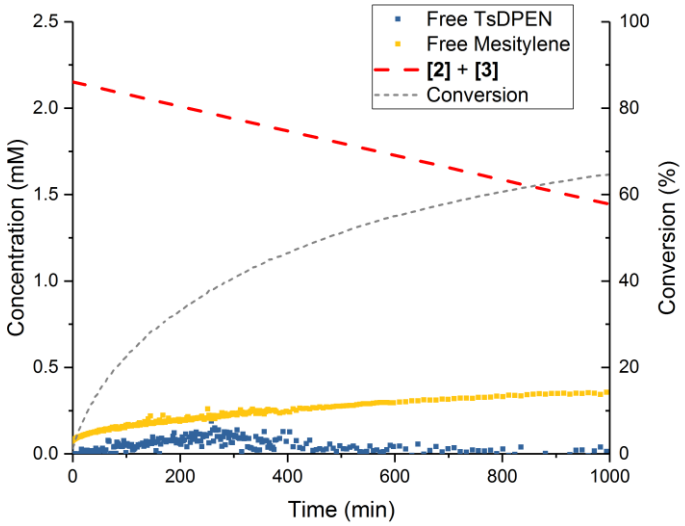

*Figure 5.20: Concentration profile of combined **2** + **3** (determined from TsDPEN CH peaks), free TsDPEN and free mesitylene during the course of catalytic transfer hydrogenation reaction of acetophenone to (R)-1-phenylethanol in flow at 2 mL/min (2 mM **1**, 400 mM acetophenone-d_8, 20 mM KOD, 9.5 mL isopropanol-d_8, 20°C). Essentially no free TsDPEN signals were observed throughout the reaction, the slight scatter between 100 and 500 minutes stems from tailing of other resonances into the chemical shift range of free TsDPEN (see Figure 5.19 for example spectrum).*

The liberation of free mesitylene kinetically correlated with the onset of catalyst deactivation, showing it to be the RDS in k_5. This observation clearly shows loss of the arene ligand to be the Achilles' heel of these widely used (arene)Ru(TsDPEN) transfer hydrogenation catalysts. When **3** was heated or left in isopropanol solution for prolonged periods of time, additional hydride peaks were observed to form at the expense of **3** in the ^{1}H NMR spectra (Figure 5.21). Although their multitude and low abundances precluded more comprehensive characterisation, their characteristic chemical shift range (-10 to -20 ppm as compared to -5.3 ppm for **3**) and T_1 values (4-5 sec as compared to 0.25 sec for **3**) are in good agreement with their formulation as hydride-bridged dimers.[194]

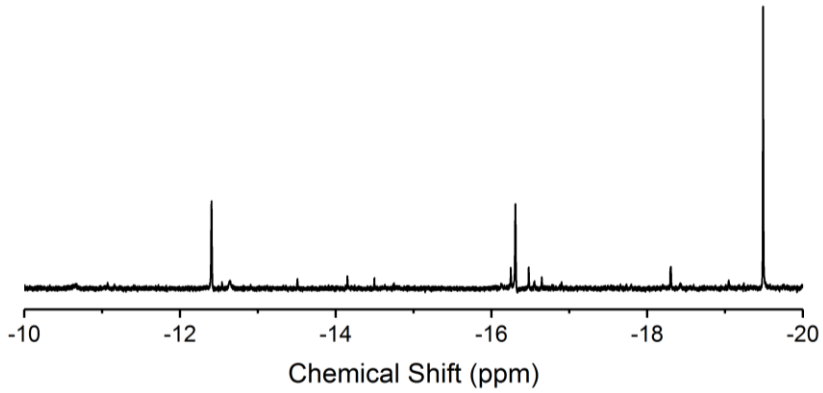

*Figure 5.21: Sample ^{1}H selective excitation NMR spectrum of **1** heated in isopropanol in the presence of excess KOH for 6 h. NB. Due to wide excitation range, signals are non-quantitative. Peak intensities of different species observed to vary over time.*

We therefore conclude that catalyst deactivation from **3** occurs by way of loss of the mesitylene ligand to form hydride bridged dimeric ruthenium species, which then oxidise further to give ruthenium nanoparticles as the final catalyst degradation product (Scheme 5.6). Although an η^6 L_3 arene ligand may be expected to be more strongly bound to the metal centre than an η^2 LX amino/amido ligand in terms of coordination chemistry principles, the situation is clearly different in catalysis where many reagents present in large excess repeatedly push the catalyst through a series of multiple species. Reversible hapticity shifts of the bound arene have been discussed in the context of the mechanism of transfer hydrogenation before (i.e. in the interconversion of **2** and **3**),[97] whereas the TsDPEN ligand is only required to switch between an LX and an X_2 η^2 coordination mode throughout the cycle.

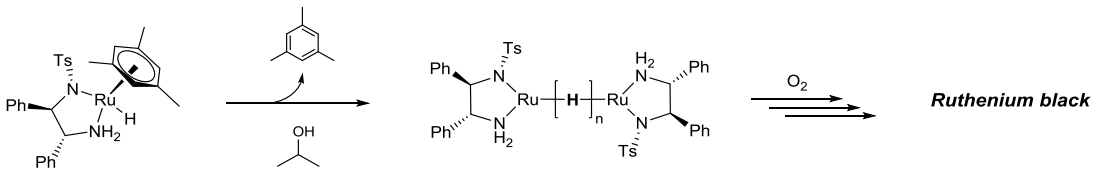

3 **5**

*Scheme 5.6: Proposed mode of catalyst deactivation by formation of hydride-bridged dimers **5** (Figure 5.21) from **3** as first step leading to complete decomposition into Ru black (n = 1, 2, 3 with remaining coordination sites occupied by solvent).*

Our finding of arene loss leading to catalyst deactivation is consistent with the increased stability reported for Noyori-type Ru catalysts containing an arene ring that is tethered to the chiral TsDPEN ligand,[185, 195-198] and similar ligand loss and formation of hydride-bridged dimers have been reported for related iridium-based transfer hydrogenation catalysts.[170, 199-200] Linking ligands together to limit catalyst decomposition by way of de-coordination is a well-known strategy in organometallic chemistry,[68] but being able to directly follow the fate of the different ligands bound to the catalyst by *operando* NMR spectroscopy to identify the point of failure in the catalyst coordination sphere during turnover allows more targeted ways of improving catalyst performance.

5.3.3 Conclusions

We have shown high resolution FlowNMR spectroscopy to be a powerful non-invasive tool for studying air-sensitive transition metal catalysis under working conditions in real time. Using variable time normalization analysis, the data is particularly well suited for reaction progress kinetic analysis as a straightforward way of obtaining relevant kinetic information of the reaction system. Highly enantioselective acetophenone transfer hydrogenation from basic isopropanol by Noyori's [(mesitylene)(TsDPEN)RuCl] catalyst system has been shown to follow ideal first-order kinetics up to ~50% conversion, after which catalyst deviations became apparent in the RPKA. By kinetically correlating reaction progress with the concentration of Ru-H intermediate **3** during transfer hydrogenation catalysis initiated by sequential addition of reagents, and comparing it with modelled profiles derived from the rate law of the reaction, we were able to find evidence for two independent catalyst deactivation/inhibition events: deactivation of hydride intermediate **3** caused by gradual loss of the arene ligand, and inhibition of unsaturated intermediate **2** by excess base. Inclusion of both pathways into the reaction mechanism resulted in a kinetic model that accurately reproduces all experimental data, and accounts for observations of the effect of varying base concentration on conversion. These new mechanistic insights gained into the widely used hydrogen transfer chemistry mediated by (arene)Ru(TsDPEN) - type complexes provide a basis for devising strategies to combat catalyst decomposition, and hopefully stimulate wider use of *operando* spectroscopy for a better understanding of the dynamic and interlinked processes operational in many other examples of solution phase catalysis.

5.3.4 Acknowledgements

This work was supported by a Research Grant from the Royal Society (Y0603), the EPSRC Centre for Doctoral Training in Sustainable Chemical Technologies (EP/L016354/1), the Dynamic Reaction Monitoring Facility at the University of Bath (EP/P001475/1), and Bruker UK Ltd. UH acknowledges the Centre for Sustainable Chemical Technologies for a Whorrod Research Fellowship and the Royal Society for University Research Fellowship (UF160458). The authors would like to thank Dr Catherine Lyall, Dr Matthew Jones and Dr Antoine Buchard from the University of Bath as well as Dr Antonio Zanotti-Gerosa from Johnson Matthey for their support and assistance with this project, and Dr Jordi Burés from the University of Manchester for many useful discussions.

5.3.5 Conflict of interest statement

AC is an employee of Bruker UK Ltd., manufacturer and supplier of NMR hard- and software solutions that have been used in this research. The other authors declare no competing financial interest.

5.4 EXPERIMENTAL

5.4.1 FlowNMR apparatus

Reactions were carried out in a standard glass round-bottomed flask, with a double-piston HPLC pump (JASCO PU-2085 Plus) with a semi-micro pump head used to circulate the mixture around the system to an InsightMR flow tube (Bruker) located within the spectrometer (Bruker 400 or 500 MHz Avance II+ Ultrashield equipped with either a broadband (BBO) probe or a nitrogen cooled Prodigy CryoProbe). In order to minimise the delay time between a change occurring in the reaction vessel and the arrival of the sample to the spectrometer for detection it is desirable to ensure that the volume of the tubing connecting the reaction vessel to the spectrometer is minimised, therefore narrow diameter polyetheretherketone (PEEK) tubing (0.762 mm i.d., Upchurch Scientific) was used. The PEEK tubing offers high chemical and mechanical stability (pH 0 – 14, -50 – 100 °C, >300 bar) along with good flexibility and low gas permeability. For reactions at atmospheric pressure standard rubber seals were used to connect the tubing with the reaction solution, and found effective for air-sensitive systems over prolonged times (>10 hours) when sealed off with silicone grease.

All other connections were made using standard HPLC-type PEEK connectors (Upchurch Scientific), allowing the apparatus to be purged with inert or reactive gases as required. All equipment was positioned on a mobile trolley made of plastic (Rubbermaid), allowing the equipment to be transported between the laboratory and the spectrometer as required. The trolley and apparatus were able to be placed at a minimum distance of 0.5 m from the shielded magnet without experiencing adverse magnetic effects.

The total volume of the flow apparatus was 3.7 mL, and the volume of the NMR flow cell was approximately 0.5 mL, corresponding to a mean residence time within the detection region of 8 seconds at a flow rate of 4 $mLmin^{-1}$.[160]

Data acquisition was performed without lock and with shimming performed using automated ^{1}H shimming routines, followed by manual fine tuning. Data processing was performed using commercially available software.

All samples were prepared using reagents and catalyst purchased from Sigma Aldrich or Alfa Aesar at reagent grade or higher. Acetophenone was distilled and isopropanol degassed prior to use. All other reagents were used without further purification.

5.4.2 Receiver Gain calibration

Since selective excitation experiments are recorded at significantly higher receiver gain than standard proton spectra, it is necessary to determine a compensation factor to allow comparison between peaks on the two different spectra.

Relative integral area of the methyl peak of a 100 $mgdm^{-3}$ solution of 1,3,5-trimethoxybenzene solution in isopropanol were recorded at a range of receiver gains, resulting in a calibration factor of 1.033 to transform integral values recorded at different receiver gains.

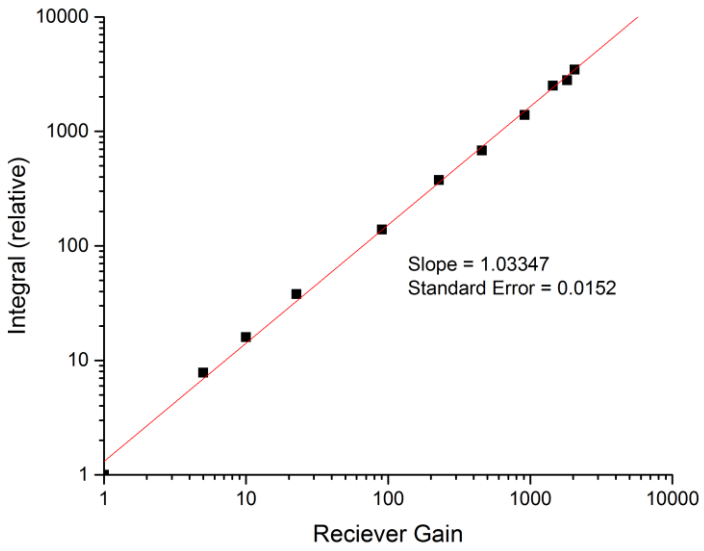

Figure 5.22: Receiver gain calibration for Bruker 500 MHz Avance II+ Ultrashield spectrometer with broadband BBO probe. 100 $mgdm^{-3}$ 1,3,5-trimethoxybenzene in isopropanol calibration standard. Selective excitation using spin echo shaped pulse sequence (8 scans, 2 s acquisition time, 1 s delay time, 1600 µs Gaussian excitation peak, 20°C).

In order to allow comparison between the integral of the hydride peak recorded using selective excitation and the 1,3,5-trimethoxybenzene concentration reference, the integral of the hydride peak is reduced to give a Reduced Integral Value (RIV) according to the following equation:

Equation 1: $$RIV = \frac{I_{hydride} \times RG_{normal} \times 1.033}{RG_{hydride}}$$

Where $I_{hydride}$ = Integral area of hydride peak, RG_{normal} = receiver gain for selective excitation experiment of internal standard (e.g. TMB), $RG_{hydride}$ = receiver gain for selective excitation experiment of hydride.

The concentration of the hydride species can then be calculated by comparison to a selective excitation experiment of the internal reference (such as 1,3,5-trimethoxybenzene (TMB)) of known concentration:

Equation 2: $$[Hydride] = RIV \times \frac{[TMB]}{I_{TMB}/Number\ of\ protons\ associated\ with\ TMB\ peak}$$

This calculation process was tested on a standard sample containing known concentrations of acetophenone and 1,3,5-trimethoxybenzene in isopropanol solvent and the accuracy of component concentrations calculated with this method compared to actual concentrations of components was found to have an error 3.6%.

5.4.3 NMR acquisition parameters

Unless specified in figure captions, the following parameters were used for the acquisition of all NMR data:

^{1}H selective excitation and ^{1}H (non-selective) spectra acquisition were interleaved with selective excitation spectra acquired every 30 seconds and non-selective spectra acquired every 60 seconds.

5.4.3.1 ^{1}H (without selective excitation)

^{1}H spectra for the determination 1-phenylethanol, acetophenone, acetone and 1,3,5-trimethoxybenzene concentration were acquired using a standard 30° pulse sequence, with a 1.64 s acquisition time and 1 s relaxation delay time, using a single transient.

5.4.3.2 ^{1}H Selective excitation

^{1}H selective excitation spectra for the determination of the concentration of catalyst species **3** were acquired using a 1D double spin echo pulse sequence with gradient refocusing. A Q3 gaussian 180° pulse with a pulse length of 2272 μs (approximately 3 ppm width), centred on -5.5 ppm was used for selective refocusing with a 200 μs gradient recovery time. 8 transients were acquired with a 2 s acquisition time and 1 s relaxation delay time.

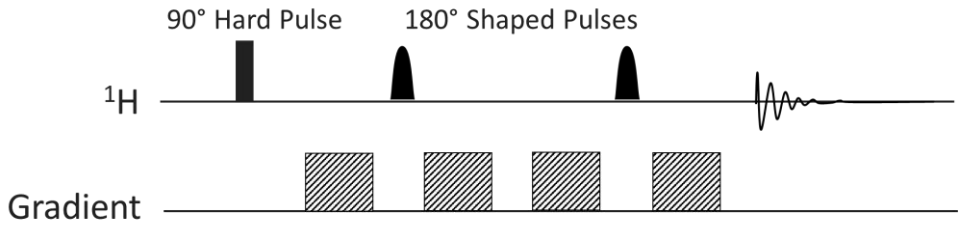

Figure 5.23: Schematic illustration of double spin echo pulse sequence with gradient refocusing

5.4.3.3 ^{1}H EXSY

^{1}H selective exchange spectroscopy (EXSY) spectra were carried out with a 1D spin echo pulse sequence with gradient refocusing using a gaussian shaped selective 180° pulse with a length of 80 ms, centred on either 4.90 or 4.02 ppm. 128 transients were acquired with 2.18 s acquisition time, 2 s relaxation delay time and 0.5 s NOESY mixing time.

5.4.4 Transfer hydrogenation of acetophenone

The FlowNMR apparatus was purged with dry nitrogen for 30 min to remove any traces or air or moisture. The apparatus was filled with 8.53 mL of a stock solution of potassium hydroxide (anhydrous, 0.112 g, 2 mmol) and 1,3,5-trimethoxybenzene (3.364 g, 0.02 mol) in dry, degassed isopropanol (200 mL).

The flow tube was then inserted into the spectrometer and automated shimming and tuning routines were performed. Best results were obtained if automated shimming and tuning was performed on static samples, however acceptable results were still obtained in flow. Frequency lock was switched off when using non-deuterated solvents, and shimming performed on proton peaks. Manual fine tuning of X and Y shims was often required to get a good peak line width. Spectra of the reagents were recorded without flow and again at the flowrate desired for the reaction. Comparison of the integral area of the peaks in each spectrum was used to calculate a correction factor for each reagent peak. (I = peak integral, CF = correction factor).[160]

Equation 3: $$I_{Corrected} = CF \times I$$

Equation 4: $$CF = \frac{I_{Static}}{I_{Flow}}$$

With the sample flowing, data acquisition was started using an automated kinetic routine or dedicated reaction monitoring software, with spectra recorded at specified time intervals. (4 s delay, 1.64 s acquisition time, 30° pulse, 4 scans) and a concentrated solution of the catalyst (R,R)-(TsDPEN)mesitylruthenium chloride (12 mg, 0.02 mmol) dissolved in 1 mL of the stock solution was added. To start the reaction, acetophenone (0.47 mL, 4 mmol) was added.

At the end of the reaction, or if intermediates of interest were observed, additional spectra were recorded with and without flow, and correction factors were calculated for the intermediate or product peaks, which were applied to each spectrum to give the final peak areas for calculation of species concentration and plotting of kinetic data.

Concentrations of species were determined by peak integrals and referenced to 1,3,5-trimethoxybenzene internal standard.

For the reverse reaction (Figure 4a), acetophenone was substituted with racemic 1-phenylethanol (0.47 mL, 4 mmol) and isopropanol was substituted with acetone (9.5 mL). For the catalyst stability test (Figure 4b), additional acetophenone (0.47 mL, 4 mmol) was added

after 100 minutes. For experiments with varying concentration of base, acetophenone or catalyst, the above method was adjusted with the appropriate quantities of each reagent.

Kinetic Isotope Effect (KIE) and deactivation studies (Figures 13 and S7) were performed using the method described above, with isopropanol replaced with perdeuterated-isopropanol and potassium hydroxide replaced with potassium deuteroxide.

EXSY data (Figure 5.8) was acquired on a sample of **1** (4.6 mg, 0.0074 mmol) and acetophenone (0.05 mL, 0.4 mmol) in 0.5 mL of a stock solution containing 1,3,5-trimethoxybenzene (0.1 M) and potassium hydroxide (0.01 M) in isopropanol (non-deuterated).

5.4.5 Catalyst Intermediate Synthesis[4]

5.4.5.1 Unsaturated intermediate (2)

Unsaturated intermediate **2** was prepared according to a modified literature procedure.[115] Noyori catalyst (80 mg, 0.13 mmol) was dissolved in dry DCM (5 mL) to give a bright orange solution. A solution of potassium tert-butoxide (0.13 mL, 1M in THF, 0.13 mmol) was added, causing the solution to immediately turn deep purple in colour. The mixture was stirred for 5 mins at room temperature before filtering. The purple filtrate was evaporated under vacuum and the resulting purple solid dried overnight under vacuum to give a purple powder: Isolated yield: 0.029 g, 36%. λ_{max} = 565 nm, ϵ_{565} = 1377 $mol^{-1}dm^3cm^{-1}$.

5.4.5.2 Hydride intermediate (3)

Hydride intermediate **3** was prepared according to a modified literature procedure.[115] Unsaturated intermediate **2** was dissolved in dry isopropanol (5 mL) to give a yellow-brown solution. Solvent was evaporated under vacuum to give a brown powder. ^{1}H NMR (400 MHz) δ ($CDCl_3$): -5.5 (s, 1H).

5.4.6 Chiral separation of enantiomers

HPLC analysis carried out using an Agilent 1260 Infinity II LC instrument fitted with a Chiracell OD-H column (Daicell chiral, 250 mm length, 4.6 mm diameter, 5 μm particule size). Samples were eluted with a 9:1 Hexane:IPA solvent mixture at 1 mL/min with detection using a UV detector at 254 nm. The (R)-1-phenylethanol peak was observed after 7.6 minutes, and (S)-1-phenylethanol at 8.2 minutes. Enantiomeric excesses were calculated using Equation 5:

Equation 5: $$\%ee = \frac{[S]-[R]}{[S]+[R]} \times 100$$

5.5 COMMENTARY

5.5.1 Variation of base

The role of the base in generating off-cycle species has been discussed above (Figure 5.12). In all cases potassium hydroxide was used, as this is was the base originally used by Noyori,[90] and remains one of the most commonly used bases for catalyst activation in isopropanol solution.

Due to the respective pK_a values of HO^- and $(CH_3)_2CHO^-$ (Table 5.2), an equilibrium will exist between the two species in solution, which may explain the fractional –0.25 reaction order observed for KOH (Figure 5.12).

Table 5.2: pK_a values of selected bases in water. Values from March, 2007.[201] a= Value from Hiyama, 2011 .[202]

Conjugate base	pKa
$HCOO^-$	3.77
$C_6F_5O^-$	5.50[a]
$C_6H_5O^-$	9.95
$(CH_3CH_3)_3N$	10.8
CH_3O^-	15.5
HO^-	15.7
$(CH_3)_2CHO^-$	16.5
$(CH_3)_3CO^-$	17.0

Some studies have also indicated that the counter ion may also play a role in mediating the hydrogen transfer reaction.[97, 203] This 'potassium effect' has been studied in the $RuCl_2$(BINAP)(DPEN) type catalysts, where a significant increase in activity is observed for potassium over other counter ions.[81, 102, 104, 119] The same acceleration effect of potassium is not observed in the RuCl(TsDPEN)(arene) catalysts, where increasing the concentration of base decreases reaction rate (Figure 5.12).

To test the effect that choice of base has on reaction rate and catalyst speciation, the reaction was repeated using ^{t}BuONa and ^{t}BuOK in place of KOH (Figure 5.24).

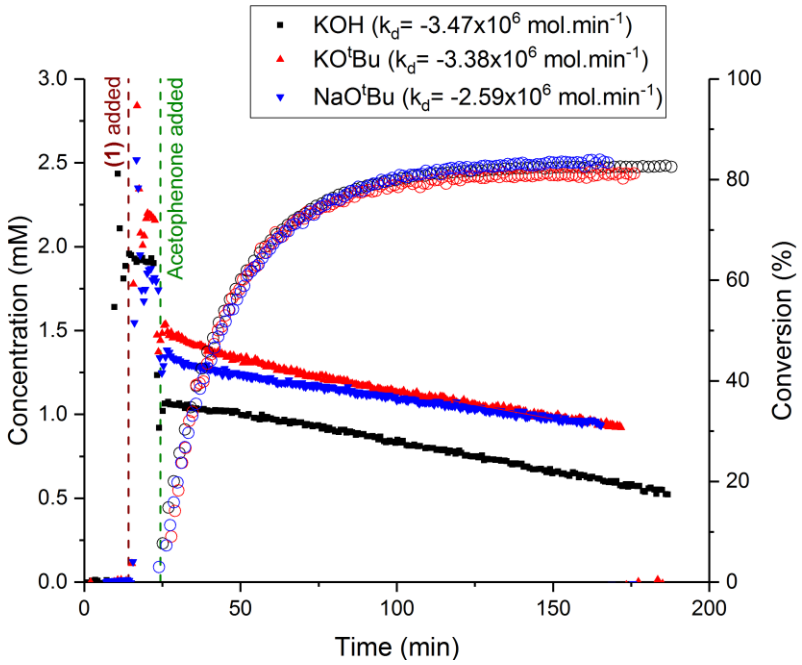

*Figure 5.24: Concentration profile of the hydride peak of **3** at -5.3 ppm, and conversion profile of acetophenone to (R)-1-phenylethanol, during the course of catalytic transfer hydrogenation of acetophenone to (R)-1-phenylethanol with either KOH, KO^{t}Bu or NaO^{t}Bu in flow at 4 mL/min (400 mM acetophenone, 10 mM base, 2 mM **1**, 9.5 mL dry isopropanol, 20°C). Selective excitation of **3** using a gradient spin echo pulse sequence with a shaped 180° pulse centred at -5.3 ppm (8 scans, 2 s acquisition time, 1 s delay time, 1600 µs Gaussian shaped pulse; spectra processed with 0.1 Hz exponential line broadening).*

The reaction proceeded with virtually identical rate for all three bases. The deactivation rate of the catalyst was the same for both KOH and KO^{t}Bu, with only a very minor difference for NaO^{t}Bu. The lack of any significant difference in catalyst deactivation rate when base anion and cation was changed, along with data for different concentrations of base (Figure 5.13), suggests that the initial, rate-limiting deactivation step to liberate mesitylene and form hydride-bridged dimeric complexes (Scheme 5.6) does not involve base. The involvement of base in subsequent steps to form ruthenium nanoparticles cannot be ruled out, and visual inspection showed reactions with KOH to darken in colour (used as a proxy for formation of ruthenium nanoparticles) more quickly than those with alkoxide bases.

The initial concentration of **3** during turnover was higher for both KO^{t}Bu and NaO^{t}Bu than for KOH. This is consistent with a base activated off-cycle species removing active catalyst from the main catalytic cycle. Since *tert*-butoxide is both bulkier and a weaker acid than hydroxide or *iso*-propoxide, formation of ruthenium alkoxide off-cycle species is predicted to be less favourable for *tert*-butoxide, resulting in a lower concentration of off-cycle species and a corresponding increase in concentration of **3** during turnover.

5.5.2 Product inhibition

In addition to the catalyst deactivation discussed above, it is also possible that the product may inhibit the reaction. Product inhibition is often difficult to distinguish from catalyst deactivation, as both manifest themselves as a decrease in reaction rate as the reaction progresses.[174] In this case, the power of NMR spectroscopy to monitor the catalytic species directly allows catalyst deactivation to be shown explicitly, and decomposition products observed (Figure 5.20). Whilst catalyst deactivation has been demonstrated for this reaction, product inhibition cannot be ruled out as an additional inhibition process without further experimentation.

Catalyst deactivation is typically a pseudo-first order reaction, depending only on catalyst concentration (Figure 5.17). Whilst the concentration of oxygen is also thought to be a factor in catalyst decomposition, this is assumed to be constant throughout the course of the reaction.

For a fixed catalyst concentration, product inhibition also displays a pseudo-first order rate dependency on product concentration. As reported by Donna Blackmond in her paper on Reaction Progress Kinetic Analysis (RPKA), the first order dependency means that both product inhibition and catalyst deactivation produce similar effects on the reaction kinetics.[174] To separate the two effects, reaction conditions are chosen such that differences in reaction rate due to one of the effects (usually product inhibition) are cancelled out.

For asymmetric reactions, determining whether product inhibition is occurring is more complex, since either or both product enantiomers may inhibit the reaction. The term 'chiral poisoning' is used to refer to a situation where the minor product enantiomer inhibits the reaction, potentially by binding to the catalytic site but not reacting. Whilst chiral poisoning is usually undesirable, by selectively inhibiting one catalyst enantiomer the effect can be used to enhance enantioselectivity in a reaction.[204-205]

For a fully reversible reaction, product inhibition (with the product formed preferentially in the reaction) is difficult to distinguish from the reverse reaction, since both result in a decrease in observed rate with increasing product concentration. In the case of the Noyori asymmetric transfer hydrogenation reaction using **(R,R)-1**, the major (R)-1-phenylethanol product would be expected to show inhibition-like behaviour due to the reversibility of the reaction, however separating out the two effects is challenging since individual forward and reverse rates are not known. Unless chiral poisoning is occurring, the minor (S)-1-phenylethanol product would not be expected to show inhibition behaviour since reaction with the (R,R) catalyst is negligible.

To test for chiral product inhibition, a mixture of acetophenone and (S)-1-phenylethanol was used to simulate starting the reaction from 50% conversion (Figure 5.25, blue). This rate may then be compared with that of the reaction started from 0% conversion (black) as a function of concentration to see if the lines overlay.[174] A third reaction starting with the same concentration of acetophenone as the 50% conversion reaction, but without added product was also carried out (red).

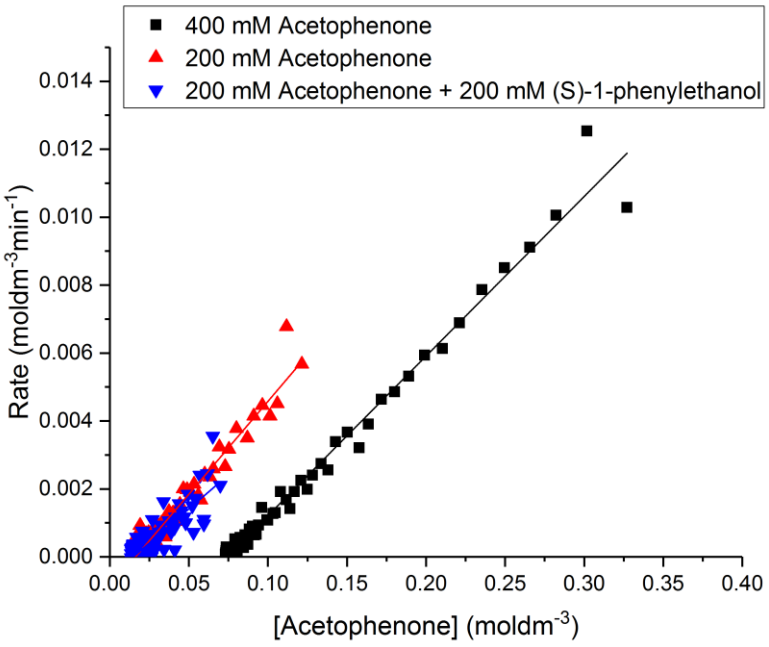

*Figure 5.25: Rate vs. Acetophenone concentration plot during the course of catalytic transfer hydrogenation of acetophenone to (R)-1-phenylethanol with a) 400 mM acetophenone and b) 200 mM acetophenone, 200 mM (S)-1-phenylethanol (10 mM base, 2 mM **1**, 9.5 mL dry isopropanol, 20°C).*

In the absence of product inhibition or catalyst deactivation, all three lines would be expected to overlay, since the reaction rate is dependent only on concentration of substrate and initial catalyst concentration. Since it has already been shown that catalyst deactivation is occurring, it is no surprise to see that the curves do not overlay.

If there is catalyst deactivation but no product inhibition, then the reactions started with half the concentration of substrate (red and blue) would be expected to have a faster rate than the equivalent concentration on the black trace since there is more active catalyst present in the reaction. The red and the blue traces would be expected to overlay, since presence of product should not affect the rate in the absence of chiral product inhibition. Under the conditions shown in Figure 5.25, both reactions started at 50% conversion overlay, indicating that there is no chiral poisoning occurring due to the presence of small quantities of (S)-1-phenylethanol in the product.

5.5.3 Alkoxide complexes

As discussed above, alkoxide and hydroxide complexes have been proposed as off-cycle intermediates in the asymmetric transfer hydrogenation reaction with Noyori's RuCl(TsDPEN)(mesitylene) catalyst.

There are no reported examples of these complexes from the experimental literature, however multiple computational papers have suggested that such complexes should be stable and are predicted to be the lowest energy structures in a disfavoured inner-sphere β-elimination/insertion mechanism.[99, 107, 109]

Complexes of **2** with primary or secondary alkoxides have the potential to reversibly exchange a CH proton with ruthenium to form **3**, and are therefore unlikely to be stable in solution. This process may occur either via arene ring-slippage and β-hydride abstraction or by dissociation of the alkoxide ligand followed by hydride transfer in an analogous process to the in-cycle reaction (Scheme 5.7). Complexes with tertiary or aromatic alkoxides are expected to be more stable due to the lack of an α-CH on the alcohol carbon.

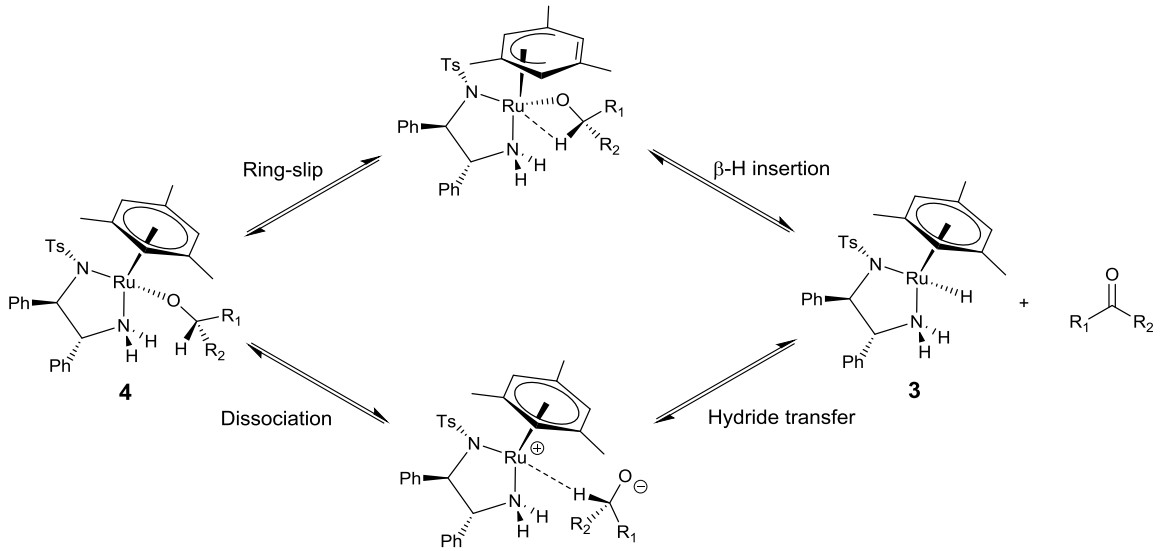

*Scheme 5.7: Possible mechanisms for reversible exchange between ruthenium primary or secondary alkoxide complex **4** and ruthenium hydride complex **3**, via either ring-slippage and β-H insertion or dissociation of the alkoxide ligand.*

DFT calculations [rM06L/LANL2DZ/6-31+G(d)] predict a linear relationship between pK_a (Table 5.2) and formation energy of alkoxide complexes from **2** and the corresponding alcohol (Figure 5.26). The reaction of **2** with *tert*-butanol is predicted to be unfavourable by 4.0 kcal/mol, and indeed, no reaction was observed experimentally. Noyori also reported that no reaction takes place between **2** and *tert*-butanol.[115] In contrast, the reaction of **2** with phenol is predicted to be favourable by 8.2 kcal/mol and reaction was observed (see below).

Of particular relevance to the Noyori reaction and discussion of off-cycle species above, is the fact that the isopropoxide complex **4b** (Scheme 5.8) has a predicted formation free energy of almost zero, meaning that an equilibrium will exist with **2** under reaction conditions. Since the equilibrium constant is close to 1, the concentration of **4b** present in the reaction will be dominated by the equilibrium between hydroxide and isopropoxide, leading to a complex reaction order as observed experimentally when concentration of hydroxide was varied.

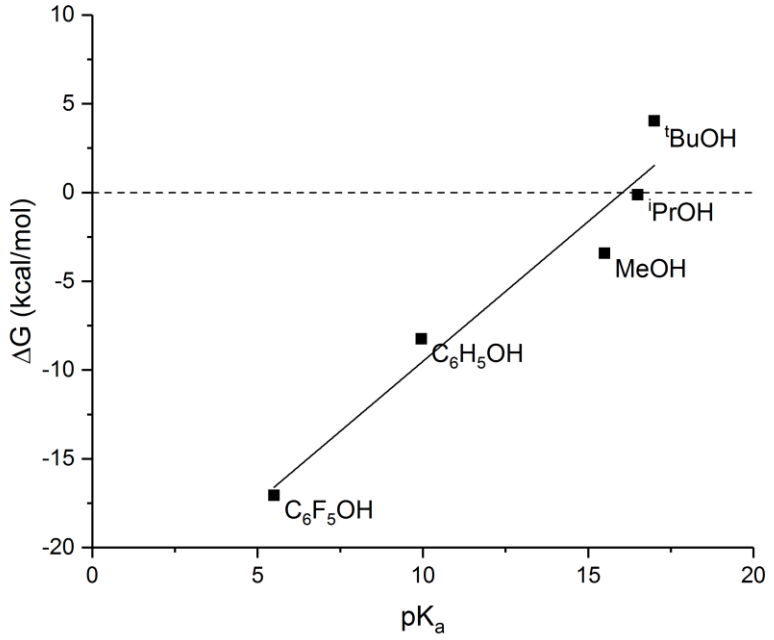

*Figure 5.26: Relationship between pK$_a$ (Table 5.2) and predicted formation energy of alkoxide complexes from **2** and the corresponding alcohol [rM06L/LANL2DZ/6-31+G(d)].*

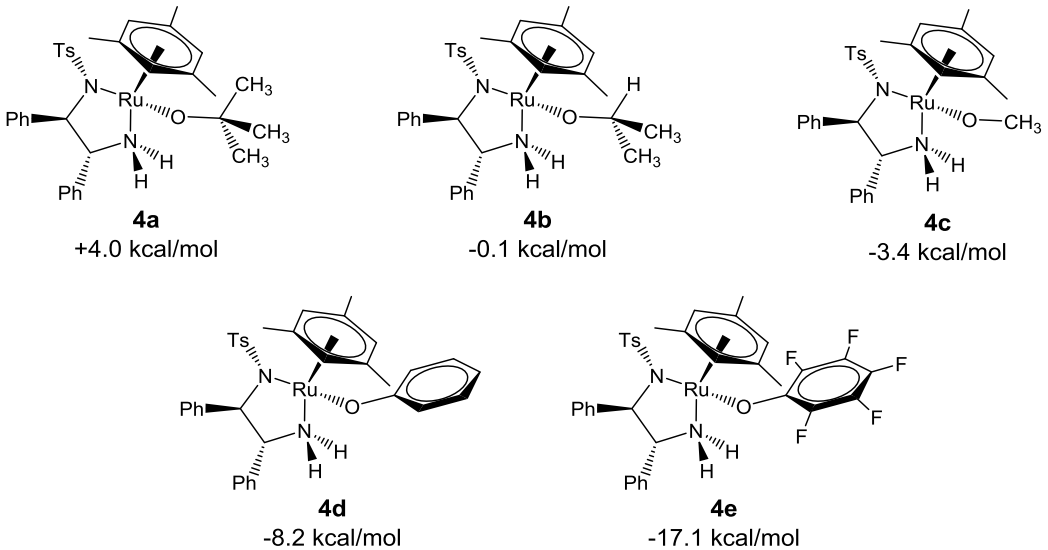

*Scheme 5.8: Structures and predicted formation energy from **2** + corresponding alcohol (rM06L/LANL2DZ/6-31+G(d)) of Noyori-tert-butoxide **4a**, Noyori-isopropoxide **4b**, Noyori-methoxide **4c**, Noyori-phenoxide **4d**, and Noyori-pentafluorophenoxide **4e**, complexes.*

Experimentally, when phenol is added to a solution of **2** in C_6D_6, a colour change from purple to orange is observed, consistent with the formation of a six-coordinate Ru(II) species. No hydride signals are observed in the region of -5 ppm in the proton NMR spectrum, ruling out formation of **3**, however the rest of the spectrum remains intractable, suggesting a mixture of different products (Figure 5.27). High resolution mass spectrometry (Figure 5.28 and Table 5.3) shows only **2** and a hydride bridged dimer (also seen at very low concentration in the ^1H NMR spectrum (-11.4 ppm) and likely to be a decomposition product or formed during the ionisation process) along with their sodium, potassium and hydrogen adducts. When heated, the mixture becomes purple, reverting to orange again upon cooling. This suggests a reversible equilibrium, explaining the complex NMR spectrum observed.

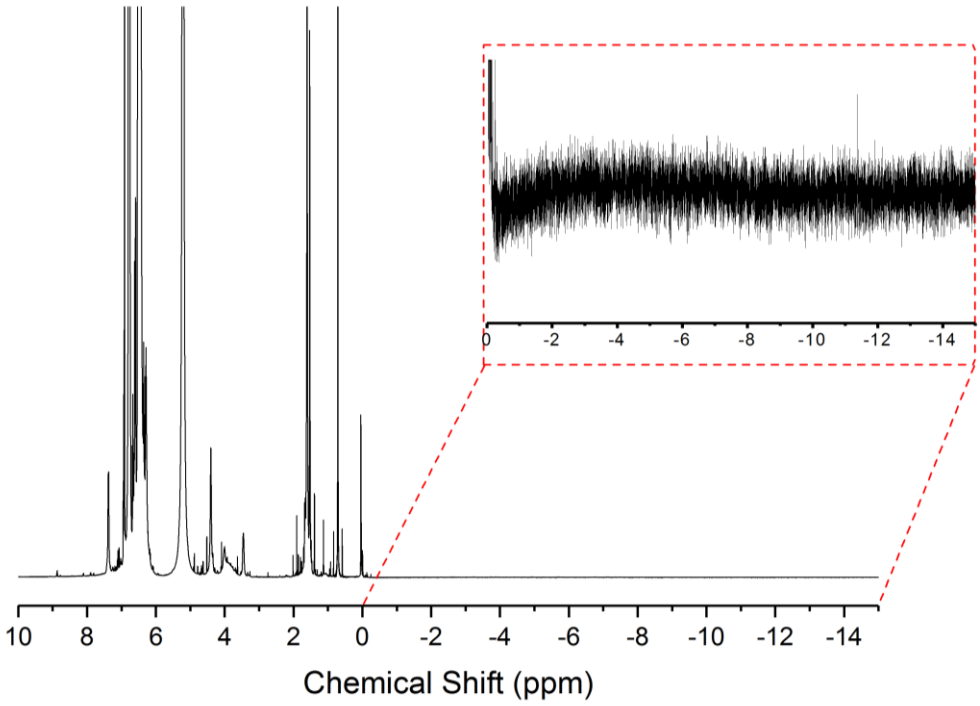

*Figure 5.27: ^1H NMR spectrum of **2** (16 mM) + phenol (200 mM) in C_6D_6 (25°C, 1.64 s acquisition time, 1 s relaxation delay time, 128 scans) . INSET: Enhancement of 0 to -15 ppm region (x75 multiplication factor).*

*Table 5.3: Assigned compounds, theoretical and experimental m/z and errors for high resolution mass spectrometry analysis of product from the reaction of **2** with phenol (positive electrospray ionisation, acetonitrile, analysis carried out at the National Mass Spectrometry facility, Swansea).*

Compound	Theoretical m/z	Experimental m/z	Error (ppm)
$C_{30}H_{33}N_2O_2RuS^+$	587.13007	587.1273	-4.72
$C_{30}H_{32}N_2NaO_2RuS^+$	609.11202	609.1090	-4.96
$C_{30}H_{32}KN_2O_2RuS^+$	625.08596	625.0829	-4.90
$C_{60}H_{67}N_4NaO_4Ru_2S_2^+$	1200.25938	1200.2600	+0.52

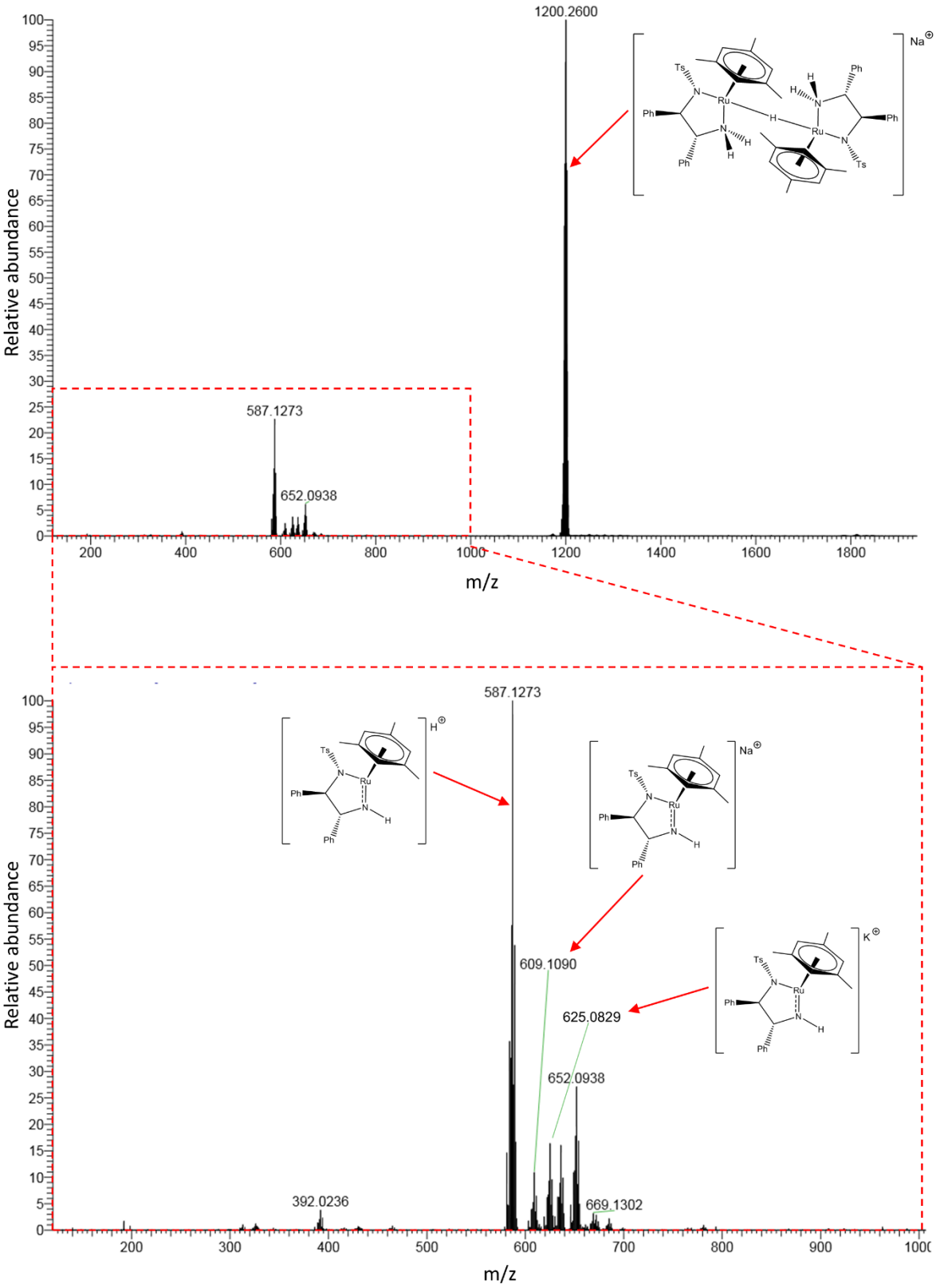

*Figure 5.28: High resolution mass spectrometry data with structures of assigned complexes for the product from the reaction of **2** with phenol (positive electrospray ionisation, acetonitrile, analysis carried out at the National Mass Spectrometry facility, Swansea).*

When the orange solid isolated from the reaction of **2** with phenol is dissolved in isopropanol, formation of hydride **3** is observed. Addition of acetophenone leads to turnover, producing 1-phenylethanol, showing that the putative phenoxide complex, **4d**, is able to re-enter the catalytic cycle. The reaction rate and concentration of **3** (Figure 5.29) are approximately half that of what would be expected for the concentration of **4d** added to the reaction (assuming complete reaction of **2** to **4d**), which is attributed to the higher acidity of phenol compared to isopropoxide (pK_a 9.95 vs. 16.5) helping to stabilise **4d** and shifting the equilibrium towards the phenoxide complex. When an additional 10 equivalents of phenol are added to the reaction, the concentration of hydride **3** is observed to drop, which is consistent with a change in the equilibrium position between on-cycle and off-cycle species (Figure 5.29).

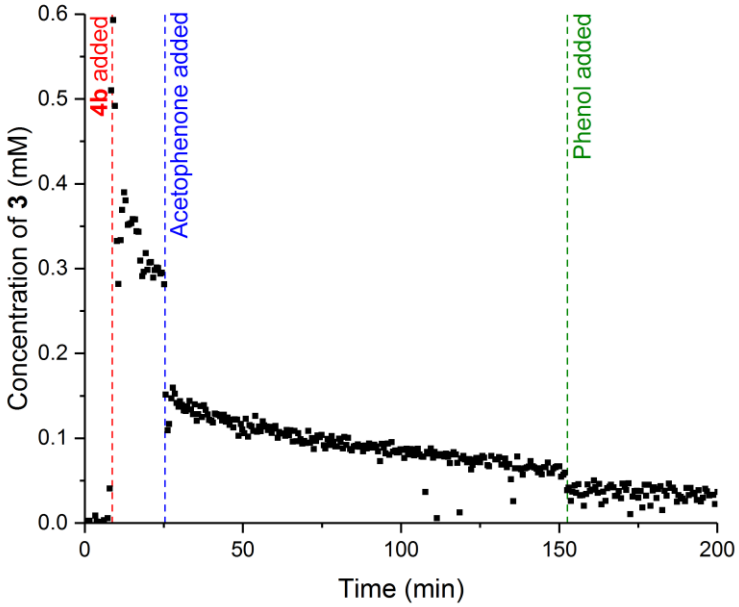

*Figure 5.29: Concentration profile of the hydride peak of **3** at -5.3 ppm during the course of catalytic transfer hydrogenation of acetophenone to (R)-1-phenylethanol in flow at 3 mL/min (0.765 mM **4b**, 400 mM acetophenone, 10 mM base, 9.5 mL dry isopropanol, 20°C). Phenol (7 mg, 7.65 mM) added after 155 min. Selective excitation of **3** using a gradient spin echo pulse sequence with a shaped 180° pulse centred at -5.5 ppm (8 scans, 2 s acquisition time, 1 s delay time, 1600 µs Gaussian shaped pulse; spectra processed with 0.1 Hz exponential line broadening).*

Whilst crystallisation of the product from the reaction between **2** and phenol repeatedly failed, and structural characterisation by other means was inconclusive, the related pentafluorophenol complex, **4e**, proved more amenable to analysis. Pentafluorophenol is more acidic than phenol, continuing the trend observed for *tert*-butanol and phenol above that more acidic alcohols are more favourable for forming alkoxide complexes with **2**. No colour change is observed for **4e** when heated to 80 °C in benzene, supporting the increased stability of the pentafluorophenoxide over the phenoxide complex.

The ^{19}F NMR spectrum for **4e** shows a shift to lower frequencies of the meta and para fluorine peaks upon complexation to ruthenium, consistent with the reported changes for deprotonation of C_6F_5OH to $C_6F_5O^-$ (Figure 5.30).[206] All fluorine peaks are significantly broadened in the complex with ruthenium, partially resolving upon cooling, suggesting a dynamic exchange process as implicated above for the phenoxide complex, **4d**.

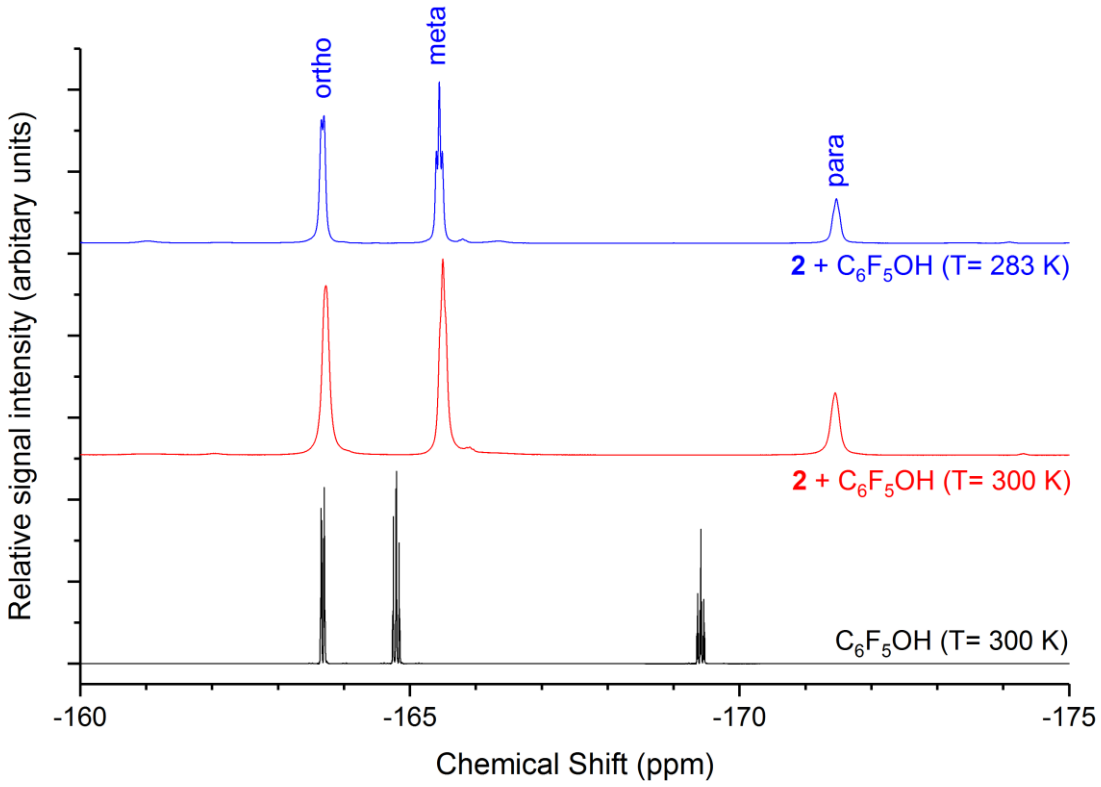

*Figure 5.30: ^{19}F NMR spectra in C_6D_6 of a) pentafluorophenol, b) **2** + pentafluorophenol at 300 K, c) **2** + pentafluorophenol at 283 K, showing shift in meta and para peaks upon complexation and peak sharpening upon cooling.*

^{19}F DOSY NMR (THF-d_8) gave a diffusion constant of 1.25×10^{-9} m^2s^{-1} for **4e** (Figure 8.7). Estimation of molecular weight based on diffusion constant[207-208] gives an approximate value of 250 $g.mol^{-1}$. This value does not correspond to any of the expected ruthenium complexes or free pentafluorophenol (even accounting for the large error of up to 50% in calculating molecular weight using this method[207]), however the value lies between that of **4e** and pentafluorophenol, which may be further indication of a dynamic exchange process resulting in averaging of diffusion rates.

Whilst no crystals suitable for diffraction have yet been isolated for either the phenol or pentafluorophenol complexes with **2**, the behaviour of both samples is consistent with a ruthenium-alkoxide structure as the most likely representation of **4**.

5.6 CONCLUSIONS

The work presented in this chapter demonstrates how FlowNMR spectroscopy can be applied to the study of an air-sensitive homogeneous catalytic reaction. In addition to monitoring overall reaction kinetics, catalytic species involved in the reaction were studied directly, allowing the catalyst to be observed at work. By following the catalyst throughout the reaction, mechanistic information about catalyst deactivation and off-cycle species to be discovered and these two processes added to the reaction mechanism for the first time.

Further investigation of the role of base on the reaction has shown that the reaction rate is unchanged using different inorganic and alkoxide bases. Catalyst deactivation rate is also similar for the different bases, supporting the proposed mechanism where base is not involved in the initial catalyst deactivation step. The concentration of **3** present during turnover is higher for *tert*-butoxide bases than for KOH, which is consistent with the proposed off-cycle alkoxide species, since formation of an off-cycle ruthenium *tert*-butoxide species is expected to be less favourable than the corresponding hydroxide species.

Addition of (S)-1-phenylethanol product to the reaction does not affect the reaction kinetics, indicating that there is no chiral poisoning taking place due to the small amount of the minor product formed in the reaction. Product inhibition by the major (R)-1-phenylethanol product cannot be ruled out, however isolating this effect from the reversibility of the reaction is very challenging and has so far not been tested.

The nature of the proposed hydroxide/alkoxide off-cycle intermediates has been investigated in more detail, using phenol and pentafluorophenol as model compounds. The favourability of Noyori-alkoxide complex formation is proportional to pK_a of the respective alcohol. For isopropanol, the formation free energy is close to zero, meaning that formation of an alkoxide complex is a viable off-cycle process. Due to the potential for further reaction, isopropoxide and other primary and secondary alkoxide complexes are too unstable to isolate.

The formation of aromatic alkoxide complexes is predicted to be more favourable than for aliphatic alkoxide complexes due to the increased acidity of the alcohol. Whilst obtaining pure samples of both phenoxide and pentafluorophenoxide complexes has so far proved challenging, there is strong indirect evidence in the form of colour changes, reactivity and NMR shifts that these complexes are formed. A test reaction using the complex formed by reaction of **2** with phenol showed catalytic activity for the transfer hydrogenation of acetophenone to 1-phenylethanol, along with formation of hydride intermediate **3**, indicating that the alkoxide complex is able to re-enter the catalytic cycle, and so is a viable off-cycle species.

5.7 Experimental Details for Commentary

5.7.1 Transfer hydrogenation reactions

5.7.1.1 With tert-butoxide base

The reaction was carried out as described in Section 5.4.4, with either sodium *tert*-butoxide (9.6 mg / 10 mL isopropanol, 0.01 M) or potassium *tert*-butoxide (11.2 mg / 10 mL isopropanol, 0.01 M) in place of potassium hydroxide.

5.7.1.2 Product inhibition

The reaction was carried out as described in Section 5.4.4, with the following quantities of reagents:

'400 mM Acetophenone': 0.1 M TMB/0.01 M KOH stock solution in isopropanol (9.53 mL), (R,R)-(TsDPEN)mesitylruthenium chloride (12 mg, 0.02 mmol) and acetophenone (0.47 mL, 4 mmol).

'200 mM Acetophenone': 0.1 M TMB/0.01 M KOH stock solution in isopropanol (9.77 mL), (R,R)-(TsDPEN)mesitylruthenium chloride (12 mg, 0.02 mmol) and acetophenone (0.23 mL, 2 mmol).

'400 mM Acetophenone + 200 mM (S)-1-phenylethanol': 0.1 M TMB/0.01 M KOH stock solution in isopropanol (9.39 mL), (R,R)-(TsDPEN)mesitylruthenium chloride (12 mg, 0.02 mmol), acetophenone (0.23 mL, 2 mmol), (S,S)-1-phenylethanol (0.23 mL, 2 mmol) and acetone (0.15 mL, 2 mmol).

5.7.1.3 With ruthenium phenoxide complex 4d

The reaction was carried out as described in Section 5.4.4, using complex **4d** (5.2 mg, 0.0077 mmol) in place of (R,R)-(TsDPEN)mesitylruthenium chloride and *without* potassium hydroxide.

5.7.2 Synthesis of complexes 4d and 4e

5.7.2.1 NMR scale reactions

(R,R)-(TsDPEN)mesitylruthenium chloride (5 mg, 0.008 mmol), potassium *tert*-butoxide (2 mg, 0.018 mmol) and either phenol (1 mg, 0.01 mmol) or pentafluorophenol (2 mg, 0.01 mmol) were dissolved in C_6D_6 (1 mL). The orange solution was syringe filtered to remove any un-dissolved particles.

^{19}F NMR spectra were recorded with standard 90° pulse program with a 0.577 s acquisition time and 1 s relaxation delay time, averaging 16 transients. ^{19}F DOSY spectra were acquired using a gradient DOSY sequence with convection compensation, with a 0.577 s acquisition

time, 1 s delay time, using a 32 point linear gradient ramp, δ of 0.0015 s and Δ of 0.0474 s, averaging 16 transient for each gradient strength. DOSY data was processed using Dynamic Centre 2.5.4 with a γ of 4005.2 Hz.

5.7.2.2 Complex 4d isolation

(R,R)-(TsDPEN)mesitylruthenium chloride (50 mg, 0.08 mmol) and potassium *tert*-butoxide (9 mg, 0.08 mmol) were dissolved in dry toluene (10 mL) to produce a purple solution of **2**. Phenol (8 mg, 0.08 mmol) was added, causing the mixture to become orange. The mixture was stirred at room temperature for 30 min before filtering to isolate an orange solid which was dried under high vacuum (approx. 10 mg, 20%).

5.7.3 Density Functional Theory calculations

Density Functional Theory calculations were carried out using the Gaussian 09 (rev. D.01-v3) [209] software package. Geometry optimisation, frequency and NMR shift calculations were performed in a SMD polarizable continuum solvent model[210] of implicit isopropanol. The restricted rM06L functional was used with a LANL2DZ basis set on ruthenium and 6-311+G(d) basis set on all other atoms. Starting geometries were taken from published crystal structures,[101] or calculated geometries,[99, 108-109] where available. DFT integration grids with 99 radial and 590 angular points (Ultrafine) were used for all transition state calculations. All ground state geometries were free of imaginary frequencies.

5.8 REFERENCES

1. Wang, D.; Astruc, D., The golden age of transfer hydrogenation. *Chem. Rev.* **2015,** 115, 6621-6686.

2. Hashiguchi, S.; Fujii, A.; Takehara, J.; Ikariya, T.; Noyori, R., Asymmetric Transfer Hydrogenation of Aromatic Ketones Catalyzed by Chiral Ruthenium(II) Complexes. *J. Am. Chem. Soc.* **1995,** 117, 7562-7563.

3. Clapham, S. E.; Hadzovic, A.; Morris, R. H., Mechanisms of the H_2-hydrogenation and transfer hydrogenation of polar bonds catalyzed by ruthenium hydride complexes. *Coord. Chem. Rev.* **2004,** 248, 2201-2237.

4. Dub, P. A.; Henson, N. J.; Martin, R. L.; Gordon, J. C., Unravelling the mechanism of the asymmetric hydrogenation of acetophenone by [RuX_2(diphosphine)(1,2-diamine)] catalysts. *J. Am. Chem. Soc.* **2014,** 136, 3505-3521.

5. Eisenstein, O.; Crabtree, R. H., Outer sphere hydrogenation catalysis. *New J. Chem.* **2013,** 37, 21-27.

6. Koike, T.; Ikariya, T., Mechanistic Aspects of Formation of Chiral Ruthenium Hydride Complexes from 16-Electron Ruthenium Amide Complexes and Formic Acid: Facile Reversible Decarboxylation and Carboxylation. *Adv. Synth. Catal.* **2004,** 346, 37-41.

7. Strotman, N. A.; Baxter, C. A.; Brands, K. M. J.; Cleator, E.; Krska, S. W.; Reamer, R. A.; Wallace, D. J.; Wright, T. J., Reaction Development and Mechanistic Study of a Ruthenium Catalyzed Intramolecular Asymmetric Reductive Amination en Route to the Dual Orexin Inhibitor Suvorexant (MK-4305). *J. Am. Chem. Soc.* **2011,** 133, 8362-8371.

8. Wu, X.; Liu, J.; Di Tommaso, D.; Iggo, J. A.; Catlow, C. R. A.; Bacsa, J.; Xiao, J., A Multilateral Mechanistic Study into Asymmetric Transfer Hydrogenation in Water. *Chem. Eur. J.* **2008,** 14, 7699-7715.

9. Yamakawa, M.; Ito, H.; Noyori, R., The Metal–Ligand Bifunctional Catalysis: A Theoretical Study on the Ruthenium(II)-Catalyzed Hydrogen Transfer between Alcohols and Carbonyl Compounds. *J. Am. Chem. Soc.* **2000,** 122, 1466-1478.

10. Haack, K.-J.; Hashiguchi, S.; Fujii, A.; Ikariya, T.; Noyori, R., The Catalyst Precursor, Catalyst and Intermediate in the Ru(II)-Promoted Asymmetric Hydrogen Transfer between Alcohols and Ketones. *Angew. Chem. Int. Ed.* **1997,** 36, 285-288.

11. Toubiana, J.; Medina, L.; Sasson, Y., The Nature of the True Catalyst in Transfer Hydrogenation with Alcohol Donors Using (arene)$_2$$Ru_2Cl_4$(II)/TsDPEN Precursor. *Mod. Res. Catal.* **2014,** 3, 68-88.

12. Trost, B. M., Atom Economy - A Challenge for Organic Synthesis: Homogeneous Catalysis Leads the Way. *Angew. Chem. Int. Ed.* **1995,** 34, 259-281.

13. Crabtree, R. H. In *The Organometallic Chemistry of the Transition Metals*, 4th ed.; John Wiley & Sons, Inc.: Hoboken, New Jersey, 2005; Vol. 1, pp 235-273.

14. Kurosawa, H.; Yamamoto, A., In *Fundamentals of molecular catalysis*. 3rd ed.; Elsevier: Amsterdam; Boston, 2003; Vol. 1, p 522.

15. Cornils, B.; Herrmann, W. A., In *Applied homogeneous catalysis with organometallic compounds: a comprehensive handbook in three volumes.* 2nd ed.; Wiley-VCH: Weinheim, 2002; Vol. 1, p 1872.

16. Moser, W. R.; Slocum, D. W., In *Homogeneous transition metal catalyzed reactions*. 1st ed.; American Chemical Society: Washington, D.C., 1992; Vol. 230, p 625.

17. Mahatthananchai, J.; Dumas, A. M.; Bode, J. W., Catalytic selective synthesis. *Angew. Chem. Int. Ed. Engl.* **2012,** 51, 10954-10990.

18. Gennari, C.; Piarulli, U., Combinatorial Libraries of Chiral Ligands for Enantioselective Catalysis. *Chem. Rev.* **2003,** 103, 3071-3100.

19. Reetz, M. T.; Becker, M. H.; Klein, H.-W.; Stöckigt, D., A Method for High-Throughput Screening of Enantioselective Catalysts. *Angew. Chem. Int. Ed.* **1999,** 38, 1758-1761.

20. Robbins, D. W.; Hartwig, J. F., A simple, multidimensional approach to high-throughput discovery of catalytic reactions. *Science* **2011,** 333, 1423-1427.

21. Troshin, K.; Hartwig, J. F., Snap deconvolution: An informatics approach to high-throughput discovery of catalytic reactions. *Science* **2017,** 357, 175-181.

22. Fisher, R. A., In *The design of experiments*. 7 ed.; Hafner: New York, 1971; Vol. 1st, p 248.

23. Kateman, G., The playground of chemometrics. *Anal. Chim. Acta* **1986,** 191, 125-131.

24. McMullen, J. P.; Stone, M. T.; Buchwald, S. L.; Jensen, K. F., An Integrated Microreactor System for Self-Optimization of a Heck Reaction: From Micro- to Mesoscale Flow Systems. *Angew. Chem. Int. Ed.* **2010,** 49, 7076-7080.

25. Skilton, R. A.; Parrott, A. J.; George, M. W.; Poliakoff, M.; Bourne, R. A., Real-Time Feedback Control Using Online Attenuated Total Reflection Fourier Transform Infrared (ATR FT-IR) Spectroscopy for Continuous Flow Optimization and Process Knowledge. *Appl. Spectrosc.* **2013,** 67, 1127-1131.

26. Catalysis as it goes. *Nature Catalysis* **2018,** 1, 165-166.

27. Blackmond, D. G., Reaction Progress Kinetic Analysis: A Powerful Methodology for Mechanistic Studies of Complex Catalytic Reactions. *Angew. Chem. Int. Ed.* **2005,** 44, 4302-4320.

28. Bures, J., Variable Time Normalization Analysis: General Graphical Elucidation of Reaction Orders from Concentration Profiles. *Angew. Chem. Int. Ed. Engl.* **2016,** 55, 16084-16087.

29. Blackmond, D. G., Kinetic Profiling of Catalytic Organic Reactions as a Mechanistic Tool. *J. Am. Chem. Soc.* **2015,** 137, 10852-10866.

30. Chung, R.; Hein, J. E., The More, The Better: Simultaneous In Situ Reaction Monitoring Provides Rapid Mechanistic and Kinetic Insight. *Top. Catal.* **2017,** 60, 594-608.

31. Jabor, R.; Ursula, B.; Reinhard, S.; Angelika, B., Selective Alcohol Oxidation by a Copper TEMPO Catalyst: Mechanistic Insights by Simultaneously Coupled Operando EPR/UV-Vis/ATR-IR Spectroscopy. *Angew. Chem. Int. Ed.* **2015,** 54, 11791-11794.

32. Brinkman, U. A. T., A review of reaction detection in HPLC. *Chromatographia* **1987,** 24, 190-200.

33. Cervera-Padrell, A. E.; Nielsen, J. P.; Jønch Pedersen, M.; Müller Christensen, K.; Mortensen, A. R.; Skovby, T.; Dam-Johansen, K.; Kiil, S.; Gernaey, K. V., Monitoring and Control of a Continuous Grignard Reaction for the Synthesis of an Active Pharmaceutical Ingredient Intermediate Using Inline NIR spectroscopy. *Org. Process Res. Dev.* **2012,** 16, 901-914.

34. Foley, D. A.; Wang, J.; Maranzano, B.; Zell, M. T.; Marquez, B. L.; Xiang, Y.; Reid, G. L., Online NMR and HPLC as a reaction monitoring platform for pharmaceutical process development. *Anal. Chem.* **2013,** 85, 8928-8932.

35. Schafer, W. A.; Hobbs, S.; Rehm, J.; Rakestraw, D. A.; Orella, C.; McLaughlin, M.; Ge, Z.; Welch, C. J., Mobile Tool for HPLC Reaction Monitoring. *Org. Process Res. Dev.* **2007,** 11, 870-876.

36. Kumar, P. In *Advanced Gas Chromatography: Progress in Agricultural Biomedical and Industrial Applications*, 1st ed.; Ali Mohd, M., Ed. InTech: 2012; Vol. 1, pp 325 - 342.

37. Hart, R. J.; Pedge, N. I.; Steven, A. R.; Sutcliffe, K., In situ Monitoring of a Heterogeneous Etherification Reaction Using Quantitative Raman Spectroscopy. *Org. Process Res. Dev.* **2015,** 19, 196-202.

38. Lamps, J. P.; Catala, J. M., Real Time Controlled Polymerization Kinetics of 2,5-Dibromo-3-decylthiophene Using UV−Vis Spectroscopy: Determination of the Reaction Rate Constants. *Macromolecules* **2009,** 42, 7282-7284.

39. Luo, J.; Oliver, A. G.; Scott McIndoe, J., A detailed kinetic analysis of rhodium-catalyzed alkyne hydrogenation. *Dalton Trans.* **2013,** 42, 11312-11318.

40. Theron, R.; Wu, Y.; Yunker, L. P. E.; Hesketh, A. V.; Pernik, I.; Weller, A. S.; McIndoe, J. S., Simultaneous Orthogonal Methods for the Real-Time Analysis of Catalytic Reactions. *ACS Catalysis* **2016,** 6, 6911-6917.

41. Morris, G. A.; Freeman, R., Selective excitation in Fourier transform nuclear magnetic resonance. *J. Magn. Reson.* **2011,** 213, 214-243.

42. Foley, D. A.; Dunn, A. L.; Zell, M. T., Reaction monitoring using online vs tube NMR spectroscopy: seriously different results. *Magn. Reson. Chem.* **2016,** 54, 451-456.

43. Hall, A. M. R.; Chouler, J. C.; Codina, A.; Gierth, P. T.; Lowe, J. P.; Hintermair, U., Practical Aspects of Real-time Reaction Monitoring using Multi-nuclear High Resolution FlowNMR Spectroscopy. *Catal. Sci. Tech.* **2016,** 6, 8406-8417.

44. Foley, D. A.; Bez, E.; Codina, A.; Colson, K. L.; Fey, M.; Krull, R.; Piroli, D.; Zell, M. T.; Marquez, B. L., NMR flow tube for online NMR reaction monitoring. *Anal. Chem.* **2014,** 86, 12008-12013.

45. Maiwald, M.; Fischer, H. H.; Kim, Y.-K.; Albert, K.; Hasse, H., Quantitative high-resolution on-line NMR spectroscopy in reaction and process monitoring. *J. Magn. Reson.* **2004,** 166, 135-146.

46. Maiwald, M.; Fischer, H. H.; Kim, Y.-K.; Hasse, H., Quantitative on-line high-resolution NMR spectroscopy in process engineering applications. *Anal. Bioanal. Chem.* **2003,** 375, 1111-1115.

47. Barrios Sosa, A. C.; Williamson, R. T.; Conway, R.; Shankar, A.; Sumpter, R.; Cleary, T., A Safe and Efficient Synthetic Route to a 2,5-Dimethyl-1-aryl-1H-imidazole Intermediate. *Org. Process Res. Dev.* **2011,** 15, 449-454.

48. Blanazs, A.; Bristow, T. W.; Coombes, S. R.; Corry, T.; Nunn, M.; Ray, A. D., Coupling and optimisation of online nuclear magnetic resonance spectroscopy and mass spectrometry for process monitoring to cover the broad range of process concentration. *Magn. Reson. Chem.* **2017,** 55, 274-282.

49. Zientek, N.; Meyer, K.; Kern, S.; Maiwald, M., Quantitative Online NMR Spectroscopy in a Nutshell. *Chem. Ing. Tech.* **2016,** 88, 698-709.

50. Baratta, W.; Ballico, M.; Baldino, S.; Chelucci, G.; Herdtweck, E.; Siega, K.; Magnolia, S.; Rigo, P., New Benzo[*h*]quinoline-Based Ligands and their Pincer Ru and Os Complexes for Efficient Catalytic Transfer Hydrogenation of Carbonyl Compounds. *Chem. Eur. J.* **2008,** 14, 9148-9160.

51. Bullock, R. M., Catalytic Ionic Hydrogenations. *Chem. Eur. J.* **2004,** 10, 2366-2374.

52. Hayes, A. M.; Morris, D. J.; Clarkson, G. J.; Wills, M., A class of ruthenium(II) catalyst for asymmetric transfer hydrogenations of ketones. *J. Am. Chem. Soc.* **2005,** 127, 7318-7319.

53. Misal Castro, L. C.; Li, H.; Sortais, J.-B.; Darcel, C., When iron met phosphines: a happy marriage for reduction catalysis. *Green Chem.* **2015,** 17, 2283-2303.

54. Noyori, R. Ryoji Noyori - Nobel Lecture: Asymmetric Catalysis: Science and Technology. http://www.nobelprize.org/nobel_prizes/chemistry/laureates/2001/noyori-lecture.html (accessed 27/06/2018).

55. Noyori, R.; Hashiguchi, S., Asymmetric Transfer Hydrogenation Catalyzed by Chiral Ruthenium Complexes. *Acc. Chem. Res.* **1997,** 30, 97-102.

56. Wang, C.; Wu, X.; Xiao, J., Broader, greener, and more efficient: recent advances in asymmetric transfer hydrogenation. *Chem Asian J* **2008,** 3, 1750-1770.

57. Blackmond, D. G.; Ropic, M.; Stefinovic, M., Kinetic Studies of the Asymmetric Transfer Hydrogenation of Imines with Formic Acid Catalyzed by Rh−Diamine Catalysts. *Org. Process Res. Dev.* **2006,** 10, 457-463.

58. Bures, J., A Simple Graphical Method to Determine the Order in Catalyst. *Angew. Chem. Int. Ed. Engl.* **2016,** 55, 2028-2031.

59. Dub, P. A.; Ikariya, T., Quantum chemical calculations with the inclusion of nonspecific and specific solvation: asymmetric transfer hydrogenation with bifunctional ruthenium catalysts. *J. Am. Chem. Soc.* **2013,** 135, 2604-2619.

60. Noyori, R., Asymmetric catalysis: Science and opportunities (Nobel lecture). *Angew. Chem.* **2002,** 41, 2008-2022.

61. Nikitin, K.; O'Gara, R., Mechanisms and Beyond: Elucidation of Fluxional Dynamics by Exchange NMR. *Chemistry* **2018**.

62. Zientek, N.; Laurain, C.; Meyer, K.; Paul, A.; Engel, D.; Guthausen, G.; Kraume, M.; Maiwald, M., Automated data evaluation and modelling of simultaneous ^{19}F-^{1}H medium-resolution NMR spectra for online reaction monitoring. *Magn. Reson. Chem.* **2016,** 54, 513-520.

63. Silva Elipe, M. V.; Milburn, R. R., Monitoring chemical reactions by low-field benchtop NMR at 45 MHz: pros and cons. *Magn. Reson. Chem.* **2016,** 54, 437-443.

64. Smallcombe, S. H.; Patt, S. L.; Keifer, P. A., WET Solvent Suppression and Its Applications to LC NMR and High-Resolution NMR Spectroscopy. *J. Magn. Reson. A* **1995,** 117, 295-303.

65. Zheng, G.; Price, W. S., Solvent signal suppression in NMR. *Prog. Nucl. Magn. Reson. Spectrosc.* **2010,** 56, 267-288.

66. Tang, H.; Wang, Y.; Nicholson, J. K.; Lindon, J. C., Use of relaxation-edited one-dimensional and two dimensional nuclear magnetic resonance spectroscopy to improve detection of small metabolites in blood plasma. *Anal. Biochem.* **2004,** 325, 260-272.

67. Asada, M.; Nemoto, T.; Mimura, H.; Sako, K., Advanced New Relaxation Filter-Selective Signal Excitation Methods for ^{13}C Solid-State Nuclear Magnetic Resonance. *Anal. Chem.* **2014,** 86, 10091-10098.

68. Esturau, N.; Espinosa, J. F., Optimization of Diffusion-Filtered NMR Experiments for Selective Suppression of Residual Nondeuterated Solvent and Water Signals from ^{1}H NMR Spectra of Organic Compounds. *J. Org. Chem.* **2006,** 71, 4103-4110.

69. Jahncke, M.; Meister, G.; Rheinwald, G.; Stoeckli-Evans, H.; Süss-Fink, G., Dinuclear (Arene)ruthenium Hydrido Complexes: Synthesis, Structure, and Fluxionality of $(C_6Me_6)_2Ru_2H_3(BH_4)$. *Organometallics* **1997,** 16, 1137-1143.

70. Cheung, F. K.; Hayes, A. M.; Hannedouche, J.; Yim, A. S.; Wills, M., "Tethered" Ru(II) catalysts for asymmetric transfer hydrogenation of ketones. *J. Org. Chem.* **2005,** 70, 3188-97.

71. Soni, R.; Hall, T. H.; Mitchell, B. P.; Owen, M. R.; Wills, M., Asymmetric Reduction of Electron-Rich Ketones with Tethered Ru(II)/TsDPEN Catalysts Using Formic Acid/Triethylamine or Aqueous Sodium Formate. *J. Org. Chem.* **2015,** 80, 6784-93.

72. Touge, T.; Hakamata, T.; Nara, H.; Kobayashi, T.; Sayo, N.; Saito, T.; Kayaki, Y.; Ikariya, T., Oxo-Tethered Ruthenium(II) Complex as a Bifunctional Catalyst for Asymmetric Transfer Hydrogenation and H2 Hydrogenation. *J. Am. Chem. Soc.* **2011,** 133, 14960-14963.

73. Nedden, H. G.; Zanotti-Gerosa, A.; Wills, M., The Development of Phosphine-Free 'Tethered' Ruthenium(II) Catalysts for the Asymmetric Reduction of Ketones and Imines. *Chem. Rec.* **2016,** 16, 2623-2643.

74. Crabtree, R. H., Deactivation in homogeneous transition metal catalysis: causes, avoidance, and cure. *Chem. Rev.* **2015,** 115, 127-150.

75. Letko, C. S.; Heiden, Z. M.; Rauchfuss, T. B., Activation and Deactivation of Cp*Ir(TsDPEN) Hydrogenation Catalysts in Water. *Eur. J. Inorg. Chem.* **2009,** 2009, 4927-4930.

76. Campos, J.; Hintermair, U.; Brewster, T. P.; Takase, M. K.; Crabtree, R. H., Catalyst Activation by Loss of Cyclopentadienyl Ligands in Hydrogen Transfer Catalysis with Cp*IrIII Complexes. *ACS Catalysis* **2014,** 4, 973-985.

77. March, J. S., Michael; . In *March's advanced organic chemistry : reactions, mechanisms, and structure*, 6th ed. ed.; March, J., Ed. Hoboken: New Jersey, 2007; pp 356-394.

78. Hiyama, T.; Yamamoto, H., In *Organofluorine compounds : chemistry and applications*. Springer: Berlin; London, 2011; p 272.

79. Berkessel, A.; Schubert, T. J. S.; Müller, T. N., Hydrogenation without a Transition-Metal Catalyst: On the Mechanism of the Base-Catalyzed Hydrogenation of Ketones. *J. Am. Chem. Soc.* **2002,** 124, 8693-8698.

80. John, J. M.; Takebayashi, S.; Dabral, N.; Miskolzie, M.; Bergens, S. H., Base-Catalyzed Bifunctional Addition to Amides and Imides at Low Temperature. A New Pathway for Carbonyl Hydrogenation. *J. Am. Chem. Soc.* **2013,** 135, 8578-8584.

81. Hartmann, R.; Chen, P., Numerical Modeling of Differential Kinetics in the Asymmetric Hydrogenation of Acetophenone by Noyori's Catalyst. *Adv. Synth. Catal.* **2003,** 345, 1353-1359.

82. Hartmann, R.; Chen, P., Noyori's Hydrogenation Catalyst Needs a Lewis Acid Cocatalyst for High Activity. *Angew. Chem. Int. Ed.* **2001,** 40, 3581-3585.

83. Faller, J. W.; Lavoie, A. R.; Parr, J., Chiral Poisoning and Asymmetric Activation. *Chem. Rev.* **2003,** 103, 3345-3368.

84. Faller, J. W.; Parr, J., Chiral poisoning: a novel strategy for asymmetric catalysis. *J. Am. Chem. Soc.* **1993,** 115, 804-805.

85. Futera, Z.; Klenko, J.; Sponer, J. E.; Sponer, J.; Burda, J. V., Interactions of the "piano-stool" [ruthenium(II) (η^6-arene)(en)Cl]$^+$ complexes with water and nucleobases; ab initio and DFT study. *J. Comput. Chem.* **2009,** 30, 1758-1770.

86. Ando, S.; Matsuura, T., Substituent shielding parameters of fluorine-19 NMR on polyfluoroaromatic compounds dissolved in dimethyl sulphoxide-d6. *Magn. Reson. Chem.* **1995,** 33, 639-645.

87. Evans, R.; Dal Poggetto, G.; Nilsson, M.; Morris, G. A., Improving the Interpretation of Small Molecule Diffusion Coefficients. *Anal. Chem.* **2018,** 90, 3987-3994.

88. Evans, R.; Deng, Z.; Rogerson, A. K.; McLachlan, A. S.; Richards, J. J.; Nilsson, M.; Morris, G. A., Quantitative Interpretation of Diffusion-Ordered NMR Spectra: Can We Rationalize Small Molecule Diffusion Coefficients? *Angew. Chem.* **2013,** 125, 3281-3284.

89. Frisch, M. J.; Trucks, G. W.; Schlegel, H. B.; Scuseria, G. E.; Robb, M. A.; Cheeseman, J. R.; Scalmani, G.; Barone, V.; Mennucci, B.; Petersson, G. A. H. N., M. Caricato, X. Li, H. P. Hratchian, A. F. Izmaylov, J. Bloino, G. Zheng, J. L. Sonnenberg, M. Hada, M. Ehara, K. Toyota, R. Fukuda, J. Hasegawa, M. Ishida, T. Nakajima, Y. Honda, O. Kitao, H. Nakai, T. Vreven, J. A. Montgomery, Jr., J. E. Peralta, F. Ogliaro, M. Bearpark, J. J. Heyd, E. Brothers, K. N. Kudin, V. N. Staroverov, T. Keith, R. Kobayashi, J. Normand, K. Raghavachari, A. Rendell, J. C. Burant, S. S. Iyengar, J. Tomasi, M. Cossi, N. Rega, J. M. Millam, M. Klene, J. E. Knox, J. B. Cross, V. Bakken, C. Adamo, J. Jaramillo, R. Gomperts, R. E. Stratmann, O. Yazyev, A. J. Austin, R. Cammi, C. Pomelli, J. W. Ochterski, R. L. Martin, K. Morokuma, V. G. Zakrzewski, G. A. Voth, P. Salvador, J. J. Dannenberg, S. Dapprich, A. D. Daniels, O. Farkas, J. B. Foresman, J. V. Ortiz, J. Cioslowski, and D. J. Fox *Gaussian 09, Revision D.01*, Gaussian Inc: Wallingford CT, 2009.

90. Marenich, A. V.; Cramer, C. J.; Truhlar, D. G., Universal solvation model based on solute electron density and on a continuum model of the solvent defined by the bulk dielectric constant and atomic surface tensions. *J. Phys. Chem. B* **2009,** 113, 6378-96.

91. Dub, P. A.; Gordon, J. C., The mechanism of enantioselective ketone reduction with Noyori and Noyori-Ikariya bifunctional catalysts. *Dalton Trans* **2016,** 45, 6756-6781.

6 STEREOCHEMISTRY OF THE NOYORI TRANSFER HYDROGENATION OF ACETOPHENONE

6.1 INTRODUCTION

One of the key benefits of the Noyori TsDPEN type catalysts is the high enantioselectivity of the reaction; typically greater than 90% enantiomeric excess in the alcohol product can be achieved.[1-2] Whilst the relationship between the stereochemistry of the ligand and the product is regularly correlated, the importance of the stereochemistry at the metal centre has received less consideration.

For each of the two enantiomers of the TsDPEN ligand there exists a diastereotopic catalyst pair, with different configurations at the ruthenium centre (Scheme 6.1). [Note: The nominal stereochemistry at ruthenium is dependent on the bound substituent (Cl or H), and the CIP descriptor will be inverted in the chloride precursor, **1,** compared to the hydride intermediate, **3**. (i.e. **(RRR)-1** will have the same structure as **(RRS)-3**)[3-4]

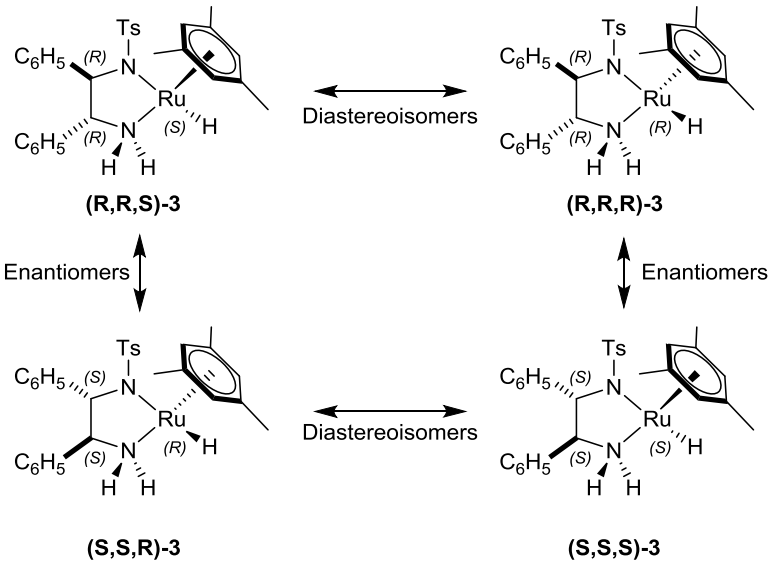

Scheme 6.1: Structure and relationship between possible enantiomers/diastereoisomers of Noyori's RuH(TsDPEN)(mesitylene) catalyst.

During the asymmetric transfer hydrogenation reaction, the catalyst undergoes an achiral-at-ruthenium intermediate state, **2** (Scheme 6.2), meaning that the distribution of diastereomeric hydrides must be a result of a directing influence from the TsDPEN ligand.

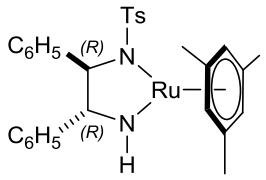

(R,R)-2

Scheme 6.2: Structure of the 16-electron Ru((R,R)-TsDPEN)(mesitylene) complex, believed to be an intermediate in the catalytic asymmetric transfer hydrogenation reaction.

For each of the two sets of catalyst diastereomers, there are six different conformational isomers, with different conformations around the ligand backbone C-C and C-N bonds (Scheme 6.3). Of these possible isomers, conformation theory, along with DFT calculations of the catalyst[5-7] suggest that the ligand backbone should adopt a *gauche* conformation (λ in the case of the RR ligand), optimising orbital overlap whilst minimising steric interaction between the two phenyl rings and the mesitylene (Scheme 6.4). This is supported by experimental crystal structures.[8-9]

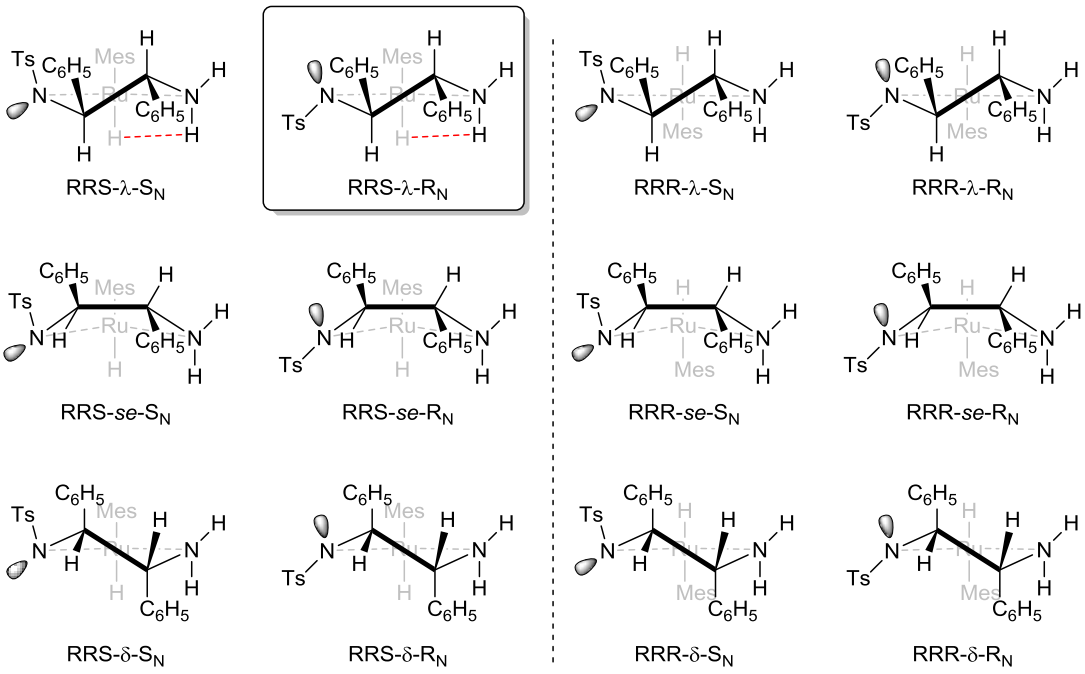

Scheme 6.3. Possible conformational isomers of Noyori's RuH(TsDPEN)(mesitylene) catalyst, with δ, λ or symmetric envelope (se) geometry of the TsDPEN ring and axial (S) or equatorial (R) configuration of the tosyl nitrogen. Adapted from Dub, 2016.[10]

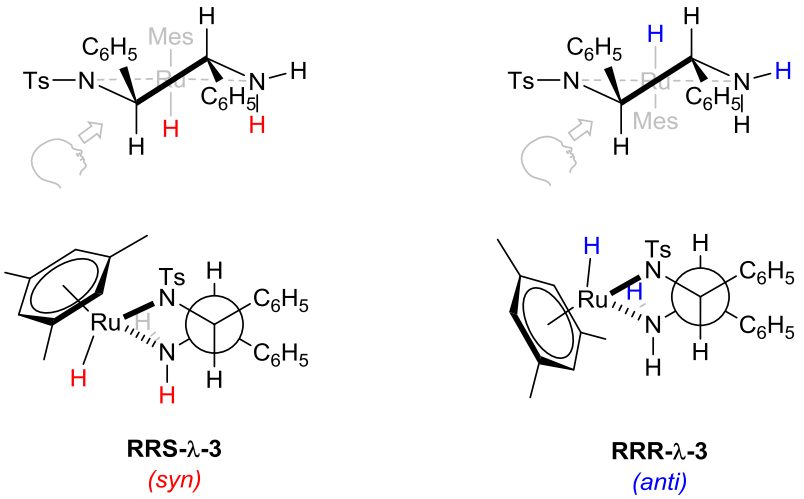

Scheme 6.4: Expected geometry of Noyori's RuH(TsDPEN)(mesitylene) catalyst for the two possible diastereomers resulting from inversion of chirality at ruthenium.

As reported in a computational study by Noyori, the δ/λ conformation of the ligand backbone results in different spacial relationships between the Ru-H and N-H bonds for the two diastereomers.[5] In the case of the (R,R)-TsDPEN ligand, the steric interaction of the phenyl groups favours the λ-conformer. This results in a *syn*-configuration for the Ru-H and N-H bonds in the RRS diastereomer, and an *anti*-configuration in the RRR diastereomer. Noyori's calculations suggested a 3-5 kcal/mol stability enhancement for the *syn* geometry, which is usually attributed to N-H---Cl/H hydrogen bonding.[5, 9]

The generally accepted mechanism for asymmetric transfer hydrogenation with Noyori's catalyst involves a 6-membered 'outer-sphere' transition state where both the Ru-H and N-H hydrogens are transferred simultaneously (Scheme 1.9). The spacial relationship between the Ru-H and N-H bonds is therefore very important for catalysis, since the hydrogen transfer is expected to be most efficient when a six-membered cyclic transition state can be formed. If all other steric and electronic interactions are ignored, the *syn*-conformation would be expected to be more catalytically active than the *anti*-configuration, since this leads to the most favourable orbital overlap between the H-Ru-N-H and substrate, and so a lower transition state energy.

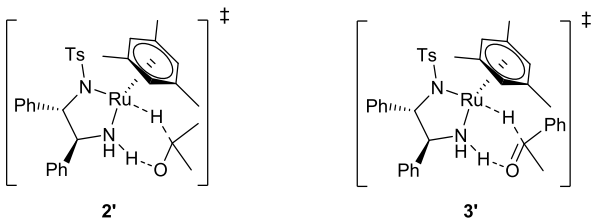

Scheme 6.5: Proposed transition states for the Noyori catalyst in the transfer hydrogenation of acetophenone.[11]

The formation of catalyst diastereomers has important implications for the stereochemistry of the product. Product enantiomeric excess (EE_{Prod}) may be considered as a product of the enantiomeric excess of the reaction using enantiopure catalyst (EE_0) and the enantiomeric excess (or diastereomeric excess) of the catalyst itself (ee_{cat}).[12-13]

Equation 6.1 $$EE_{Prod} = EE_0 \cdot ee_{cat}$$

This is a somewhat over-simplified approach and assumes that the reaction rate and catalyst enantioselectivities are identical for both catalyst enantiomers. This is by no means the case, and there are well documented examples where one catalyst enantiomer is much more active, and dominates the product forming reaction.[14-15] Improved models have been devised, which take into account the non-linear effects produced by differing catalytic rates, or inversion of catalyst stereochemistry (usually shown as a result of a dimerisation process).[12-13, 16]

6.2 Experimental Evidence for Diastereomers of Complex 3

The formation of a minor diastereomer of hydride complex **3** was first reported by Noyori and Haack in 1997,[8] where it was observed in the ^{1}H NMR spectrum of the hydride complex **3** as a small peak, <1% of the size of the major hydride peak. Based on the crystal structure of the isolated hydride complex, Noyori assigned the major diastereomer as **(S,S,R)-3**, with a chemical shift of -5.47 in toluene-d_8.[8] The same paper also reported the crystal structures of the catalyst chloride precursor, **1**, and unsaturated intermediate, **2** (referred to by Noyori as the 'true catalyst').

Noyori's 1997 paper did not provide evidence for the existence of either isomer of **3** during catalysis, however it was shown that both **2** and **3** (presumably containing <1% of the minor hydride diastereomer observed in the NMR spectrum) were able to catalyse the asymmetric transfer hydrogenation of acetophenone with a range of alcohols, and in the absence of base.[8]

Since first reported by Noyori, diastereomeric hydride pairs have been observed and discussed in the literature for both the Noyori TsDPEN catalyst and tethered derivatives.[17-20] The reported ratio of the two diastereomer peaks in the ^{1}H NMR spectrum appears to vary considerably depending on reaction conditions and catalyst structure.

With the exception of one study looking at the kinetics of Wills' C3-tethered catalyst,[18] most reported spectra of the diastereomeric hydride complexes were performed under non-catalytic conditions with stoichiometric reagents, and there have been no reported examples of multiple catalyst diastereomers being observed during catalytic turnover. Indeed, as noted in Chapter 5, the low concentrations of catalyst employed in the reaction makes detecting catalytic species in situ challenging.

6.2.1 Observation of catalyst diastereomers using FlowNMR

Using FlowNMR spectroscopy, in combination with selective excitation of the hydride region, two hydride peaks were observed at -5.26 and -6.54 ppm (isopropanol-h_8) during the catalytic asymmetric transfer hydrogenation of acetophenone using (R,R)-**1** (Figure 6.1).

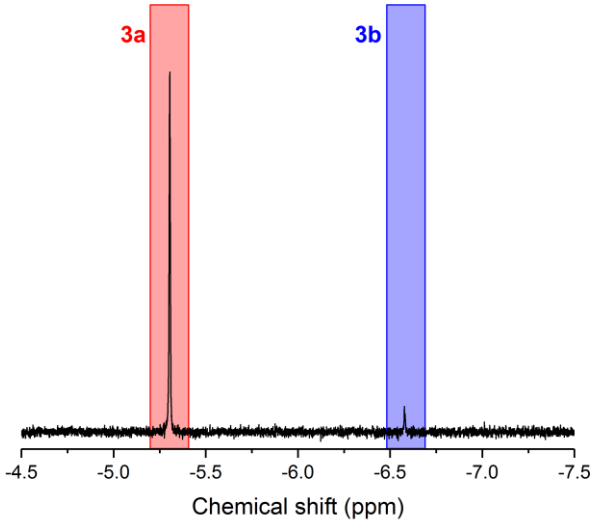

*Figure 6.1: ^{1}H NMR spectra of hydrides **3a** and **3b**, during the course of catalytic transfer hydrogenation of acetophenone to (R)-1-phenylethanol in flow at 4 mL/min (400 mM acetophenone, 10 mM KOH, 2 mM **(1)**, 9.5 mL dry isopropanol, 20°C). Selective excitation using a gradient spin echo pulse sequence with a shaped 180° pulse centred at -5.5 ppm (8 scans, 2 s acquisition time, 1 s delay time, 1600 µs Gaussian shaped pulse; spectra processed with 0.1 Hz exponential line broadening).*

When pre-catalyst **1** was dissolved in 0.01 M KOH solution in isopropanol, hydride **3a** is formed immediately (Figure 6.2). Although **3a** slowly deactivates (see Chapter 5), no other hydride species were observed until the addition of the acetophenone substrate, at which point hydride **3b** started to form. Unlike **3a**, the formation of **3b** did not happen instantaneously, instead requiring around 30 minutes to reach equilibrium.

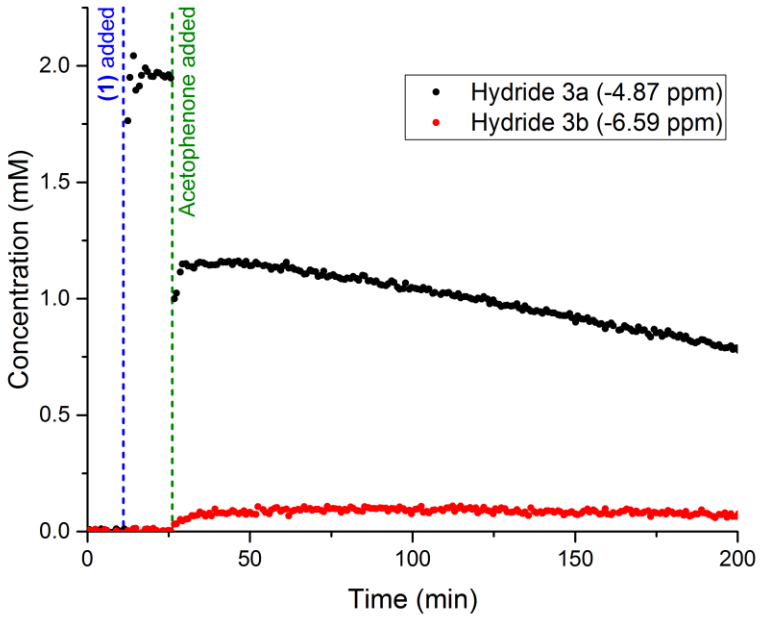

*Figure 6.2: Concentration profiles of hydride peaks **3a** (-4.87 ppm) and **3b** (-6.59 ppm), during the course of catalytic transfer hydrogenation of acetophenone to (R)-1-phenylethanol in flow at 4 mL/min (400 mM acetophenone, 10 mM KOH, 2 mM **(1)**, 9.5 mL dry isopropanol, 20°C). Selective excitation using a gradient spin echo pulse sequence with a shaped 180° pulse centred at -5.5 ppm (8 scans, 2 s acquisition time, 1 s delay time, 1600 µs Gaussian shaped pulse; spectra processed with 0.1 Hz exponential line broadening).*

The absence of any **3b** prior to the addition of acetophenone supports the assignment of this peak as a diastereoisomer of **3a**, since the catalyst must pass through achiral intermediate **2** (Scheme 6.2) to convert between the two diastereomers, which is only possible when substrate is present to turn over the catalyst.

6.2.2 Achiral ligand

An alternative explanation for the appearance of **3b** could be that either acetophenone or the products, 1-phenylethanol and acetone, bind to the hydride, altering its chemical shift. Formation of an acetophenone adduct may be ruled out, as this would be expected to form immediately after addition of acetophenone, which is not observed, however an adduct with product would be expected to produce a similar concentration profile to that observed in Figure 6.2.

To test whether this was the case, catalyst **6**, with an achiral Ts(ethylenediamine) ligand was synthesised (Scheme 6.6). Whilst still chiral at ruthenium, the absence of any chirality in the ligand ensures that no diastereomeric hydride species are possible.

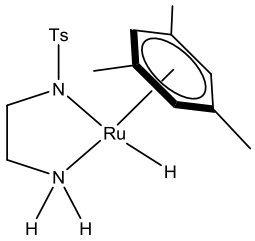

6

*Scheme 6.6: Structure of the RuH(Ts(ethylenediamine))(mesitylene) catalyst, **6**, showing the achiral Ts(ethylenediamine) ligand.*

Under identical conditions to Figure 6.2, **6** exhibited a single hydride peak at -6.20 ppm throughout the entire course of the reaction (>3 hours), remaining unchanged in the presence of base, substrate and product (Figure 6.3). This confirms that that the two peaks observed previously were a result of diastereomers with differing chirality at ruthenium, and not a result of product adducts.

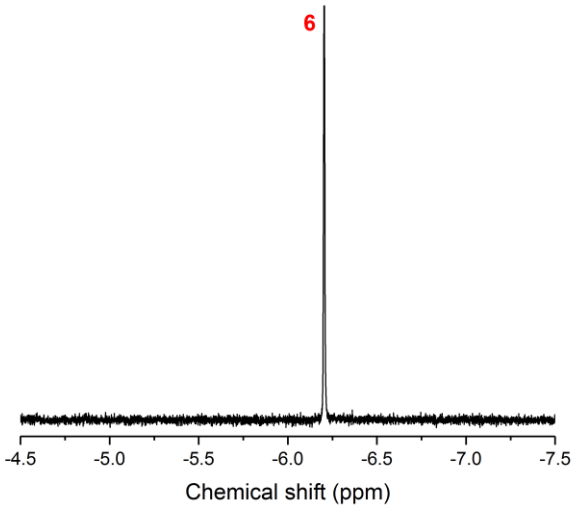

*Figure 6.3: ^{1}H NMR spectra of hydride **6**, during the course of catalytic transfer hydrogenation of acetophenone to (R)-1-phenylethanol in flow at 4 mL/min (400 mM acetophenone, 10 mM KOH, 2 mM **(6)**, 9.5 mL dry isopropanol, 20°C). Selective excitation using a gradient spin echo pulse sequence with a shaped 180° pulse centred at -5.5 ppm (8 scans, 2 s acquisition time, 1 s delay time, 1600 µs Gaussian shaped pulse; spectra processed with 0.1 Hz exponential line broadening).*

The ethylenediamine complex was also able to catalyse the transfer hydrogenation of acetophenone to 1-phenylethanol, however at a slower rate than **1**, and without favouring either product enantiomer of course (Figure 6.4). The concentration of hydride present during turnover was lower for the ethylenediamine complex, which is likely to be due to a difference in catalyst speciation due to the different electronic properties of the ligand. The deactivation rate also appeared lower for the ethylenediamine complex, which may indicate that the phenyl rings play a role in promoting the loss of the mesitylene, possibly due to the increased steric interactions between the amine and arene ligands.

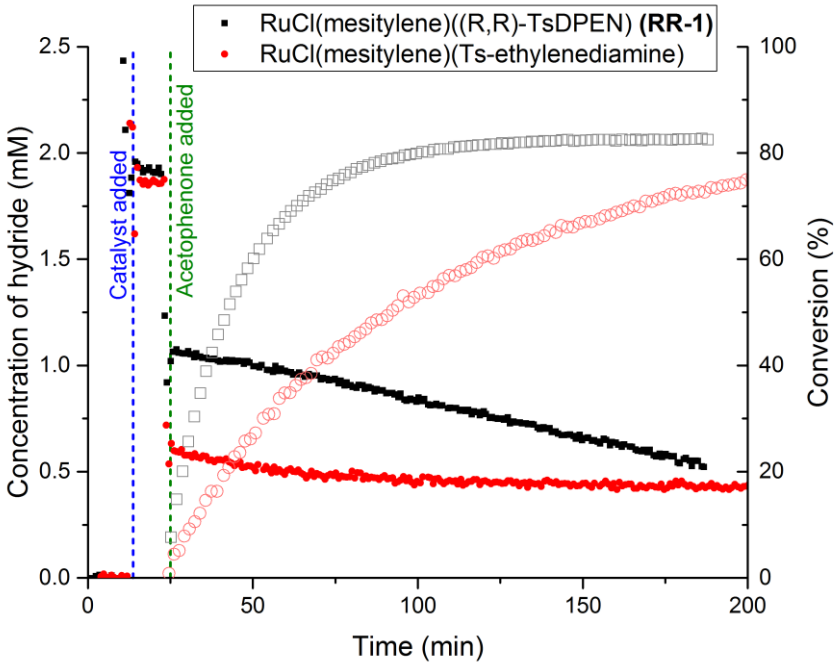

*Figure 6.4: Concentration of hydride intermediate (**3** or **6**), during the course of catalytic transfer hydrogenation of acetophenone to (R)-1-phenylethanol in flow at 4 mL/min with either **1** or RuCl(mesitylene)(Ts-ethylenediamine) catalyst (400 mM acetophenone, 10 mM KOH, 2 mM cat., 9.5 mL dry isopropanol, 20°C). Selective excitation using a gradient spin echo pulse sequence with a shaped 180° pulse centred at -5.5 ppm (8 scans, 2 s acquisition time, 1 s delay time, 1600 µs Gaussian shaped pulse; spectra processed with 0.1 Hz exponential line broadening).*

6.2.3 Interconversion of Diastereomers

The evolution of the ratio between the two diastereomers, **3a** and **3b**, over time has been discussed previously in the literature.[18, 20] The process appears to be strongly dependent on reaction conditions and ligand modification, with observed ratios of diastereomers varying between 65:1 to 1:5.

Whilst less noticeable than for **3a**, **3b** also underwent slow deactivation over a period of several hours under reaction conditions (Figure 6.5). The ratio between **3a** and **3b** remained unchanged, indicating that the deactivation rate is the same for both diastereomers. This suggests that either the deactivation pathway is the same for both diastereomers, or that exchange between the two diastereomers is rapid enough to maintain the relative concentrations of each diastereomer throughout the deactivation.

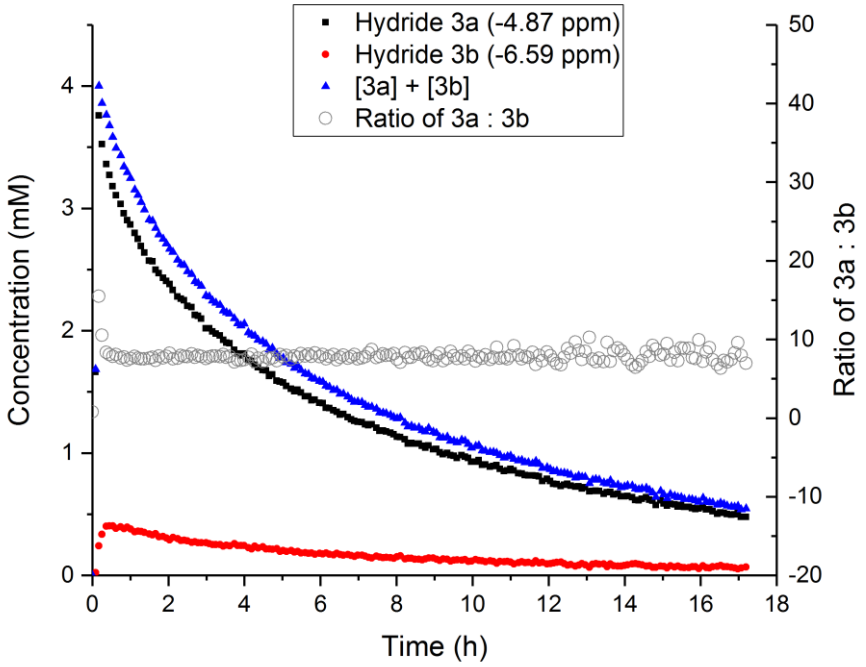

*Figure 6.5: Concentration profiles of hydride peaks **3a** (-4.87 ppm) and **3b** (-6.59 ppm) in flow at 4 mL/min (40 mM acetophenone, 360 mM rac-1-phenylethanol, 360 mM acetone, 10 mM KOH, 4 mM **(1)**, 9.5 mL dry isopropanol, 20°C). Selective excitation using a gradient spin echo pulse sequence with a shaped 180° pulse centred at -5.5 ppm (8 scans, 2 s acquisition time, 1 s delay time, 1600 µs Gaussian shaped pulse; spectra processed with 0.1 Hz exponential line broadening).*

Analysing the hydride (formed by reaction of **2** with 10 equivalents of IPA) in an inert solvent such as C_6D_6 and without product or substrate present allowed the relationship between the two diastereomers to be investigated over longer time periods (Figure 6.6). In the absence of substrate, the interconversion between **3a** and **3b** relies on trace acetone from catalyst activation, resulting in a much slower rate of exchange. Over the course of 36 h, slow interconversion between the two catalyst species resulted in an equilibrium ratio of 4.2:1 under these conditions.

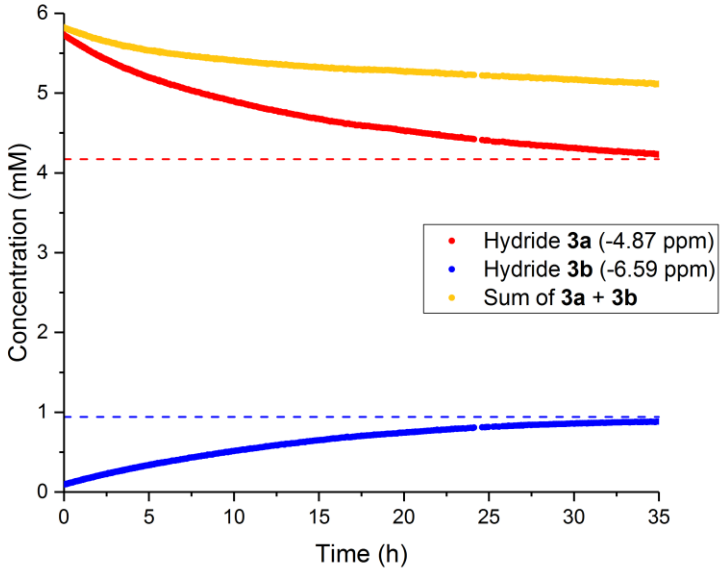

*Figure 6.6: Concentration profiles of hydride peaks **3a** (-4.87 ppm) and **3b** (-6.59 ppm), during the interconversion between diastereomers **3a** and **3b** in the absence of product or substrate. (6 mM (**1**), 12 mM NaO^{i}Pr, 0.5 mL C_6D_6, 20 µL isopropanol, 25 °C, Ar atmosphere, conventional NMR tube). Selective excitation using a gradient spin echo pulse sequence with a shaped 180° pulse centred at -5.5 ppm (8 scans, 2 s acquisition time, 1 s delay time, 1600 µs Gaussian shaped pulse; spectra processed with 0.1 Hz exponential line broadening).*

6.2.4 Assignment of Diastereomers

To assign the absolute stereochemistry of each of the two hydride peaks observed in the ^{1}H NMR spectra, Nuclear Overhauser Effect (NOE) NMR experiments were performed to identify through-space interactions within the complex.

Similar NOE experiments have been performed previously by Strotman *et al.* on the related formic acid/triethylamine system,[20] however the reported peak positions for the two diastereomers are substantially different to the isopropanol system, making comparison difficult.

As the assignment of the two backbone CHs is vital for the correct assignment of absolute stereochemistry, TOCSY spectra of the interaction between the CH and NH_2 protons were acquired with varying mixing times. A medium range $^{4}J_{HH}$ coupling is observed for the N$\underline{H}_2$-CH-C$\underline{H}$-NTs proton and a shorter range $^{3}J_{HH}$ coupling for the N$\underline{H}_2$-C$\underline{H}$ proton , which may also be observed in the additional splitting of the C$\underline{H}$-NH_2 proton peak, confirming the assignment of the two CH protons.

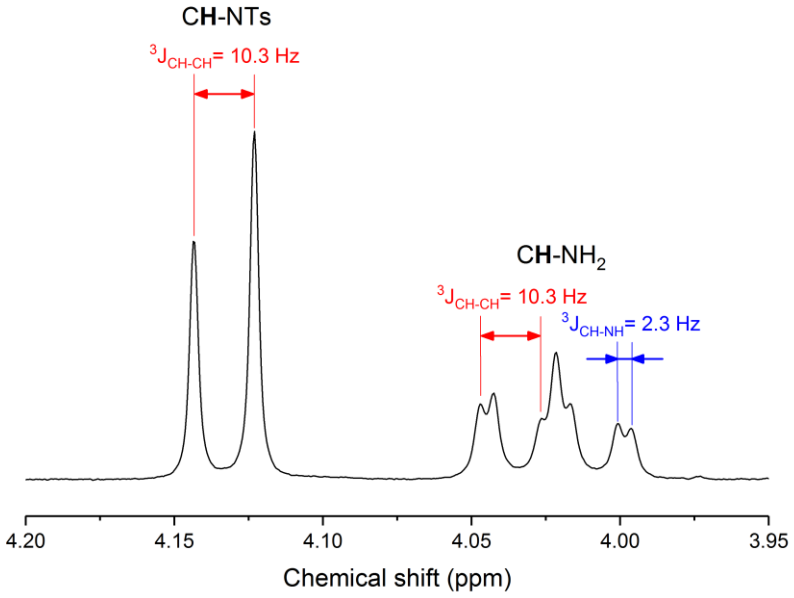

*Figure 6.7: ^{1}H NMR spectrum of hydride complex **3a** showing ligand backbone CH peaks with $^{3}J_{CH\text{-}CH}$ and $^{3}J_{CH\text{-}NH}$ coupling values indicated.*

6.2.4.1 Hydride 3a

Hydride **3a** (-4.87 ppm in C_6D_6) shows correlation to the mesitylene CH_3 and CH protons at 2.00 and 4.60 ppm respectively and tosyl C<u>H</u>-C-SO_2 protons at 7.68 ppm, along with the C<u>H</u>-NTs proton at 4.13 ppm and axial-NH proton at 4.54 ppm (Figure 6.8). In all cases, a corresponding NOE interaction was observed at the hydride when these protons were excited, confirming that the signals observed are true NOE interactions and not spectral artefacts.

The presence of an NOE interaction between the hydride and the C<u>H</u>-NTs proton indicates that the two nuclei are in close proximity, suggesting that they are on the same face of the complex. This is reinforced by the absence of any NOE interaction between the C<u>H</u>-NH_2 proton at 4.01 ppm and the hydride, which despite being more closely connected through bonds, are on opposing faces of the molecule and therefore do not show any NOE interaction. This indicates the assignment of the hydride at -4.87 ppm to be the **(R,R,*S*)-3** diastereomer in the λ (*syn*) configuration.

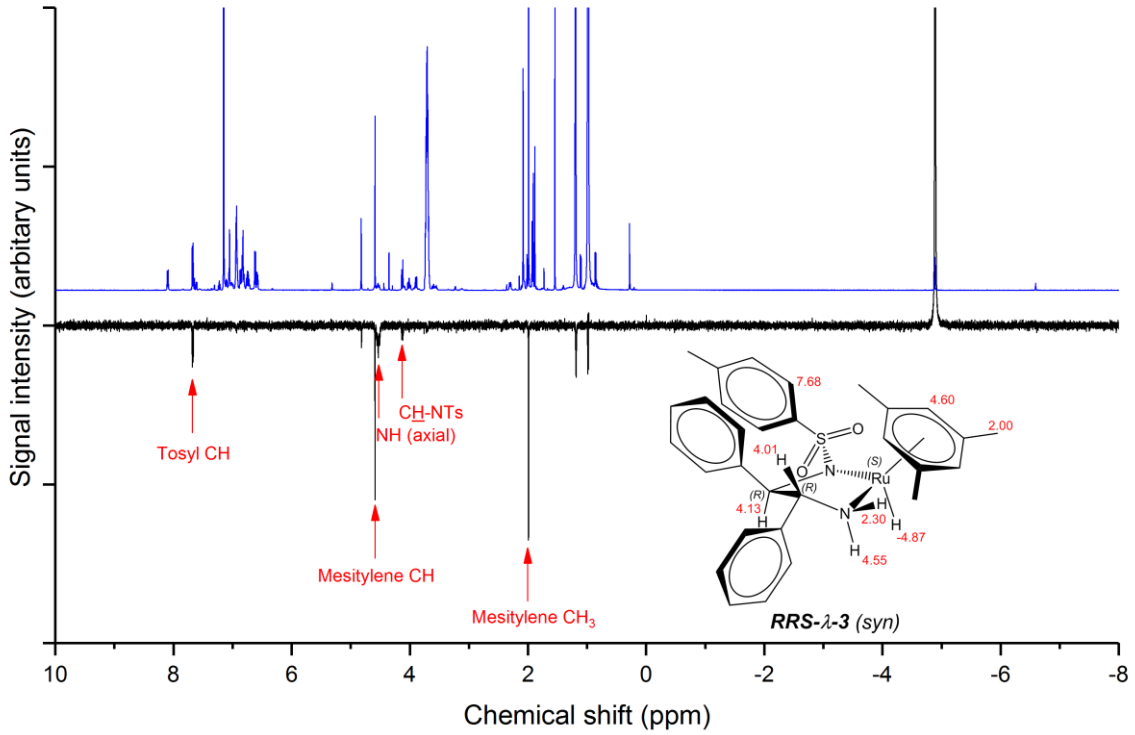

*Figure 6.8: ^{1}H and selective NOE NMR spectra of hydride **3a** (-4.87 ppm), showing NOE interactions of the hydride with other protons within the molecule, chemical shifts and assignment (6 mM (**1**), 12 mM NaO^{i}Pr, 0.5 mL C_6D_6, 20 µL isopropanol, 25 °C, Ar atmosphere, conventional NMR tube). ^{1}H acquisition (16 scans, 2.18 s acquisition time, 1 s delay time, spectra processed with 0.3 Hz exponential line broadening). Selective NOE using a gradient spin echo pulse sequence with a shaped 180° pulse centred at -4.88 ppm (2048 scans, 2.18 s acquisition time, 2 s delay time, 1600 µs Gaussian shaped pulse; spectra processed with 0.1 Hz exponential line broadening).*

To confirm the assignment, NOE interactions between the backbone CH protons and the mesitylene were also measured. The mesitylene exhibited strong, mutual NOE interactions with the C<u>H</u>-NH_2 and equatorial-NH protons, but not with the C<u>H</u>-NTs proton, supporting the assignment of the hydride as RRS.

A significant difference in the chemical shift values of the axial (4.55 ppm) and equatorial (2.30 ppm) NH protons was observed. The higher chemical shift value for the axial NH suggests a more acidic proton, which is consistent with the greater reactivity at this position in plane with the Ru-H bond.

6.2.4.2 Hydride 3b

Hydride **3b** (-6.59 ppm in C_6D_6) showed NOE correlations to a different set of mesitylene peaks at 1.91 and 4.35 ppm, however no reliable NOE interactions with either backbone CH proton were observed at this concentration (Figure 6.9). A small peak at 3.13 ppm might possibly be an interaction with a shifted NH proton, however concentrations are too low for assignment with any confidence, even when 10240 transients were acquired.

Whilst conclusive assignment of **3b** is hampered by low concentrations, the fact that the mesitylene protons were shifted supports the theory that the second hydride peak is the **(R,R,R)-3** diastereomer in the λ (*anti*) configuration, as inversion of stereochemistry at ruthenium will affect the magnetic environment of all bound ligands.

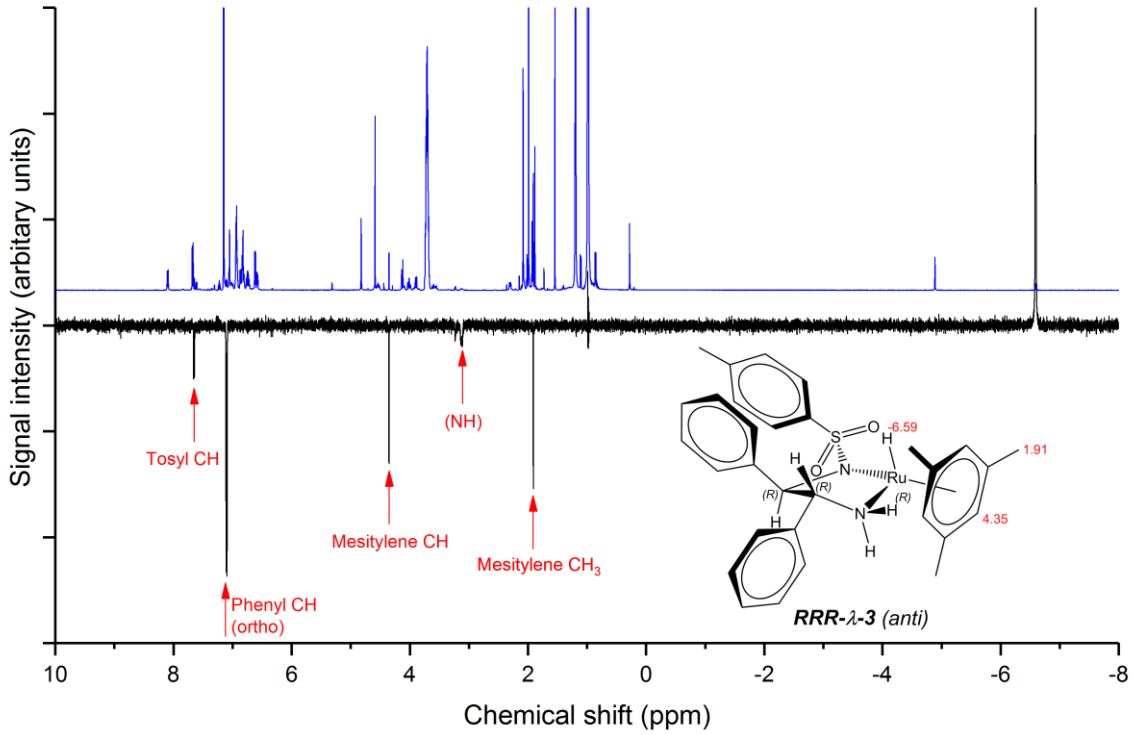

*Figure 6.9: ^{1}H and selective NOE NMR spectra of hydride **3b** (-6.59 ppm), showing NOE interactions of the hydride with other protons within the molecule, chemical shifts and assignment (6 mM (**1**), 12 mM NaO^{i}Pr, 0.5 mL C_6D_6, 20 µL isopropanol, 25 °C, Ar atmosphere, conventional NMR tube). ^{1}H acquisition (16 scans, 2.18 s acquisition time, 1 s delay time, spectra processed with 0.3 Hz exponential line broadening). Selective NOE using a gradient spin echo pulse sequence with a shaped 180° pulse centred at -4.88 ppm (2048 scans, 2.18 s acquisition time, 2 s delay time, 1600 µs Gaussian shaped pulse; spectra processed with 0.1 Hz exponential line broadening).*

6.2.5 Prediction of NMR shifts from computed tensors

To confirm the NMR assignments of the diastereomers and ascertain the configuration of each structure, Density Functional Theory (DFT) calculations were used to predict the NMR chemical shifts of both diastereomers.

The calculation of isotropic NMR shifts requires fully energy minimised structures calculated at a high level of theory to gain accurate results. For this study, an SDD effective core potential basis set was used for ruthenium, with a 6-311++G(d,p) basis set on the arene, ligand backbone and heteroatoms and a 6-31+G(d) basis set for the phenyl rings. This basis set combination has previously been reported to provide good energy and frequency prediction results with ruthenium hydrides.[6, 10, 21]

To convert the calculated isotropic shifts into predicted NMR chemical shifts, a calibration model is needed. A linear correction curve, constructed from a library of ruthenium hydride complexes with known NMR shifts is reported to give accurate results for a range of ruthenium hydrides.[22] For each of the four functionals used to calculate the NMR shifts, a range of ruthenium hydride complexes with known NMR shifts were also optimised and used to produce a calibration curve (Figure 6.10).

Library compounds:

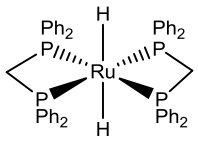

trans-$Ru(H)_2(dppm)_2$

δ_{exp}= -4.7 ppm

δ_{theor}= -5.23 ppm

δ_{theor}= -2.98 ppm

δ_{theor}= -5.33 ppm

δ_{theor}= -7.53 ppm

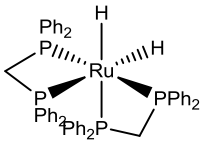

cis-$Ru(H)_2(dppm)_2$

δ_{exp}= -7.4 ppm

δ_{theor}= -7.4 ppm

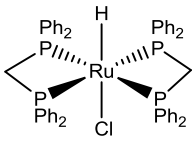

trans-$Ru(H)Cl(dppm)_2$

δ_{exp}= -14.0 ppm

δ_{theor}= -13.88 ppm

δ_{theor}= -14.00 ppm

δ_{theor}= -14.00 ppm

δ_{theor}= -14.53 ppm

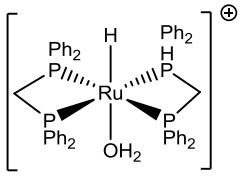

trans-$[Ru(H)(OH_2)(dppm)_2]^+$

δ_{exp}= -18.8 ppm

δ_{theor}= -15.43 ppm

δ_{theor}= -17.17 ppm

δ_{theor}= -16.63 ppm

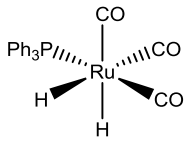

fac-$Ru(H)_2(CO)_3(PPh_3)$

δ_{exp}= -6.7, -6.7 ppm

δ_{theor}= -5.23, -5.58 ppm

δ_{theor}= -6.69, -6.84 ppm

δ_{theor}= -6.09, -6.70 ppm

δ_{theor}= -6.20, -6.70 ppm

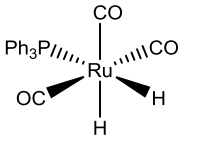

mer-$Ru(H)_2(CO)_3(PPh_3)$

δ_{exp}= -6.7, -7.3 ppm

δ_{theor}= -5.51, -6.65 ppm

δ_{theor}= -6.79, -7.15 ppm

δ_{theor}= -6.74, -8.13 ppm

δ_{theor}= -6.95, -6.95 ppm

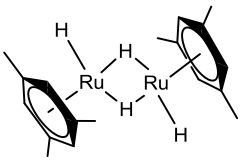

$[RuH(mesitylene)(\mu\text{-}H)_2]_2$

δ_{exp}= -1.52, -17.18 ppm

δ_{theor}= -1.03, -1.88, -18.14, -18.24 ppm

Functional:

rωB97X-D

rB3PW91

rPBE1PBE

rM06L

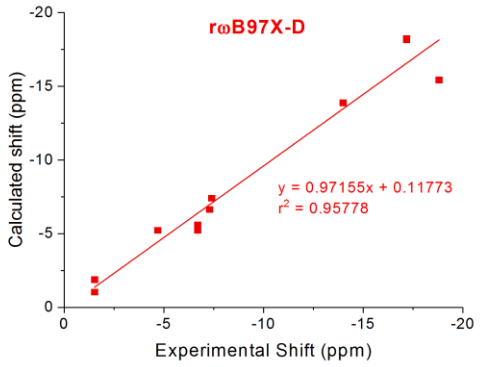

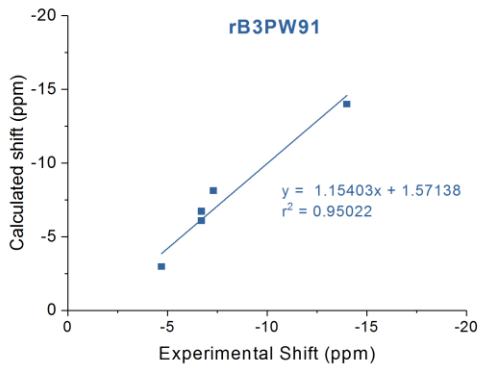

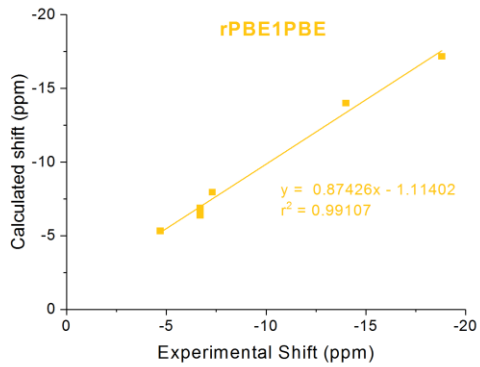

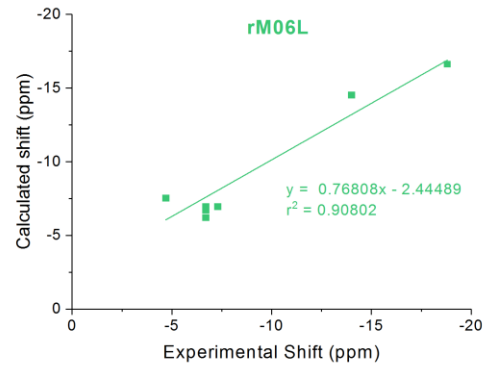

Figure 6.10: a) Ruthenium hydride complexes used to build calibration curves for NMR shift prediction, with their corresponding literature[22-23] and calculated [SDD/6-311++G(d,p)/6-31+G(d)] chemical shift values. b) Calibration curves for the rωB97X-D, rB3PW91, rPBE1PBE and rM06L functionals.

Using the correction curves for each functional, the predicted chemical shifts for both **RRS-3** and **RRR-3** were calculated (Table 6.1). Although the predicted shifts are all significantly lower than the experimentally observed peaks, there is a consistent trend across all four functionals of the major RRS diastereomer, **3a**, being more de-shielded than the minor RRR diastereomer, **3b**. This is also consistent with the assignments based on NOE interactions.

*Table 6.1 Calculated [SDD/6-311++G(d,p)/6-31+G(d)] and experimental (C_6D_6) NMR shifts of complexes **RRS-3a** and **RRR-3b**.*

Functional	Predicted Chemical Shift (ppm)	
	RRS-3a	RRR-3b
Experimental	**-4.87**	**-6.59**
rωB97X-D	-2.66	-2.71
rPBE1PBE	-2.11	-4.04
rB3PW91	-2.79	-3.89
rM06L	-3.54	-3.65

The discrepancies between the predicted and experimental shifts and separation of the peaks may be ascribed to the solvation model used in the calculation of NMR tensors. In all cases a continuum solvation model was applied, surrounding the molecule with a field of uniform charge. Explicit solvation of the hydride may enable more accurate NMR shift prediction; however this is computationally expensive. As observed experimentally, both **3a** and **3b** are very sensitive to changes in solvation, with the chemical shift changing by up to 1 ppm depending on solvent choice.

6.3 Implications of Diastereomeric Hydride Complexes in Asymmetric Transfer Hydrogenation Catalysis

Consideration of the minor **RRR-3b** hydride diastereomer requires a modification of the mechanism discussed in Chapter 5, to include a second cycle as shown in Scheme 6.7. The enantioselectivity of the 'minor' cycle has not been previously reported, and so whilst the cycle is assumed to proceed with opposite selectivity to the 'major' cycle to produce the minor (S)-1-phenylethanol product, this has not yet been proven (this will be discussed further in Section 6.3.3).

Whilst the chiral pocket of **RRS-3a** favours the formation of (R)-1-phenylethanol, reverse binding of acetophenone is also possible, resulting in the formation of the minor (S)-1-phenylethanol product (Scheme 6.7, Grey). Computational studies have indicated that the enantioselectivity of **RRS-3a** is dependent on a C-H···π interaction between mesitylene and the acetophenone phenyl ring, which is expected to result in an enantioselectivity of >97% for this cycle.[10] The same process for the minor **RRR-3b** hydride would result in the formation of (R)-1-phenylethanol. This gives four possible product forming steps, with the overall product enantioselectivity depending on both substrate binding and catalyst enantiopurity.

Although **RRS-3a** is the highest concentration ruthenium hydride species present in the reaction mixture, this does not mean that it is necessarily the major product forming species. Paradoxically, it is frequently the case that intermediates which are long-lived enough to observe under reaction conditions are too stable to be involved in producing the major product, and it is the highly reactive 'minor' intermediates that are responsible for product formation ('major-minor' mechanism).[14-15] Switching between a 'major-minor' mechanism and the more straightforward 'lock-and-key' mechanism (major catalyst intermediate forms the major product) may be possible by changing reaction conditions to reduce the concentration of minor intermediate present in the reaction.[14]

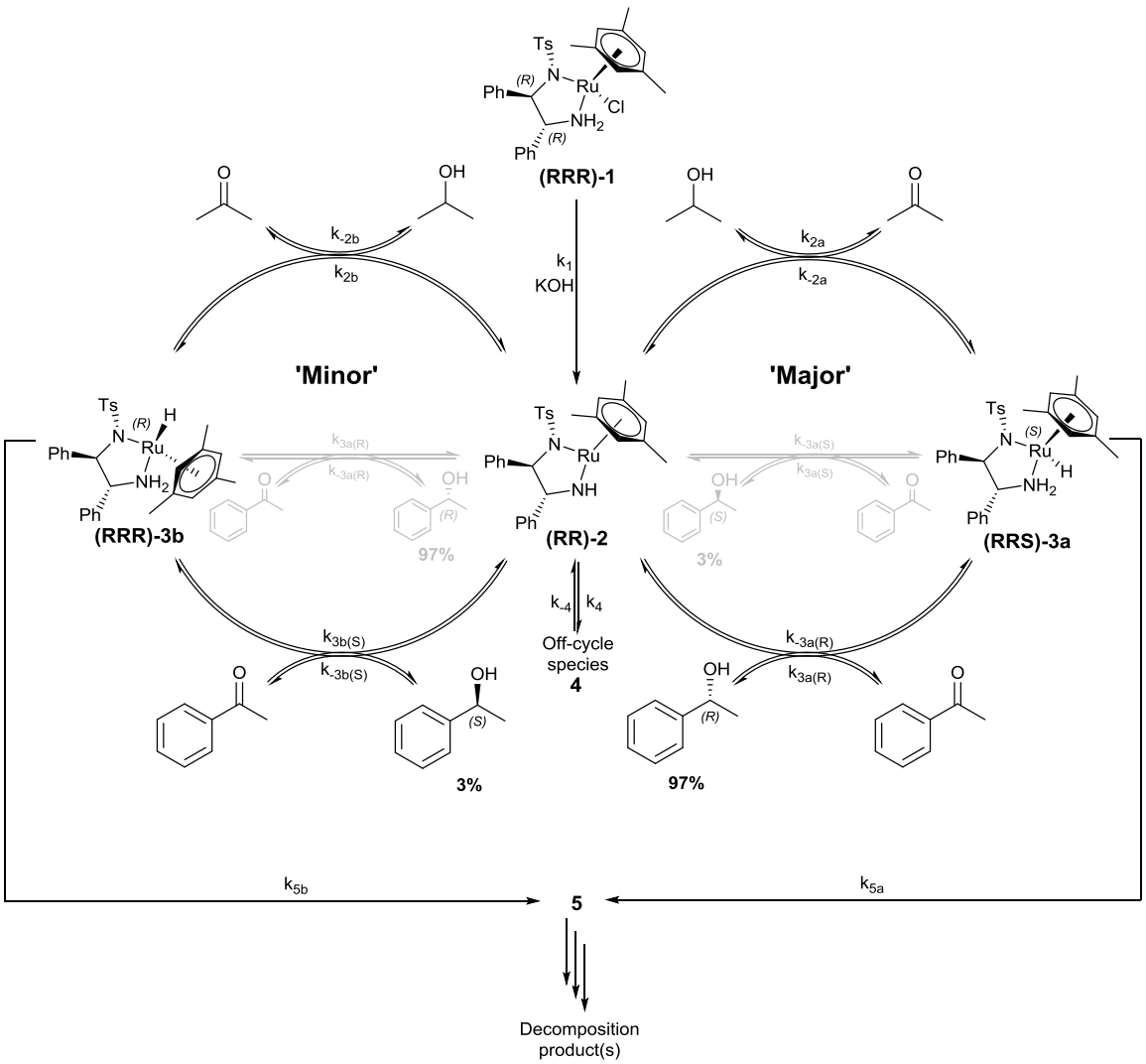

*Scheme 6.7: Expanded mechanism for catalytic transfer hydrogenation using **(1)** including base-induced formation of off-cycle species **(4)** from **(2)** and deactivation of **(3)** to **(5)** showing possible major and minor hydride pathways. The relative rates of the formation of (S) and (R)-1-phenylethanol with **(RRR)-3** are not known, so the stereochemistry of the major product from this cycle may be inverted.*

'Major-minor' product distributions require a pre-equilibrium of catalyst intermediates where both major and minor species are present.[14] No such pre-equilibrium exists for the Noyori asymmetric transfer hydrogenation reaction, since no **RRR-3b** was observed until acetophenone was added (Figure 6.2). As product formation began immediately after addition of acetophenone, with no induction time, this strongly suggests that the product is formed by the major **RRS-3a** intermediate in a 'lock-and-key' mechanism. Computational studies indicate that the minor **RRR-3b** hydride diastereomer should favour the (S)-1-phenylethanol product as expected,[10] again supporting a 'lock-and-key' mechanism where the major hydride diastereomer **RRS-3a** forms the major (R)-1-phenylethanol product.

6.3.1 Reactivity of diastereomeric hydrides 3a and 3b

To test the reactivity of the two diastereomeric hydrides **3a** and **3b**, carbon dioxide gas was bubbled into a solution containing the two diastereomers. Carbon dioxide is known to react rapidly with the hydride complex to form a ruthenium-formate species, which is the most abundant intermediate observed during transfer hydrogenation carried out in a triethylamine-formic acid solvent mixture.[20] As shown in Figure 6.11, the major hydride diastereomer, **3a**, reacted rapidly with CO_2, disappearing from the NMR spectrum almost entirely. In contrast, the minor hydride, **3b**, barely reacted at all, with the concentration of **3b** remaining unchanged after bubbling with CO_2.

This is a clear indicator that **3a** is much more reactive than **3b** (as is expected from the orientation of the RuH and NH bonds and computational studies[5, 10]), supporting the 'lock-and-key' mechanism, where the major **RRS-3a** hydride diastereomer leads to the formation of the major (R)-1-phenylethanol product.

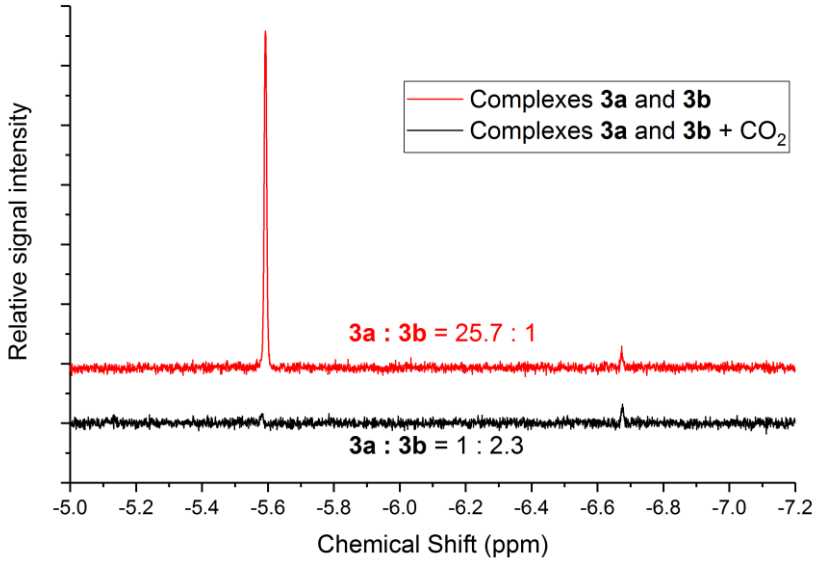

*Figure 6.11: ^{1}H NMR spectra of a) hydride complexes **3a** and **3b** b) hydride complexes **3a** and **3b** after bubbling with CO_2 leading to reaction of **3a** to form the corresponding ruthenium-formate complex. (THF-H_8, 20°C). Selective excitation using a gradient spin echo pulse sequence with a shaped 180° pulse centred at -9 ppm (12 scans, 1.33 s acquisition time, 1 s delay time, 1000 µs Gaussian shaped pulse; spectra processed with 0.3 Hz exponential line broadening). Data courtesy of Dan Berry.*

6.3.2 Tethered catalyst

Tethered versions of the Noyori catalyst have been developed, using either ether or alkyl linkages to attach the arene ring to the TsDPEN ligand, either via the NH_2 nitrogen or sulfonyl groups.[17-18, 24-26] These catalysts are highly active at low catalyst loadings, but more importantly are much more stable than the non-tethered catalyst under reaction conditions, allowing evolution of catalyst species to be monitored over longer time periods.

For this study, Wills' C3-tethered pre-catalyst, **7** (Scheme 6.8) was chosen, as it is one of the most selective and versatile of the tethered catalysts.[17] As with the non-tethered Noyori catalyst, the 16-electron 'unsaturated' intermediate, **8**, and 18-electron hydride intermediate, **9**, are both known to exist in the reaction mixture (Scheme 6.8). In isopropanol solution, the tethered catalyst existed predominantly as **8**, with less than a third of the catalyst in the hydride intermediate **9**. This is contrary to the non-tethered catalyst, where hydride intermediate **3** comprises >90% of the catalyst speciation prior to entering turnover (Figure 6.12). The difference in catalyst speciation may also be clearly seen in the colour of the reaction mixture (Figure 6.13), with the deep purple colour observed for the tethered catalyst indicating a high concentration of unsaturated intermediate, **8**.

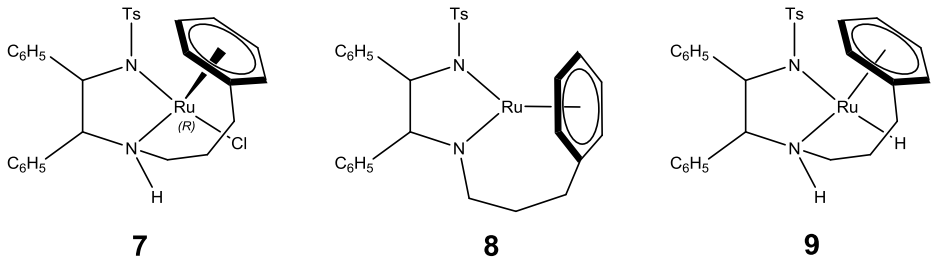

*Scheme 6.8: Structures of Wills' RuCl(TsDPEN-C3-benzene) pre-catalyst, **7**, along with active species **8** and **9**.*

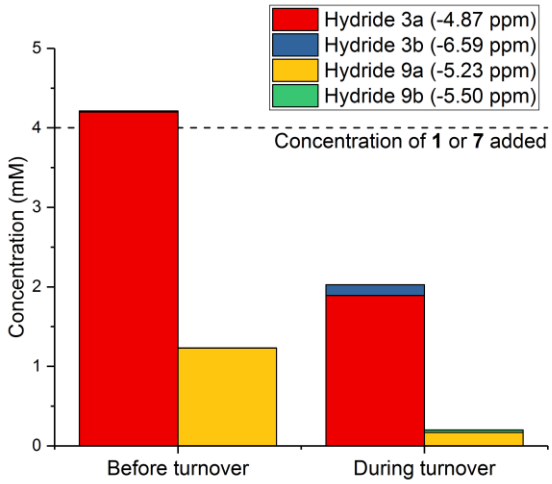

*Figure 6.12: Comparison between the concentration of non-tethered hydride intermediates **3a** and **3b**, and tethered hydride intermediates **9a** and **9b** before entering turnover and during turnover (4 mM **(1)** or **(7)**, 20 mM KOH, 400 mM acetophenone, 10 mL isopropanol, 20°C). Selective excitation using a gradient spin echo pulse sequence with a shaped 180° pulse centred at -5.5 ppm (8 scans, 2 s acquisition time, 1 s delay time, 1600 µs Gaussian shaped pulse; spectra processed with 0.1 Hz exponential line broadening).*

a)  b) 

*Figure 6.13: Photographs of reaction mixtures for the asymmetric transfer hydrogenation of acetophenone using a) non-tethered catalyst **1**, and b) tethered catalyst **7** (4 mM cat., 20 mM KOH, 400 mM acetophenone, 10 mL isopropanol, 20°C).*

Under the same conditions (4 mM cat, 20 mM KOH, 400 mM acetophenone, 10 mL isopropanol), the tethered catalyst, **7**, was less active than **1** in the reduction of acetophenone (k_{obs} = 6.19 mM/min for **7**, compared to k_{obs} = 18.7 mM/min for **1**). The lower activity may be linked to the difference in catalyst speciation, since a lower concentration of hydride **9** during catalysis is indicative of the reaction of unsaturated intermediate, **8**, with isopropanol being rate limiting (k_2 in Scheme 6.7). The lower reactivity (and therefore higher turnover concentration) of **8** compared to **2** is due to the more donating nature of the secondary amine, leading to a greater stabilisation of the 16 electron complex **8** in the tethered catalyst.

As with the non-tethered catalyst, the concentration of hydride **9a** immediately droped when acetophenone was added and turnover began, due to reaction with substrate forming **8** (Figure 6.14). Whilst the concentration of acetophenone remained high, the concentration of **9** remained low; again indicating that the reaction of **8** with isopropanol to regenerate **9** is the rate limiting step (k_2 in Scheme 6.7). As acetophenone was consumed, the overall reaction rate slowed down until the point at which the reaction of **9** with acetophenone became rate limiting (k_3 in Scheme 6.7) and the concentration of **9** increased again. The concentration of **9** never reached pre-turnover values as even after the reaction had reached equilibrium, the catalyst was still actively involved in cycling between substrate and product. This deviation in hydride concentration during the initial stages of turnover was also observed for the non-tethered hydride, **3**, although the effect is less pronounced (Chapter 5, Figure 5.9).

Over longer periods of time, a slow decrease in concentration of **9a** was observed, along with an increase in the concentration of **9b**. Whilst the same exchange has been observed for the non-tethered catalyst between hydride diastereomers, **3a** and **3b** (Figure 6.6), the rate of catalyst deactivation was much faster than for the tethered catalyst, meaning that the interconversion of the hydride diastereomers under reaction conditions cannot be studied over long periods of time for the non-tethered catalyst, **1**. For the tethered catalyst, **7**,

deactivation was much slower, allowing tracking of the concentration of both diastereomers over periods of 24 h without significant catalyst deactivation (Figure 6.14).

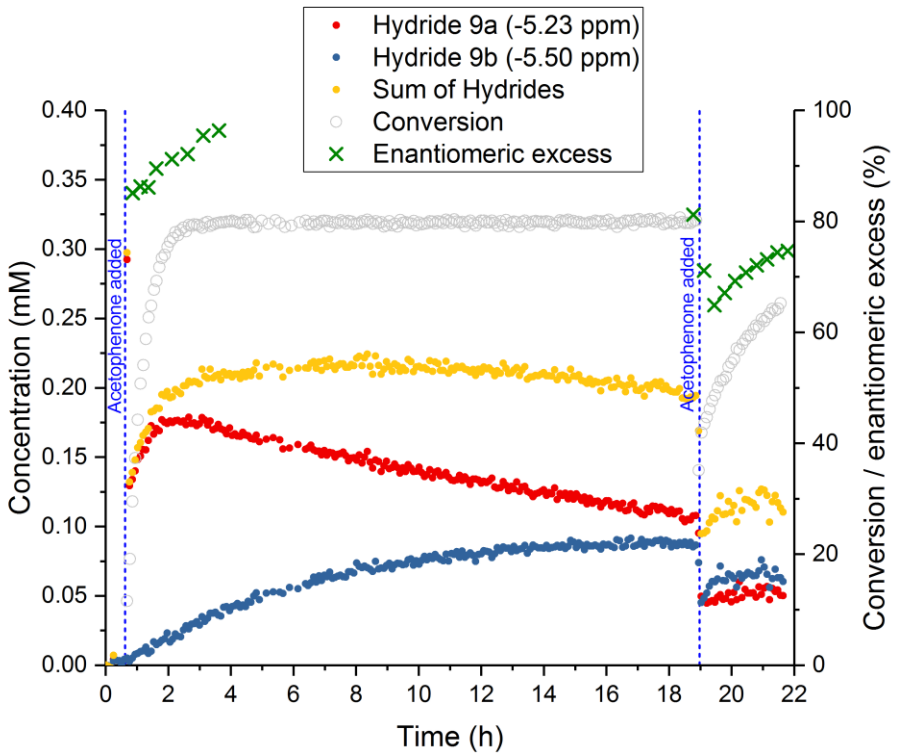

*Figure 6.14: Concentration of hydride species **9a** and **9b**, conversion and enantioselectivity data for the asymmetric transfer hydrogenation of acetophenone to (S)-1-phenylethanol (4 mM **RR-7**, 20 mM KOH, 400 mM acetophenone (additional 400 mM acetophenone added after 19 h), 10 mL isopropanol, 20°C).*

The distribution of the two diastereomers, **9a** and **9b**, appeared to reach equilibrium after approximately 18 h, with roughly equal concentrations of each diastereomer. To test whether the catalyst speciation between the two diastereomers has any effect on reaction rate, an additional 400 mM of acetophenone was added to restart the reaction.

The reaction rate was substantially reduced for the second addition of acetophenone (k'_{obs}= 1.05 mM.min^{-1} compared to k_{obs}= 6.19 mM.min^{-1} for the initial reaction). As the overall catalyst concentration remains constant over the course of the reaction, this suggests that diastereomer **9b** has minimal catalytic activity.

This may be confirmed by comparing the turnover frequency (TOF) for both initial and secondary reactions, calculated using the concentration of **9a** only; this gives a value for the initial reaction of $TOF^{9a}_{t=0}$ = 31.0 min^{-1}, compared to $TOF^{9a}_{t=19\ h}$ = 23.3 min^{-1} for the second addition of acetophenone. If **9b** were active in the reaction, the apparent TOF with respect to **9a** would be expected to be greater for the second addition of acetophenone than the first. Since this is not the case, it may be concluded that **9b** has minimal catalytic activity. Together with the evidence for the lack of reactivity of non-tethered hydride diastereomer **3b**, this

strongly supports a 'lock-and-key' mechanism for product formation. The small decrease in TOF for the second addition of acetophenone is attributed to an increased rate component from the reverse reaction, due to the presence of product from the initial reaction.

The lack of activity of **9b** is consistent with the structure of the RRR diastereomer, where the Ru-H and NH proton are not in the same plane (Scheme 6.9), which is expected to increase the barrier to reaction.

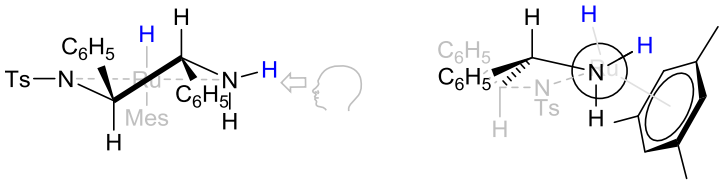

RRR-λ-3b
(anti)

*Scheme 6.9: Schematic of **RRR-λ-3b** structure, showing the (anti)-configuration of the Ru-H and N-H bonds.*

6.3.3 Density Functional Theory calculations

Density Functional Theory (DFT) calculations have previously been used to explore possible reaction pathways for the Noyori asymmetric transfer hydrogenation reaction.[5-7, 10, 21, 27] Whilst most studies have focused on the differences between the concerted outer-sphere hydrogen transfer mechanism proposed by Noyori,[5, 28] and the conventional inner-sphere mechanism (with or without cooperative ligand effects),[9] a few have investigated the role that the ligand plays in directing stereochemistry of the product.[7, 9-10]

A 2013 paper by Dub *et al.* demonstrated the differences in transition state energy barriers for the formation of R- and S-1-phenylethanol from **RRS-3** in the gas state, and with explicit solvation.[7] In this work, they propose that the acetophenone first forms a hydrogen bonded ion pair with the catalyst NH, which helps to stabilise the hydride, as well as positioning the acetophenone in the correct geometry to be reduced (Scheme 6.10). The catalyst and substrate then undergo a 6-member, planar transition state to form the product as a hydrogen bonded ion pair with **RR-2**. The energy barrier for the transition state is higher for the reaction forming S-1-phenylethanol than for R-1-phenylethanol, which is used as the rationale for the difference in product selectivity. Although energy barriers were decreased when explicit solvation with isopropanol was included, the same overall trends in transition state energies were observed.

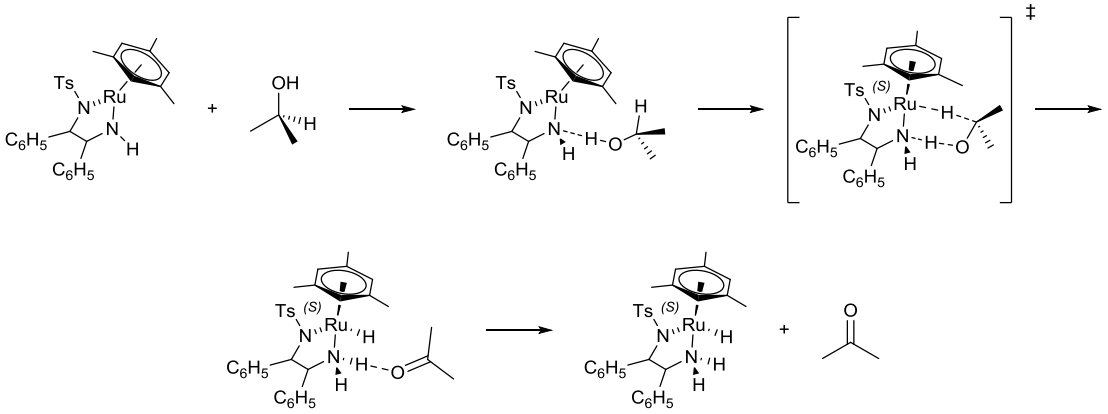

*Scheme 6.10: Reaction mechanism and transition state proposed by Dub (2013), for the reaction of **2** with isopropanol to give **(RRS)-3** and acetone.*[7]

This was then followed up in a 2016 paper investigating the cause of enantioselectivity in asymmetric transfer hydrogenation catalysed by **1**, along with $RuCl_2$(BINAP)(DPEN).[10] They demonstrate using absolute rate theory that a 2 kcal/mol difference in the transition state energies for the two product enantiomers is expected to result in >90 % ee.[29] The difference in transition state energies was attributed to arene C-H···π attractions between the mesitylene and acetophenone arene rings, along with oxygen lone pair-π repulsion between the SO_2 group and acetophenone favouring the transition state where the acetophenone is pointing towards the mesitylene and away from the tosyl group (Scheme 6.11).

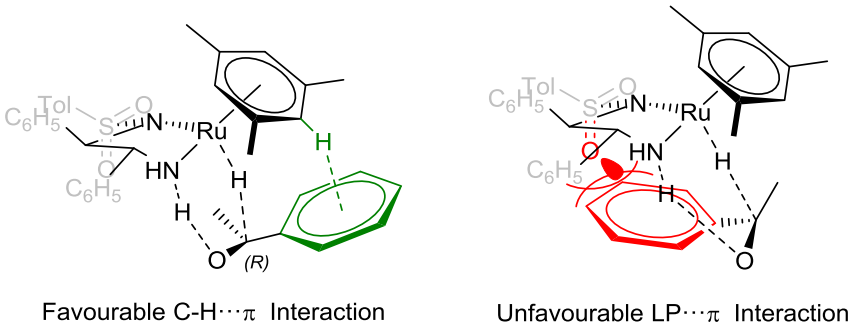

*Scheme 6.11: Schematic of a) favourable C-H···π attractions between the mesitylene and acetophenone arene rings and b) unfavourable oxygen lone pair-π repulsion between the SO_2 group and acetophenone in the transition state between **(RRS)-3a** and acetophenone.*

Although some consideration was given to the probable effects of inversion of stereochemistry at ruthenium, leading to the opposite product enantiomer being formed, no calculations were performed to support this.[10]

To explore the role of the minor catalyst diastereomer in the reaction, DFT calculations were performed to calculate free energies of reaction intermediates and transition states. Calculations were optimised using the rM06L functional and an implicit SMD solvation model (isopropanol), with a simplified basis set of LANL2DZ applied for ruthenium, and 6-31+G(d) for all other atoms.

The first step in the generation of **RRS-3a** or **RRR-3b** is the reaction of **2** with isopropanol. Depending on which face of **2** the isopropanol attacks, different diastereomers of **3** will be produced. The mechanism proposed by Dub[7] (Scheme 6.10) involves the initial formation of a hydrogen bonded ion pair between the isopropanol and NH. Dub reported that these ion pairs are between 1 to 2.5 kcal/mol lower in energy than the free catalyst and substrate.[7]

Using the less computationally expensive rM06L functional, basis set and implicit solvation as described above, these ion pairs were found to have ground state energies that lie between the unbound catalyst and the transition state (Scheme 6.12). Despite this discrepancy, the overall transition state energy barriers are comparable to those reported by Dub.[7] Since the Curtin-Hammett principle dictates that relative reaction rates depend only on transition state energies, the ground state ion-pairs have no influence on the relative reaction rate of each pathway , and are therefore ignored in subsequent calculations.

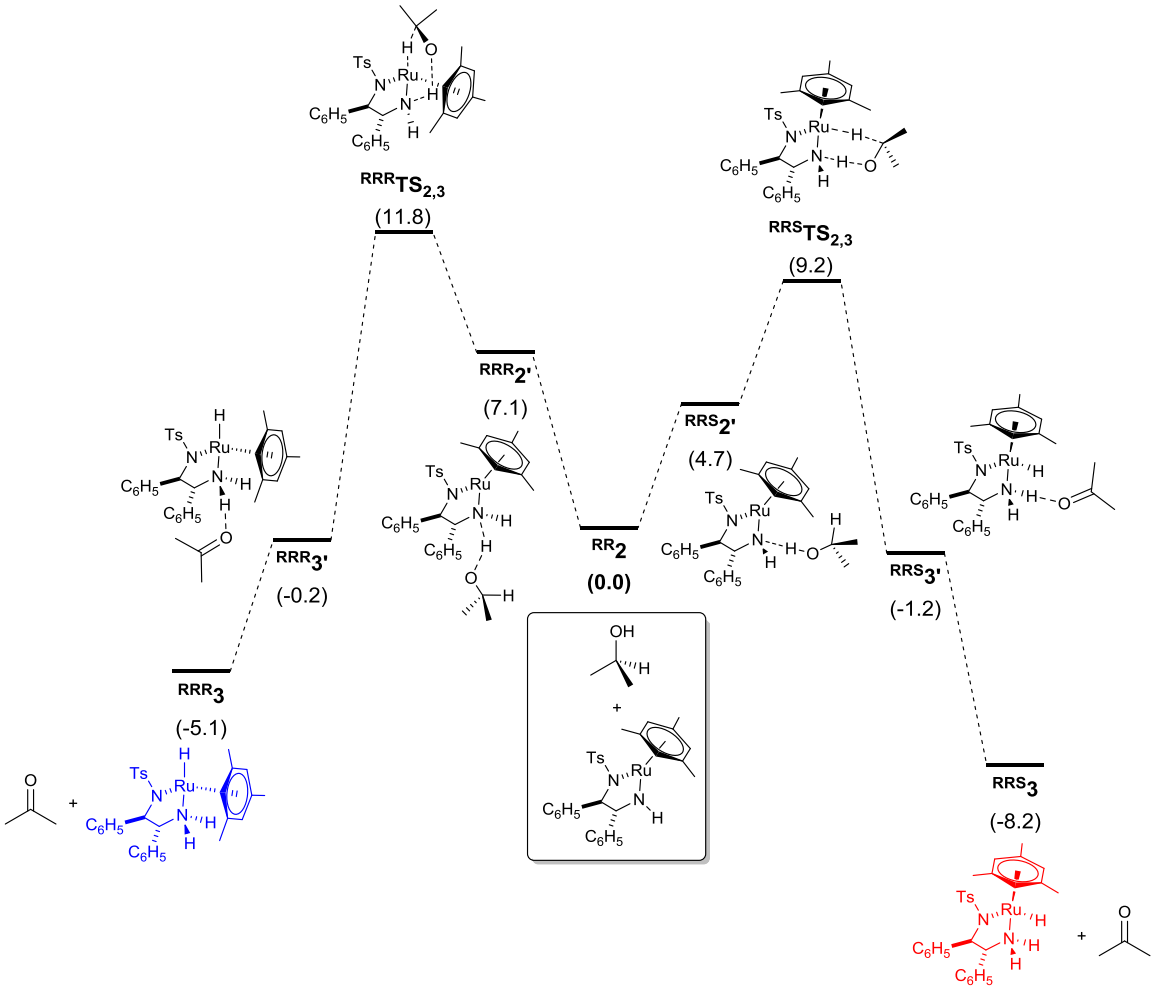

*Scheme 6.12: Proposed mechanism and calculated ground and transition state energies for the formation of either (RRR)-**3** or (RRS)-**3** from (RR)-**2** and isopropanol. [rM06L, LANL2DZ (Ru), 6-31+G(d)].*

As shown in Scheme 6.12, the energy barriers for formation of the **RRS-3a** diastereomer are between 2.4 – 2.6 kcal/mol lower than for the formation of the **RRR-3b** diastereomer, both

for the initial complexation of isopropanol and for the subsequent transition state barrier. The energy span model[30] predicts that for every turnover, the RRS pathway should be around 80 times more favourable than the RRR pathway. Whilst predicting the equilibrium ratio of the two hydrides over many turnover cycles is more complex, involving both forward and reverse rates, the calculations are in good agreement with experimental results which show the major **RRS-3a** hydride dominating in early stages of the reaction.

Calculated ground state energies and transition state energy barriers are reported for the reaction of the major **RRS-3a** isomer with acetophenone.[7] The difference in transition state energy barriers is only 0.8 kcal/mol in the gas phase (0.5 kcal/mol with explicit solvation), which would not be enough to cause the large difference in enantioselectivity observed experimentally. Instead Dub proposed that it is the initial formation of a chiral hydrogen bonded ion pair with the catalyst and substrate that is predicted to determine the stereochemistry of the product, with a difference in predicted ground stage energies of 3.3 kcal/mol in the gas phase (1.5 kcal/mol with explicit solvation) resulting in theoretical enantioselectivities of >97%.[10] As discussed above, using the rM06L/LANL2DZ/6-31+G(d), SMD=Isopropanol method, no reduction in ground state energy was found for these hydrogen bonded ion-pairs, however the difference in energy barrier for the pathways was found to be comparable with Dub's results.

Scheme 6.13 and Scheme 6.14 show the different reaction pathways and energy barriers for the formation of (R) and (S)-1-phenylethanol from acetophenone with **RRS-3a** and **RRR-3b** respectively. Calculated energy barriers differ from those reported by Dub[7] due to differences in solvation, functional and basis sets used in the calculations.

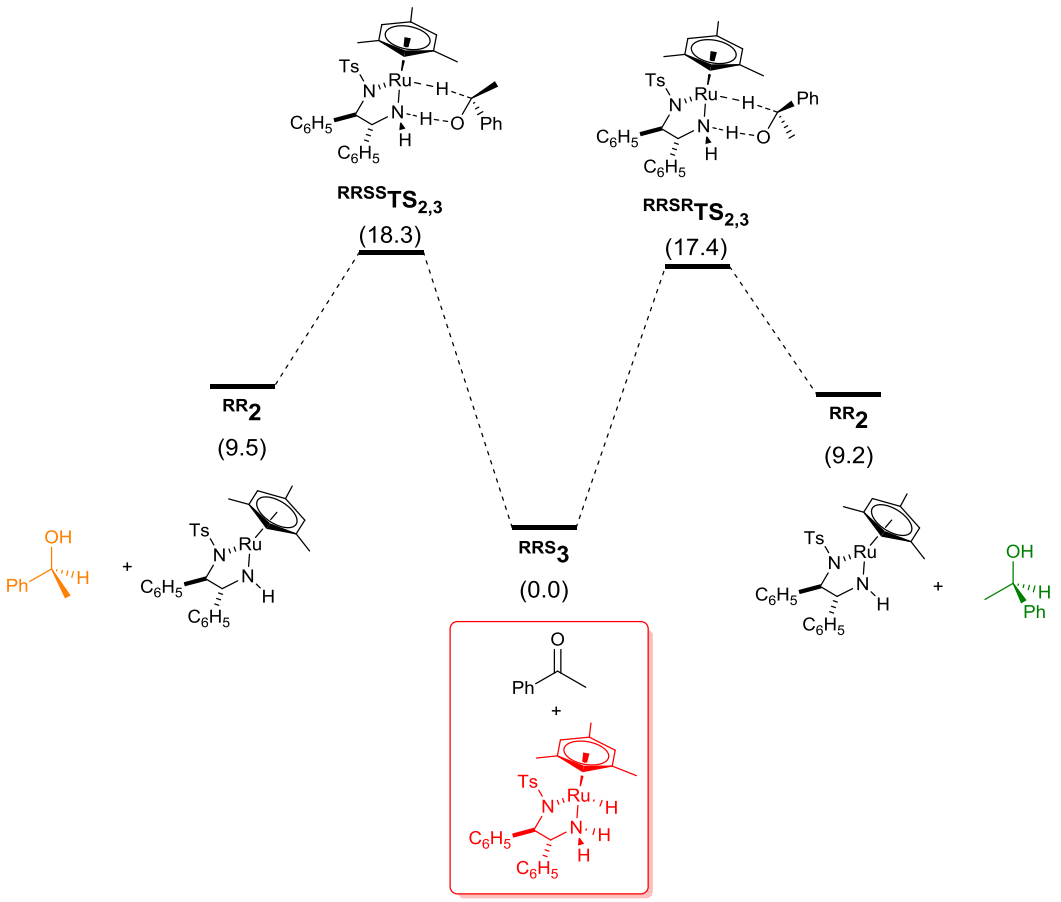

*Scheme 6.13: Proposed mechanism and calculated ground and transition state energies for the reaction of acetophenone and **RRS-3** to form **RR-2** and either (S) or (R)-1-phenylethanol [rM06L, LANL2DZ (Ru), 6-31+G(d)].*

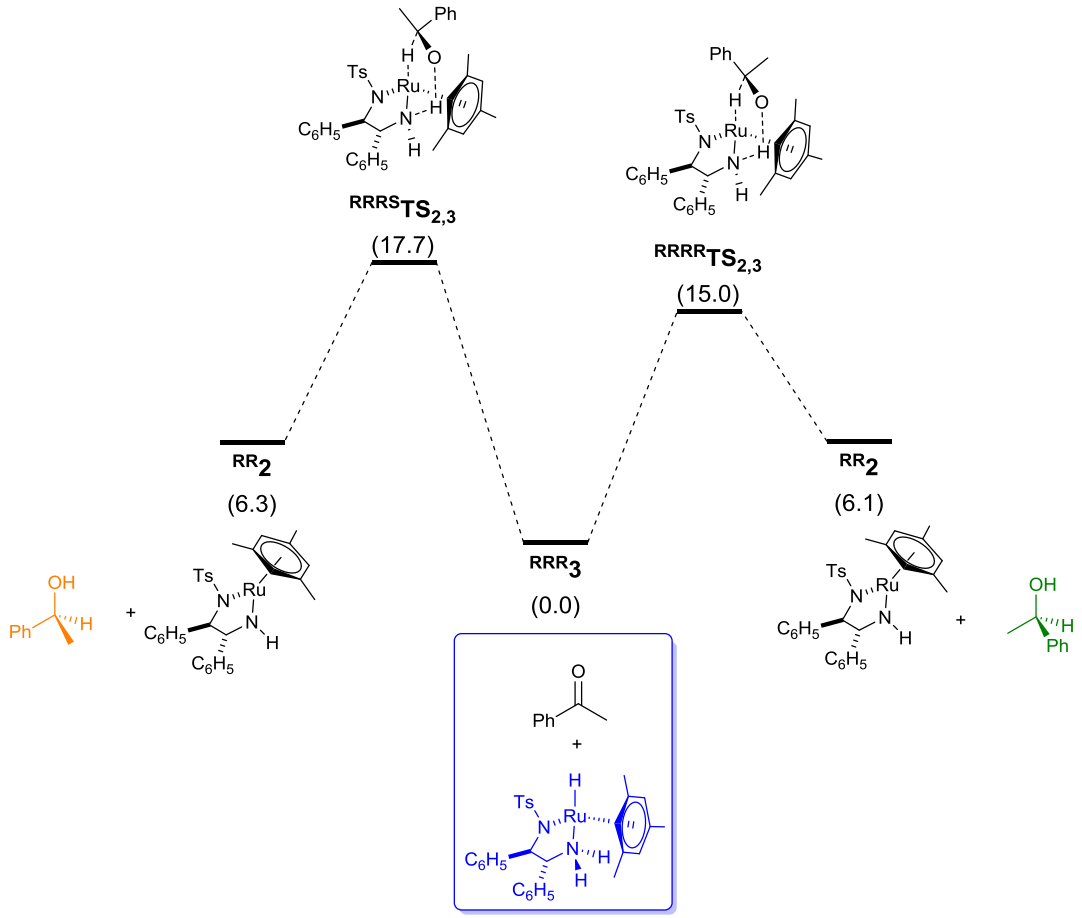

*Scheme 6.14: Proposed mechanism and calculated ground and transition state energies for the reaction of acetophenone and **RRR-3** to form **RR-2** and either (S) or (R)-1-phenylethanol [rM06L, LANL2DZ (Ru), 6-31+G(d)].*

As expected from observed experimental selectivities, **RRS-3a** is also predicted to favour the (R)-1-phenylethanol product, with a difference in predicted energy barriers of 0.9 kcal/mol – very close to the 1.5 kcal/mol reported by Dub.[7]

The result for **RRR-3b** is more surprising. Not only is the complex predicted to favour the formation of the (R)-1-phenylethanol product, rather than the (S)-1-phenylethanol that would be expected, but the calculated energy barrier for doing so is 2.4 kcal/mol lower than for **RRS-3a**. **RRR-3b** is therefore predicted to be the more active catalyst, although both **RRS-3a** and **RRR-3b** are expected to favour the (R)-1-phenylethanol product. This would predict a 'major-minor' product formation mechanism, where the minor catalyst diastereomer results in the major product. Experimental results (Figures 6.11 and 6.14) contradict this finding, showing minimal catalytic activity for the minor **RRR-3b** diastereomer. Since calculated energy barriers may vary slightly depending on the computational method, comparison with results calculated using different functionals and basis set are required to confirm the relative energy barriers for the (R) and (S) reaction pathways, and whether the lower energy barrier for $^{RRRR}TS_{2,3}$ is anomalous.

6.4 A New Tethered Catalyst Architecture

Existing tethered catalyst designs have frequently shown improved stability, enantioselectivity and substrate scope compared to their non-tethered partners.[17, 19, 25] There have been no detailed studies into why the tether improves the catalyst properties, however, as seen in Chapter 5, suppression of catalyst deactivation by arene loss is likely to play a significant role in the improved stability of tethered catalysts.

So far, all tethered catalysts in the literature have the tether attached via one of the TsDPEN nitrogen atoms, either directly, or through the sulfonyl group. Whilst this is an effective means of connecting the two ligands, with a straightforward synthetic route, the existence of an unsaturated intermediate which is achiral at ruthenium means that inversion of stereochemistry may occur (Scheme 6.15), still leading to the two diastereomers previously observed.

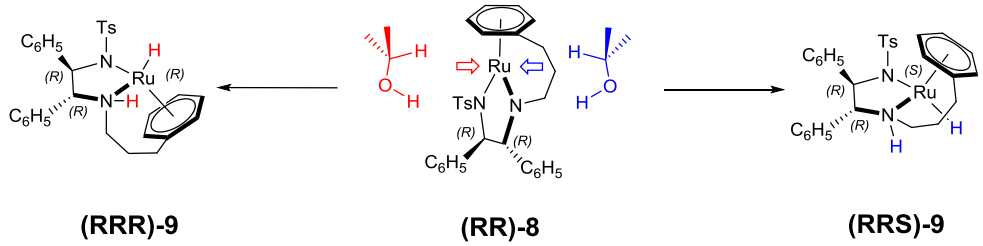

*Scheme 6.15: Inversion of stereochemistry at ruthenium in Wills' tethered catalyst **9** via planar unsaturated intermediate **8**.*

Attachment of the tethering group to the nitrogen atom alters the electronic properties of the ligand, leading to a change in the distribution of catalytic intermediate present in the reaction. In the case of the three-carbon linkage used in Wills' catalyst, **7**, the change in electronic properties of the ligand causes the reaction of unsaturated intermediate, **8**, with isopropanol to become less favourable, reducing the concentration of hydride intermediate, **9** and decreasing the overall reaction rate (Figures 6.12, 6.13 and 6.14).

If a new tether could be designed which both prevents arene loss, whilst also selectively forming the most active diastereomer at the same time, it would improve both catalyst stability and activity, whilst retaining maximum enantioselectivity.

We therefore propose a new tethered catalyst architecture, **10**, where the tether is attached to one of the TsDPEN phenyls. Since steric interaction with the tether prevents approach of substrate to this face of the catalyst, only one hydride diastereomer is possible (Scheme 6.16). Providing that the tether is short enough, interconversion by rotation of the tethered arene is also prevented, locking the catalyst into a single configuration. As shown earlier in this

chapter, the RRS (or SSR) hydride diastereomer is both the major and most active catalyst species, therefore the new catalyst architecture aims to selectively form this diastereomer only.

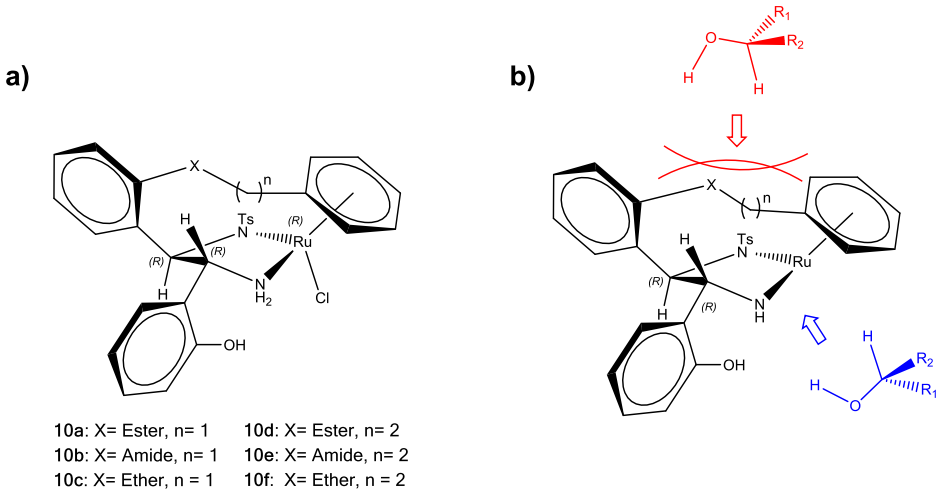

Scheme 6.16: a) Proposed new tethered catalyst architecture. b) Steric interaction with tether prevents substrate approach from top face of catalyst, whilst bottom face remains unhindered.

The proposed new ligand is based around a N-para-toluenesulfonyl-1,2-bis(2-hydroxyphenyl)-1,2-ethylenediamine (TsDPOHEN) backbone, with one of the phenol groups tethered back to the arene ligand by either a 3 or 4 atom linker.

6.4.1 Selection of tethering group

To gain a better understanding of the relative stability and likely geometry of the different catalysts **10a-f**, DFT calculations were performed to predict minimum energy geometries [rM06L functional, LANL2DZ basis set on Ruthenium, 6-31+G(d) basis set on all other atoms].

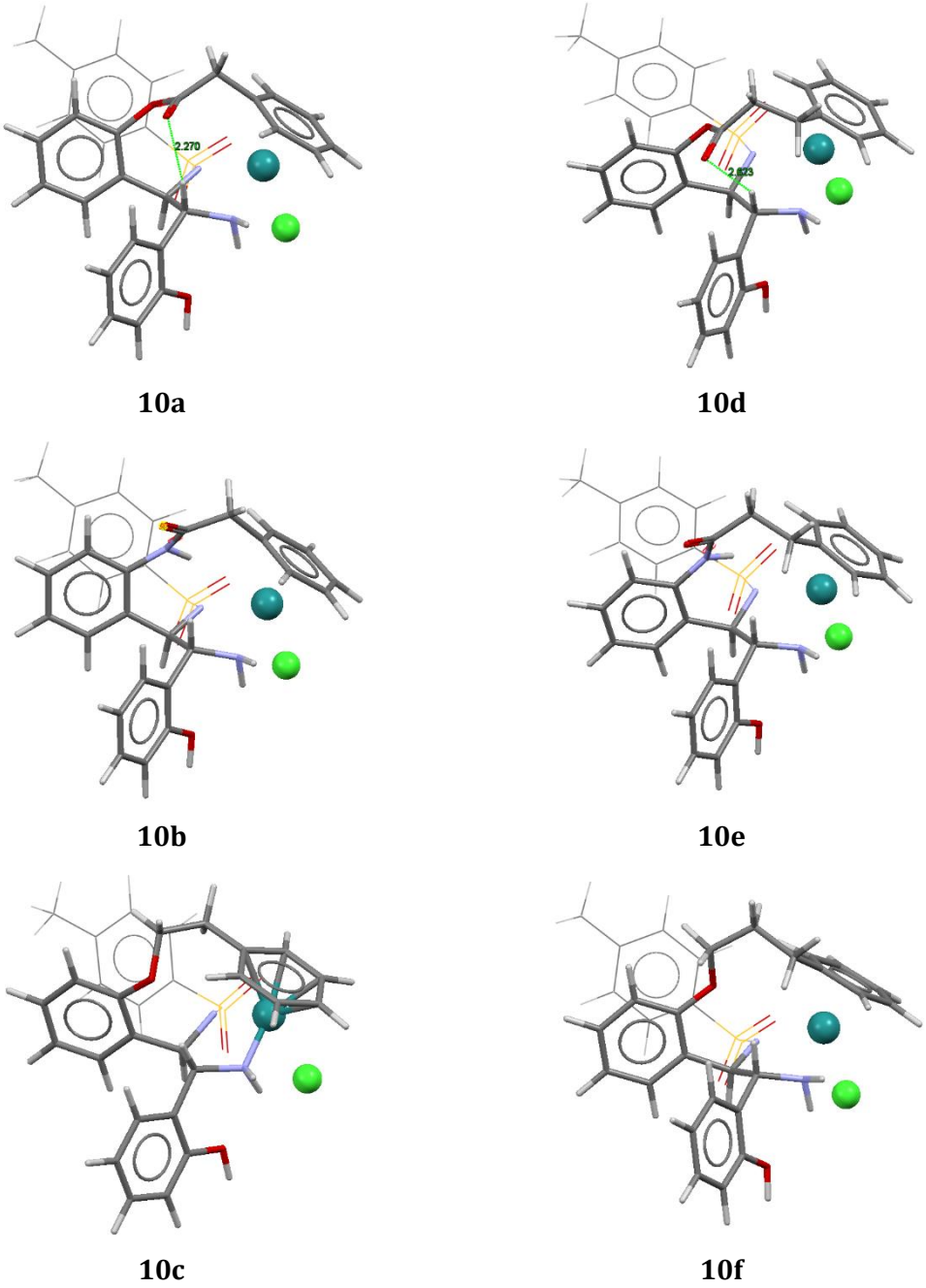

*Figure 6.15: Calculated minimal energy geometries of tethered complexes **10a - f** [rM06L/LANL2DZ/6-31+G(d)].*

As can be seen from the optimised geometries (Figure 6.15), both 3 and 4 atom linkers provide enough flexibility to allow both the arene and amine ligands to remain fully coordinated without putting too much strain on the tether. In the case of the four atom linker, the arene ring is rotated by approximately 60° to accommodate the extra CH_2 unit.

For complexes **10a** and **10e** with ester linkages, a close (2.2 – 2.6 Å) interaction between the C=O and backbone CH may help stabilise the complex via weak hydrogen bonding. In contrast, complexes **10b** and **10f** adopts a geometry that is closer to planar between the phenyl ring and the amide bond (θ= ~60°), preventing the oxygen from coming into contact with the backbone CH.

Whilst the three atom linkers are too short to reach the second phenyl ring, the four atom linkers are easily able to do so, leading to a possible structural isomer, **11** (Figure 6.16). For the ester linked complex **10d**, the phenyl-NH_2 tethered isomer, **11**, is disfavoured by around 1.7 kcal/mol compared to the phenyl-NTs tethered isomer.

Unlike in **10d**, inversion of stereochemistry at ruthenium is possible in **11** by rotation of the phenyl-CH bond, forming the RRS diastereomer.[§§] Although this diastereomer is disfavoured by 12.3 kcal/mol for the chloride complex, **11** (13.5 kcal/mol for the hydride complex, **12**), and the barrier to rotation is likely to be high, the possibility of multiple structural and stereochemical isomers means that the four atom linkers make a poor choice for tethering the arene ring.

[§§] Note: RRS configuration in chloride precursor corresponds to RRR in hydride due to the difference in CIP priorities for chloride and hydride when assigning absolute configuration.

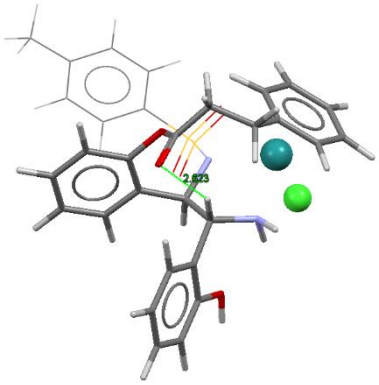

10d, 0.0 kcal/mol

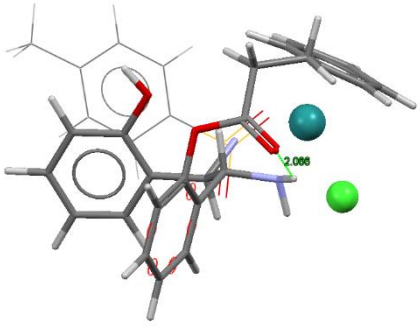

RRR-11, 1.7 kcal/mol

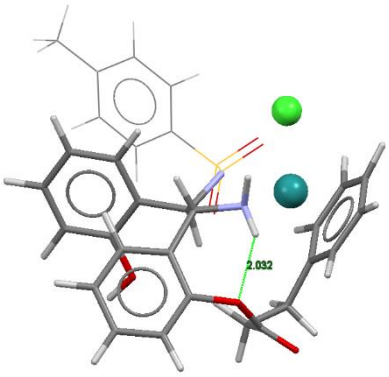

RRS-11, 12.3 kcal/mol

*Figure 6.16: Calculated geometries and relative ground state energies of tethered complexes **10d**, **RRR-11** and **RRRS-11** [rM06L/LANL2DZ/6-31+G(d)].*

Of the three atom linkers, the ester linked **10a** (Scheme 6.17) was selected due to the expected ease of synthesis. However, as there is potential for hydrolysis of the ester in the basic alcohol reaction conditions, amide, ether or thioether linkages may prove more stable for future catalyst designs.

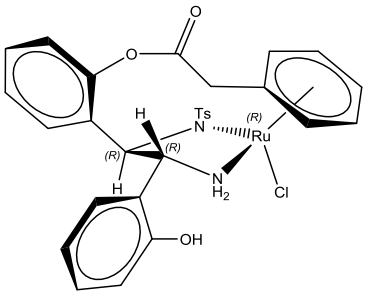

RRR-10a

*Scheme 6.17: Structure of tethered complex **RRR-10a** (RuCl(TsDPOHEN-phenylacetate)).*

One potential limitation of the three-atom tethered catalyst, is the increased strain that the tether induces into the 16-electron, unsaturated intermediate, **13** (Figure 6.17). By tethering the arene to the amine ligand, the catalyst is unable to adopt a trigonal bipyramidal geometry with the diamine ligand perpendicular to the arene, and is forced to remain in a distorted

square planar geometry with a vacant site at ruthenium. Whilst this raises the energy of the unsaturated intermediate by 10.8 kcal/mol relative to the hydride, **12**, the active site of the catalyst is exposed, increasing reactivity and limiting approach of substrate to a single face of the ruthenium.

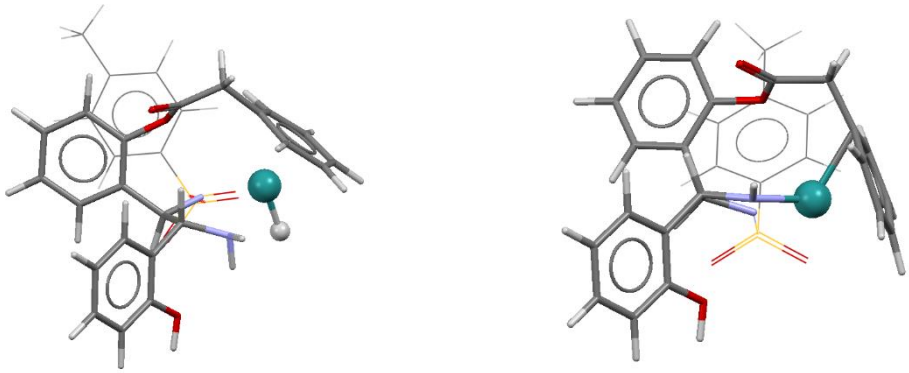

RRS-12 **RR-13**

*Figure 6.17: Calculated geometries of tethered 18-electron complex **RRR-12** (RuH (TsDPOHEN-phenylacetate)) and 16-electron complex **RRRS-13** (Ru(TsDPOHEN-phenylacetate)). [rM06L/LANL2DZ/6-31+G(d)].*

6.4.2 DFT modelling of reaction pathway

As discussed in Section 6.3.3 above, DFT modelling of the likely reaction pathway can provide insights into how stereochemistry is induced into the products. In the case of tethered catalyst **10a**, only the RRS (or SSR) diastereomer can exist; eliminating the need to consider the pathway for forming product via the minor RRR (SSS) diastereomer.

Although the net catalytic pathway is expected to be the same for both the tethered and non-tethered catalyst, changes in electronic and steric properties of the ligand will alter the energy levels and barriers. To compare the different energetic pathways for the two catalysts, DFT calculations were performed, using the same functional and basis set as before [rM06L / LANL2DZ (Ru) / 6-31+G(d)].

The position of the arene ring and steric interaction with the tether mean that attack of the isopropanol on the 'R' face of **13** is strongly disfavoured. The tether ensures that attack via the 'S' face is the only favourable means of forming **12**, meaning that only the RRS catalyst diastereomer is formed (Scheme 6.18).

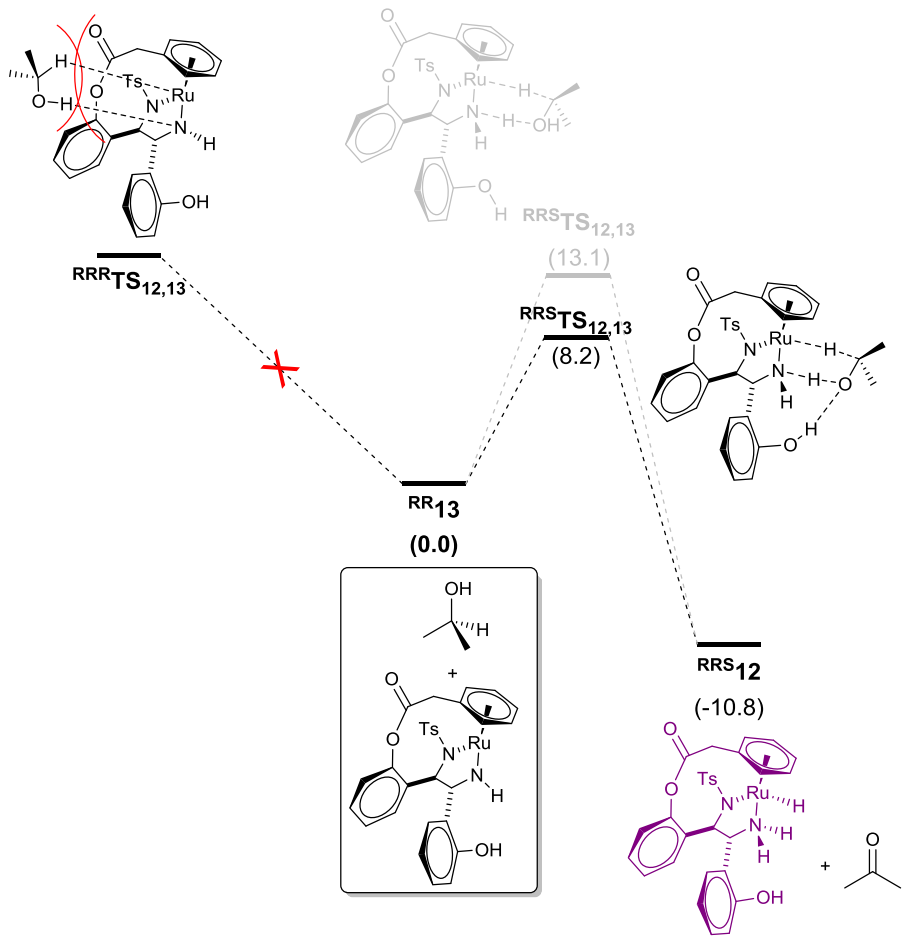

*Scheme 6.18: Proposed mechanism and calculated ground and transition state energies for the formation of either **RRS-12** from **RR-13** and isopropanol. [rM06L, LANL2DZ (Ru), 6-31+G(d)].*

The free phenol group is predicted to play a non-innocent role in the catalysis, forming a hydrogen bond to the substrate, and helping to stabilise the transition state. The stabilisation provided by the phenol group is very fortuitous, and helps to reduce the reaction energy barriers, which is expected to lead to faster kinetics. Removing the stabilising effect of the phenol-substrate hydrogen bond results in a transition state energy, $^{RRS}TS_{12,13}$, that is both 4.9 kcal/mol higher in energy, and which contains additional imaginary frequencies, indicating incomplete optimisation of the geometry.

As with the non-tethered catalyst, hydrogen transfer may occur on either face of the acetophenone, forming either the (S) or (R)-1-phenylethanol product. As with the non-tethered catalyst the (R) product is slightly favoured by 0.9 kcal/mol. The difference in energy between the two transition state barriers is the same as that calculated for the non-tethered catalyst (Scheme 6.13), and the enantioselectivity of the reaction is therefore expected to be similar to that of the non-tethered catalyst.

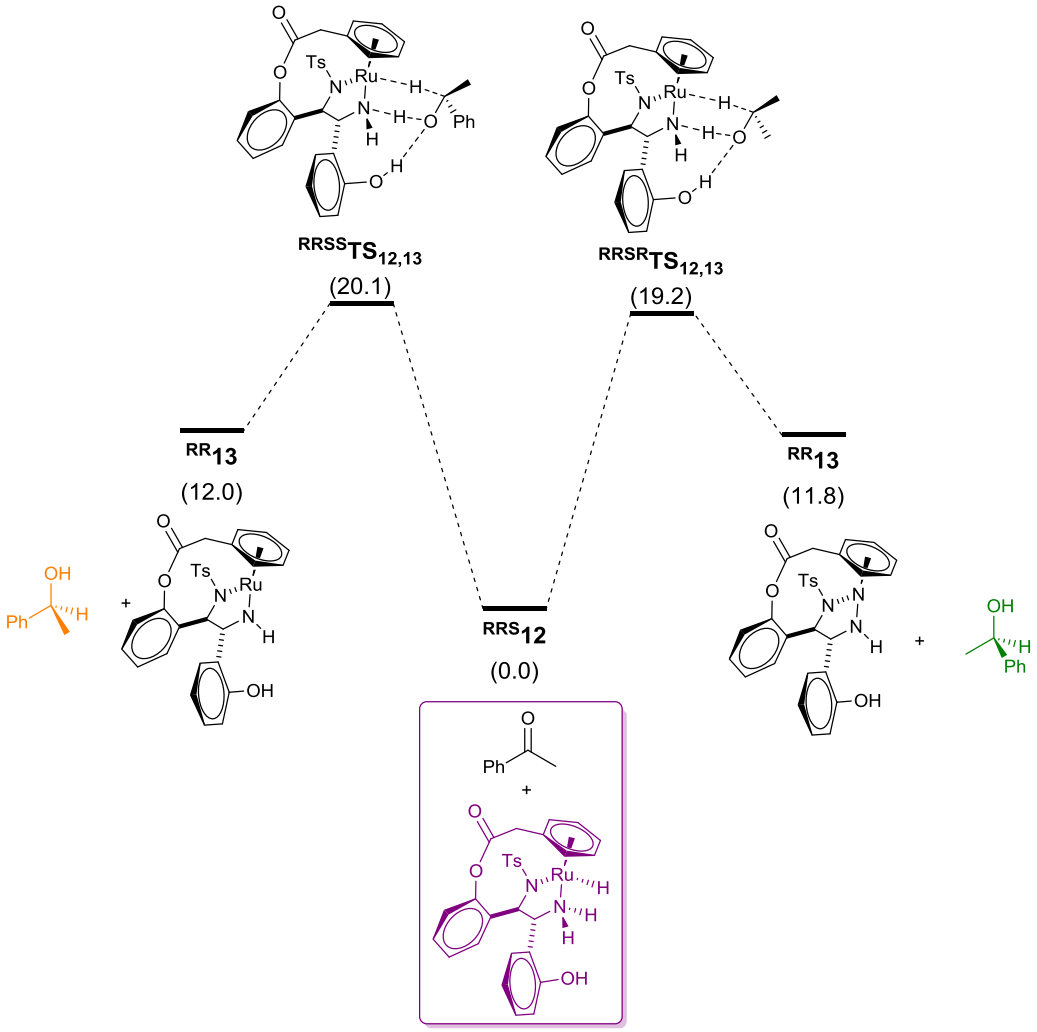

*Scheme 6.19: Proposed mechanism and calculated ground and transition state energies for the reaction of acetophenone and **RRS-12** to form **RR-13** and either (S) or (R)-1-phenylethanol [rM06L, LANL2DZ (Ru), 6-31+G(d)].*

The overall energy barriers for the tethered catalyst are around 3 kcal/mol higher than for the non-tethered catalyst. This may in part be due to the additional strain introduced by the tether resulting in a destabilisation of the unsaturated intermediate, **13**, and transition state relative to the hydride intermediate, **12**. The reaction of **13** with acetone has a comparatively low energy barrier, suggesting that the reaction with acetophenone is likely to be rate limiting, with the majority of the catalyst residing in hydride intermediate, **12**, during turnover.

The increase in energy barriers compared to the non-tethered catalyst is consistent with the trend observed for other tethered catalysts, which typically exhibit greater selectivities and stabilities than their non-tethered counterparts, although at the expense of slightly decreased reaction rate.[17, 24-25] The stabilising effects of the phenol OH on the transition state means that the new catalyst **10a** is likely to perform better than other tethered catalysts where this stabilisation is not possible. The expected increase in stability to deactivation resulting from the tethering of the arene prolongs the lifetime of the catalyst, meaning that slightly reduced kinetics can be tolerated as the catalyst remains active for longer.

6.4.3 Synthesis

The conventional route for forming tethered catalysts used by Wills and Ikariya, involves tethering the arene to the TsDPEN ligand prior to complexation to ruthenium (Scheme 6.20).[17, 25]

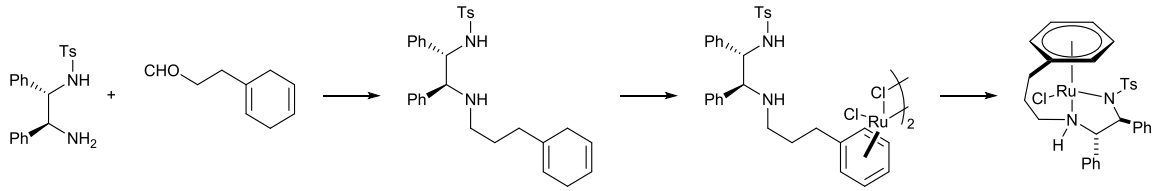

Scheme 6.20: Example synthesis of a tethered catalyst. Adapted from Hayes, 2005.[17]

This route would be challenging for **10a**, due to the difficulty in selectively controlling which of the multiple regio-isomers possible for the tosyl and tethered arene groups are formed. Instead, a new synthetic route was devised, where both ligands are complexed to the ruthenium before tethering, which then allows the ruthenium to be used as a chiral template for the formation of the arene-TsDPOHEN linkage (Scheme 6.21). This method of forming the arene-TsDPOHEN linkage in-situ takes advantage of the stereochemistry of the chloride complex, where the configuration at ruthenium is effectively locked due to strong hydrogen bonding between the chloride and axial-NH.[5]

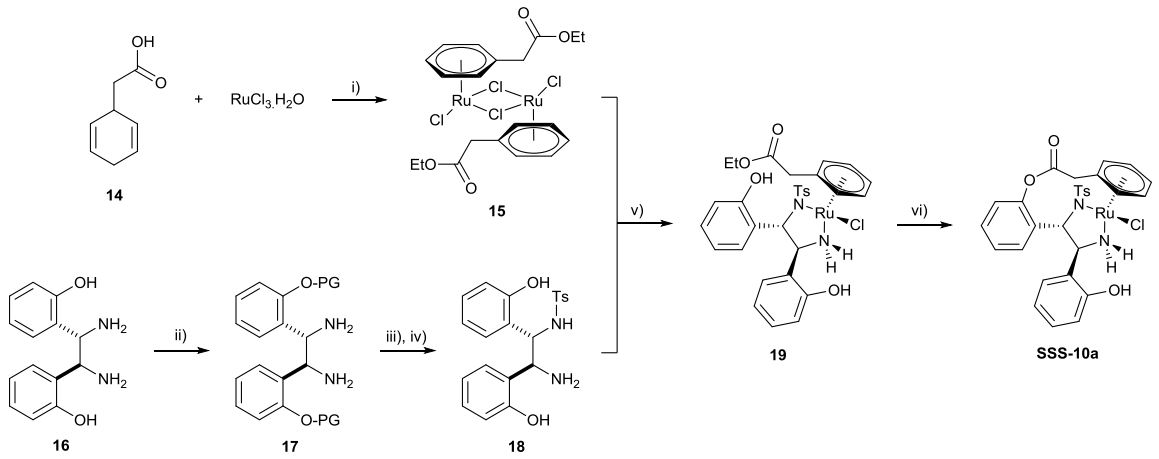

*Scheme 6.21: Proposed synthetic route to **SSS-10a**. Reaction conditions: i) EtOH, 78 °C, 2 h; ii) Selective protection of phenol OH iii) TsCl (1 equiv.), THF, 0 °C; iv) Deprotection of phenol OH.; v) NEt_3, IPA, 82 °C, 1 h; vi) Toluene, HBF_4, 110 °C, 1 h. PG= protecting group.*

The ruthenium precursor, **15** was formed from dihydro-phenylacetic acid and ruthenium trichloride under the same conditions as for the analogous mesitylene and *p*-cymene complexes.[31] Under the alcoholic reaction conditions, the ethyl ester was formed. Hydrolysis back to the carboxylic acid was easily achieved by heating in 2M sodium hydroxide solution, however it is more convenient to leave the ester as a protecting group, preventing unwanted coordination of the carboxylic acid to ruthenium.

Initial attempts to form **18** by direct tosylation of 1,2-bis(2-hydroxy phenyl)-1,2-ethylenediamine using literature procedures[32-33] for tosylation of DPEN were unsuccessful. Despite there being literature precedent for tosylation of 2-hydroxybenzylamine,[34] under the dilute conditions required for selective mono-tosylation no reaction is observed.

Protection of the phenol OH groups with a suitable O-selective protecting group such as acetate or trimethyl silane should allow mono-tosylation of the 1,2-bis(2-hydroxy phenyl)-1,2-ethylenediame, however suitable conditions have not yet been found. Work within the research group is ongoing to identify a suitable synthetic route to produce the mono-tosylated amine, with microwave assisted methods appearing promising.[35]

Complexation of the TsDPOHEN ligand to ruthenium is expected to proceed under the same conditions used for TsDPEN, with refluxing isopropanol solvent and triethylamine added to remove HCl formed during the complexation. Protection of the phenylacetic acid as the ethyl ester should prevent the carboxylic acid from binding to the ruthenium.

The final transesterification step to form the tethered catalyst uses a strong acid in a high boiling point non-ionising organic solvent such as toluene, so that the ethanol (or isopropanol) is driven off, pushing the equilibrium towards the desired product. Stereochemistry of the final product is dependent on that of the precursor, **19**. Due to the directing influence of the N-H···Cl hydrogen bond,[5] the configuration with (S) chirality at ruthenium is expected to be the dominant structure for the (S,S)-diamine. This (S,S,S) configuration means that the phenol closest to the tosyl group is in the same plane as the phenylacetic acid ligand, leading to reaction at this alcohol only, forming product (S,S,S)-**10a**.

When treated with base to remove the chloride ligand, unsaturated intermediate **13** is expected to form, with intermediate **12** expected upon reaction with a hydrogen donor such as isopropanol or formic acid.

6.5 CONCLUSIONS

The Noyori RuH(TsDPEN)(arene) catalyst can form two different diastereoisomers due to inversion of stereochemistry at ruthenium. Two hydride peaks were observed in varying ratios in the ^{1}H NMR spectrum of the catalyst and have previously been assigned as the two different diastereomers of the catalyst.

Assignment of the two hydride peaks as diastereomers has been confirmed using through-space correlation NMR spectroscopy. The major diastereomer, **3a**, was found to correspond to the RRS-diastereomer, which is in agreement with the assignment literature conformation based on single crystal X-ray diffraction. The concentration of the minor diastereomer, **3b**, was too low to allow absolute assignment by NOE interactions, however computational modelling and predicted NMR shifts for both diastereomers supports the assignment and relative positions of the NMR peaks for the two diastereomers. Synthesis of the corresponding catalyst with an achiral Ts-ethylenediamine ligand shows only a single hydride peak, again supporting the assignment of **3a** and **3b** as diastereomers.

The Ts-ethylenediamine catalyst appears to be much more stable to deactivation than **3**, indicating that the different electronic or steric properties of this ligand may help to stabilise the catalyst. Further work is required to investigate the stability of the Ts-ethylenediamine catalyst over time, by addition of further substrate after the completion of the reaction.

Using online FlowNMR spectroscopy it was possible to track the concentration of both diastereomers over the course of the reaction. From this data it can be shown that the minor diastereomer, **3b**, was formed during the initial stages of the reaction at the expense of the major diastereomer, **3a**. The rate of interconversion between the two diastereomers was accelerated in the presence of substrate, which is consistent with the proposed interconversion pathway via complex **2** which is achiral at ruthenium. Both diastereomers are observed to undergo slow deactivation, as discussed in Chapter 5.

Formation of the major (R)-1-phenylethanol may occur from either the major **(RRS)-3a** hydride diastereomer (lock-and-key mechanism) or the minor **(RRR)-3b** hydride diastereomer (major-minor mechanism). Bubbling CO_2 into a reaction containing a mixture of **3a** and **3b** showed rapid reaction of **3a**, but negligible reaction for **3b**, indicating that the minor diastereomer is inactive and that product formation occurs via a lock-and-key mechanism as is expected from the structure of each diastereomer and literature computational studies.

Whilst the tethered catalyst **RR-7**, also exhibited faster kinetics when the concentration of **RRS-9a** was high than when the concentrations of **RRS-9a** and **RRR-9b** were equal, again supporting a lock-and-key mechanism for product formation.

DFT calculations appear to contradict these experimental results, predicting both a faster rate and a selectivity towards the (R)-1-phenylethanol product for **RRR-3b**, which would result in a major-minor mechanism for product formation. Since these calculations are dependent on a small number of optimised transition state geometries, the predicted energy barriers and reaction mechanism are susceptible to small changes in optimised geometry. Further work is therefore required to calculate the energy barriers using different functionals and basis sets to determine whether the predicted reactivity is correct.

Since experimental results indicate that the minor hydride diastereomer **RRR-3b** is inactive in the reaction, a new tethered catalyst architecture is proposed, which should minimise the formation of the unwanted RRR diastereomer, whilst favouring reaction via the RRS pathway. Tethering the arene and diamine ligand has been shown to improve the stability of the catalyst to deactivation via the mechanisms discussed in Chapter 5, so the new tethered catalyst is also expected to show better stability than the non-tethered equivalent.

DFT calculations were used to screen possible tethering linkages. A three-atom linkage was found to be optimal for preventing inversion of stereochemistry at ruthenium without inducing too much strain into the complex. The calculations predict a similar product distribution to the non-tethered catalyst, with a difference in energy barrier of around 1 kcal/mol favouring the formation of (R)-1-phenylethanol over (S)-1-phenylethanol. The reaction rate of the tethered catalyst is predicted to be slower than the non-tethered catalyst, however this is offset by the expected greater selectivity and stability. As with the DFT calculations for **3a** and **3b**, further work using different functionals and basis sets is required to confirm these results.

A new synthetic route to the formation of tethered catalysts is proposed, where the ruthenium chloride precursor is used as a template for the formation of the tether. Using the ruthenium as a template means that only one enantiomer may be formed as the tether is restricted to the closest phenyl group. Due to time limitations, the full synthetic route has not been tested, with selective mono-tosylation of the diamine ligand proving challenging. This synthesis is the subject of ongoing work within the research group, investigating the use of protecting groups on the phenol oxygens to prevent unwanted side reactions.

6.6 EXPERIMENTAL

6.6.1 Density Functional Theory calculations

Density Functional Theory calculations were carried out using the Gaussian 09 (rev. D.01-v3) [36] software package. Geometry optimisation, frequency and NMR shift calculations were performed in a SMD polarizable continuum solvent model[37] of implicit isopropanol. Restricted rωB97X-D, rB3PW91, rPBE1PBE and rM06L functionals, along with SDD or LANL2DZ (Ru) and 6-311++G(d,p) or 6-311+G(d) basis sets were used as indicated. Starting geometries were taken from published crystal structures,[38] or calculated geometries,[5, 7, 10] where available. DFT integration grids with 99 radial and 590 angular points (Ultrafine) were used for all transition state calculations. All ground state geometries were free of imaginary frequencies.

6.6.2 Catalyst synthesis

Ruthenium chloride and complexes **1** and **7** were purchased from Alfa Aesar. $[RuCl_2(mesitylene)]_2$ was synthesised according to literature procedure.[31] All other compounds were purchased from Sigma Aldrich and used without further purification. Unless otherwise specified, all reactions were carried out under argon atmosphere with dry and degassed solvents. THF, toluene, methanol, hexane and ammonia were all freshly distilled before use.

NMR spectra were collected on a Bruker AVIII 400 MHz (broad band observe probe) or a Bruker AVANCE 500 MHz (broad band observe nitrogen cryoprobe) NMR spectrometer. Mass spectra were recorded on a Bruker Daltonics MicroTOF mass spectrometer fitted with an electrospray ionisation source. IR spectra were recorded on a Bruker Alpha spectrometer fitted with an ATR accessory.

6.6.2.1 Ts(ethylenediamine)

Synthesis modified from a literature procedure.[32] Ethylene diamine (0.27 mL, 4.8 mmol) and triethylamine (2 mL, 14.3 mmol) were dissolved in dry THF (40 mL) and cooled to 0 °C in an ice bath. A solution of *para*-toluene sulfonyl chloride (0.9 g, 4.8 mmol) in THF (10 mL) was added dropwise to the reaction over 30 min. The mixture was warmed to room temperature before stirring overnight. The mixture was washed with saturated sodium hydrogen carbonate solution (80 mL) and dichloromethane (80 mL). The organic phase was washed with brine and evaporated to give a white powder. 0.85 g, 83%, m.p. 116 – 117 °C [lit. 118–120 °C][39]. ^{1}H NMR (500 MHz, $CDCl_3$) δ: 7.74 (d, 2H, J_{HH}= 7.3 Hz, Ts arom.), 7.28 (d, 2H, J_{HH}= 7.5 Hz, Ts arom.), 3.67 (br, 3H, N<u>H</u>), 2.96 (t, 2H, J_{HH}= 5.2 Hz, NC<u>H</u>), 2.83 (t, 2H, J_{HH}= 5.0 Hz, NC<u>H</u>), 2.40 (s, 3H, TsC<u>H</u>$_3$).

6.6.2.2 [$RuCl_2$(mesitylene)]$_2$

Sythesis was performed according to a literature procedure.[31] Ruthenium trichloride hydrate (0.5 g, 1.9 mmol) and 1,3,5-trimethylcyclohexyl-1,4-diene (1.4 mL, 9.4 mmol) were dissolved in absolute Ethanol (20 mL) and heated at reflux for 16 h. The mixture was allowed to cool, before filtering to isolate an orange-brown powder which was washed with Ethanol (2x 5 mL) and dried under high vacuum. 0.38 g, 68%. ^{1}H NMR (400 MHz, DMSO-d_6) δ: 7.21 (s, 1H), 3.32 (s, 3H).

6.6.2.3 RuCl(Ts(ethylenediamine))(mesitylene), 6.

Synthesis modified from a literature procedure.[32] Mono-tosyl ethylene diamine (0.2 g, 0.93 mmol), [$RuCl_2$(mesitylene)]$_2$ (0.28 g, 0.47 mmol) and triethylamine (0.5 mL, 3.58 mmol) were dissolved in isopropanol (20 mL) and heated to 80 °C for 2 h. The volume of the mixture was reduced to approx. 10 mL under vacuum and filtered to remove a fine black solid. The bright orange filtrate was evaporated to give an orange crystalline solid, which was washed with water (approx. 2 mL) and dried under high vacuum. 0.39 g, 89%. ^{1}H NMR (500 MHz, $CDCl_3$) δ: 7.66 (d, 2H, J_{HH}= 8.0 Hz, Ts arom.), 7.06 (d, 2H, J_{HH}= 7.8 Hz, Ts arom.), 5.28 (s, 3H, mesitylene CH), 2.85 (br, 2H, CH_2), 2.63 (br, 2H, CH_2), 2.25 (s, 3H, Ts CH_3), 2.20 (s, 9H, mesitylene CH_3).

6.6.2.4 1,3-dihydro phenylacetic acid

Phenylacetic acid (2 g, 14.7 mmol) was dissolved in dry THF (10 mL) and cooled to -78 °C. Liquid ammonia (approx. 10 mL) was distilled into the flask and lithium granules (0.4 g, 58.8 mmol) added slowly before stirring for 1 h. Absolute ethanol (1.7 mL, 29.4 mmol) was added dropwise before stirring for a further 1 h. Absolute ethanol (2 mL) and ammonium chloride (5 g) were added to quench the reaction, and the mixture was slowly warmed to room temperature to evaporate the ammonia. Ethanol (10 mL) and water (10 mL) were added and the mixture separated. The organic layer was washed with water (10 mL). The combined aqueous layers were acidified with conc. HCl until a white precipitate formed. Dichloromethane (50 mL) was added to dissolve the precipitate and the aqueous layer was extracted with a further 50 mL DCM. The combined DCM layers were dried over $MgSO_4$ and filtered. The solvent was evaporated under vacuum to give a white crystalline powder which was dried under high vacuum. (1.8 g, 89%) m.p. 107.7 – 109.0 °C, %. ^{1}H NMR (400 MHz, $CDCl_3$) δ: 11.59 (br, 1H, COO<u>H</u>), 5.64 - 5.63 (m, 2H, C<u>H</u>=C<u>H</u>), 5.87 (m, 1H, (CH_2COOH)C=C<u>H</u>), 2.97 (s, 2H, C<u>H$_2$</u>COOH), 2.68 – 2.65 (m, 4H, C<u>H$_2$</u>-C<u>H$_2$</u>). ^{13}C NMR (100 MHz, $CDCl_3$) δ: 178.6, 127.7, 123.8, 123.7, 123.6, 42.8, 28.9, 26.8.

6.6.2.5 [$RuCl_2$(ethyl phenylacetate)]$_2$

Ruthenium trichloride hydrate (0.5 g, 1.9 mmol) and dihydro phenylacetic acid (0.5 g, 3.6 mmol) were dissolved in absolute ethanol (25 mL) and heated at reflux for 2 h. The mixture

was allowed to cool, before filtering to isolate an orange powder which was washed with ethanol (10 mL) and diethyl ether (10 mL) and dried under high vacuum. (0.64 g, 50%) ^{1}H NMR (400 MHz, DMSO-d_6) δ: 6.05 (t, 2H, J_{HH}= 5.9 Hz, *meta*-C<u>H</u>), 5.95 (d, 2H, J_{HH}= 5.9 Hz, *ortho*-C<u>H</u>), 5.86 (t, 1H, J_{HH}= 5.9 Hz, *para*-C<u>H</u>), 4.12 (q, 2H, 7.3 Hz, C<u>H</u>$_2$CH$_3$), 3.58 (s, 2H, C<u>H</u>$_2$C(O)), 1.21 (t, 3H, J_{HH}= 7.1 Hz, CH$_2$C<u>H</u>$_3$).

6.7 REFERENCES

1. Hashiguchi, S.; Fujii, A.; Haack, K.-J.; Matsumura, K.; Ikariya, T.; Noyori, R., Kinetic Resolution of Racemic Secondary Alcohols by Ru(II)-Catalyzed Hydrogen Transfer. *Angew. Chem. Int. Ed.* **1997,** 36, 288-290.

2. Fujii, A.; Hashiguchi, S.; Uematsu, N.; Ikariya, T.; Noyori, R., Ruthenium(II)-Catalyzed Asymmetric Transfer Hydrogenation of Ketones Using a Formic Acid−Triethylamine Mixture. *J. Am. Chem. Soc.* **1996,** 118, 2521-2522.

3. Connelly, N. G.; Damhus, T.; Hartshorn, R. M.; Hutton, A. T. In *Nomenclature of Inorganic Chemistry: IUPAC Recommendations 2005*, International Union of Pure and Applied Chemistry: Cambridge, 2005; pp 174 - 199.

4. Stanley, K.; Baird, M. C., A demonstration of controlled asymmetric induction in organoiron chemistry. Suggestions concerning the specification of chirality in pseudotetrahedral metal complexes containing polyhapto ligands. *J. Am. Chem. Soc.* **1975,** 97, 6598-6599.

5. Yamakawa, M.; Ito, H.; Noyori, R., The Metal−Ligand Bifunctional Catalysis: A Theoretical Study on the Ruthenium(II)-Catalyzed Hydrogen Transfer between Alcohols and Carbonyl Compounds. *J. Am. Chem. Soc.* **2000,** 122, 1466-1478.

6. Dub, P. A.; Henson, N. J.; Martin, R. L.; Gordon, J. C., Unravelling the mechanism of the asymmetric hydrogenation of acetophenone by [RuX_2(diphosphine)(1,2-diamine)] catalysts. *J. Am. Chem. Soc.* **2014,** 136, 3505-3521.

7. Dub, P. A.; Ikariya, T., Quantum chemical calculations with the inclusion of nonspecific and specific solvation: asymmetric transfer hydrogenation with bifunctional ruthenium catalysts. *J. Am. Chem. Soc.* **2013,** 135, 2604-2619.

8. Haack, K.-J.; Hashiguchi, S.; Fujii, A.; Ikariya, T.; Noyori, R., The Catalyst Precursor, Catalyst and Intermediate in the Ru(II)-Promoted Asymmetric Hydrogen Transfer between Alcohols and Ketones. *Angew. Chem. Int. Ed.* **1997,** 36, 285-288.

9. Clapham, S. E.; Hadzovic, A.; Morris, R. H., Mechanisms of the H_2-hydrogenation and transfer hydrogenation of polar bonds catalyzed by ruthenium hydride complexes. *Coord. Chem. Rev.* **2004,** 248, 2201-2237.

10. Dub, P. A.; Gordon, J. C., The mechanism of enantioselective ketone reduction with Noyori and Noyori-Ikariya bifunctional catalysts. *Dalton Trans* **2016,** 45, 6756-6781.

11. Ohkuma, T.; Utsumi, N.; Tsutsumi, K.; Murata, K.; Sandoval, C.; Noyori, R., The Hydrogenation/Transfer Hydrogenation Network: Asymmetric Hydrogenation of Ketones with Chiral η 6 -Arene/ N -Tosylethylenediamine−Ruthenium(II) Catalysts. *J. Am. Chem. Soc.* **2006,** 128, 8724-8725.

12. Guillaneux, D.; Zhao, S.-H.; Samuel, O.; Rainford, D.; Kagan, H. B., Nonlinear Effects in Asymmetric Catalysis. *J. Am. Chem. Soc.* **1994,** 116, 9430-9439.

13. Puchot, C.; Samuel, O.; Dunach, E.; Zhao, S.; Agami, C.; Kagan, H. B., Nonlinear effects in asymmetric synthesis. Examples in asymmetric oxidations and aldolization reactions. *J. Am. Chem. Soc.* **1986,** 108, 2353-2357.

14. Schmidt, T.; Dai, Z.; Drexler, H.-J.; Hapke, M.; Preetz, A.; Heller, D., The Major/Minor Concept: Dependence of the Selectivity of Homogeneously Catalyzed Reactions on Reactivity Ratio and Concentration Ratio of the Intermediates. *Chemistry – An Asian Journal* **2008,** 3, 1170-1180.

15. Landis, C. R.; Halpern, J., Asymmetric hydrogenation of methyl (Z)-.alpha.-acetamidocinnamate catalyzed by [1,2-bis(phenyl-o-anisoyl)phosphino)ethane]rhodium(I): kinetics, mechanism and origin of enantioselection. *J. Am. Chem. Soc.* **1987,** 109, 1746-1754.

16. Blackmond, D. G., Kinetic aspects of non-linear effects in asymmetric synthesis, catalysis, and autocatalysis. *Tetrahedron: Asymmetry* **2010,** 21, 1630-1634.

17. Hayes, A. M.; Morris, D. J.; Clarkson, G. J.; Wills, M., A class of ruthenium(II) catalyst for asymmetric transfer hydrogenations of ketones. *J. Am. Chem. Soc.* **2005,** 127, 7318-7319.

18. Cheung, F. K.; Clarke, A. J.; Clarkson, G. J.; Fox, D. J.; Graham, M. A.; Lin, C.; Crivillé, A. L.; Wills, M., Kinetic and structural studies on 'tethered' Ru(II) arene ketone reduction catalysts. *Dalton Trans.* **2010,** 39, 1395-1402.

19. Wills, M., Imino Transfer Hydrogenation Reductions. *Top. Curr. Chem.* **2016,** 374, 1-14.

20. Strotman, N. A.; Baxter, C. A.; Brands, K. M. J.; Cleator, E.; Krska, S. W.; Reamer, R. A.; Wallace, D. J.; Wright, T. J., Reaction Development and Mechanistic Study of a Ruthenium Catalyzed Intramolecular Asymmetric Reductive Amination en Route to the Dual Orexin Inhibitor Suvorexant (MK-4305). *J. Am. Chem. Soc.* **2011,** 133, 8362-8371.

21. Dub, P. A.; Scott, B. L.; Gordon, J. C., Why Does Alkylation of the N-H Functionality within M/NH Bifunctional Noyori-Type Catalysts Lead to Turnover? *J. Am. Chem. Soc.* **2017,** 139, 1245-1260.

22. del Rosal, I.; Maron, L.; Poteau, R.; Jolibois, F., DFT calculations of ^{1}H and ^{13}C NMR chemical shifts in transition metal hydrides. *Dalton Trans* **2008**, 3959-3970.

23. Bennett, M. A.; Ennett, J. P.; Gell, K. I., Dinuclear μ-hydrido arene complexes of ruthenium(II). *J. Organomet. Chem.* **1982,** 233, C17-C20.

24. Cheung, F. K.; Hayes, A. M.; Hannedouche, J.; Yim, A. S.; Wills, M., "Tethered" Ru(II) catalysts for asymmetric transfer hydrogenation of ketones. *J. Org. Chem.* **2005,** 70, 3188-3197.

25. Touge, T.; Hakamata, T.; Nara, H.; Kobayashi, T.; Sayo, N.; Saito, T.; Kayaki, Y.; Ikariya, T., Oxo-Tethered Ruthenium(II) Complex as a Bifunctional Catalyst for Asymmetric Transfer Hydrogenation and H_2 Hydrogenation. *J. Am. Chem. Soc.* **2011,** 133, 14960-14963.

26. Nedden, H. G.; Zanotti-Gerosa, A.; Wills, M., The Development of Phosphine-Free 'Tethered' Ruthenium(II) Catalysts for the Asymmetric Reduction of Ketones and Imines. *Chem. Rec.* **2016,** 16, 2623-2643.

27. Wu, X.; Liu, J.; Di Tommaso, D.; Iggo, J. A.; Catlow, C. R. A.; Bacsa, J.; Xiao, J., A Multilateral Mechanistic Study into Asymmetric Transfer Hydrogenation in Water. *Chem. Eur. J.* **2008,** 14, 7699-7715.

28. Eisenstein, O.; Crabtree, R. H., Outer sphere hydrogenation catalysis. *New J. Chem.* **2013,** 37, 21-27.

29. Eyring, H., The Activated Complex in Chemical Reactions. *J. Chem. Phys.* **1935,** 3, 107-115.

30. Kozuch, S.; Shaik, S., How to conceptualize catalytic cycles? The energetic span model. *Acc. Chem. Res.* **2011,** 44, 101-10.

31. Bennett, M. A.; Smith, A. K., Arene ruthenium(II) complexes formed by dehydrogenation of cyclohexadienes with ruthenium(III) trichloride. *J. Chem. Soc., Dalton Trans.* **1974**, 233.

32. Tietze, Lutz F.; Zhou, Y.; Töpken, E., Synthesis of Simple Enantiopure Tetrahydro-β-carbolines and Tetrahydroisoquinolines. *Eur. J. Org. Chem.* **2000,** 2000, 2247-2252.

33. Blacker, A. J.; Duckett, S. B.; Grace, J.; Perutz, R. N.; Whitwood, A. C., Reactivity, Structures, and NMR Spectroscopy of Half-Sandwich Pentamethylcyclopentadienyl Rhodium Amido Complexes Relevant to Transfer Hydrogenation. *Organometallics* **2009,** 28, 1435-1446.

34. Yar, M.; McGarrigle, E. M.; Aggarwal, V. K., Bromoethylsulfonium salt - a more effective annulation agent for the synthesis of 6- and 7-membered 1,4-heterocyclic compounds. *Org. Lett.* **2009,** 11, 257-260.

35. Lakrout, S.; K'Tir, H.; Amira, A.; Berredjem, M.; Aouf, N.-E., A simple and eco-sustainable method for the sulfonylation of amines under microwave-assisted solvent-free conditions. *RSC Advances* **2014,** 4, 16027-16032.

36. Frisch, M. J.; Trucks, G. W.; Schlegel, H. B.; Scuseria, G. E.; Robb, M. A.; Cheeseman, J. R.; Scalmani, G.; Barone, V.; Mennucci, B.; Petersson, G. A. H. N., M. Caricato, X. Li, H. P. Hratchian, A. F. Izmaylov, J. Bloino, G. Zheng, J. L. Sonnenberg, M. Hada, M. Ehara, K. Toyota, R. Fukuda, J. Hasegawa, M. Ishida, T. Nakajima, Y. Honda, O. Kitao, H. Nakai, T. Vreven, J. A. Montgomery, Jr., J. E. Peralta, F. Ogliaro, M. Bearpark, J. J. Heyd, E. Brothers, K. N. Kudin, V. N. Staroverov, T. Keith, R. Kobayashi, J. Normand, K. Raghavachari, A. Rendell, J. C. Burant, S. S. Iyengar, J. Tomasi, M. Cossi, N. Rega, J. M. Millam, M. Klene, J. E. Knox, J. B. Cross, V. Bakken, C. Adamo, J. Jaramillo, R. Gomperts, R. E. Stratmann, O. Yazyev, A. J. Austin, R. Cammi, C. Pomelli, J. W. Ochterski, R. L. Martin, K. Morokuma, V. G. Zakrzewski, G. A. Voth, P. Salvador, J. J. Dannenberg, S. Dapprich, A. D. Daniels, O. Farkas, J. B. Foresman, J. V. Ortiz, J. Cioslowski, and D. J. Fox *Gaussian 09, Revision D.01*, Gaussian Inc: Wallingford CT, 2009.

37. Marenich, A. V.; Cramer, C. J.; Truhlar, D. G., Universal solvation model based on solute electron density and on a continuum model of the solvent defined by the bulk dielectric constant and atomic surface tensions. *J. Phys. Chem. B* **2009,** 113, 6378-6396.

38. Noyori, R.; Hashiguchi, S., Asymmetric Transfer Hydrogenation Catalyzed by Chiral Ruthenium Complexes. *Acc. Chem. Res.* **1997,** 30, 97-102.

39. Andna, L.; Miesch, L., Trapping of N-Acyliminium Ions with Enamides: An Approach to Medium-Sized Diaza-Heterocycles. *Org. Lett.* **2018,** 20, 3430-3433.

7 Conclusions and Future Work

This thesis has presented the use of on-line FlowNMR spectroscopy for monitoring catalytic reactions, providing kinetic data that may be used to help derive reaction mechanisms and identify catalyst species.

The design and construction of four generations of FlowNMR apparatus for on-line reaction monitoring was, considering the advantages and disadvantages of different designs and materials. Early apparatus designs using HPLC-NMR flow probes were found to have limited sensitivity and signal-to-noise ratio compared to standard NMR probes, and are only able to tune to proton and carbon resonance frequencies, restricting the quality of data and range of experiments possible using this apparatus.

Second and third-generation apparatus designs used a commercial NMR flow tube, which allowed the use of standard NMR probes, leading to an increase in sensitivity due to the larger sample volume. Other analytical techniques, including UV-Vis spectroscopy, High Performance Liquid Chromatography and Mass Spectrometry were integrated into the reaction monitoring system, allowing information from multiple techniques to be compared and used together to give a more detailed understanding of reaction kinetics and mechanism.

The choice of material for the capillary tubing through which the reaction mixture flows was found to be very important. Flexible fluoropolymers such as PTFE offer high chemical compatibility, but have poor mechanical properties, leading to twisting of the tubing within the sample cell, reducing magnetic field homogeneity and increasing peak line width. More rigid polymers such as PEEK show improved properties compared to PTFE, however are still able to bend, resulting in peak broadening. The best magnetic field homogeneity was found when using a rigid fused-silica capillary, however the brittleness of this material makes handling the flow tube more challenging.

Achieving good temperature control throughout the flow system proved challenging, due to the number of apparatus connections, and the small volume of the sample tubing, leading to rapid cooling. A jacketed tubing design was used to help regulate the temperature of the transfer line tubing, and was found to perform adequately for temperatures close to room temperature, but requires further work to improve regulation at higher temperatures.

General considerations for the operation of a FlowNMR system were discussed in Chapter 3, including measurement of apparatus volume and residence time. The effect of flowing samples on NMR acquisition was discussed, with high flow rates or nuclei with long T_1 relaxation times found to result in a decrease in observed signal intensity due to 'in-flow' effects caused by the sample having insufficient time to build up complete magnetisation before reaching the sample cell. It was found that these in-flow effects may be corrected for by a simple linear calibration factor, determined by comparing the peak integrals with and without the sample flowing.

It was found that flow of the sample out of the NMR observation cell leads to an apparent increase in the decay rate of the FID, leading to a slight broadening of the peaks. The contribution towards peak line broadening due to out-flow effects was found to be small compared to the increase in linewidth due to magnetic field inhomogeneity resulting from the capillary within the flow tube. Replacement of the sample volume due to sample flow was found to allow measurements at a faster rate than would be possible for a static sample, meaning that more transients can be acquired in a given time, leading to signal-to-noise improvements.

Techniques that are applicable to reaction monitoring in non-deuterated solvents were reviewed, including methods for solvent suppression and deconvolution of overlapping peaks. WET solvent suppression was found to be more effective than simple presaturation techniques, due to the shorter pulse sequences and greater tolerance to changes in T_1 and magnetic field strength.

Two examples of reactions that have been monitored by FlowNMR spectroscopy were presented. The first was the photochemical oxidation of N-allylbenzylamine, which requires conditions that would make it very challenging to monitor using conventional NMR techniques. Data acquired using on-line NMR spectroscopy was shown to be of higher quality than the same data acquired by sampling from the reaction off-line, due to the variability in sample preparation for off-line measurements. Variation of light intensity showed the reaction to be photon limited, requiring a sustained input of light for the reaction to proceed. The reaction was also found to require the presence of oxygen, presumably as the oxidant in the reaction, however no change in rate or product distribution was observed when water was added to the reaction.

A by-product of the reaction, benzaldehyde, which was observed in all off-line samples, was found to result from a secondary reaction that only occurs when the concentration of product

is high. The formation of benzaldehyde was found to be dependent on both light and oxygen. Other expected by products of the reaction including allylamine and hydrogen were not observed in the reaction mixture, however both were found to be volatile under reaction conditions. Future work to investigate the mechanism of this reaction may use additional techniques such as headspace mass spectrometry that are able to detect volatile complexes evaporating from the reaction.

The second reaction studied was the Noyori asymmetric transfer hydrogenation of acetophenone. The kinetics of the overall reaction were studied, and the reaction was found to be first order with respect to both catalyst and acetophenone. No chiral product inhibition was found to result from the minor (S)-1-phenylethanol formed during the reaction, however the effect of product inhibition from the major (R)-1-phenylethanol product cannot be ruled out. Using selective excitation, the concentration of hydride intermediate, **3**, was tracked throughout the course of the reaction, allowing catalyst speciation to be determined. By kinetically correlating reaction progress with the concentration of ruthenium mono-hydride intermediate **3** during transfer hydrogenation catalysis initiated by sequential addition of reagents, and comparing it with modelled profiles derived from the rate law of the reaction evidence was found for two independent catalyst deactivation/inhibition events: deactivation of hydride intermediate **3** caused by gradual loss of the arene ligand, and inhibition of unsaturated intermediate **2** by excess base. Inclusion of both pathways into the reaction mechanism resulted in a kinetic model that accurately reproduces all experimental data, and accounts for observations of the effect of varying base concentration on conversion.

Further investigation into the role of base in the reaction showed that changing base anion or cation had little effect on catalyst decomposition rate, although it did alter the catalyst speciation during the reaction. The higher concentration of hydride observed during turnover for *tert*-butoxide base is consistent with the proposed off-cycle alkoxide species formed by reaction with base, since the reaction of **2** with the bulkier, more weakly acidic *tert*-butoxide is expected to be less favourable than with hydroxide or isopropoxide bases.

Identification and isolation of alkoxide complexes is important for determining the nature of the off-cycle species, **4**, that is inferred from the reaction kinetics. Computational studies have demonstrated that such complexes should theoretically be stable, however no ruthenium alkoxide complexes are reported in the literature. The instability of the alkoxide species and tendency to dissociate or react makes isolation of these complexes challenging. DFT calculations indicate a relationship between the acidity of the alcohol and the stability of the corresponding alkoxide complex, predicting that aromatic phenoxides should form more

stable ruthenium-alkoxide than aliphatic alkoxides. The synthesis of both phenoxide and pentafluorophenoxide-ruthenium complexes was attempted. Whilst the sample colour, ^{19}F NMR spectra and reactivity all indicate that an 18-electron octahedral Ru(II) complex was formed, ^{1}H NMR and Mass Spectrometry do not show any conclusive structural evidence for this complex. Work to identify and crystallise these complexes is ongoing.

The relationship between the two hydride peaks observed in the NMR spectrum during turnover was investigated, and the peaks were found to correspond to two diastereomeric hydride complexes. Using a combination of ^{1}H NOESY experiments and DFT calculations, the major NMR peak was found to correspond to the RRS diastereomer that has previously been isolated and crystallised. Interconversion between the two diastereomers occurs in the presence of a ketone, however the decomposition of the hydride species under reaction conditions means that the relationship between the two diastereomers cannot be studied over longer periods of time. Reaction of a mixture of the two hydride diastereomers with CO_2 indicates that the major RRS diastereomer is more reactive than the minor RRR diastereomer, which is essentially inert under these conditions. This suggests that the product formation occurs via a 'lock-and-key' mechanism, with the major catalyst diastereomer forming the major product.

The related tethered complex **9** is more stable, and interconversion of the two diastereomers was observed to continue until the concentrations were approximately equal. Greater reactivity of the RRS diastereomer was found for the tethered catalyst, **9**, again supporting the proposed 'lock-and-key' mechanism. Further work to identify the catalytic activity of the minor hydride **RRR-3b** is necessary, using an analogous experiment to that shown in Figure 6.14 for the tethered catalyst.

DFT calculations of the reaction mechanism of **1**, support the experimentally observed result that the **RRS-3a** hydride is the favoured diastereomer from the reaction of **2** with isopropanol, however the calculations also predict that the minor **RRR-3b** hydride diastereomer should be more reactive towards product formation ('major-minor' mechanism), contradicting the experimentally observed behaviour. The DFT result is therefore treated with caution, and further work is required to establish whether the relative energy barriers are the same with other functionals and basis sets.

Based on the conclusions that the major **RRS-3a** hydride diastereomer is the more active catalyst species and that catalyst decomposition occurs via loss of the arene ligand, a new tethered catalyst structure was proposed. This tethered catalyst features a tethering group

that connects the arene ligand to one of the diamine ligand phenyl groups, preventing inversion of ruthenium stereochemistry. The tether is also expected to improve stability of the complex by preventing the loss of the arene ligand, in the same manner that has been used to justify the increased stability of other tethered catalysts.

Density Functional Theory calculations were used to predict the structure of various tethering groups, to determine which structures are likely to be stable. A three-atom ester linkage was selected for further investigation, as this short enough to prevent inversion of the ruthenium stereochemistry, whilst being long enough not to induce too much additional strain into the molecule. Calculations predicted that this catalyst should be active for the transfer hydrogenation of acetophenone, favouring the (R) product, although at a slower rate than the non-tethered catalyst. The availability of a free phenol OH close to the active catalyst site is predicted to help stabilise the catalyst transition state by hydrogen bonding to the substrate.

Conventional methods for synthesising tethered catalysts typically involve the complexation of a pre-formed tethered ligand with a metal, making it challenging to control the absolute stereochemistry at the metal. A new synthetic route to selectively forming a single diastereomer of the proposed tethered catalyst has been devised, utilising the favoured geometry of the ruthenium chloride complex as a chiral template for the formation of the tether linkage. Obtaining the mono-tosylated diamine ligand has so far proved challenging, meaning that the chiral templating synthesis is yet to be tested. Future work to investigate the role of this complex in the asymmetric transfer hydrogenation of acetophenone is needed. Should the complex prove to be a successful catalyst then other tethering groups could be investigated to try and improve stability towards hydrolysis under reaction conditions.

8 Appendices

8.1 Appendix to Chapter 3

8.1.1 Reynolds Number calculation

The Reynolds number for the FlowNMR apparatus was calculated using the equation for Reynolds number in a circular cross-section pipe:

$$R_e = \frac{QD_h}{\nu A}$$

R_e = Reynolds Number, Q = Volumetric Flowrate (m^3s^{-1}), D_h = Pipe Diameter (m), ν = Kinematic Viscosity (m^2s^{-1}), A = Cross-sectional area (m^2).

For the 1/16" PEEK tubing (I.D. 0.75 mm) with a flowrate of 4 $mLmin^{-1}$ water (ν = $1x10^{-6}$ m^2s^{-1}) the Reynolds number is calculated as follows:

$$R_e = \frac{6.67 \times 10^{-8}\, m^3 s^{-1} \cdot 7.5 \times 10^{-4}\, m}{1.00 \times 10^{-6}\, m^2 s^{-1} \cdot 4.42 \times 10^{-7}\, m^2} = 112.7$$

Systems with $R_e < 2300$ are usually considered to be in the laminar flow regime.[10]

8.1.2 Diagrams

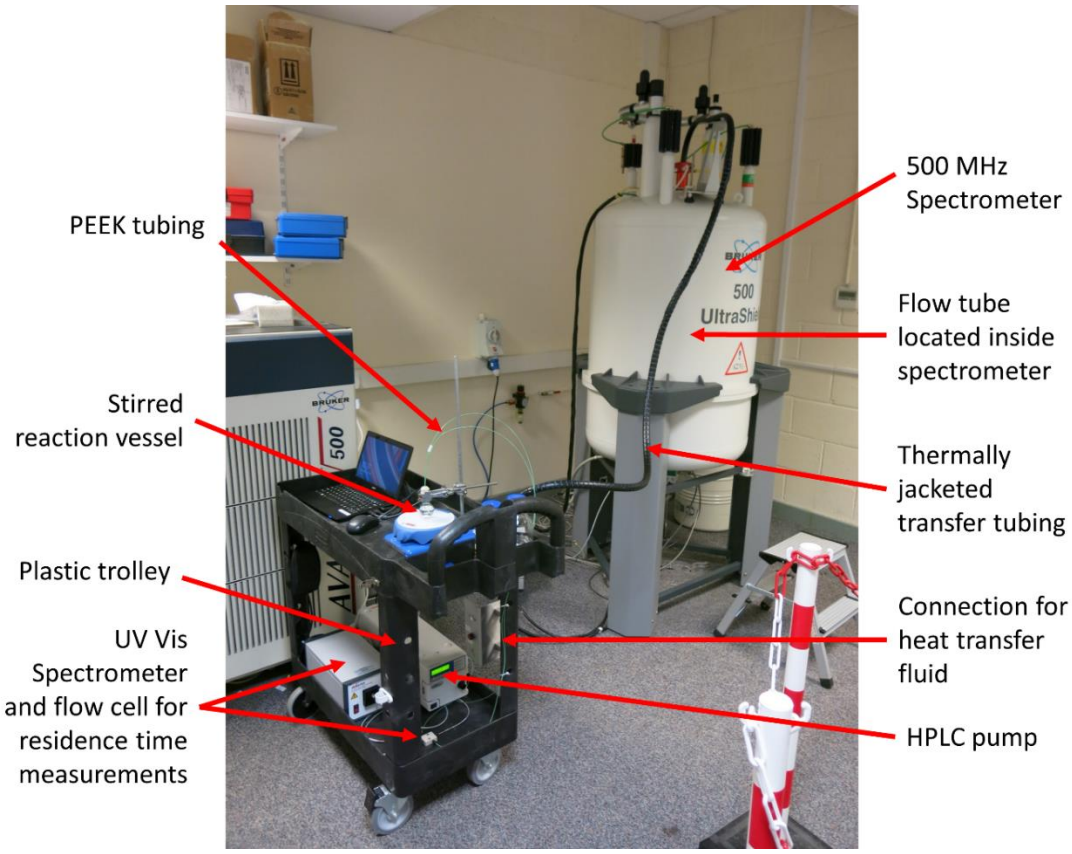

Figure 8.1.1: *FlowNMR experimental setup, showing location of apparatus on trolley next to NMR spectrometer.*

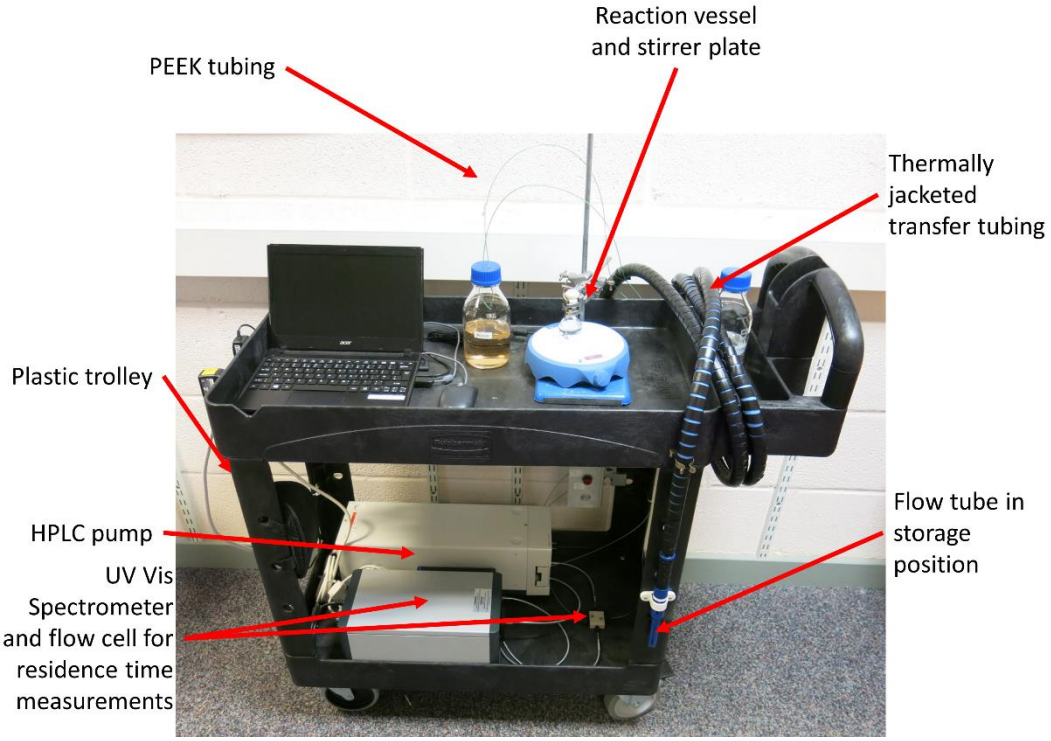

Figure 8.1.2: *FlowNMR experimental setup, showing apparatus in storage position.*

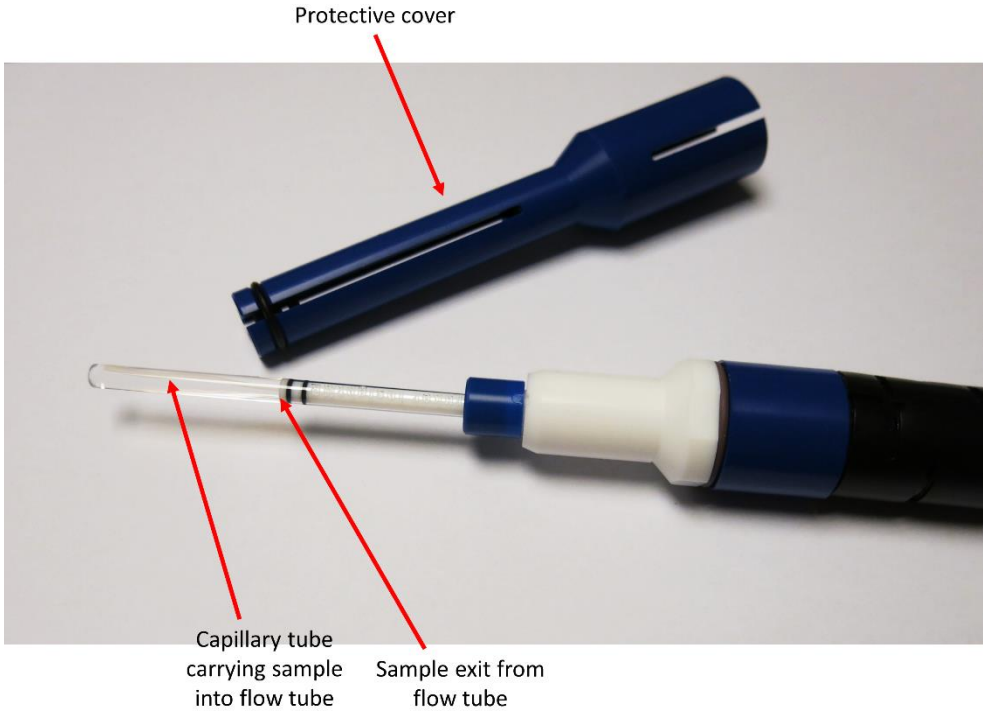

Figure 8.1.3: *FlowNMR flow tube.*

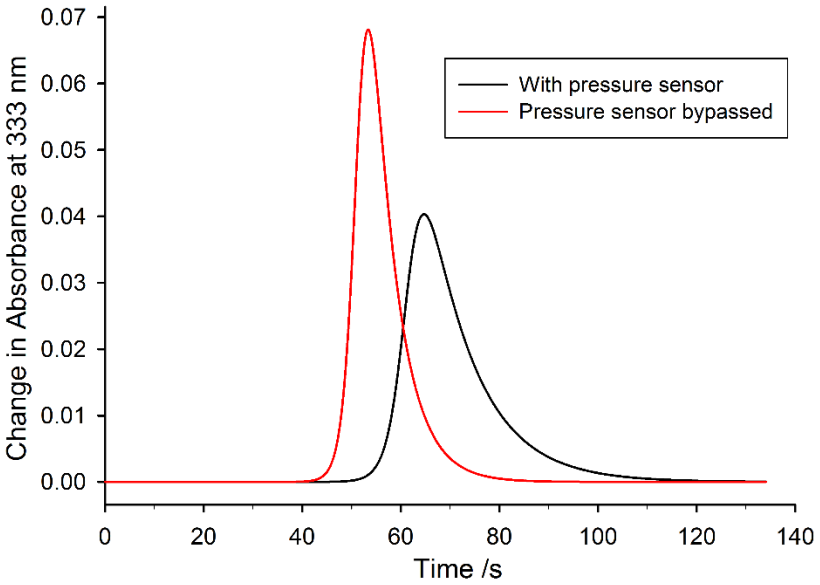

Figure 8.1.4: Residence time distribution profiles for the apparatus described in Figure 1 at a flowrate of 4 mLmin-1 (acetone, 25˚C), comparing the effects on residence time distribution with and without the pump pressure sensor (flow tube connected; cf. Figure 2).

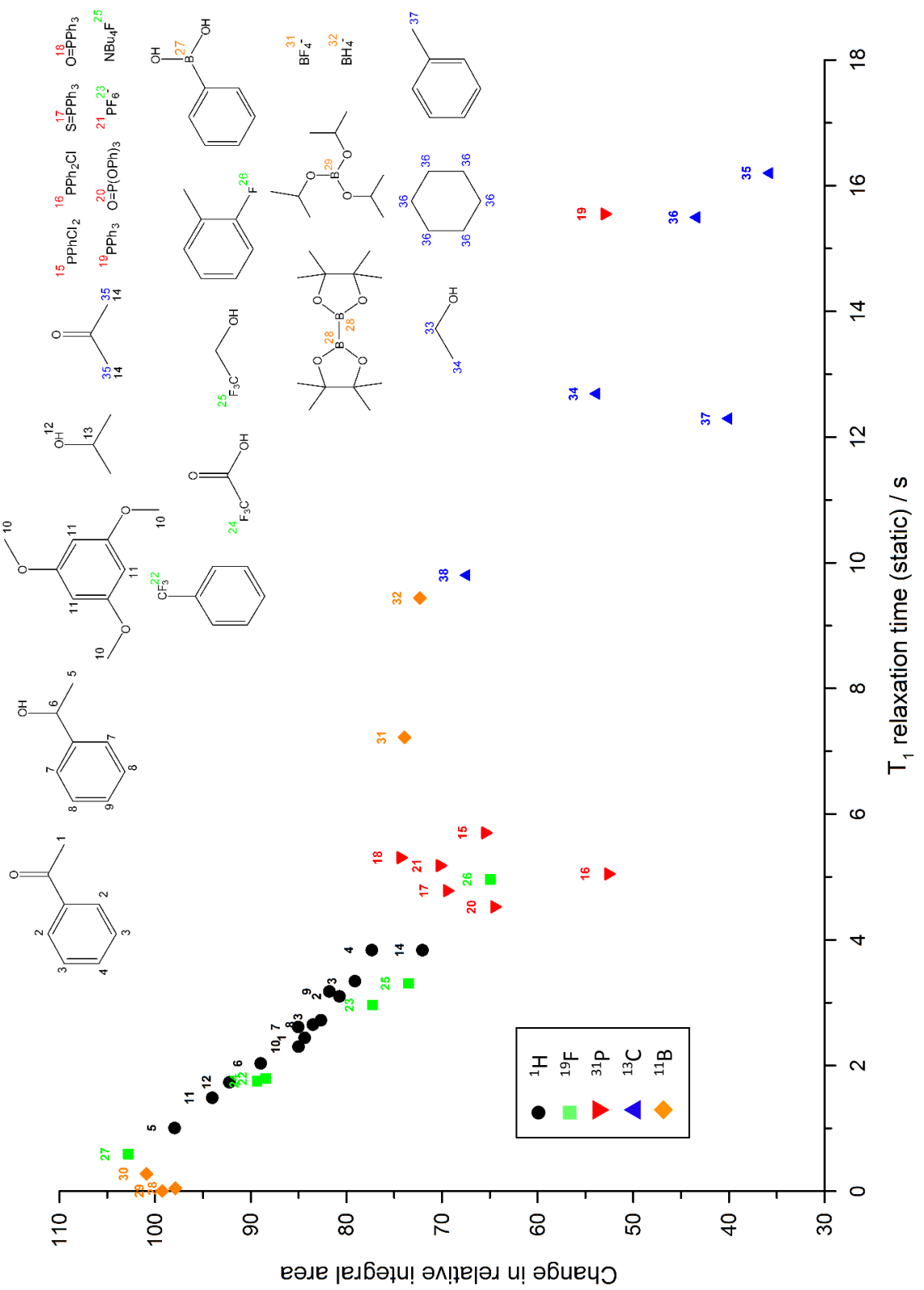

Figure 8.1.5: *Correlation between the decrease in integral area at a flow rate of 4 mLmin^{-1} and the T_1 relaxation time at a flow rate of 0 mLmin^{-1} for a variety of commonly used NMR nuclei, with structural assignment (25°C, 30° pulse, inverse gated decoupling for ^{31}P and ^{13}C, various delay and acquisition times – see experimental section for details).*

8.1.3 Additional Experimental Details

Comparison between different spectrometers was performed using a mixture of acetophenone, 1-phenylethanol, acetone and 1,3,5-trimethoxybenzene in isopropanol with a standard 30° pulse sequence (15 sec delay, 4 sec acquisition time, 8 scans) at flowrates between 0-4 $mLmin^{-1}$. Tests were performed using a Bruker 500 MHz Avance II+ Ultrashield spectrometer (broadband BBO probe), a Bruker 400 MHz Avance Ultrashield Spectrometer (broadband BBO probe), a Bruker 250 MHz Avance Spectrometer ($^{13}C/^{1}H$ dual probe) with an Oxford/Spectrospin unshielded magnet, and a Bruker Avance III 400 MHz spectrometer (broadband BBO probe) with an Oxford Instruments unshielded magnet.

Triple solvent suppression using WET was carried out with the Bruker pulse program "wetdc", using a standard LC-NMR automated acquisition program, "au_lc1d" that first acquires a scout scan to identify and subsequently suppress the desired number of solvent peaks.

8.1.4 Example Methodology for FlowNMR reaction:

In the case of air sensitive reactions, the flow tube and apparatus were purged with a flow of dry nitrogen for at least 30 minutes before use to remove any traces of air or moisture in the system. The system was then purged with fresh, inert solvent for a minimum of 5 minutes at 4 $mLmin^{-1}$ before connecting to the reaction vessel containing the reagents and solvent under an atmosphere of dry nitrogen. The solution volume in the flask was adjusted considering the volume of solvent already in the apparatus; typically an overall liquid volume of 10 mL was used. Where possible the final reagent or catalyst was not added to the reaction mixture until ready to start the reaction. The reaction mixture was circulated around the apparatus for several residence times to ensure the sample was uniformly mixed throughout the apparatus.

The flow tube was then inserted into the spectrometer and automated shimming and tuning routines were performed. Best results were obtained if automated shimming and tuning was performed on static samples, however acceptable results were still obtained in flow. Frequency lock was switched off when using non-deuterated solvents, and shimming performed on proton peaks. Manual fine tuning of X and Y shims was often required to get a good peak line width. Spectra of the reagents were recorded without flow and again at the flowrate desired for the reaction. Comparison of the integral area of the peaks in each spectrum was used to calculate a correction factor for each reagent peak. (I = peak integral, CF = correction factor).

$$I_{Corrected} = CF \times I$$

$$CF = \frac{I_{Static}}{I_{Flow}}$$

With the sample flowing, data acquisition was started using an automated kinetic routine or dedicated reaction monitoring software, with spectra recorded at specified time intervals. The reaction was then started by the addition of the final reagent or catalyst to the stirred flask using a syringe.

At the end of the reaction, or if intermediates of interest were observed, additional spectra were recorded with and without flow, and correction factors were calculated for the intermediate or product peaks, which were applied to each spectrum to give the final peak areas for calculation of species concentration and plotting of kinetic data.

8.2 Appendix to Chapter 4

8.2.1 Characterisation data for N-allylbenzylamine (1)

^{1}H NMR (500 MHz, CH_3CN) δ = 7.38 – 7.33 (m, 4H, Ar), 7.28 – 7.25 (m, 1H, Ar), 5.96 (ddt, *J* = 17.3, 10.5, 5.4 Hz, 1H, $CH_2C\underline{\mathbf{H}}=CH_2$), 5.23 (dq, *J* = 17.2, 1.8 Hz, 1H, $CH_2CH=C\underline{\mathbf{H}}_2$), 5.12 (ddt, *J*=10.3, 2.1, 1.4 Hz 1H, $CH_2CH=C\underline{\mathbf{H}}_2$), 3.77 (s, 2H, benzylic), 3.24 (dt, *J* = 5.8, 1.5 Hz, 2H, $C\underline{\mathbf{H}}_2CH=CH_2$).

Impurities: Ethyl acetate, N-Allyl-1-phenylmethanimine **(2)**

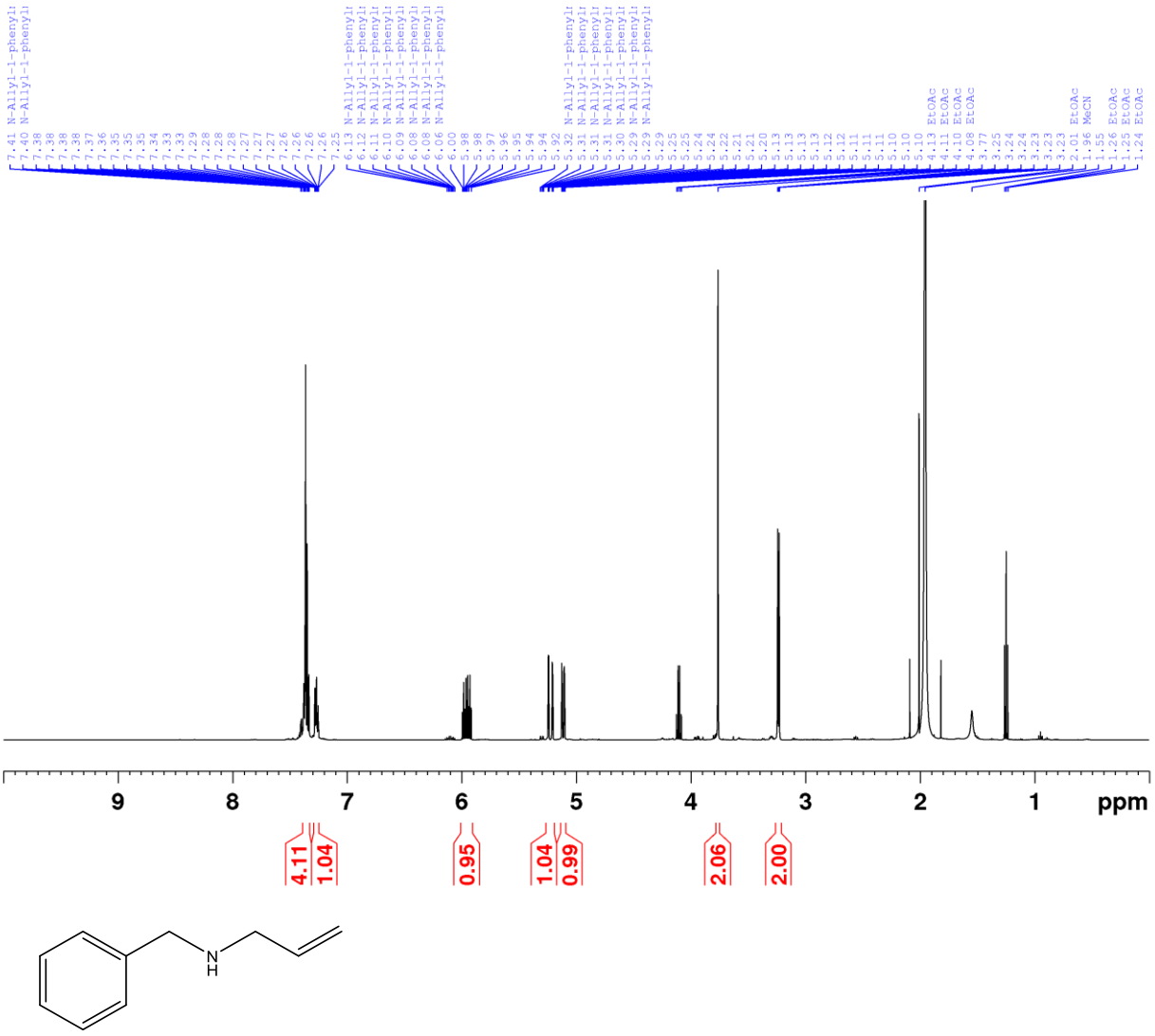

8.2.2 Characterisation data for N-Allyl-1-phenylmethanimine (2)

^{1}H NMR (500 MHz, $CDCl_3$) δ = 8.30 (s, 1H Ar**C<u>H</u>**=N), 7.80 – 7.72 (m, 2H, Ar), 7.46 – 7.38 (m, 3H, Ar), 6.07 (ddt, 1H, J = 17.1, 10.3, 5.7 Hz, CH_2**C<u>H</u>**=CH_2), 5.24 (dq, 1H, J = 17.2, 1.7 Hz, CH_2CH=C**<u>H</u>**$_2$), 5.17 (dq, 1H, J = 10.3, 1.7 Hz, CH_2CH=C**<u>H</u>**$_2$), 4.27 (dq, 2H, J = 5.7, 1.5 Hz, C**<u>H</u>**$_2CH$=CH_2).

Impurities: Acetone, Water, N-allylbenzylamine **(1)**, Benzaldehyde.

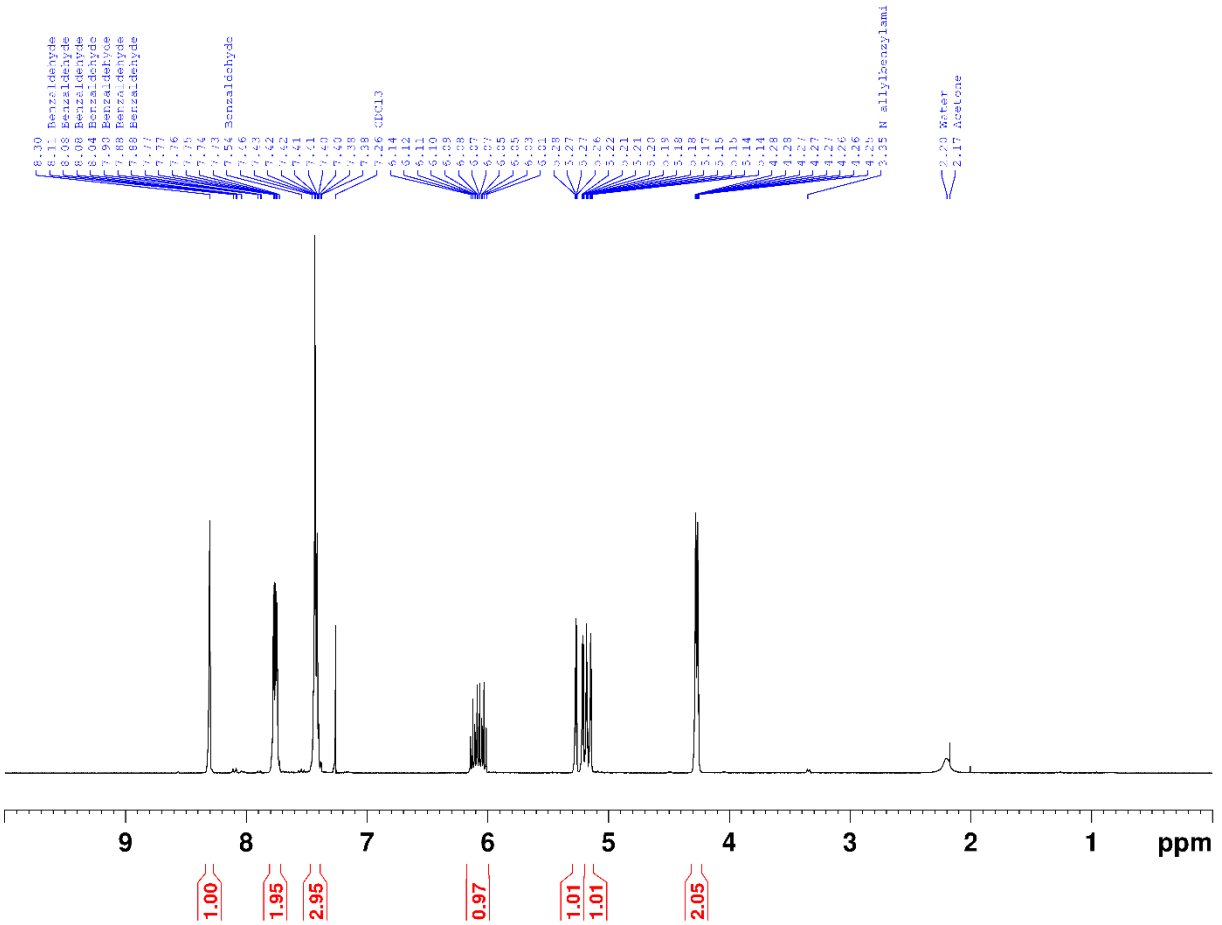

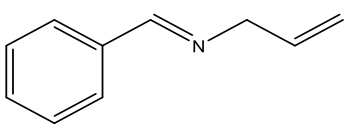

.

8.2.3 Characterisation data for N-Benzyl-1-phenylmethanimine (3)

^{1}H NMR (500 MHz, $CDCl_3$) δ = 8.41 (t, 1H, 1.5 Hz, ArC**H**=N), 7.84 – 7.77 (m, 2H, Ar), 7.46 – 7.41 (m, 3H, Ar), 7.38 – 7.34 (m, 4H, Ar), 7.32 – 7.27 (m, 1H, Ar), 4.85 (d, 2H, J = 1.5 Hz, NC**H**$_2$Ar).

Impurities: Acetone, Benzaldehyde

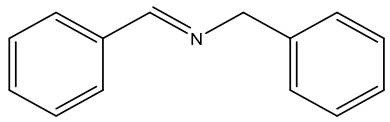

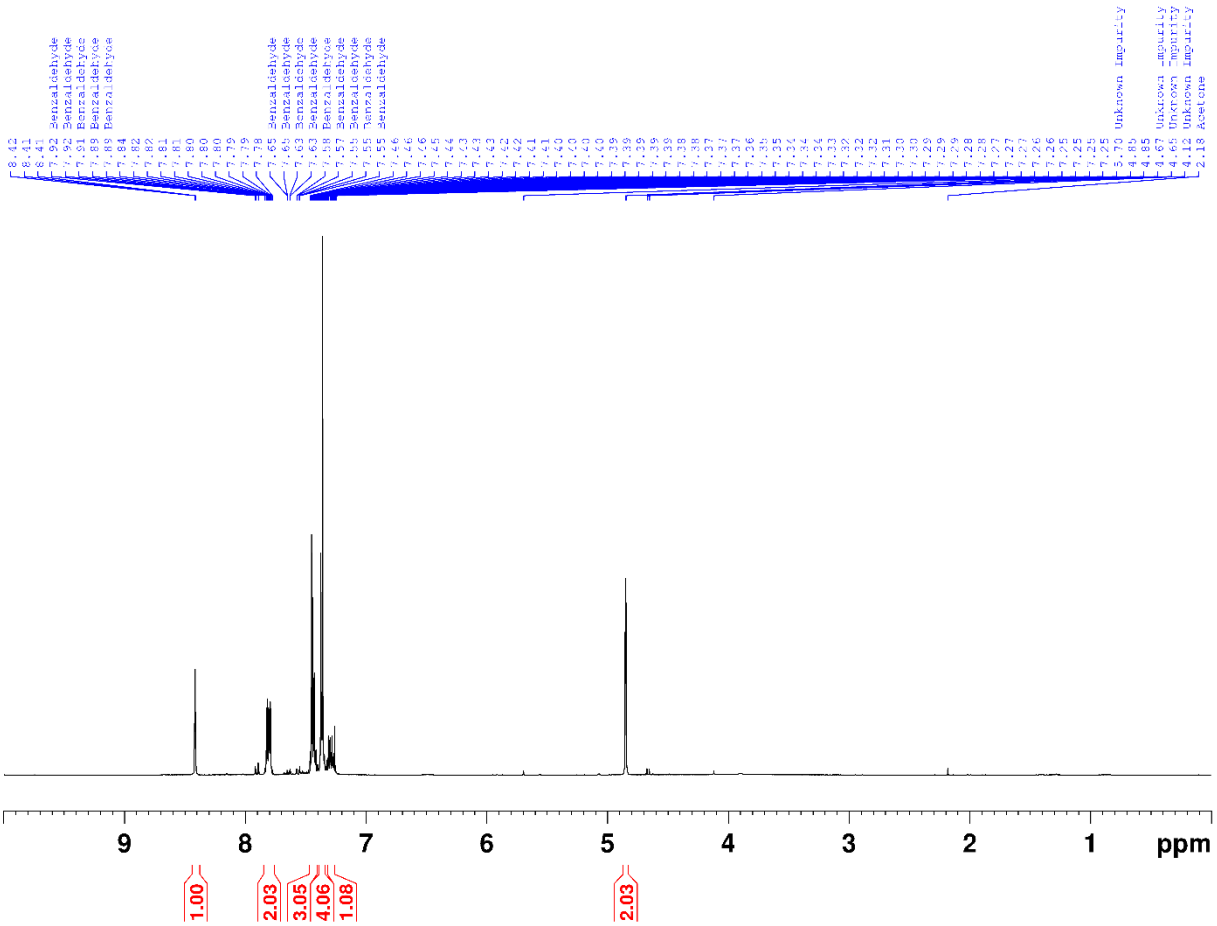

8.3 APPENDIX TO CHAPTER 5

8.3.1 Figures

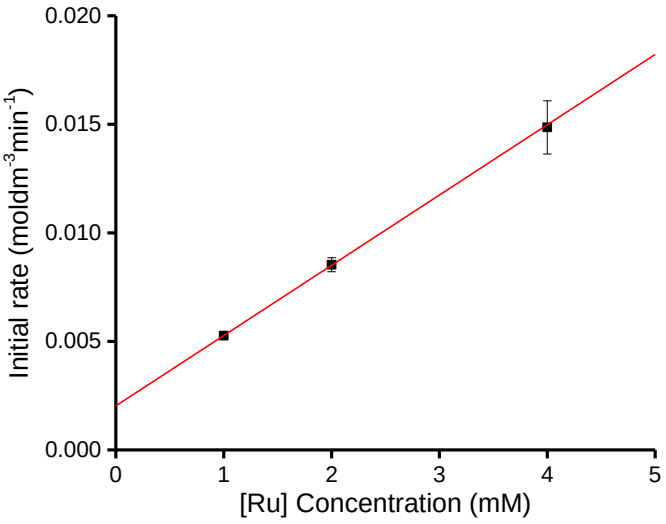

Figure 8.3.1: Initial rate data for the asymmetric transfer hydrogenation of acetophenone and isopropanol catalysed by the Noyori catalyst, (R,R)-1, (0.4 M acetophenone, 0.01 M KOH, 9.5 mL dry isopropanol, 0.1 M 1,3,5-trimethoxybenzene (internal concentration reference), 25°C), showing first order dependence of catalyst concentration on reaction rate.

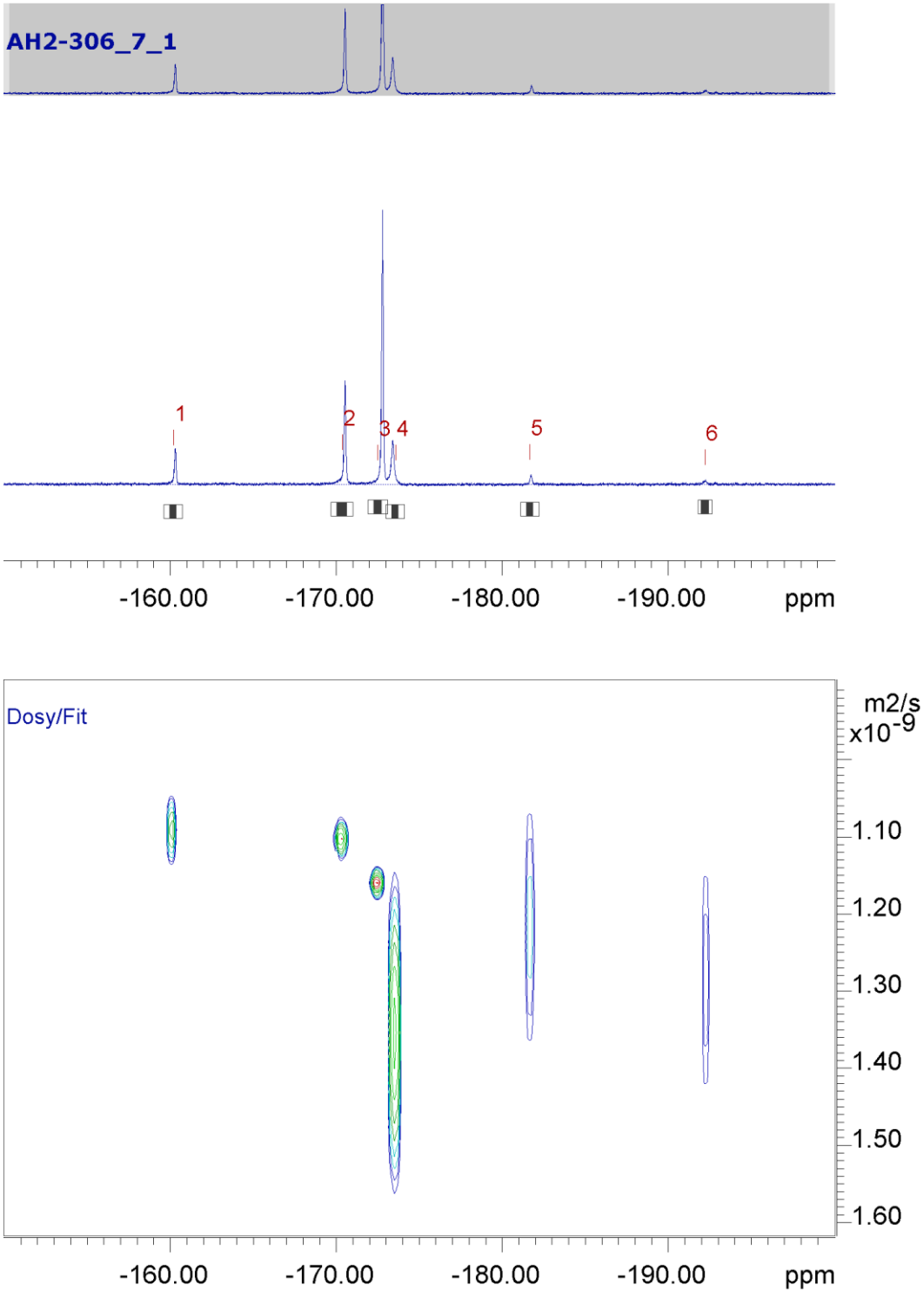

*Figure 8.3.2: ^{19}F DOSY data for complex **4**e in THF-d_8. Peaks 1,2, and 5 correspond to the ortho, meta and para fluorines respectively (peaks are shifted due to solvent interactions). Other peaks were not assigned and show no COSY correlations (Figure 8.3.3) but may correspond to other complexes resulting from interactions with THF solvent molecules.*

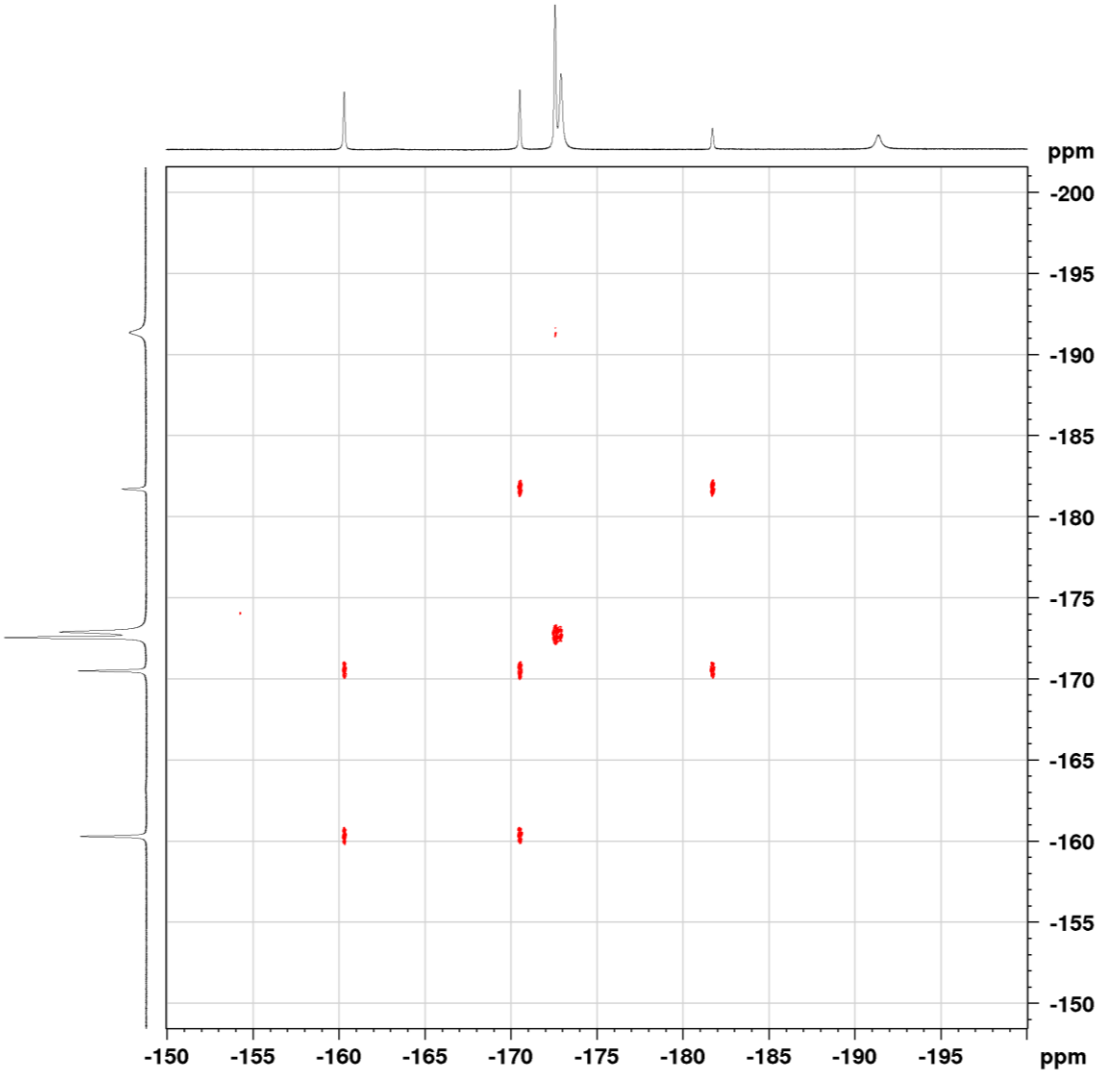

*Figure 8.3.3: ^{19}F COSY spectrum of complex **4**e in THF-d_8.*

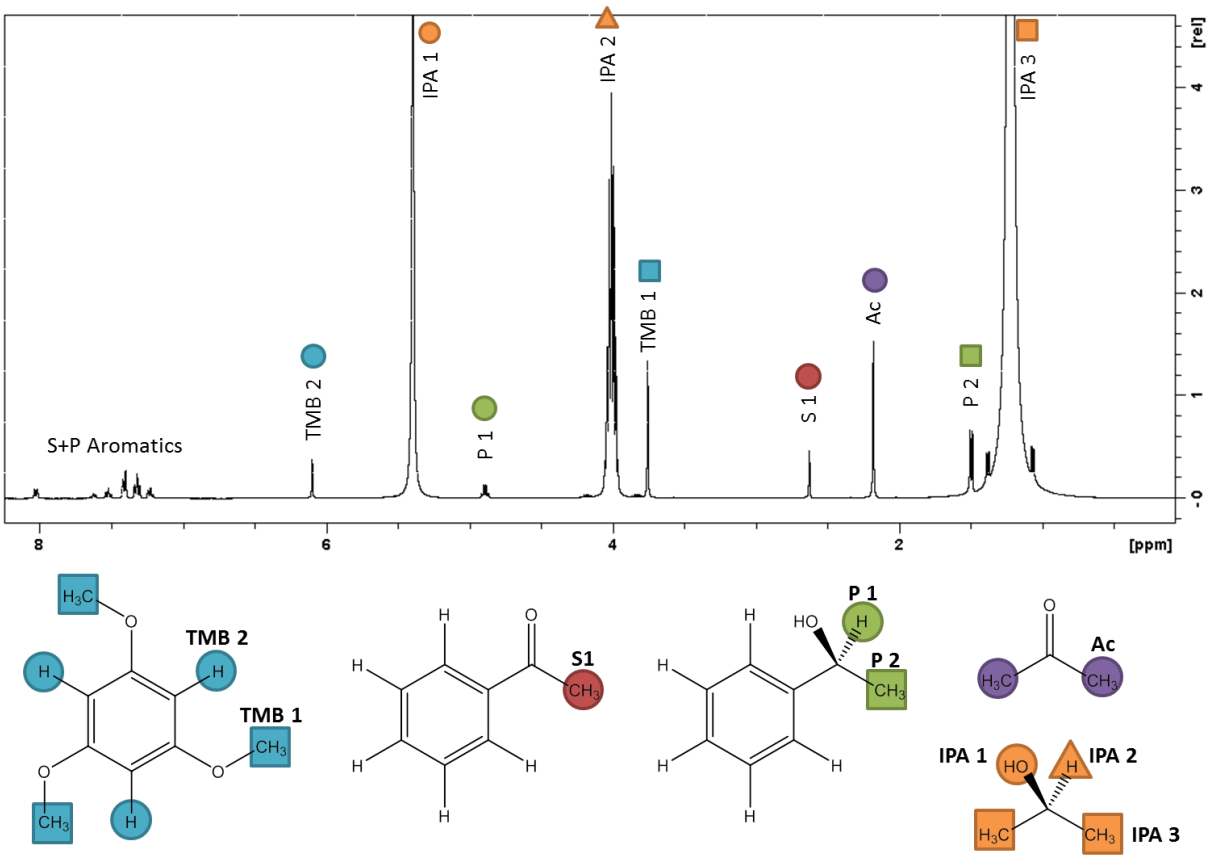

Figure 8.3.4: Sample spectrum of reaction mixture showing product, substrate, reference and solvent ^1H NMR peaks. [TMB: trimethoxy benzene, S: Substrate (Acetophenone), P: Product (1-phenylethanol), Ac: Acetone, IPA: Isopropanol].

8.3.2 Kinetic Modelling

Kinetic modelling was performed with COPASI 4.15 Biochemical modelling software, using a deterministic (LSODA) time course model (10000 s duration, 1 s time interval).[229] Since individual rates of elementary reaction steps are not known, values for the kinetic parameters were chosen to qualitatively provide a good visual fit with experimental data. The purpose of the kinetic model is to assess the viability of the proposed mechanism by comparison of experimental and simulated trends, and kinetic parameters do not necessarily represent true reaction rates.

Species and starting concentrations:

Species	**Starting Concentration (mmol/mL)**
Propan-2-ol	12.64
Acetone	0
Acetophenone	0.4
1-phenylethanol	0
KOH	0.02
1	0.002
2	0
3	0
4	0
5	0

Reactions:

1	**1** + KOH -> **2**	irreversible	k_1
2	**2** + Propan-2-ol = **3** + Acetone	mass action (reversible)	k_2, k_{-2}
3	**3** + Acetophenone = **2** + 1-phenylethanol	mass action (reversible)	k_3, k_{-3}
4	**2** + KOH = **4**	mass action (reversible)	k_4, k_{-4}
5	**3** -> **5**	mass action (irreversible)	k_5

Events:

Time = 600 s	Catalyst **1** added
Time = 1200 s	Acetophenone added

Kinetic parameters:

k_1	1000	mL/(mmol*s)
k_2	1	mL/(mmol*s)
k_{-2}	0.032	mL/(mmol*s)
k_3	1	mL/(mmol*s)
k_{-3}	0.168	mL/(mmol*s)
k_4	1	mL/(mmol*s)
k_{-4}	0.1	1/s
k_5	0.0001	1/s

8.3.3 Acetophenone concentration variation

To simulate the effect of varying concentration of acetophenone, the model was run using starting concentrations of acetophenone between 0.2 and 1 moldm^{-3}. All other parameters were identical to those described above. The simulated curves reproduce the trend observed experimentally in Figure 8.3.1 , including the change in equilibrium conversion.

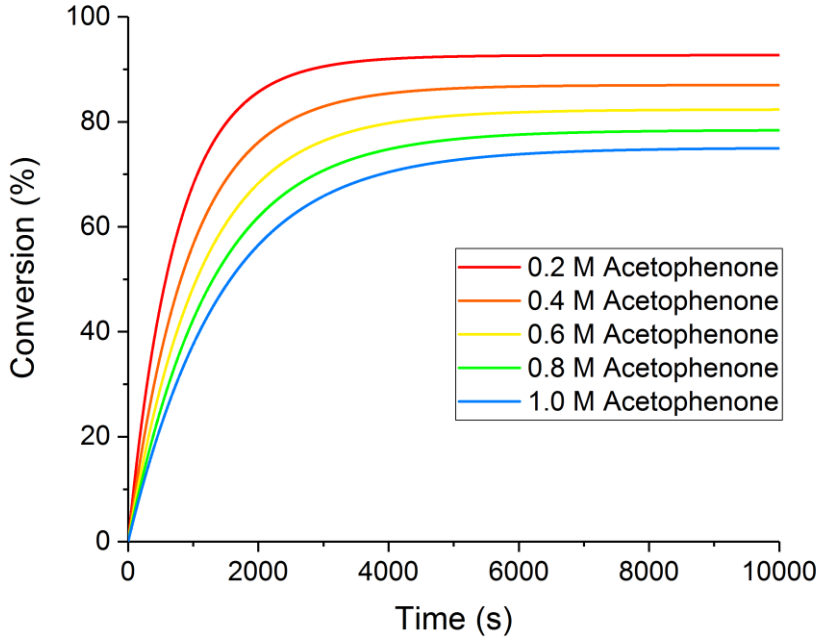

Figure 8.3.5: Simulated reaction kinetics for proposed mechanism of the catalytic transfer hydrogenation of acetophenone to 1-phenylethanol, showing the effect of acetophenone concentration on the reaction rate and equilibrium conversion.

8.3.4 Catalyst concentration variation

To simulate the effect of varying concentration of catalyst, the model was run using starting concentrations of ruthenium chloride complex (1) between 0.001 and 0.005 moldm-3. All other parameters were identical to those described above. The simulated curves reproduce the trends observed experimentally in Figure 5.3 and Figure 8.3.1, including change in reaction rate and catalyst deactivation rate.

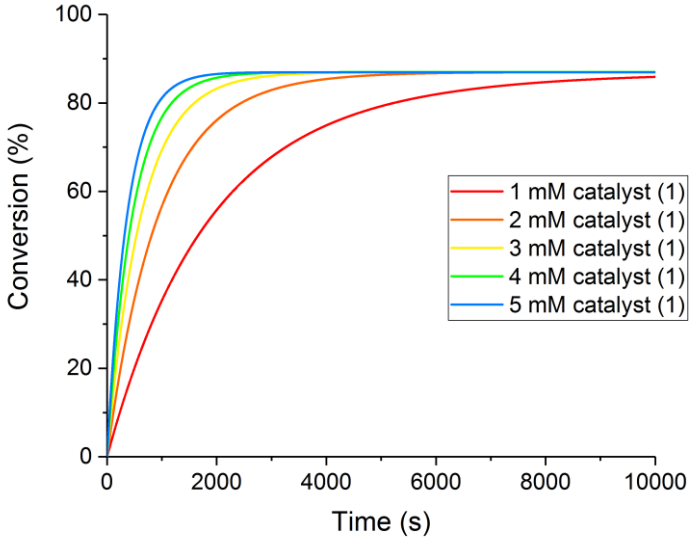

Figure 8.3.6*: Simulated reaction kinetics for proposed mechanism of the catalytic transfer hydrogenation of acetophenone to 1-phenylethanol, showing the effect of catalyst concentration on the reaction rate.*

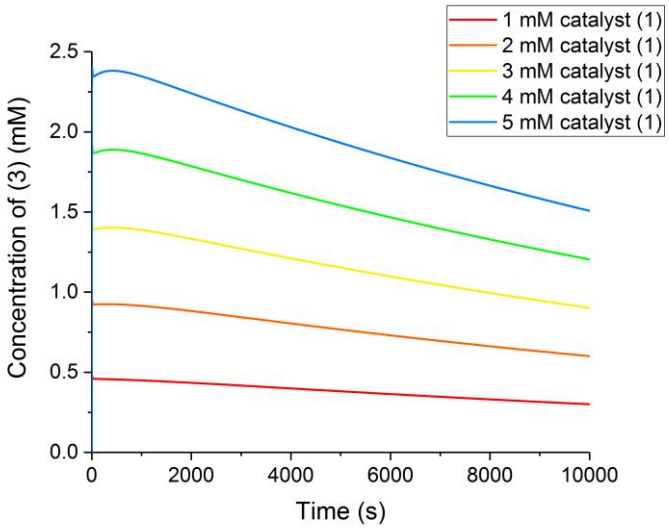

Figure 8.3.7: Simulated reaction kinetics for proposed mechanism of the catalytic transfer hydrogenation of acetophenone to 1-phenylethanol, showing the effect of catalyst concentration on the concentration of hydride ***(3)*** *present during turnover, and deactivation rate.*

8.3.4.1 Modelling of enantiomeric excess

To assess the effect of catalytic turnover on the enantioselectivity of the product, the model was repeated with additional terms for (*R*) and (*S*)-1-phenylethanol. The 98.5 : 1.5 ratio of reaction rates for (*R*) and (*S*) product was determined using the predicted enantioselectivity of the reaction reported from DFT calculations of the transition states.[108]

Species and starting concentrations:

Species	Starting Concentration (mmol/mL)
Propan-2-ol	12.64
Acetone	0
Acetophenone	0.4
(R)-1-phenylethanol	0
(S)-1-phenylethanol	0
KOH	0.02
1	0.002
2	0
3	0
4	0
5	0

Reactions:

1	**1** + KOH -> **2**	irreversible	k_1
2	**2** + Propan-2-ol = **3** + Acetone	reversible	k_2, k_{-2}
3R	**3** + Acetophenone = **2** + (R)-1-phenylethanol	reversible	k_{3R}, k_{-3R}
3S	**3** + Acetophenone = **2** + (S)-1-phenylethanol	reversible	k_{3S}, k_{-3S}
4	**2** + KOH = **4**	reversible	k_4, k_{-4}
5	**3** -> **5**	irreversible	k_5

Events:

Time = 600 s	Catalyst **1** added
Time = 1200 s	Acetophenone added

Kinetic parameters:

k_1	1000	mL/(mmol*s)
k_2	1	mL/(mmol*s)
k_{-2}	0.032	mL/(mmol*s)
k_{3R}	0.985	mL/(mmol*s)
k_{-3R}	0.165	mL/(mmol*s)
k_{3S}	0.015	mL/(mmol*s)
k_{-3S}	0.003	mL/(mmol*s)
k_4	1	mL/(mmol*s)
k_{-4}	0.1	1/s
k_5	0.0001	1/s

The simulated enantioselectivity plot starts at a maximum enantioselectivity of 97% and slowly decreases over the course of the reaction due to the reversible reaction and the cumulative effect of the enantioselectivity of the elementary reaction steps. Both the initial enantioselectivity and the subsequent decline match the experimentally observed data (Figure 5.2) well.

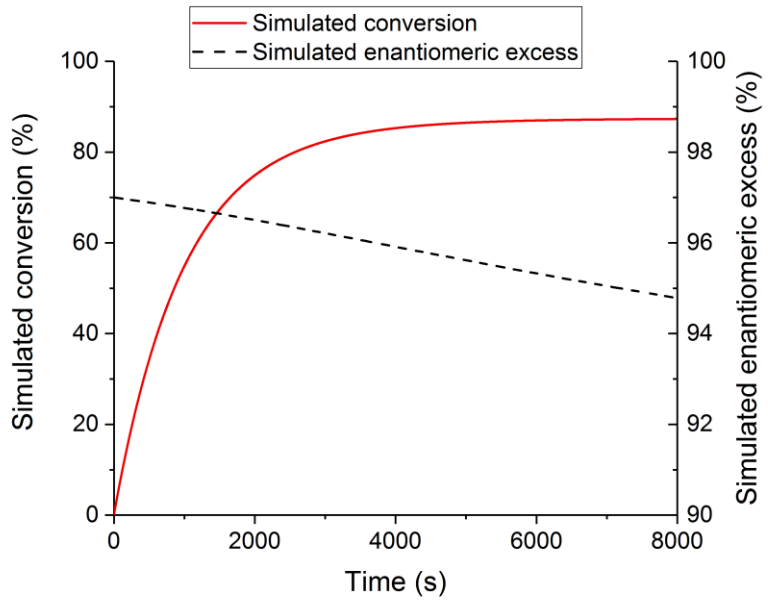

Figure 8.3.8: Simulated reaction kinetics for proposed mechanism of the catalytic transfer hydrogenation of acetophenone to (R) or (S)-1-phenylethanol along with change in enantioselectivity during course of reaction.

8.3.5 Rate law derivation

8.3.5.1 Simple mechanism

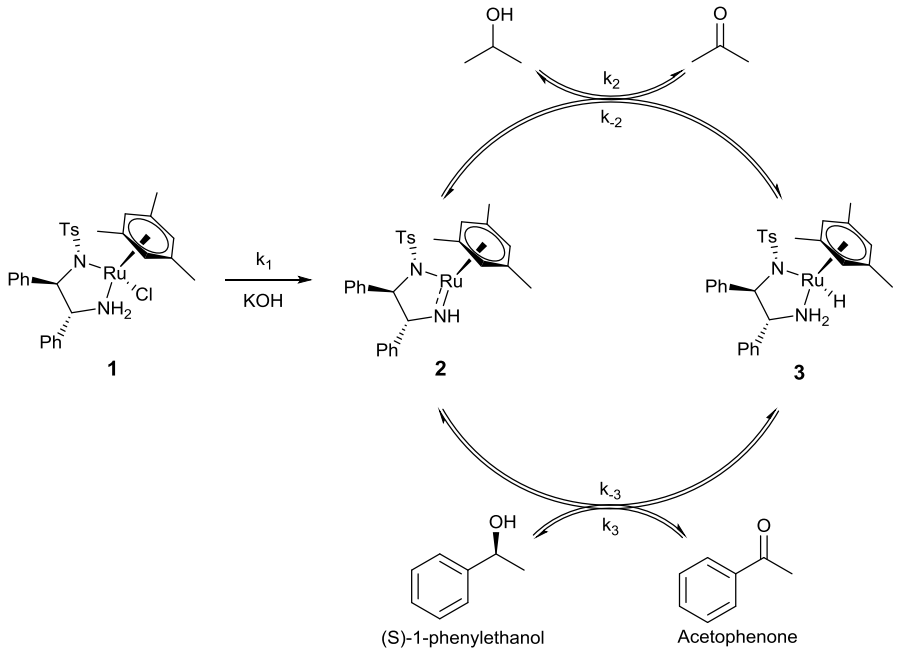

Assumptions:

- $k_1 \gg k_2, k_{-2}, k_3, k_{-3}$, therefore can be neglected from calculation, and **[1]**≈0
- Steady State Approximation

From the mechanism:

Equation A: $rate = \frac{d[PE]}{dt} = k_3[3][Acp] - k_{-3}[2][PE]$

Equation B: $\frac{d[2]}{dt} = -k_2[2][IPA] + k_{-2}[3][Ac] + k_3[3][Acp] - k_{-3}[2][PE] \cong 0$

Equation C: $[Ru] \cong [2] + [3]$

Rearranging Eq. B: $k_2[2][IPA] + k_{-3}[2][PE] = k_{-2}[3][Ac] + k_3[3][Acp]$

$$\frac{[2]}{[3]} = \frac{k_{-2}[Ac]+k_3[Acp]}{k_2[IPA]+k_{-3}[PE]} = K_{cat} \quad \text{[Equation D]}$$

Combining Eq. C + D: $[Ru] = K_{cat}[3] + [3] = (K_{cat} + 1)[3]$

$$[3] = (K_{cat} + 1)^{-1}[Ru] \quad \text{[Equation E]}$$

Combining Eq. A + D: $rate = k_3[3][Acp] - k_{-3}[3][PE]K_{cat}$

$$= (k_3[Acp] - k_{-3}[PE]K_{cat})[3]$$

$$\boldsymbol{rate = (k_3[Acp] - k_{-3}[PE]K_{cat})(K_{cat} + 1)^{-1}[Ru]}$$

8.3.5.2 With deactivation

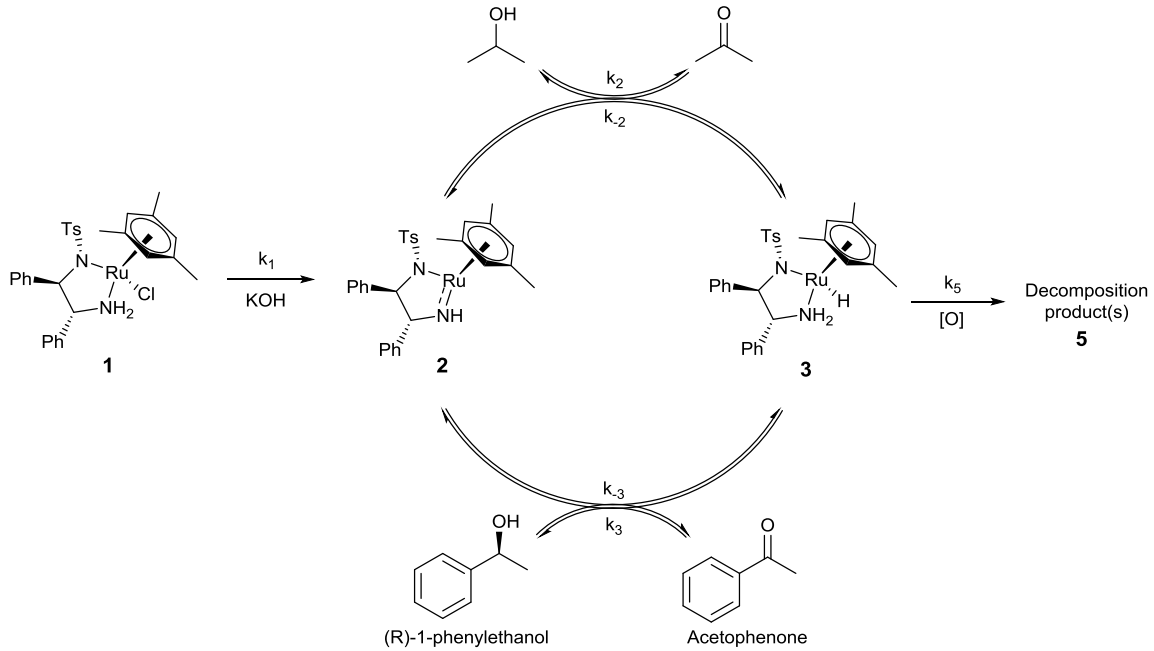

For the reaction without deactivation:

$$rate = (k_3[Acp] - k_{-3}[PE]K_{cat})(K_{cat} + 1)^{-1}[Ru]$$

$$K_{cat} = \frac{k_{-2}[Ac] + k_3[Acp]}{k_2[IPA] + k_{-3}[PE]}$$

Since k_2, k_{-2}, k_3, k_{-3} are assumed to be independent of catalyst deactivation, the on-cycle reaction is unchanged, however the overall reaction rate decreases over time as catalyst is removed from the cycle:

Equation F: $$\frac{d[Ru]_{active}}{dt} = -k_5[3]$$

Equation E: $$[3] = (K_{cat} + 1)^{-1}[Ru]_{active}$$

Combining Eq. E and F: $$\frac{d[Ru]_{active}}{dt} = -k_5(K_{cat} + 1)^{-1}[Ru]_{active}$$

$$\int_0^t \frac{d[Ru]_{active}}{[Ru]_{active}} = -\int_0^t (K_{cat} + 1)^{-1} k_5 dt$$

$$[Ru]_{active} = [Ru]_0 \exp\left(\frac{-k_5 t}{K_{cat}+1}\right)$$

Combining this with the previously derived rate law:

$$\boldsymbol{rate = (k_3[Acp] - k_{-3}[PE]K_{cat})(K_{cat} + 1)^{-1}[Ru]_0 \exp\left(\frac{-k_5 t}{K_{cat} + 1}\right)}$$

8.3.5.3 With deactivation and off-cycle species

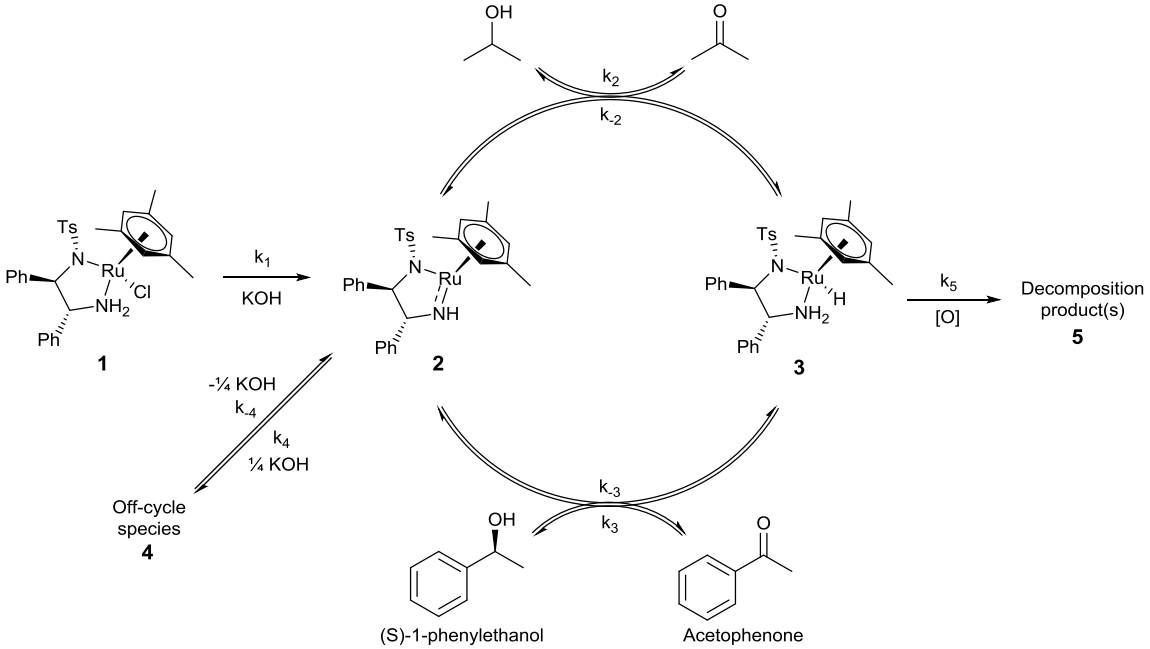

Assumptions:

- $k_1 \gg k_2, k_{-2}, k_3, k_{-3}$, therefore can be neglected from calculation. $[1] \approx 0$
- Steady State Approximation for on-cycle equilibria
- Quasi-equilibrium approximation for off-cycle equilibria

From the mechanism:

Equation A: $$rate = \frac{d[PE]}{dt} = k_3[3][Acp] - k_{-3}[2][PE]$$

Equation G: $$k_4[2][KOH]^{0.25} \cong k_{-4}[4]$$

Equation H: $$\frac{d[2]}{dt} = -k_2[2][IPA] + k_{-2}[3][Ac] + k_3[3][Acp] - k_{-3}[2][PE] - k_4[2][KOH]^{0.25} + k_{-4}[4] \cong 0$$

Equation I: $$[Ru]_{active} \cong [2] + [3] + [4]$$

Combining Eq. G and H: $$\frac{d[2]}{dt} = -k_2[2][IPA] + k_{-2}[3][Ac] + k_3[3][Acp] - k_{-3}[2][PE] - \cancel{k_{-4}[4]} + \cancel{k_{-4}[4]} \cong 0$$

Therefore the on-cycle equilibrium simplifies to that of the simple mechanism:

$$K_{cat} = \frac{k_{-2}[Ac] + k_3[Acp]}{k_2[IPA] + k_{-3}[PE]} \qquad \text{[Equation D]}$$

Combining this with Eq. I: $$[Ru]_{active} = K_{cat}[3] + [3] + [4]$$

$$= K_{cat}[3] + [3] + \frac{k_4[2][KOH]^{0.25}}{k_{-4}}$$

$$= K_{cat}[3] + [3] + \frac{k_4 K_{cat}[3][KOH]^{0.25}}{k_{-4}}$$

$$= \left(K_{cat} + 1 + \frac{k_4 K_{cat}[KOH]^{0.25}}{k_{-4}}\right)[3]$$

$$[3] = \left(K_{cat} + 1 + \frac{k_4 K_{cat}[KOH]^{0.25}}{k_{-4}}\right)^{-1} [Ru]_{active}$$

[Equation J]

Combining Eq. A and J: $rate = k_3[3][Acp] - k_{-3}K_{cat}[3][PE]$

$$= (k_3[Acp] - k_{-3}[PE]K_{cat})[3]$$

Equation K:

$$= (k_3[Acp] - k_{-3}[PE]K_{cat})\left(K_{cat} + 1 + \frac{k_4 K_{cat}[KOH]^{0.25}}{k_{-4}}\right)^{-1} [Ru]_{act.}$$

Including catalyst deactivation:

Equation F: $\frac{d[Ru]_{active}}{dt} = -k_5[3]$

Combining Eq. F and J: $\frac{d[Ru]_{active}}{dt} = -k_5\left(K_{cat} + 1 + \frac{k_4 K_{cat}[KOH]^{0.25}}{k_{-4}}\right)^{-1} [Ru]_{active}$

$$\int_0^t \frac{d[Ru]_{active}}{[Ru]_{active}} = -\int_0^t \left(K_{cat} + 1 + \frac{k_4 K_{cat}[KOH]^{0.25}}{k_{-4}}\right)^{-1} k_5\, dt$$

Equation L:

$$[Ru]_{active} = [Ru]_0 \exp\left(-\left(K_{cat} + 1 + \frac{k_4 K_{cat}[KOH]^{0.25}}{k_{-4}}\right)^{-1} k_5 t\right)$$

Combining Eq. K and L gives the final rate law:

$$\boldsymbol{rate = (k_3[Acp] - k_{-3}[PE]K_{cat})\left(K_{cat} + 1 + \frac{k_4 K_{cat}[KOH]^{0.25}}{k_{-4}}\right)^{-1} [Ru]_0 \exp\left(-\left(K_{cat} + 1 + \frac{k_4 K_{cat}[KOH]^{0.25}}{k_{-4}}\right)^{-1} k_5 t\right)}$$

8.3.5.4 Catalyst equilibrium

From previous equations, the equilibrium between **2** and **3** may be expressed in terms of the equilibrium constant K_{cat}:

$$K_{cat} = \frac{[2]}{[3]} = \frac{k_{-2}[Ac] + k_3[Acp]}{k_2[IPA] + k_{-3}[PE]}$$

The stoichiometry of the reaction allows reagents and products to be expressed in terms of the overall reaction conversion, χ:

Equation M: $[PE] = [Ac]$

Equation N: $[Acp]_0 = [Acp] + [PE]$

Equation O: $[IPA]_0 = [Ac] + [IPA]$

Equation P: $[Ac] = \chi[Acp]_0$

Substituting in Eq. N and O: $K_{cat} = \frac{k_{-2}[Ac]+k_3([Acp]_0-[PE])}{k_2([IPA]_0-[Ac])+k_{-3}[PE]}$

Combining with Eq. M: $= \frac{k_{-2}[Ac]+k_3([Acp]_0-[Ac])}{k_2([IPA]_0-[Ac])+k_{-3}[Ac]}$

Combining with Eq. P: $= \frac{k_{-2}\chi[Acp]_0+k_3[Acp]_0(1-\chi)}{k_2([IPA]_0-\chi[Acp]_0)+k_{-3}\chi[Acp]_0}$

Since isopropanol is in large excess, saturation kinetics may be assumed, simplifying the expression further:

$$\boldsymbol{K_{cat} = \frac{k_{-2}\chi[Acp]_0+k_3[Acp]_0(1-\chi)}{k_2[IPA]_0+k_{-3}\chi[Acp]_0}}$$

8.4 APPENDIX TO CHAPTER 6

8.4.1 Ts(ethylenediamine)

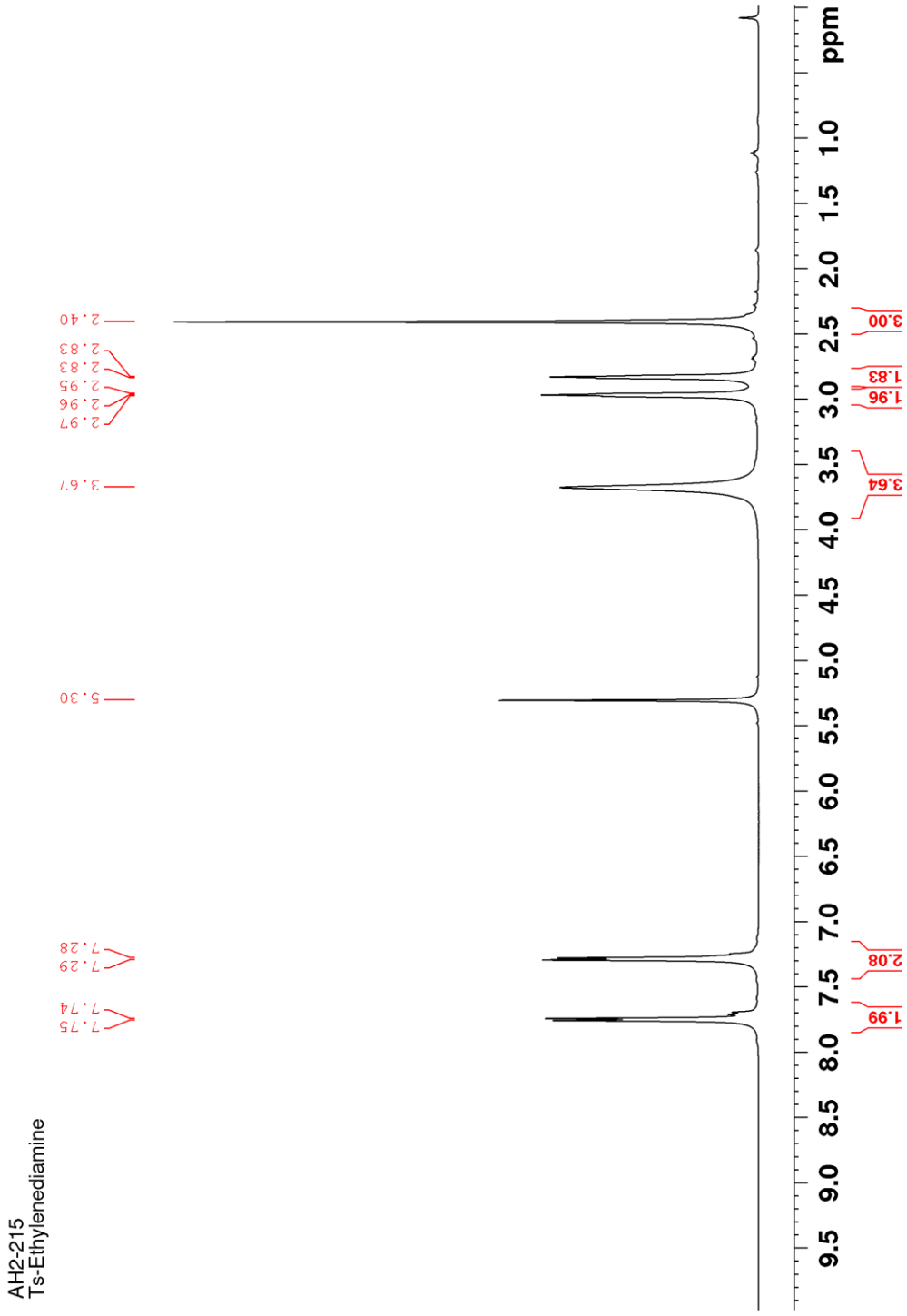

8.4.2 $[RuCl_2(mesitylene)]_2$

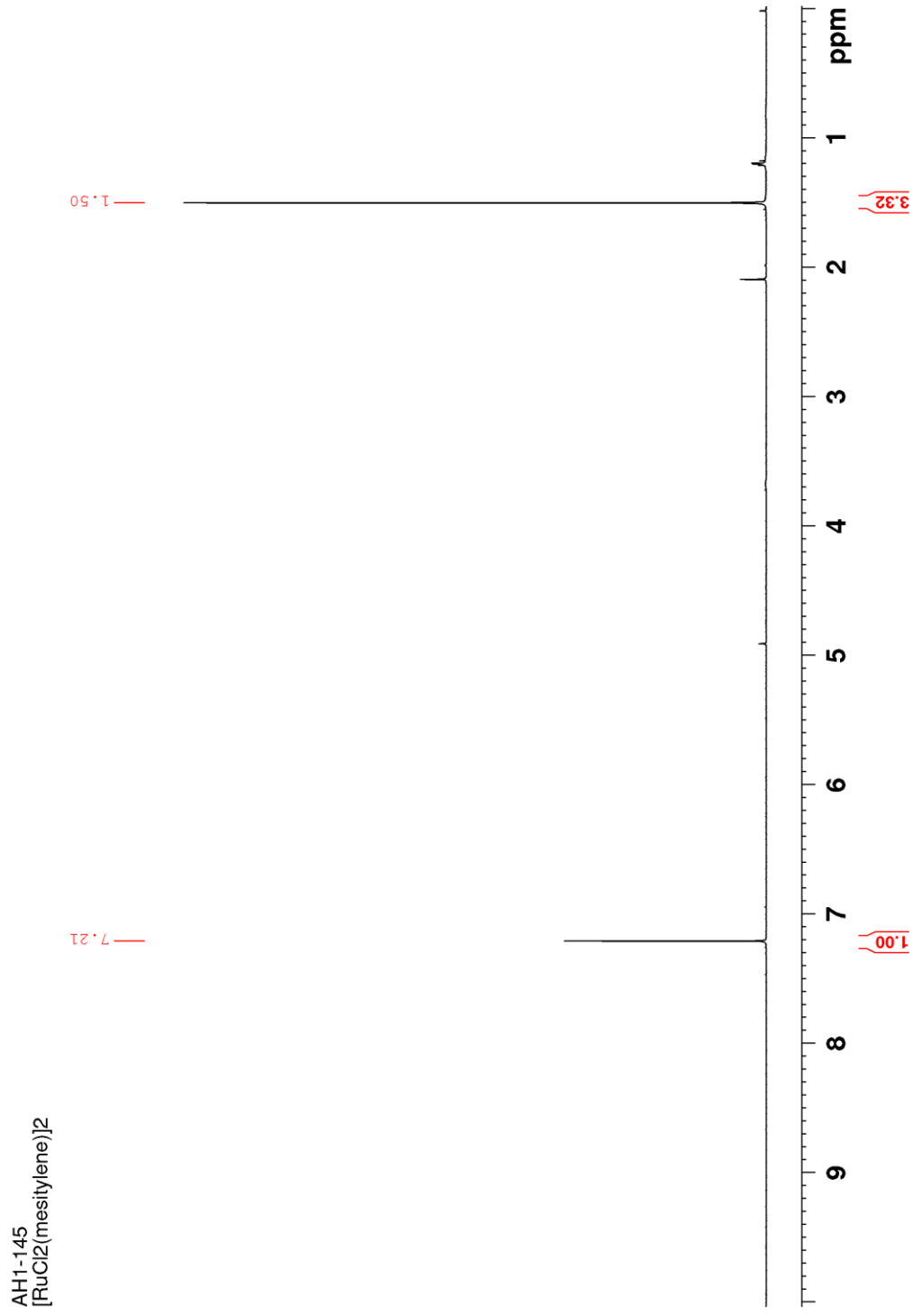

8.4.3 1,3-dihydro phenylacetic acid

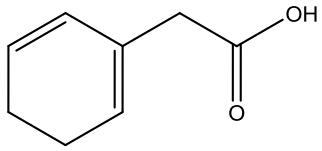

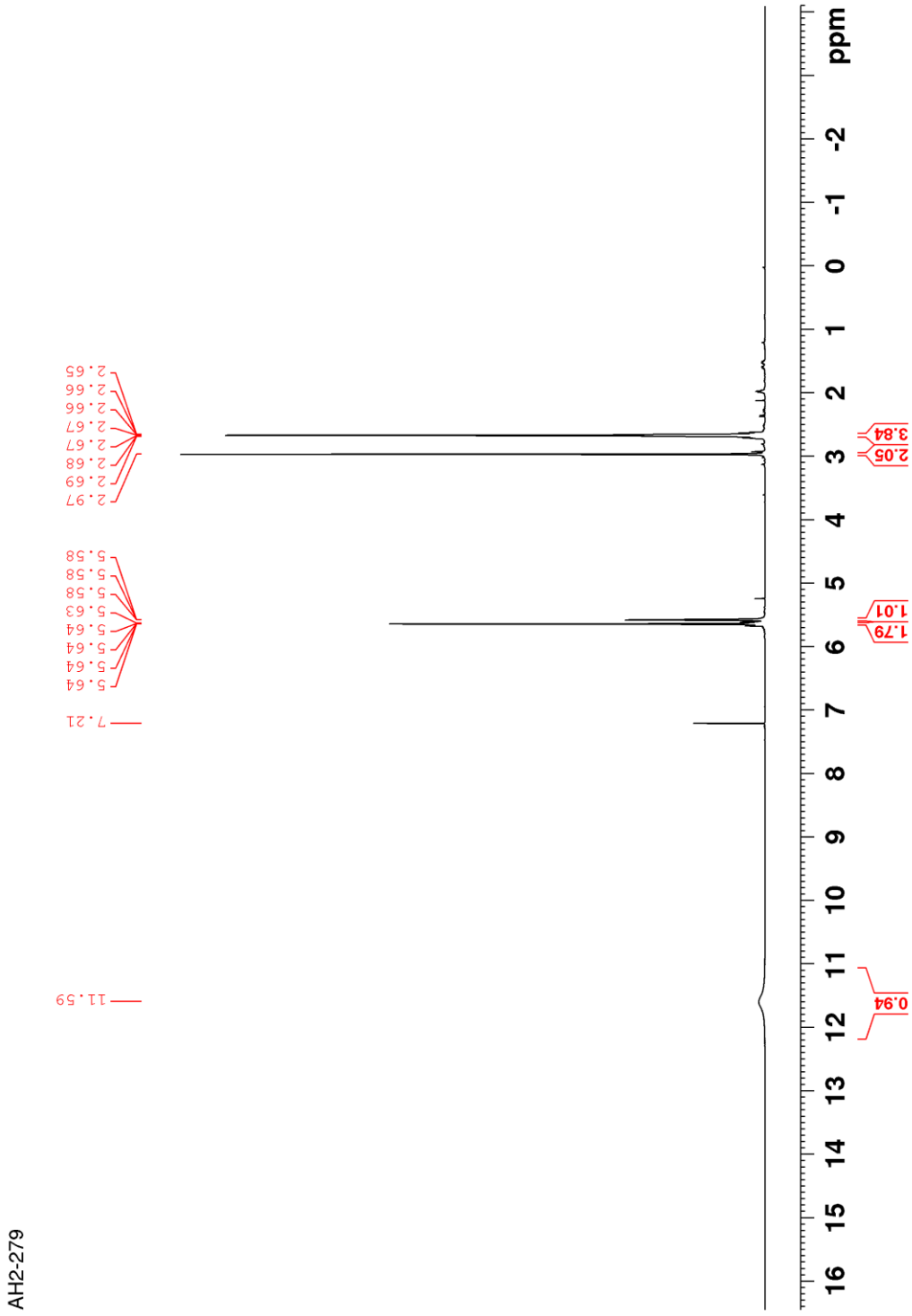

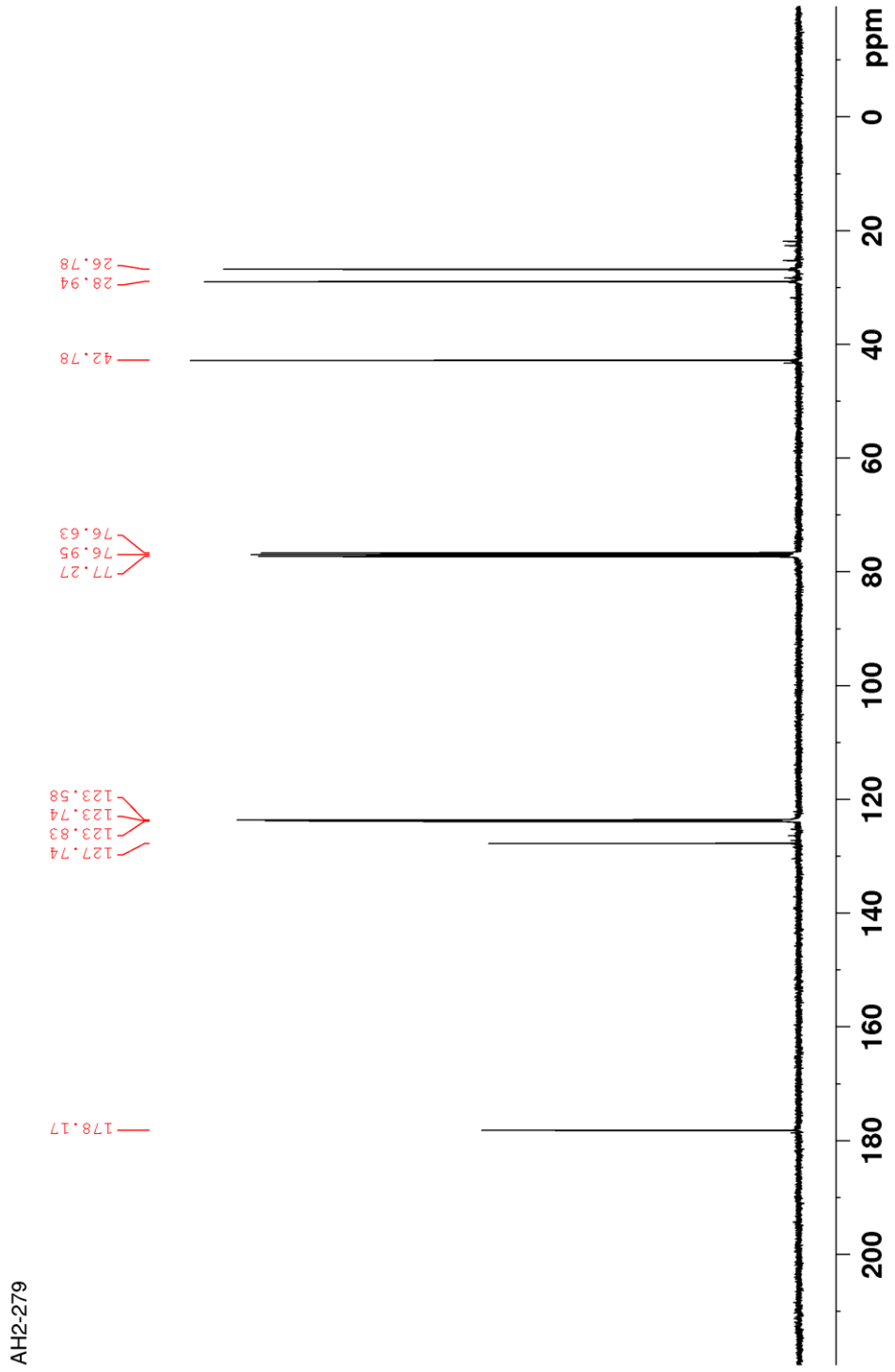
AH2-279
178.17
127.74
123.83
123.74
123.58
77.27
76.95
76.63
42.78
28.94
26.78
ppm
0
20
40
60
80
100
120
140
160
180
200

8.4.4 $[RuCl_2(\text{ethyl phenylacetate})]_2$

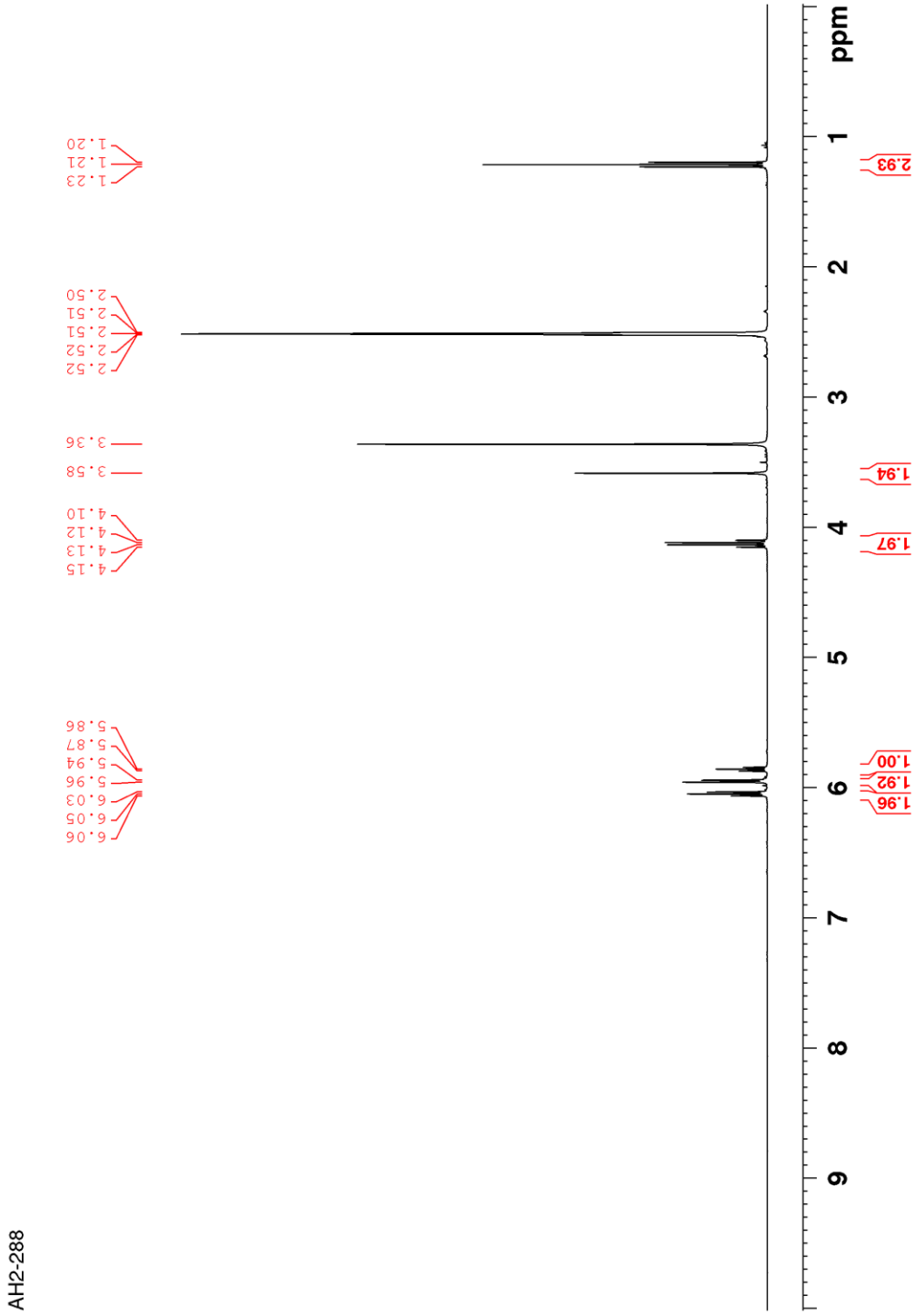

Hidden Force Looking Machine

This machine looks at things using radio waves and a special hidden force made by putting power through very cold metal. Lots of the machine is taken up keeping the metal cold using two different sorts of cold water-like air, but there are other bits that make the radio waves and listen to them too.

Very tiny spinning things

The thing we want to look at (as well as everything else) is made up of lots of tiny bits. The tiny bits spin around like a spinning top.

When you put the spinning tops inside the hidden force maker they all line up and start pointing the same way.

If you use the radio to shout at the spinning tops then some of them will start spinning the other way.

Once you stop shouting at them they will start to turn back again, and you can use the radio to listen to them and make a picture to help you understand what the thing looks like.

Radio bit

This bit is like a radio set that sits inside the hidden force maker. If you put the thing you want to look at inside, the radio can listen to it and make a picture to help understand what it is like.

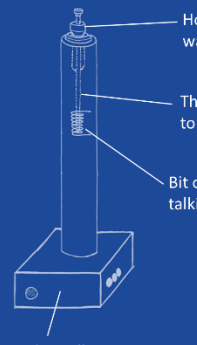

There are also more small hidden force makers around the radio bit to help make sure the hidden force is the same everywhere.

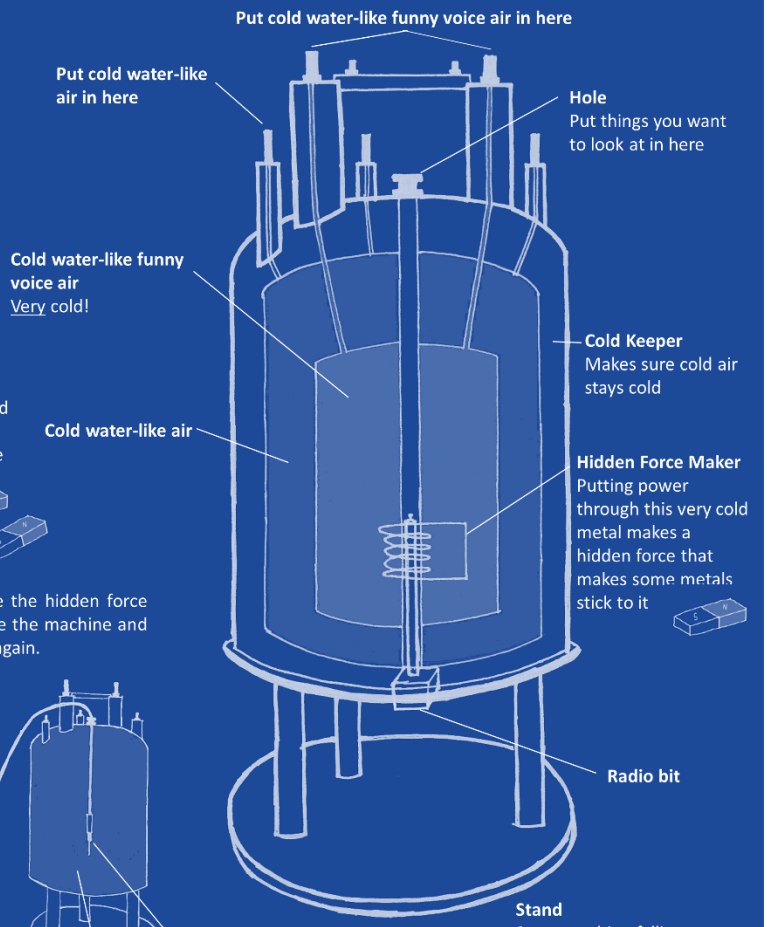

Moving things

If you want to look at something that can't go inside the hidden force machine, then one way to look at it is to put it outside the machine and then move little bits of it inside the machine and back again.